ACCELERATED DEVELOPMENT AND FLIGHT EVALUATION OF ACTIVE CONTROLS CONCEPTS FOR SUBSONIC TRANSPORT AIRCRAFT

VOLUME 1 - LOAD ALLEVIATION/EXTENDED SPAN DEVELOPMENT AND FLIGHT TESTS

LOCKHEED-CALIFORNIA COMPANY
COORDINATED BY: J. F. JOHNSTON

SUMMARY

This is Volume 1 of a two-volume final report on Contract NAS1-14690. The contract covers a cooperative NASA/Lockheed program investigating the use of active controls in a modern wide body transport, the Lockheed L-1011, for increased energy efficiency. Volume 1 covers active wing load alleviation, Tasks 1 (Baseline Tests) and 3 (Extended-Span Tests) of the contract, and Volume 2 (NASA CR-159098) covers the Task 2 aft-cg simulation work and active stability augmentation for use with a significantly smaller horizontal tail. The extended span and small tail each result in a 3% fuel saving, for a combined saving of 6%.

The active wing load alleviation uses symmetric motions of the outboard ailerons for Maneuver Load Control (MLC) and Elastic Mode Suppression (EMS), and stabilizer motions for Gust Load Alleviation (GLA). The control laws were derived, after initial exploration of optimal control theory, with the aid of large-scale maneuver loads, flutter and gust loads programs. They were basically similar for both the baseline and extended-span configurations.

Results of laboratory and flight tests in both configurations showed good agreement with analysis. Slow maneuvers verified the MLC, and open- and closed-loop flight frequency response tests verified the aircraft dynamic response to symmetric aileron and stabilizer drives as well as the active system performance. Flight tests in turbulence verified the effectiveness of the active controls in reducing gust-induced wing loads. It was concluded that active wing load alleviation/extended span is proven in the L-1011 and is ready for application to airline service; it is a very practical way to obtain the increased efficiency of a higher aspect ratio wing with minimum structural impact.

TABLE OF CONTENTS

TABLE OF CONTENTS (Cont)

LIST OF FIGURES

LIST OF FIGURES (Cont.)

LIST OF FIGURES (Cont.)

LIST OF FIGURES (Cont.)

LIST OF FIGURES (Cont.)

LIST OF FIGURES (Cont.)

LIST OF TABLES

SYMBOLS AND ACRONYMS

$\bar{A}$	RMS response (load, acceleration, etc.) per unit RMS gust velocity, Section 5.7
ACEE	Aircraft Energy Efficiency
ACS, ACT	Active Control System, Active Control Technology
AFCS	Automatic Flight Control System
AIC	Aerodynamic Influence Coefficient
AO	Automatic Observer
AS	Augmented Stability
BL	Butt Line
CAA	Civil Aviation Authority (British)
CCV	Control Configured Vehicle
CDC	Central Data Computer
CG, c.g.	Center of Gravity
CRT	Cathode Ray Tube
EET	Energy Efficient Transport
EHV	Electrohydraulic Valve
EMS	Elastic Mode Suppression
f	Frequency, Hz
FAA	Federal Aviation Administration
FAMAS	Flutter and Matrix Algebra System
FAR	Federal Aviation Regulations
FCES	Flight Control Electronic System
FET	Field Effect Transistor

FFT	Fast Fourier Transform
FM	Frequency Modulation
FMA	Flutter Margin Augmentation
FS	Fuselage Station
G, g	Gravity, Damping
GA, GLA	Gust (load) Alleviation
GFAM	Graphics Flutter Analysis Methods
GLP	Gust Loads Programs
GT/FD	Ground Test/Failure Detection
H_s, H_c	Transfer Functions by Spectrum and Cross Spectrum Methods
HS	Horizontal Stabilizer
IRIG	Inter-Range Instrumentation Group
KEAS	Knots Equivalent Airspeed
L	Scale of Turbulence
HEX	Six Elements
LC-X	Load Condition
LVDT	Linear Variable Differential Transducer (position measurement)
M	Mach Number
M_x, M_y	Bending Moment, Torsion Moment
MLC	Maneuver Load Control
NAND	Not And
N_o	Characteristic Frequency (associated with $\bar{A}$)
n_x, n_y, n_z	Longitudinal, Lateral and Normal Load Factors
OA	Outboard Aileron
PCM	Pulse Code Modulation
PFCS	Primary Flight Control System
PSD, psd	Power Spectral Density

q	Dynamic Pressure, Pitch Rate
RC	Roller Coaster maneuver
RE	Reduced Energy
RMS, rms	Root Mean Square
S	Laplace Operator, Wing Area
S_z	Vertical Shear
SAS	Stability Augmentation System
SIC	Structural Influence Coefficient
t	Time
V, V_T	True Airspeed
V_E	Equivalent Airspeed
V_g, V_G	Gust Velocity
VFS	Visual Flight Simulator
VGA	Vertical Gust Analysis (program)
VSS	Vehicle Systems Simulator
WBL	Wing Butt Line
WL	Water Line
WUT	Wind-Up Turn
WWV	Bureau of Standards Radio Station (Time and Frequency Standard)
x, y, z	Longitudinal, Lateral and Vertical Displacements
δ_a, δ_{OA}	Outboard Aileron Deflection
δ_H, δ_{HS}	Horizontal Stabilizer Deflection
η	Fraction of Semispan
ζ	Fraction of Critical Damping
ω, ω_o	Frequency, Natural Frequency, radians/sec

ϕ, θ, ψ	Roll, Pitch, Yaw angles
ϕ_x, ϕ_y	Power Spectrum of Input or Output
ϕ_{xy}	Cross Spectrum between Input and Output
ϕ_i, ϕ_{i-1}, etc.	Power Spectral Value at $f = f_i$, $f_i - \Delta f$, etc., where Δf = frequency spacing in FFT
γ^2	Coherency between Input and Output Power Spectral Values

Subscripts

a, OA	Outboard Aileron
C, c	Commanded
W	Wing
WT, wt	Wing Tip
183, etc.	Butt Line or Fuselage Station designation

SECTION 1

INTRODUCTION

This report covers the application of active controls to a modern wide-body transport, the Lockheed L-1011, for increased aerodynamic efficiency. The term "active controls" is applied to aircraft systems in which controls are moved automatically, independently of the pilot, in response to signals from appropriate sensors. Active controls may be used for flight path control, for load alleviation, and for ride comfort control. This aircraft already contained active controls for flight path management in its Autoland automatic landing system, Reference 1, and for vertical stabilizer design load reduction, Reference 2. These developments were important in setting up some of the basic principles and techniques for active controls in commercial transports: the use of probability-based analyses to maintain a level of safety consistent with past experience (Reference 2), and definition and mechanization of the related redundancy and monitoring requirements (Reference 1).

Building on this base, research was started in 1974 on use of active controls for wing load alleviation and for longitudinal stability augmentation. Although the initial objective of the load alleviation was an increase in gross weight using existing wing structure - an increase of 12 percent was found possible - the rising costs of fuel soon made it apparent that load alleviation could best be used to increase the wing span for improved fuel efficiency. The objective of the stability augmentation studies was drag reduction by use of a smaller horizontal tail and reduced stability margin. Studies and wind tunnel tests indicated that the extended span and the smaller tail would each result in a 3 percent fuel saving, for a combined saving of 6 percent.

Starting in February 1977, these studies were funded on a cost-sharing basis by NASA's Aircraft Energy Efficiency (ACEE) Program, Reference 3, through the Energy Efficient Transport Element (EET), Reference 4, under Contract NAS1-14690. At that time a breadboard load alleviation system was already under test on the full-scale L-1011 Vehicle Systems Simulator (VSS) at Lockheed's Rye Canyon research facility.

Three tasks were defined for the program:

Task 1 - Flight testing of the load alleviation system on an L-1011 aircraft (Baseline Tests).

Task 2 - Design and pilot-in-the-loop simulator testing of a longitudinal stability augmentation system.

Task 3 - Flight testing and evaluation of a modified L-1011 with extended span and active controls.

These tasks have been successfully completed.

This is the Final Report on the basic tasks. The Final Report is divided into two volumes. This is Volume 1, covering the load alleviation work, Tasks 1 and 3. Volume 2, NASA CR 159098, covers the augmented stability work, Task 2.

Lockheed's background philosophy and guidelines for use of active controls in commercial transports have been covered in previous publications and are not repeated here. As previously noted, Reference 1 defined a practical redundant active control system and Reference 2 defined the probability-based analyses. Reference 5, giving the results of Tasks 1 and 2, reiterates the principles of equivalent safety, the probabilistic approach, and their attainment without sacrificing dispatch reliability. Certification considerations are discussed in Reference 6, and details of the design loads task and active load alleviation tradeoffs are given in Reference 7.

SECTION 2

SYSTEM DESCRIPTIONS

2.1 L-1011 AIRFRAME

The L-1011 is a triple-turbofan wide-body transport having the relatively high fuel efficiency and low noise of the high-bypass-ratio fan engine. Figure 2-1 is a plan view showing the 5.8% extended span discussed in this volume and the smaller tail covered in Volume 2. The airplane with extended span is shown in Figure 2-2. Pertinent dimensions of the baseline and extended span configurations are given in Table 2-1.

The baseline wing aspect ratio of 6.95 was proportioned for minimum direct operating costs when fuel costs were about 15 cents per gallon. A relatively low design stress, wide-tread gear and outboard engine location all led to a relatively stiff wing in both bending and torsion, with the result that the outboard ailerons remain effective to the maximum design speed. This characteristic facilitates use of active wing load alleviation which in turn permits the increased span and aspect ratio, with minimum structural impact, appropriate to design for a higher fuel cost level.

2.1.1 Structural Modifications for Extended Span

The span extension is shown in more detail in Figure 2-3. The tip planform was selected to maintain high lift without need for a leading edge slat. The tip does not require anti-icing provisions. The aileron was extended the same amount as the wing; two hinges were added. Although an added aileron damper was not required for the conditions of the test, a third damper is added to the production extended-span aircraft to ensure flutter safety in event of dual hydraulic system failures.

The experimental span extension consists of an aluminum structural box between the extended front and rear spars; a fiberglass formed leading edge,

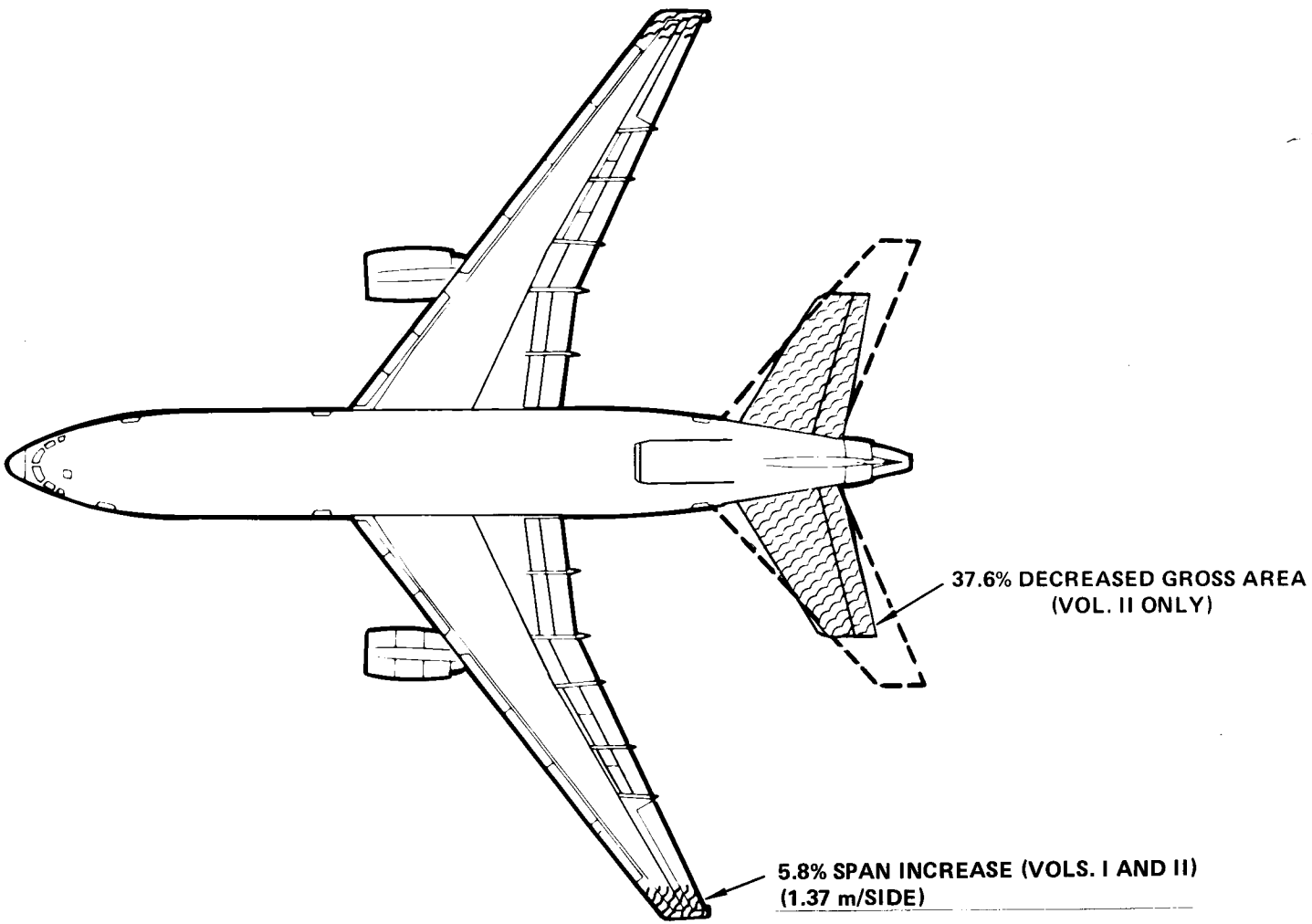

Figure 2-1. L-1011 Modifications for Increased Energy Efficiency

Figure 2-2. L-1011 S/N 1001 Advanced TriStar with Extended Span

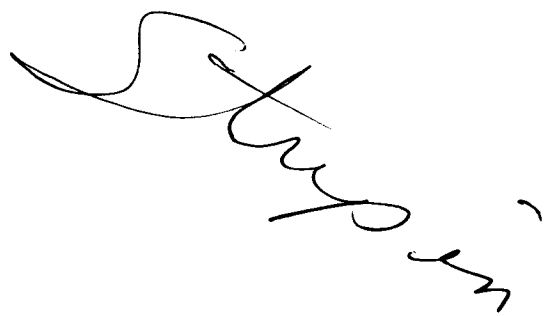

Figure 2-2. L-1011 S/N 1001 Advanced TriStar with Extended Span

TABLE 2-1. CHARACTERISTIC DIMENSIONS OF TEST AIRPLANE

	Baseline (Task 1)	Extended Span (Task 3)
Wing		
Area (Reference)	321.0m^2 (3456 ft.^{2})	328.9m^2 (3541 ft^2)
Span (Reference)	47.24m (155.0 ft.)	50.09m (164.33 ft)
Aspect Ratio	6.95	7.63
Taper Ratio	.30	.26
Sweep at 0.25C	35°	35°
Outboard Aileron		
Area, 2 S_{OA}/S_W	.0260	.0314
Root at	η = .811 (Avg.)	η = .769 (Avg.)
Tip at	η = .988	η = .990
Horizontal Stabilizer		
Area	119.1m^2 (1282 sq. ft.)	
Span	21.82m (71.58 ft.)	
Aspect Ratio	4	
Taper Ratio	.33	

aluminum-covered for lightning protection; a trailing-edge section with ribs supporting the aileron hinge; and a removable fiberglass-and-metal tip section. The rear-facing light was unchanged, but the forward-facing light required new mounting hardware and a new formed transparent cover.

Design loads for the span extension were selected as those of the L-1011-500, which is the version having the most severe loads. The extension was designed by the roll maneuver and symmetric maneuver load analysis cases.

The outer wing was strengthened for about 2 meters inboard of the WBL 910.4 structural joint. This area, which has previously had

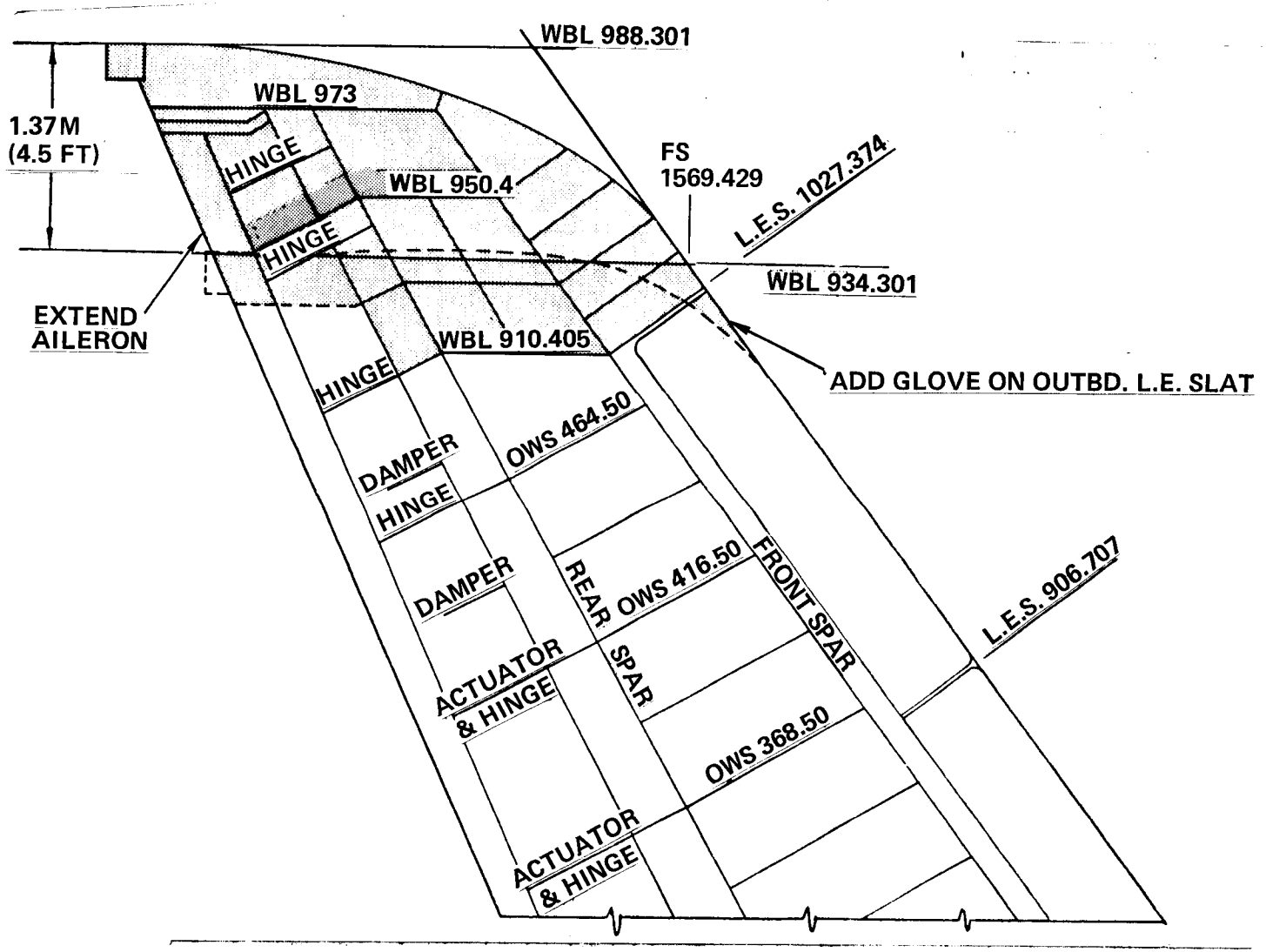

Figure 2-3. Wing Tip and Aileron Extension

near-negligible design loads, required addition of stringers, more area on existing stringers, and doubler sheets on the spar webs and wing box upper and lower skins.

The extensions were similar in mass to the production values of 249 kg (550 lb) per ship; i.e., 31.5 kg/m^2 (6.5 psf). In production, the wing structural modifications inboard of the extensions add a mass of 46 kg (102 lb) per ship.

2.2 PRIMARY FLIGHT CONTROL SYSTEM

The Primary Flight Control System (PFCS) consists of controls for the horizontal stabilizer, rudder, inboard ailerons, outboard ailerons, and spoilers. Geared elevators, driven mechanically by the stabilizer, improve the effectiveness of the horizontal stabilizer. The control systems are irreversible hydro-mechanical systems. All mechanical and electrical controls and instrumentation necessary for operation of the aircraft are located in the flight station compartment. Dual control wheels, columns, and rudder pedals are provided for the captain and first officer. These flight controls are conventional in operation and connect to control cable paths (dual in pitch and roll) which terminate at the pitch, roll, and yaw aft cable quadrants. The surface actuators are multiply redundant for all axes. In the flight station area, the pitch and the roll dual-control paths are interconnected by couplers so that either pilot has control of both control paths. In the event of a malfunction, the dual-control paths may be separated by either pilot by a manual uncoupling mechanism. Inflight reconnection may be made if desired.

2.2.1 Pitch Control System

The pitch attitude of the aircraft is controlled by the incidence angle of the horizontal stabilizer. Four linear hydraulic servos act in unison to position the stabilizer as commanded by control column inputs or by the autopilot. The effectiveness of the horizontal stabilizer is increased by two elevators which are geared directly to the stabilizer. They move with a fixed relationship as a function of the stabilizer motion and are not controllable independently.

An overall schematic of the pitch control system is shown in Figure 2-4. The power servos are controlled by means of two separate control channels from the columns to the servo inputs with separate cables and a feel and trim system. These channels are coupled by interconnecting linkages between the columns and between the servo inputs. Both connections incorporate couplers which can be opened to allow independent control in case of input system failures or jams. An input system monitoring system is provided which warns the pilot in case of a failure or jam by indicating which channel is affected. Pilot feel forces are generated by means of mechanical springs. The spring gradient is automatically scheduled as a function of the stabilizer position and the Mach number.

Failure warning lights, system monitoring lights, and mode control switches are mounted on three panels located in the flight station above the windshield.

Stabilizer Servo System

The Stabilizer Servo System is composed of two power servo assemblies, four actuators, and four mechanical feedback link mechanisms, two of which are feedback monitors. Hydromechanical safety provisions are included for failure detection and isolation.

The system is powered by four independent hydraulic sources. The actuators, any one of which is capable of controlling the airplane, act in unison and are controlled by the two separate servo valve assemblies on opposite sides of the airplane. Each valve assembly contains a dual four-way, tandem spool which controls two adjacent actuators. The control valves operate in response to mechanical inputs at the input arms from the pilot or autopilot to port fluid flow and pressure to each actuator. The hydraulic flow to the actuators is approximately proportional to the control valve displacement, except during overtravel. The stabilizer displacement is mechanically fed back and compared with the input commands in summing linkage arrangements internal to the servo valve assemblies to null the servo control valves when the commanded position is attained. The actuators are normally all four active, but the shutoff/bypass functions permit the system to operate also

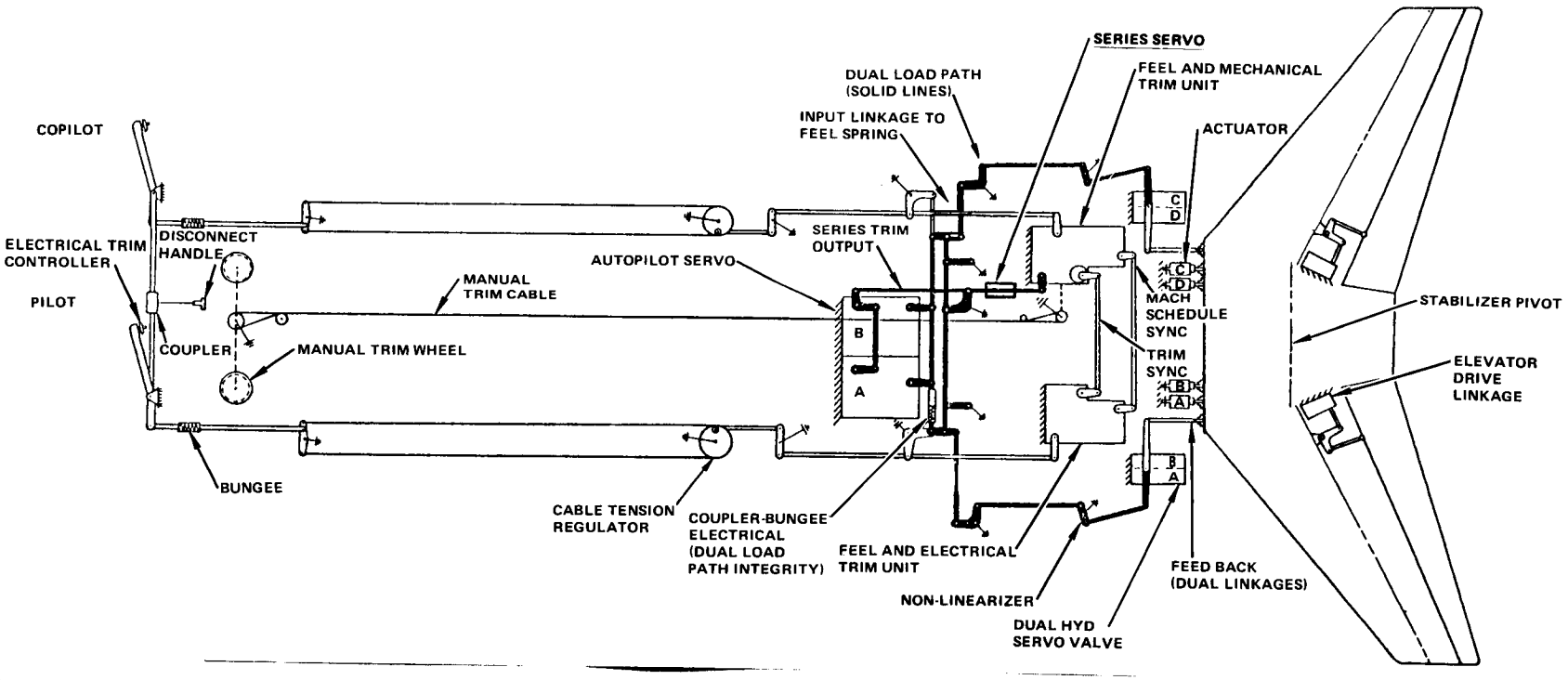

Figure 2-4. Modified Stabilizer Control Schematic

with two or three active actuators. They have balanced pistons, each able to support a load of 74,700 newtons (16,800 lb) when the static pressure differential is at the expected minimum of 19MPa (2750 psid). They have teflon seals with very low friction. Snubbers provide smooth piston deceleration at each end of the cylinder. The full stroke is 0.71 m (28 inches).

2.2.2 Roll Control System

The roll control system controls the motion of the aircraft about the longitudinal axis by the use of "full-time" inboard and outboard ailerons supplemented by the five outboard (of six per wing) spoilers during low-speed flaps-extended flight. The four inboard spoilers also operate symmetrically for speedbrake and direct lift control. Motion of the spoilers for roll control is asymmetric, upward only, regardless of previous symmetric inputs.

Outboard Aileron Servo System

The outboard aileron servo system, Figure 2-5, includes a hydromechanical position servo on each wing. Each servo contains a tandem valve dual hydraulic servo module which provides control of fluid pressure and flow to two parallel acting unequal area actuators which drive the corresponding outboard aileron. A command input from an inboard aileron opens the corresponding outboard aileron control valves, pressurizing the hydraulic cylinders. The external dual feedback linkage nulls the valves when the commanded position is attained. The input linkage is a dual redundant load path system; one primary path for input from the inboard aileron, and the other secondary path an internal centering spring arrangement to return the surface to faired position in the event of loss of the primary input connection or the primary feedback. The feedback linkages are dual to prevent an open loop failure due to loss of either feedback link. The control valve consists of two four-way spools in tandem. The valve ends are ported to the static cavity. The valve has been designed with over-travel provisions.

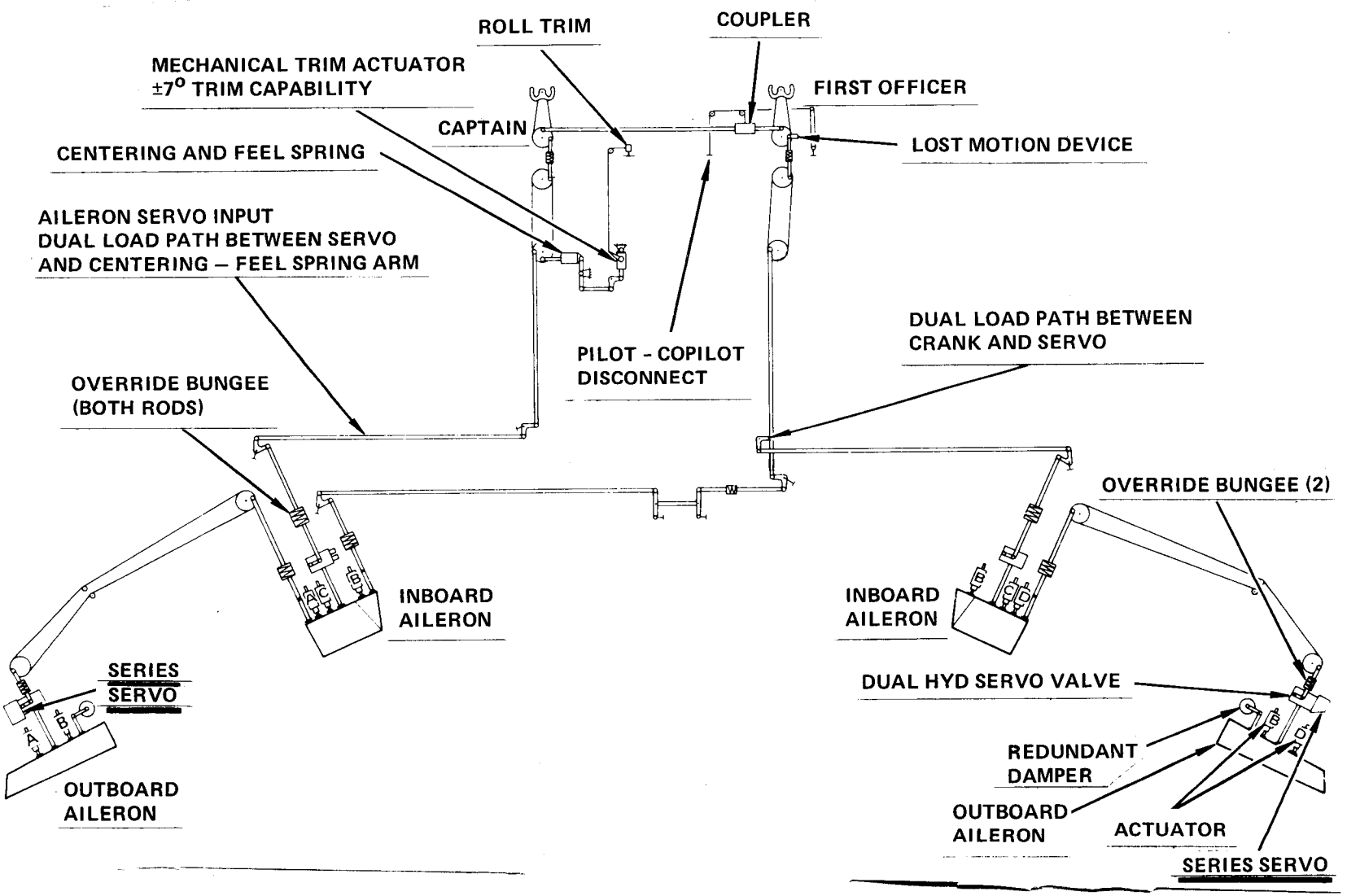

Figure 2-5. Aileron Control System (Active Control Elements Underlined)

2.3 ACTIVE CONTROL SYSTEM (ACS)

2.3.1 Functional Description

Reductions in wing design loads are achieved by automatically moving the outboard ailerons symmetrically in response to accelerations sensed at the wing tips and in the fuselage. In a positive-g maneuver (pullup or banked turn) or long-term updraft, the ailerons deflect upward (and downward for negative maneuvers and downdrafts) thus moving the wing center of pressure inboard and reducing the wing bending stresses. This active controls application is designated maneuver load control, or MLC. In continuous atmospheric turbulence, in addition, motion in the first wing bending mode in the 1-2 Hz frequency range is sensed by accelerometers at the wing tips. The ailerons are moved symmetrically so that the resulting air pressures oppose the wing tip velocities and thus further reduce the stresses produced by the turbulence. This function is designated elastic mode suppression, or EMS.

In addition to moving the ailerons symmetrically, the system moves the horizontal stabilizer automatically to compensate for the airplane pitching moment produced by the airplane as it enters a gust. This function is designated gust alleviation, or GA.

2.3.2 Servo System Modifications

In order to provide incremental motion to the power servo input linkages without interfering with the primary commands from the pilot or autopilot, series servos are utilized for the active control system. The original outboard aileron (OA) power servo modules in the flight test airplane (and in the laboratory "iron bird") included series servos with an authority of $\pm 7^{\circ}$ as an early precaution against possible need for a roll damper. The MLC/EMS command capability is added in the same manner as if from a roll stability augmentation system, except that the commands are symmetrical. The series servo in the horizontal stabilizer (HS) channel, an electro-hydraulic extensible link servo, was added by replacing that part of the series trim output link which is connected to the output arm of the feel and mechanical trim unit (see Figure 2-5). The authority of the HS series servo is ± 8.1 mm

(±.32 inches). The corresponding deflection at the horizontal stabilizer varies from ±0.6° at high speed to about ±1.7° at approach as a function of the column to stabilizer gearing. For this "off-the-shelf" extensible-link servo, a module to reduce the pressure from 21 MPa (3000 psi) to 7 MPa (1000 psi) was utilized. The HS series servo was found to limit the available stabilizer rate unacceptably in the baseline tests. It was modified before the extended-span tests by doubling the valve flow and increasing the pressure to 10.5 MPa (1500 psi).

The breadboard ACS servo system includes:

4 HS power servos (dual-dual configuration)

4 OA power servos (dual configuration per wing)

2 OA series servos (single servo, dual winding per wing)

1 HS series servo (with in-line monitoring)

Cross monitoring of the OA series servos is accomplished by comparisons between corresponding left wing and right wing coil signals. In-line monitoring of the HS series servo compares its response (feedback signal) with the output of a linear first-order analog model (.1 second time constant) of the series servo in the HS driver card of the ACS computer.

2.3.3 ACS Sensors

The experimental ACS sensor system includes:

4 wing tip accelerometers (two per wing)

2 fuselage accelerometers

2 fuselage pitch rate gyros

2 column force transducers (one per column)

2 horizontal stabilizer position transducers

The wing-tip and fuselage accelerometers are identical having a dynamic range of ±5 g's and a first-order filter characteristic with a time constant of .03 second. The design utilizes a force-balance servo loop to constrain the seismic element within a very small range of displacement. The

first-order filter, which is inside the servo loop, attenuates the response of the seismic element at frequencies above five hertz, thus avoiding saturation due to high frequency vibrations. The seismic natural frequency is 500 rad/sec with a damping ratio of 60% of critical damping. The scale factor is 1 volt per g.

The rate gyros have a natural frequency of 120 rad/sec with a damping ratio of 50% of critical damping. The dynamic range is $\pm$40 deg/sec. The scale factor (D.C. volts demodulated from 400 Hz) is .129v per deg/sec.

Calibrated torquing currents can be applied to the accelerometer or to the rate gyros by operating appropriate switches in the ground test module (GT/FD terminal described in Section 2.3.6).

The column-force transducers are the same ones used for control wheel steering in the autopilot. The signals are generated by force sensors in the hubs of the pilot wheels.

The horizontal stabilizer position transducers are LVDT's (one in each power servo module) which measure the surface feedback at each side of the horizontal stabilizer center box. These LVDT's are in the flight test airplane and in the laboratory "iron bird".

2.3.4 ACS Computer - Analog

The active control computer (breadboard model) and interface equipment were designed and fabricated at the Lockheed Rye Canyon Research Laboratories. The block diagram shown in Figure 2-6 represents half of the dual redundant analog system for the baseline tests. Figure 2-7 gives the corresponding diagram for the extended-span tests, including specific characteristics in each block.

In both cases, a monitoring system compares the dual redundant channels at strategic points and automatically disengages the system when the comparators detect a significant mismatch. The computer is a solid state analog type, composed of operational amplifier chips which are "wired" with input and feedback impedances to generate the prescribed transfer function characteristics. In Figure 2-6, the airplane dynamic sensors are represented by

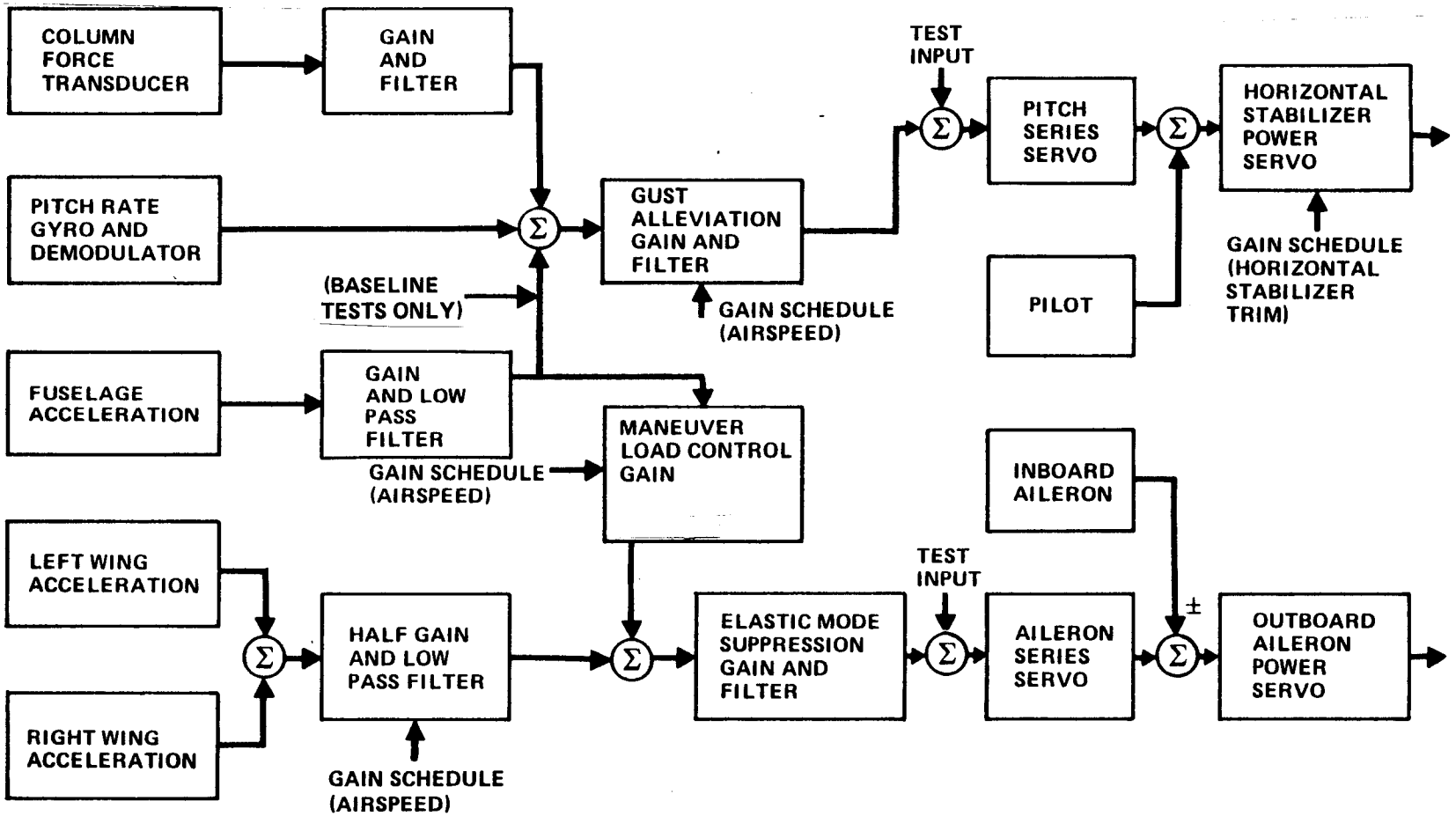

Figure 2-6. Active Control System Block Diagram - Baseline Tests

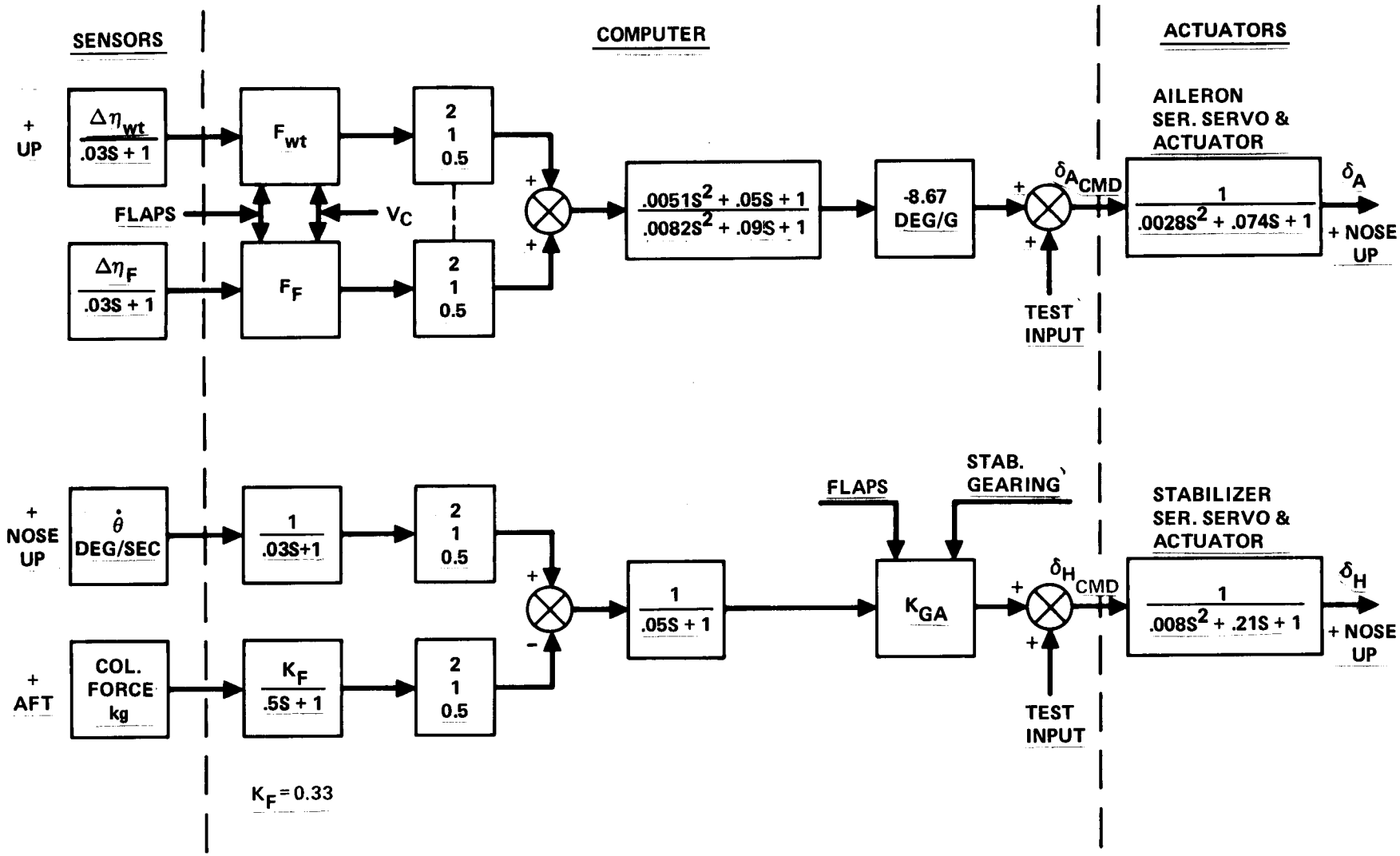

Figure 2-7. Active Control System Block Diagram - Extended Span Tests

the blocks which are adjacent to the left margin; and the control surface driver cards are represented by the blocks which are adjacent to the right margin. Figure 2-7 also shows the dynamic characteristics of the series servo/actuator systems. The outboard ailerons receive EMS commands from the wing-tip accelerometers and MLC commands from a blend of wing-tip and body acceleration signals. The horizontal stabilizer received GA commands from a blend of pitch rate and body acceleration signals in the baseline case, and from pitch rate alone for the extended-span tests. This signal alone more nearly fitted the objective of having no increase in stabilizer fatigue loading environment. The column force transducers feed compensating signals from the pilot to the horizontal stabilizer in order to preserve correct column forces during maneuvers.

The column force signal is the sum of signals from the two columns. It is filtered by a first order time constant (0.5 second) which produces the approximate lag required to cancel ACS responses to a pilot command. Each of the other sensor signals is filtered by a first-order time constant (.03 second) in order to attenuate the effects of vibration and noise above five hertz (each accelerometer filter is inside its corresponding module and not in the ACS computer). A constant bias, corresponding to gravity, is subtracted from each accelerometer signal. Incremental acceleration signals from the left and right wing tips are averaged before passing on through the MLC/EMS channel.

2.3.5 Control Laws

The gain scheduling sequences indicated in Figures 2-6 and 2-7 are shown quantitatively in Figure 2-8 for the ailerons (MLC/EMS) and in Figure 2-9 for the stabilizer GA (later changed to GLA) function. The gain scheduling was simplified for the extended-span case into a basic change with flap position for both ailerons and stabilizer. A relatively smaller additional change with speed takes place for the aileron function, at 315-330 KCAS. This modification reduced the possibility of very large gain changes with a malfunctioning speed sensor. As noted on Figure 2-9, higher stabilizer gains were selected with the digital computer (see Section 2.3.8) in order to explore the maximum gains considered usable with the test system.

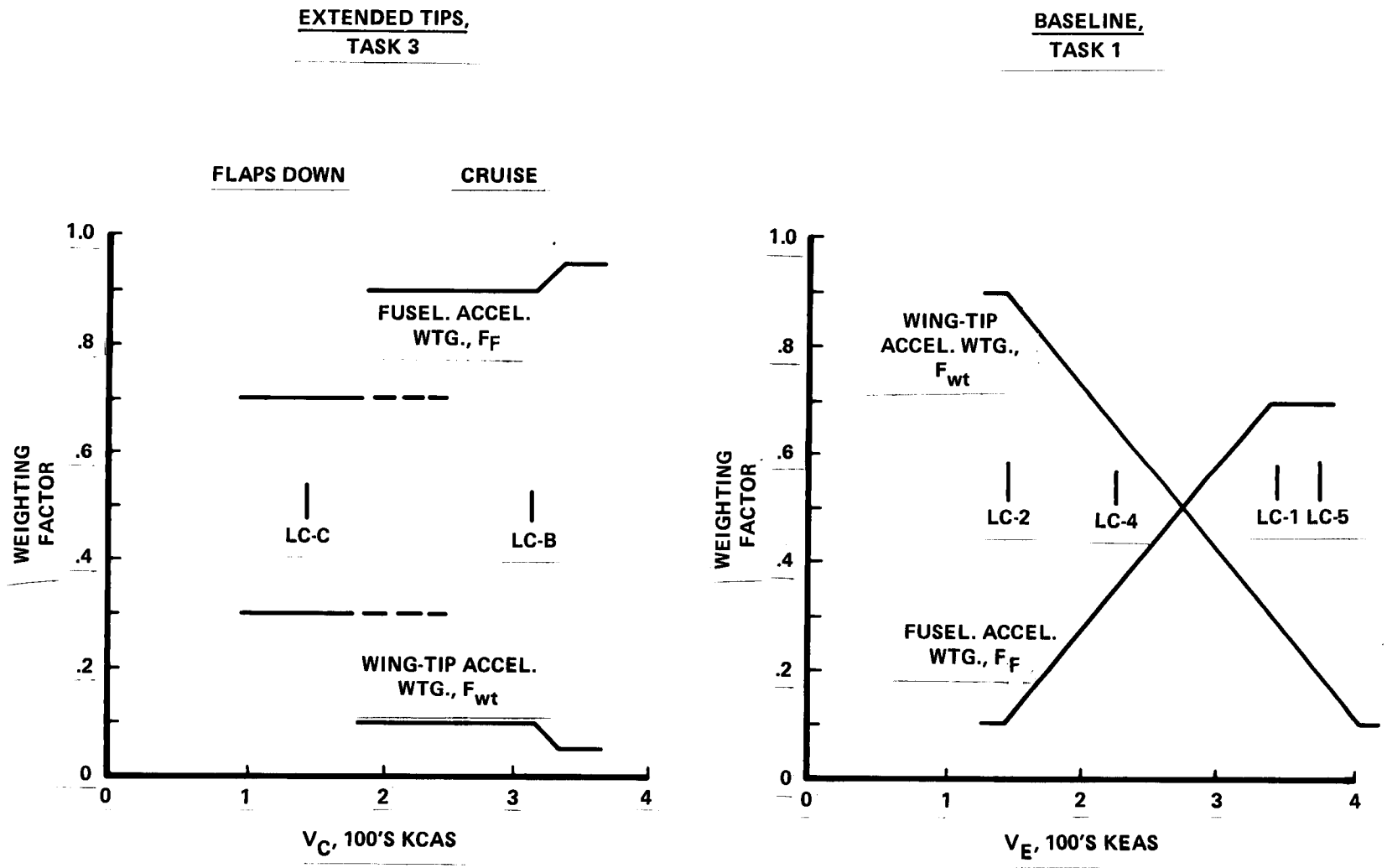

$$\Delta\delta_A = 8.7\,(F_F\ \Delta n_F + F_{wt}\ \Delta n_{wt}) \times f_{EMS}(\omega)$$

Figure 2-8. MLC/EMS Sensor Weighting Factors - Aileron

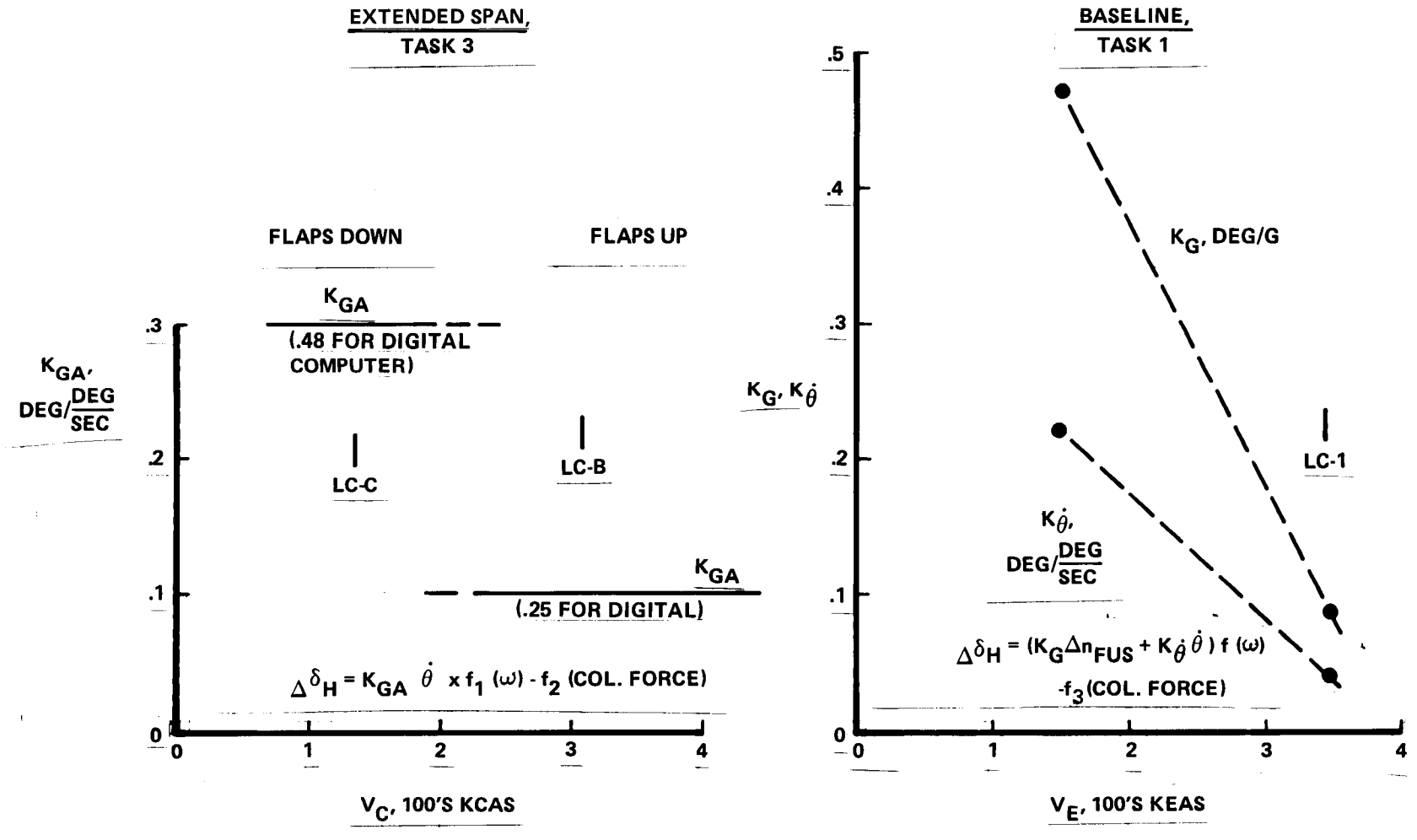

Figure 2-9. GLA Sensor Gains - Stabilizer

Specific flight test conditions are indicated on the figures by the "LC-X" notation, for "Load Condition-X". They will be discussed in the Results section.

The dynamic characteristics of the control laws are compared in Figure 2-10 for the ailerons, and in Figure 2-11 for the stabilizer. The gains shown are those for the cruise cases, LC-1 and LC-B. Other cases with different gains have the same phases and the same gain/frequency variation (i.e., shape of the gain curve) as shown here. The gain curves are simply displaced vertically by a change in steady-state gain, such as changing to flaps-down. The aileron phase curves, Figure 2-10(b), apply to the melded wing-tip/fuselage acceleration signals. Similarly the baseline stabilizer phase curve, Figure 2-11, applies to the melded pitch rate/fuselage acceleration signal.

The aileron function is to provide 8.7 deg per g of wing/body acceleration at low frequency (0.1 to 0.3 Hz), with a phase near 180°, and to provide wing bending damping in the wing bending frequency range of 1 to 2 Hz, with a phase near 90° to the wing-tip acceleration. Some additional gain and phase control is used in the 2-3 Hz range, where engine motions are significant, for the extended span case.

The stabilizer control law dynamic requirements, Figure 2-11, are to provide damping in the short-period frequency range of 0.1 to 0.3 Hz, and to avoid excitation of elastic modes. The trend toward simplification is underlined by deletion of the fuselage acceleration function for the extended span case.

2.3.6 Interface System

The ACS computer contains twelve "cards" which are interfaced with each other through the "motherboard" at the base of the chassis. Each card is plugged into the motherboard through pins arranged in two rows. The twelve cards are assigned as follows:

3 cards for Channel A computation

3 cards for Channel B computation (channels A and B are redundant)

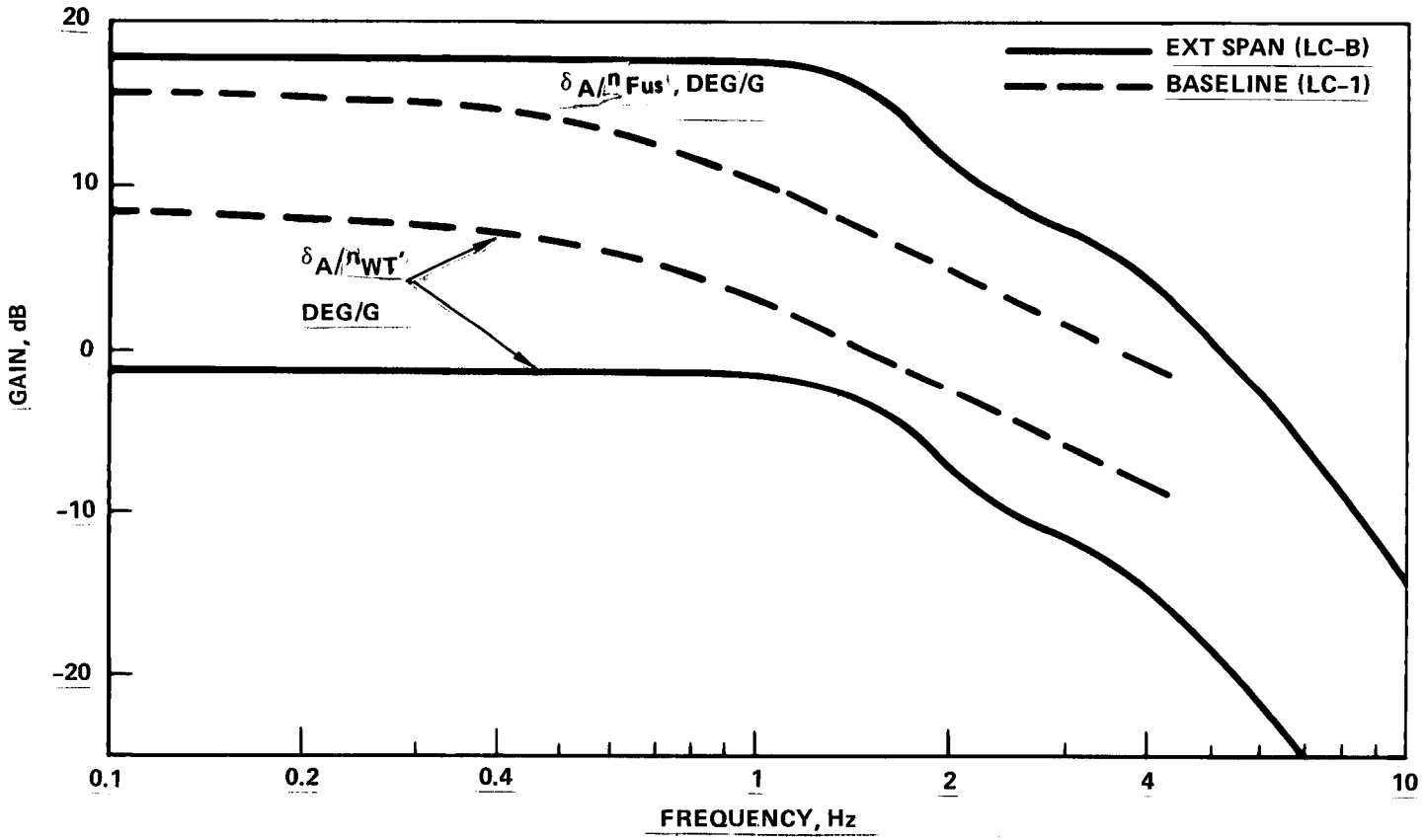

Figure 2-10. Aileron Control Law Comparison, Cruise (Sheet 1 of 2)

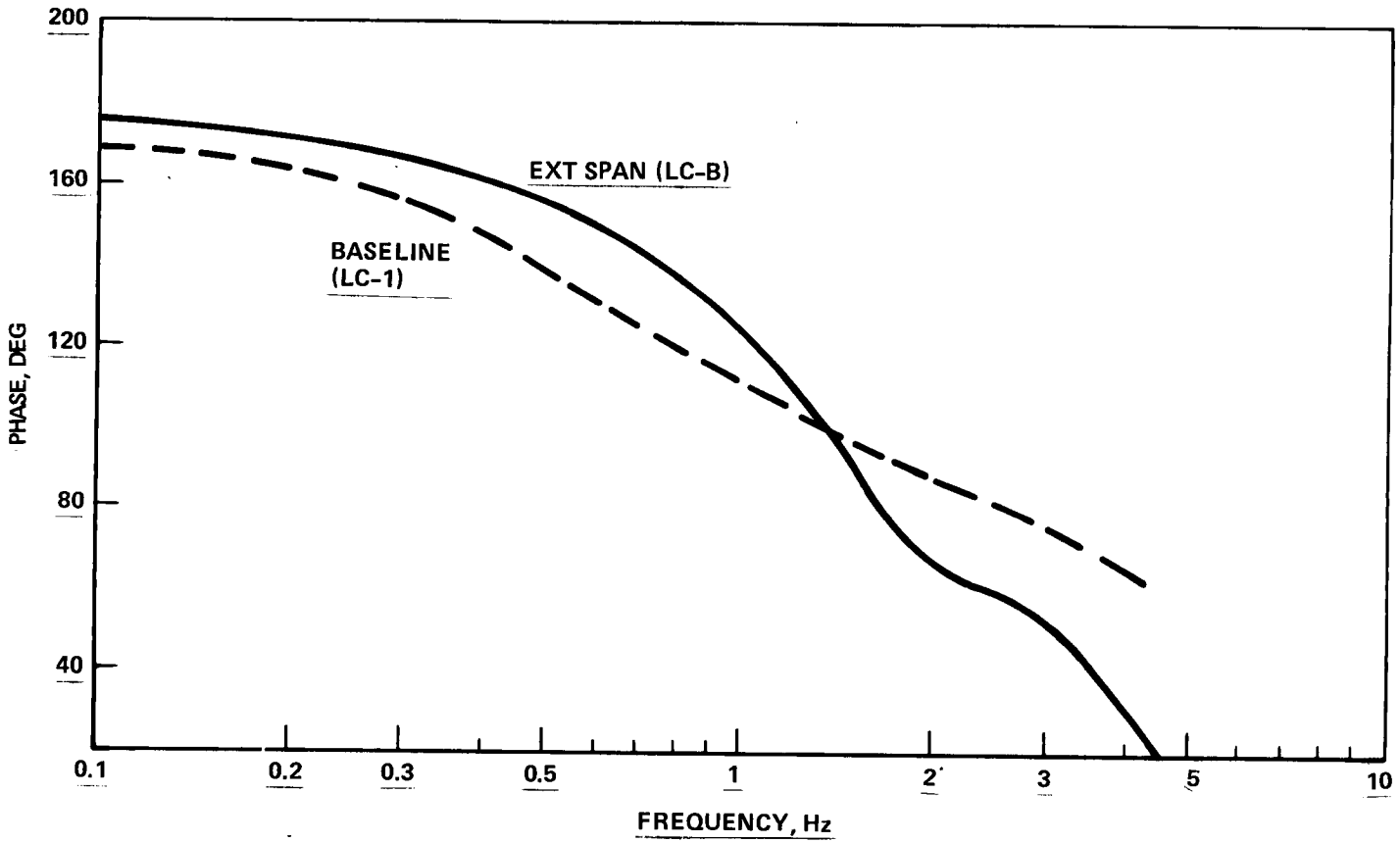

Figure 2-10. Cont'd (b) Phase

Figure 2-10. Aileron Control Law Comparison, Cruise (Sheet 2 of 2)

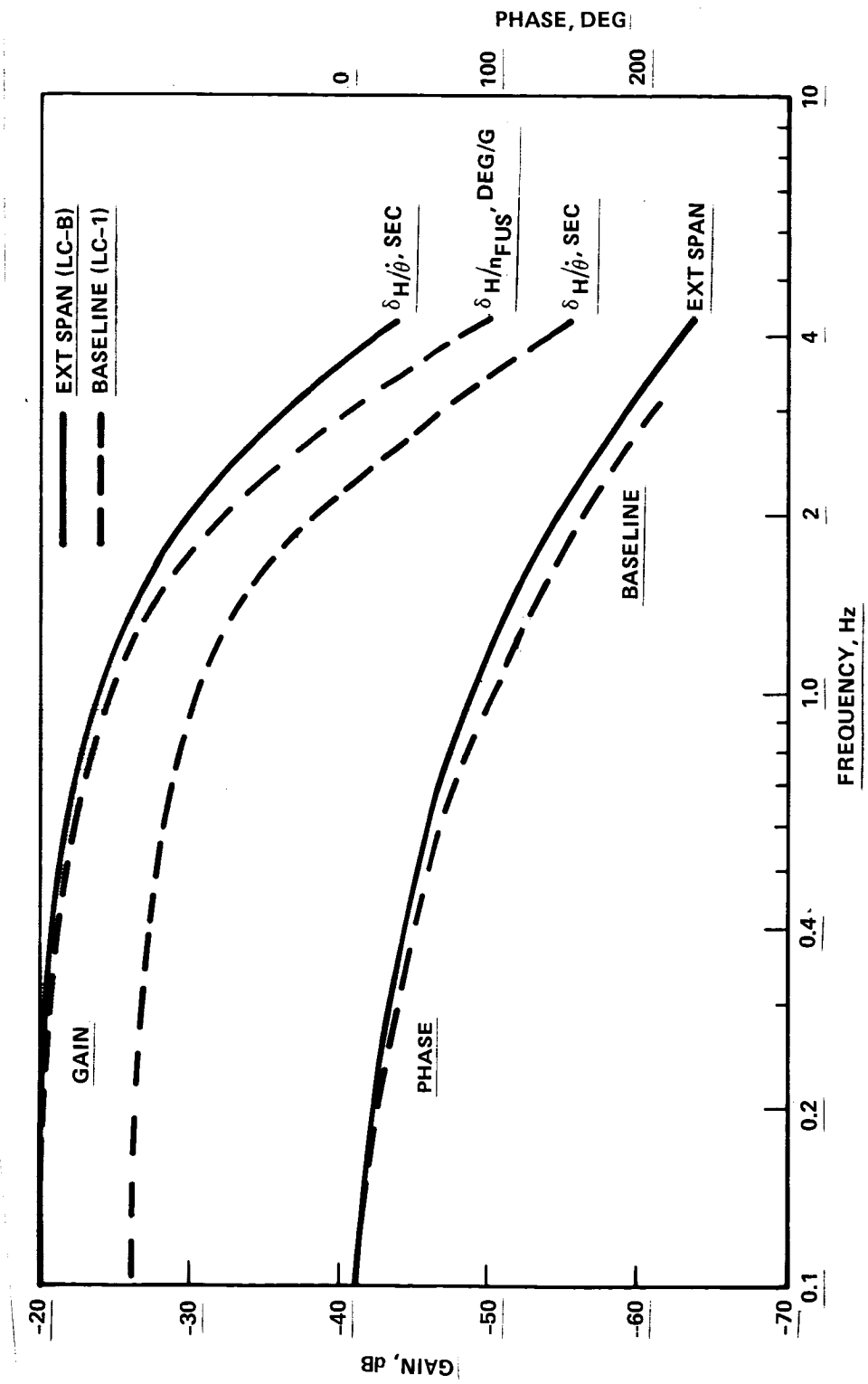

Figure 2-11. Stabilizer Control Laws, Cruise

2 OA driver cards (1 each for Channels A and B)

1 HS driver card

1 Comparator system card

2 power supply cards.

The ACS computer control panel contains function selector switches and fifteen jacks connected to test points inside the computer (buffered).

Interfacing among the various ACS components, which are distributed over the airplane, is accomplished through a system of cables (wiring harnesses) connected at two major junctions: (1) the "blue slipper" and (2) the "ground test/failure detector" (GT/FD) terminal.

The "blue slipper" is a tray upon which the ACS computer is mounted and which fits into a rack in the lower bay of the airplane. The tray is slipped into direct interface with the ship wiring cable connectors through two sets of four 57 pin plugs at the rear end of the tray. Corresponding pins of the two plug sets are soldered together with wires that are contained within the framework of the tray. Underneath the front end of the tray are two similar plugs (Elco plugs) which interface with special ACS cables. The ship wiring cables lead to the wing tips (OA servos), to the flight station (FCES panel), and to the ship power supplies. The special ACS cables lead to the ACS test engineering station (ACS control panel and GT/FD terminal).

The GT/FD terminal includes a control panel, an ACS status annunciator, and a patch board. Torque command signals to the accelerometers and the rate gyros are supplied through switches on the GT/FD control panel. Two potentiometers on the GT/FD control panel supply manually controlled (optional) gain scheduling signals to the ACS computer. The jacks on the patch board are:

24 to the flight test instrumentation station

3 to the control surface command points in the ACS computer (HS channel and OA channels A and B)

4 from the wing tip accelerometers (unbuffered)

4 from the fuselage sensors (unbuffered)

2 from the gain schedule potentiometers

2 from the gain schedule sensors

2 to the ACS gain schedule input points.

The GT/FD terminal has nine input/output connectors for cables leading to the:

Left wing tip accelerometers

Right wing tip accelerometers

Fuselage sensors (accelerometers and pitch rate gyros)

Flight Station (column force sensor)

Lower bay (blue slipper)

Aft bulkhead (HS series servo)

ACS test engineering station (ACS computer control panel)

Flight test instrumentation station (Recorders)

Ship power supply.

2.3.7 Safety Provisions

The following provisions in the breadboard system design and operating procedures were specified in order to assure flight test reliability and safety.

- The series servo authorities were limited to levels that are structurally tolerant to hardover or oscillatory failures.
- The fail-passive monitoring system restores the airplane to its baseline configuration when the comparators detect a malfunction.
- A short-stroke bungee parallels the HS series servo extensible link to complete the dual link arrangement which replaced the dual series trim output link.
- Flight restrictions were imposed to avoid undesirable situations which are peculiar to the breadboard ACS.

A few of these flight restrictions are stated as follows:

1. The pitch series servo must be turned off for stabilizer trim beyond -1.0 degrees at the one extreme and -6.5 degrees at the other extreme. Otherwise it is possible for the ACS signals to command the series trim rod beyond its stops. The servo force is well below limit load but might cause fatigue damage of shear rivets in the autopilot servo module.

2. The pitch series servo must be turned off during operation of the autopilot, except when specifically prescribed otherwise. The autopilot servo activity would have the effect of doubling the series servo amplitude response.

3. The ACS must be turned off in the event of failure of either the A or D hydraulic system. It will operate properly without the B or C hydraulic system.

These restrictions do not apply to the production active control system.

The monitoring system utilizes comparator circuitry at strategic locations to perform the following functions:

1. To compare corresponding computer signals from redundant channels A and B at the OA driver card input.

2. To compare corresponding OA actuator coil signals at opposite wings.

3. To compare the HS series servo actuator displacement to a corresponding analog model output in the HS driver card.

4. To supply a disengage command signal to (1) the solenoid valves which control the series servos and to (2) the FET switches which short out the computed signals into both driver cards.

After the ACS is tripped by the monitor, any channel can be re-engaged independently of the others.

The comparator circuits are configured with operational amplifiers driving disengage logic circuitry composed of NAND gates and HEX inverters. The comparators were originally set to permit signal differences equal to thirty percent of full scale. This was later changed to fifty percent in the HS channel, because the HS series servo analog model did not include rate saturation. In order to accommodate large amplitude signals, the time constant was increased from .05 to 0.1 second; then the thirty percent comparator

setting produced nuisance disengages at the higher frequencies. The required fifty percent setting is considered adequate for monitoring the pitch system.

2.3.8 Digital Computer

The last part of the extended-span testing took place with a Collins breadboard digital computer in place of the analog computer. This computer interfaced into the ship wiring cable connectors through the same two sets of four 57 pin connectors as the "blue slipper" tray did. It used the same ground test/failure detector (GT/FD) terminal and control panel. The breadboard digital computer setup included a separate console for digital diagnostics.

The digital computer control laws were functionally similar to those of the analog computer for MLC and EMS.

2.4 VFS/VSS TEST SYSTEM

Lockheed-California Company developed and tested the ACS breadboard system during 1976 at its Vehicle Systems Laboratory, which is a part of the Rye Canyon Research Laboratories. The laboratory simulation facilities were used to test the control law performance in a real-hardware environment. The ACS computer ("black box") was installed to receive signals from an aeroelastic model in the visual flight simulation (VFS) computers and to transform them into the specified command signals for driving the control surfaces on the vehicle systems simulator (VSS). Deflection signals from the VSS control surfaces were sent back to the VFS computers to drive the aerolastic model, thus closing the ACS loops.

Figure 2-12 shows how the ACS computer and the VFS/VSS components were interfaced for operation with or without the real hardware. The simulator design permitted various options, among which were the use of a simulated "black box" instead of the real one and of simulated control servos instead of the real ones. Pilot-in-the-loop capability was also included for evaluating the influence of the ACS upon pilot acceptance.

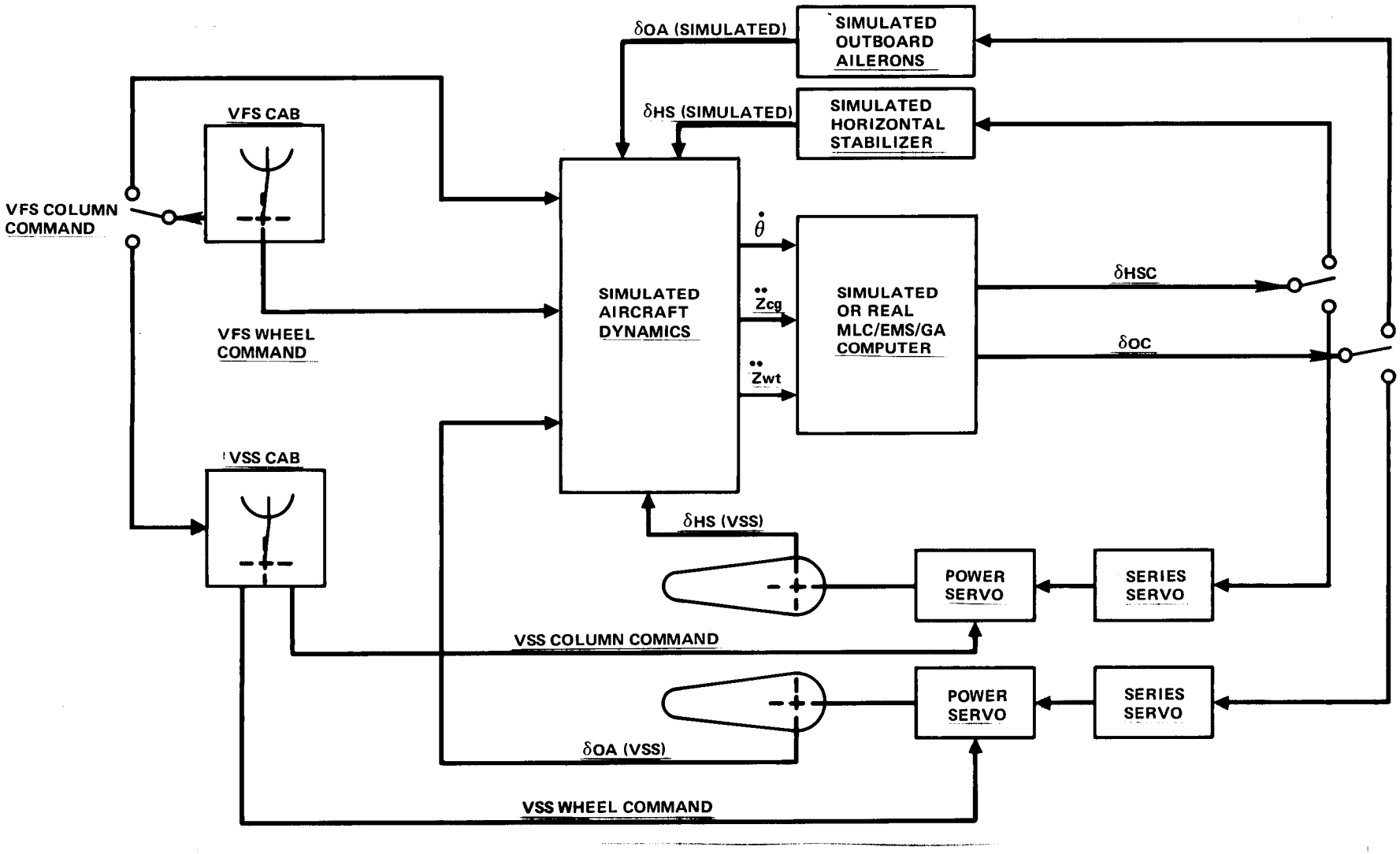

Figure 2-12. V.S.S. - V.F.S. Hardware Integration

2.4.1 The Visual Flight Simulator (VFS)

The VFS facility contains all of the components necessary to conduct a complete real time aircraft simulation. The components include: digital and hybrid-analog computers, cockpits with instrument displays, visual displays, a motion system, a sound synthesizer, and a complete computer software library.

The computers are programmed to simulate all of the aircraft's parameters so that the simulated aircraft will properly respond to piloted inputs and to extraneous conditions, such as turbulence. As a result, variances in aircraft speed, crab angles, vertical and lateral displacements, velocities, and accelerations are depicted. In addition, Instrument Landing System (ILS) signal anomalies, wind gusts, wind shears, and turbulence can all be introduced into the problem.

One of the VFS cockpits has been built to represent the L-1011 wide-bodied jet transport. A Category III aircraft cockpit environment is provided for both the pilot and copilot, with all the necessary controls, instruments, and indicators to accurately duplicate manual and automatic flight control for approach, touchdown, and rollout.

For those studies requiring motion, the facility includes an advanced uncoupled four-degree-of-freedom motion system which was configured to accept a variety of different cockpits. This hydraulically driven system has independent freedoms of movement in pitch, roll, heave (up and down movement), and lateral (sideways) directions.

2.4.2 The Vehicle Systems Simulator (VSS)

The VSS test facility ("iron bird") contains among others, all of the hardware components of the L-1011 primary control system. This real hardware environment introduces many secondary effects (structural feedbacks, nonlinearities, etc.) that cannot be accurately simulated by an analytical model. Figure 2-13 shows the geometric layout of the VSS relative to other facilities within the Vehicle Systems Lab.

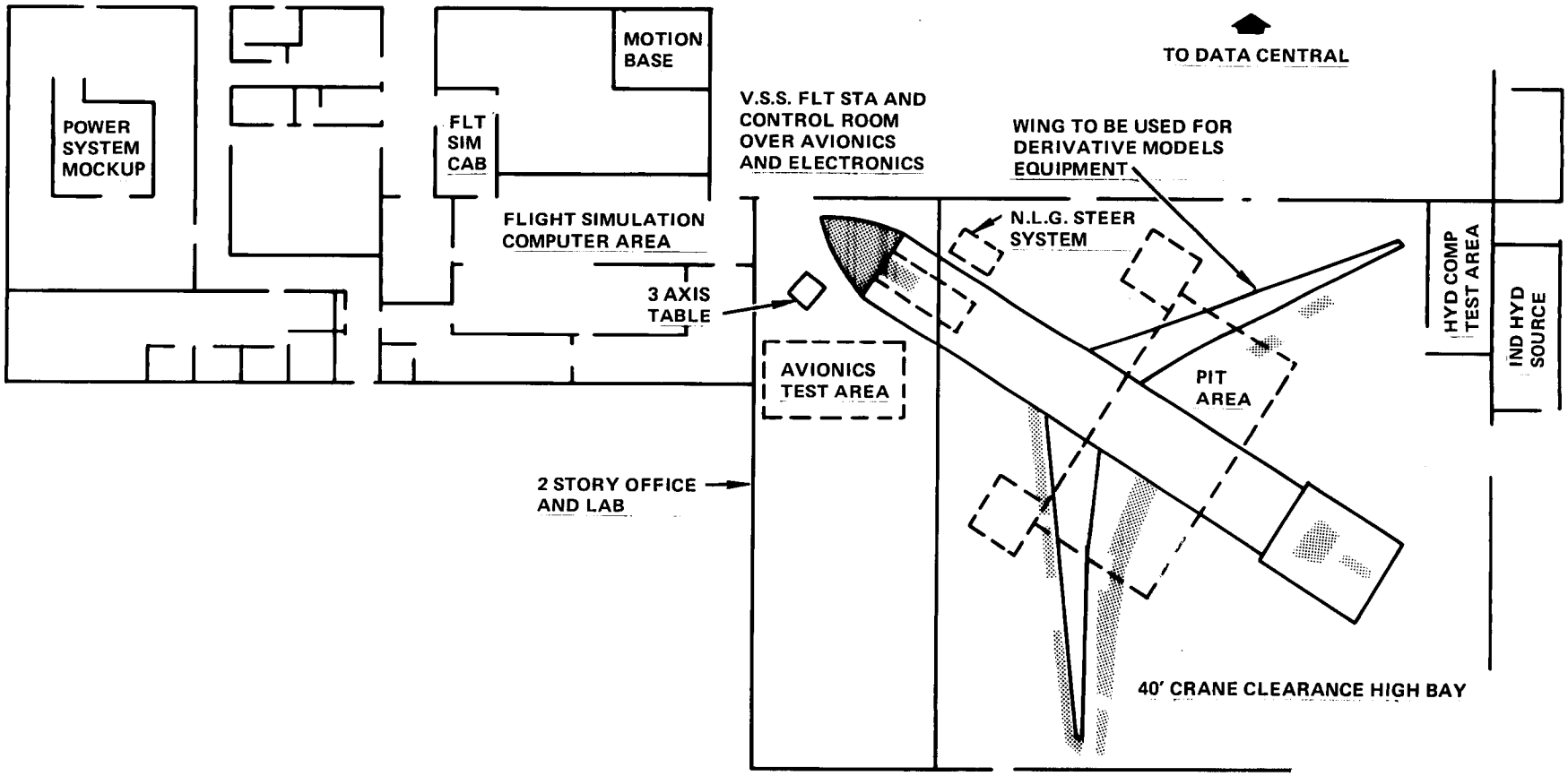

Figure 2-13. V.S.S. Test Facilities - Rye Canyon

A description of the VSS and its capabilities might be conveyed by describing its use during the development and testing of the following L-1011 vehicle systems: primary flight controls, automatic flight controls and avionics, hydraulics, flaps, slats, landing gear, brakes, and nose-wheel steering. Integrated testing of these systems, while subjected to simulated aerodynamic influences, provided aircraft realism. It was therefore possible to verify proper system operation during performance and failure mode testing and while applying the endurance excitation prior to certification (Reference 8). Participation of the FAA in these laboratory demonstrations supported the certification of the category III Autoland system simultaneously with the certification of the basic airplane.

All of the VSS systems were installed on a steel jig structure with the plan form of the aircraft which is erected in a specially constructed 150 ft. x 150 ft. building having a 40 ft. clear height. Significant segments of aircraft structure were constructed and installed prior to their availability from production assembly and were incorporated to aid the functional realism of the testing. Fabrication of these elements of structure identified many assembly problems which were corrected prior to production.

The VSS utilized all of the essential elements of each system. For example, in the pitch axis control system, it included all elements from the flight station control columns to the center box of the horizontal stabilizer. Aircraft structure was used to support the control columns, input mechanisms, cables, and servos so that the correct structural compliance and effects of friction were reflected in the performance evaluations. Additional large segments of aircraft structure were also used to support the servos, actuators, and center box. The outer sections of the horizontal stabilizer were simulated by carefully designed dynamic models to provide the capability for assessing system dynamics and structural feedback effects out to a frequency of 20 Hz.

All four hydraulic systems were included in the VSS with fluid distribution as nearly identical to the aircraft as practical.

The plumbing distribution included an accurate installation of all components within a service center. All four engine-driven pumps were located

at what would be the accessory gearbox face of the engine. Plumbing was subsequently routed according to the provisions within the pylon, nacelle, wing, or fuselage leading to the reservoirs and on to the components requiring the power.

Operational efficiency, in terms of sharing instrumentation and controlling the daily activities was aided by installing the flight station on the second floor in an office environment. These areas overlooked the high bay and served as VSS master control. With this arrangement, the cabin floor was permitted to extend at a 3 m (10 ft.) elevation into the high bay portion of the building which contained the jig with vehicle systems and load simulations.

The flight station was adjacent to the VFS digital and analog computers which provided the full aerodynamic envelope simulation and/or segments representing takeoff, cruise, approach, or landing. Additional realism was provided by headwind, tailwind, windshear, and the effects of atmospheric turbulence.

A completely independent Central Data System, not associated with flight simulation, acquired and processed data on a time-sharing basis with 20 other remote stations distributed within the Rye Canyon Laboratory complex. Instrumentation throughout the VSS was installed to permit conventional monitoring by direct reading X-Y plotters, strip recorders, or oscillographs. In addition, the Central Data System was able to monitor two simultaneous tests, comprising a total of 800 channels, at rates of either 1,000 or 10,000 samples per second. This valuable tool permitted the direct plotting of hundreds of performance criteria to aid the systems' development phase and ultimately was used for direct inclusion within FAA demonstration reports.

2.4.3 Simulator Configuration for ACS Testing

The ACS breadboard was tested in the manner described above. Some particulars are:

- The accelerometers and rate gyros were tested in an open-loop configuration only. Simulated sensors were used in the closed-loop tests.
- The ACS computer was installed in the avionics test area.

- The aileron and stabilizer series servos received signals from the ACS computer in the avionics test area. The series servos had been installed in the VSS as described in Section 2.3.2.

- Aerodynamic hinge moments generated through the surface loaders were not utilized.

- Pilot-in-the-loop flights were controlled from the VFS flight station.

The airplane was simulated on the 271 R analog computer. The model was relatively simple because it was restricted to longitudinal motion, except that it included banking capability with inherent turn coordination. The pilot "flew" the system from the VFS flight station. A roll command signal from the wheel controlled the inboard and outboard ailerons through the roll autopilot servo. The pilot commanded the HS power servos through the VSS column, which was slaved to the VFS column through a position servo; thus permitting a realistic representation of the cable and input linkage system. Control from the VFS column required that the feel forces be simulated. Realistic open-loop feel force disturbances from the HS series servo were checked separately from the VSS flight station column.

2.5 AIRPLANE TEST PROVISIONS

The active controls flight test program was conducted on the in-house L-1011, S/N 1001. It is shown in Figure 2-2 in the extended-span configuration. S/N 1001 is extensively instrumented for flying qualities, performance, loads, flutter, and automatic flight control testing. Figure 2-14 depicts the test provisions in the airplane. They include:

- Gust Probe - The gust probe is a Giannini Controls Corporation Model 2811 vertical and lateral differential pressure sensing probe. This particular probe has been fully wind tunnel calibrated by Lockheed, and successfully employed on C-141A, C-5A, and L-1011-1 gust loads flight test programs. The gust probe was installed during the maneuver loads and gust flight testing.

- Weight Engineer Monitor Station - All necessary readouts for in-flight calculation of gross weight and center of gravity are located at this station. In addition, all controls necessary for transferring water to specified tanks of the water ballast system for in-flight c.g. control are located at this station.

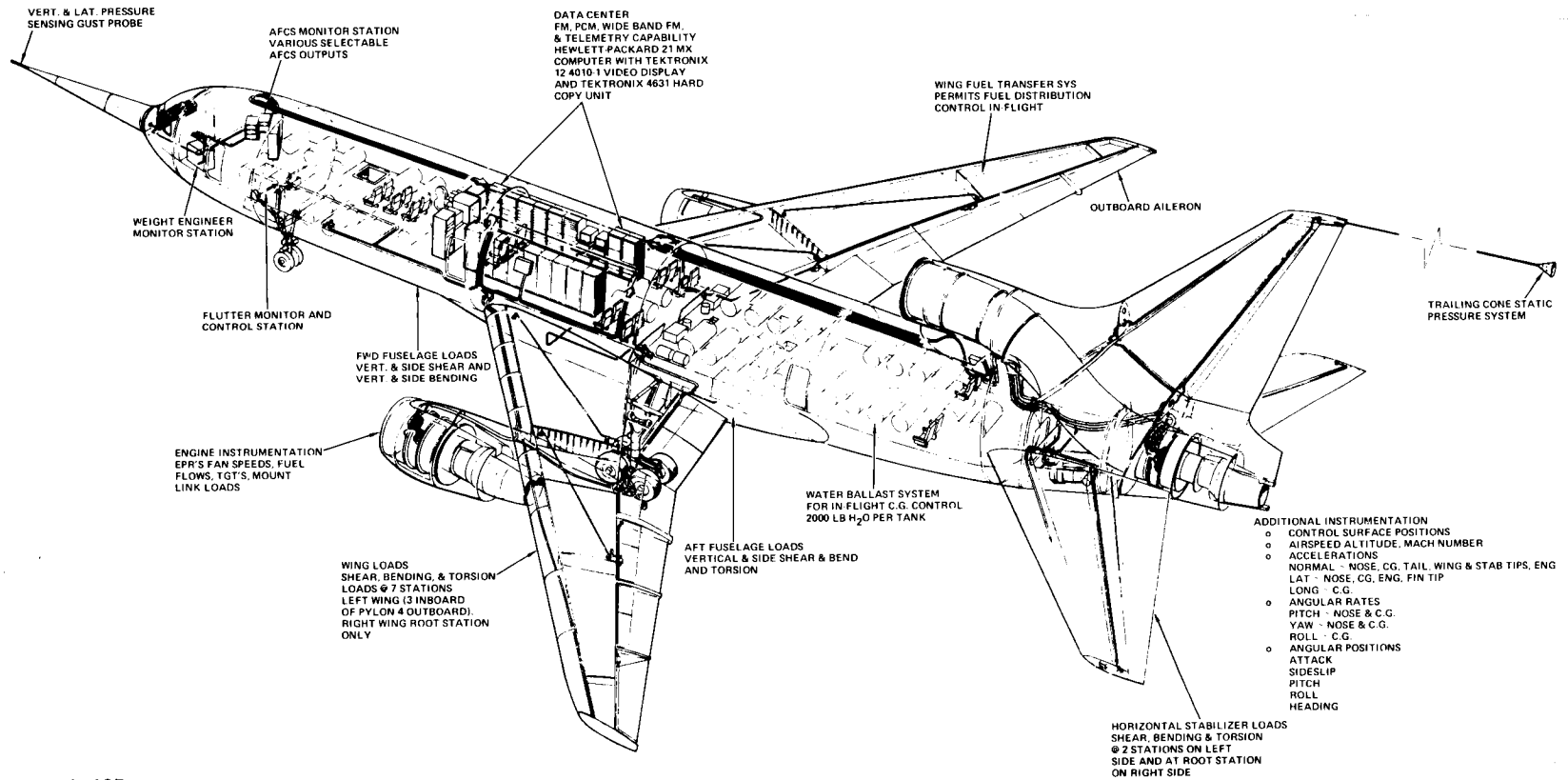

Figure 2-14. S/N 1001 Test Provisions

- Automatic Flight Controls (AFCS) Monitor Station - This station provides access to AFCS/Active Controls and PCM/FM recorded data for in-flight changes to parameters which can be monitored via 16 analog channels and 11 discrete channels. In addition, the station has provision for in-flight excitation of the AFCS/Active Controls systems and provisions for ground/airborne testing using simulated sensor inputs. The station also contains logic light displays for 55 discrete channels.

- Flutter Monitor and Control Station - This station has provisions for in-flight monitoring of up to 12 preselected channels of analog information. Additionally, provisions for incorporation of an oscilloscope and X-Y plotter exist.

- Data Center - The data center contains all equipment necessary for the conditioning and recording of the test data with the capability of 3 tracks constant bandwidth FM (63 channels), 2 tracks PCM (125 channels each), 1 track PCM (60 channels) and 14 tracks wide band FM for high frequency data requirements. In addition, certain data readouts are provided on an AO panel. An onboard digital computer which can access any PCM channel, and telemetry capability for any selectable FM track are also available.

- Fuel Transfer System - This system provides the capability to transfer fuel between inboard and outboard wing tank compartments thus providing additional ability to control c.g. and wing inertia in flight.

- Instrumentation - The basic instrumentation is felt to be self explanatory. An eighth loads strain gage station was added at 84% of the new span for the extended-span tests. It should be noted that the shear, bending moment, and torsion moment loads mentioned are measured in the swept axis system with torsion being referenced to an arbitrary load axis approximating the elastic axis of each applicable component.

SECTION 3

TESTS

3.1 ACS TESTS IN THE VFS/VSS

Each subsystem was functionally bench tested before interfacing or installation into the VFS/VSS. Each sensor was bench tested to verify specified frequency and step responses to excitations from the tilt table and from torquer signals; then used to command the ACS/VSS hardware in open-loop step response tests. The series servos were open-loop tested on the VSS to check frequency and step responses, each servo at three different amplitudes. Additional tests were conducted to check effects due to system threshold and hysteresis and to observe servo saturation effects (amplitude saturation and rate saturation). Input signals to command the series servos included step and oscillatory signals from the VSS console signal generator superimposed onto control column inputs from the VSS cab.

Closed-loop tests were conducted with and without the pilot in the loop. They were configured by closing signal paths through the simulated aeroelastic dynamics. At first, linearized models of the ACS hydraulic servo transfer functions were simulated; then the linearized models were replaced in two steps by real hardware: (1) the hydraulic servos were added through the VSS/VFS interface system; then (2) the ACS computers were added through the VFS/ACS/VSS interface system.

Without the pilot, the signals commanding or affecting the simulated airframe were from the VSS servo position transducers, from an input signal generator, and/or from a noise generator programmed to simulate gust power spectral densities at several intensities. With the pilot in the loop, flying qualities and feel characteristics were observed for evaluation of feed-forward signal effectiveness and for effects of failure modes.

For documentation, selected test signals were stored in digital form in the Central Data Computer (CDC). These were recalled in the form of tabulations, Bode plots, X-Y plots, or time response plots, as desired. The CDC outputs were available on the "quick-look" video tube or on "hard copy" as needed. The CDC data were stored permanently for future retrieval.

Selected tests for permanent data storage were outlined according to the place where the test input activity was performed (the VSS test console, the VSS cab, the VFS computer room, or the VFS cab). Selected data were retrieved from the CDC by use of the labels identifying each test run in the outline.

3.2 GROUND TESTS IN THE AIRCRAFT

Prior to the flight testing of the Active Control System, a series of ground tests were performed on the aircraft.

The first group of tests were to verify the functional and operational integrity of the system prior to flight. These tests included checks for positive engagement and disengagement of active control servos, operation of all system monitors, end-to-end response checks for all sensor inputs, and isolation of computational modes from extraneous signals and cross-talk.

The second group of tests were performed to determine the dynamic response of the Active Control System as installed in the aircraft. Direct stimulus was applied to the servo amplifiers to determine the frequency response of the combined Active Controls series servos and Primary Control surface servos. The servo frequency response was performed at three amplitudes, and, for pitch, at two different trim positions to identify any control system nonlinearities. Open loop end-to-end frequency response tests were made separately for the MLC/EMS channel and the Gust Alleviation channel to verify the computational transfer function.

Closed loop frequency sweeps were made with stimulus applied directly to the servo amplifiers to identify the maximum structural response frequency. The servos were then excited at the maximum response frequency with

saturation level drive signals to verify that there was no sustained oscillation when the excitation signal was removed. The test was repeated with the computational gain doubled to verify adequate gain margin.

Results of the ground tests are discussed in Section 5.1 of this report.

3.3 FLIGHT TESTS

Flight testing was accomplished per an agreed test plan. The tests were as follows.

(a) Inflight Functional Checkout

(b) Flutter Clearance Tests

(c) System Transfer Function Tests

(d) Maneuver Loads Tests

(e) Gust Loads Tests

During the course of testing, modifications, additions, and deletions were incorporated as follows.

(a) During the Functional Checkout and Flutter Tests, the system gains verified were normal gain and twice normal gain rather than one-half normal gain and normal gain as originally planned. The ACS was demonstrated to perform acceptably at twice normal gain.

(b) A limited series of tests to evaluate the possible effect of observed minor column motion on system transfer functions was added for the baseline configuration. These tests consisted of discrete sinusoidal inputs with the control wheel restrained by the pilot, the control column restrained by the pilot, and hands off. The test results showed no significant effect on ACS performance and pilot comments were that the minor column motion would not be noticed under non-test (i.e., operational) conditions.

(c) Turbulence data for the flaps down baseline configuration was deleted due to lack of turbulence of sufficient magnitude and duration.

(d) A Collins breadboard digital computer was installed for the latter part of the extended-span testing, including the cruise-speed transfer function tests and all gust response tests.

3.3.1 Flight Data Reduction Techniques

The number of recorded channels required for all phases of the test program exceeded the capability of the FM system alone, and a mixture of FM and PCM recorded data was used. Amplitude and phase critical parameters for the transfer function tests were arranged to the extent possible on adjacent channels on the FM system; non-phase critical but amplitude critical parameters such as total and static pressures were recorded on PCM at 20 frames per second with 5 Hz pre-sample filters; and all parameters required to derive gust velocity were recorded on PCM at a frame rate of 40 samples per second with 25 Hz pre-sample filters.

The basic data reduction technique involved digitizing the airborne tape FM data using a sample rate as required to effectively obtain the goal of flat frequency response and phase lag of no greater than 5 degrees up to 10 Hz. During this digitizing process a constant amplitude low pass filter was applied to the raw FM data. The upper frequency cutoff of this filter was 0.25 times the selected sample rate. The digitized FM and PCM data were combined on a single tape in the form of digital counts, and then the appropriate calibrations were applied to provide an "engineering units" tape for use by the analysis computer programs.

SECTION 4

ANALYTICAL METHODS

4.1 MANEUVER LOADS ANALYSIS

The analysis of the effects of the MLC system on maneuver loads for both the baseline and extended span configurations used the existing L-1011 static aeroelastic loads programs. These programs utilize analytical representations of aerodynamics (Aerodynamic Influence Coefficients, AIC's), stiffness (Structural Influence Coefficients, SIC's), and mass characteristics to perform closed form solutions to obtain the aeroelastic loads. The size of the grid systems to represent these characteristics is indicated in Table 4-1 for both the baseline and extended span configurations. The additional grid points in all cases are added to represent the span extension.

The production programs utilize an extensive amount of supporting data such as airplane geometry, aerodynamic data, stiffness data, weight data, and systems data. These data have been added to and refined extensively from the first preliminary analysis through flight and ground testing of the L-1011.

An example of the extensive data base and how it was generated and refined as the baseline L-1011 advanced through various stages of design is the aerodynamic data used for structural design. Subsonic lifting surface theory was used during preliminary design of the L-1011 to develop AIC's. These AIC's were adjusted to reflect measured wind tunnel force and moment data as it became available. The wind tunnel testing program spanned several years so the test results were updated periodically and the AIC's were likewise updated. During the wind tunnel test program, when the L-1011 configuration was fairly firm, high and low speed wind tunnel pressure models were defined. The purpose of these models was to obtain detail aerodynamic pressure distributions for determining airload distributions for structural design. The pressure data is used directly to account for the airloads associated with a rigid airplane while the AIC's are still used to determine the incremental

TABLE 4-1. MATH MODEL FOR MANEUVER LOADS ANALYSIS

Item	Analytical Representation (grid points per side)	
	Baseline Configuration	Extended Span Configuration
AIC	152	161
SIC	156	163
Mass	251	261
Net Aeroelastic Loads	251	261

airloads due to flexibility, control surface deflections and aerodynamic derivatives not measured in the tunnel. The pressure data was helpful in adjusting the AIC's in conjunction with the measured force data, since it provided more information on the distribution between airplane components. In some cases the "alpha-delta" matrix associated with control surfaces was modified to reflect the pressure data rather than the AIC itself. The extensive nature of the pressure data for the L-1011 is indicated by the fact that over 2000 wind tunnel hours were accumulated, which produced an estimated nine million pressure coefficients. A more detailed description of the loads programs and the data base for the L-1011 is given in Reference 9.

4.2 VGA AND GLP PROGRAMS — GUST LOADS

Two dynamic gust loads analysis computer program systems were used in the NASA-Lockheed active controls program. Both program systems compute the dynamic response of the airplane to random vertical gust velocities on a power spectral density basis. Both also have options for computing the response to steady sinusoidal oscillations of the control surfaces. These two systems are similar in their mathematical modeling of the airplane but differ somewhat in their computational details. Results given by the two systems have been found to agree satisfactorily.

The older program system is called the VGA ("vertical gust analysis") system. It was developed initially in connection with the start of loads work on the L-1011 in 1967, and it has been used extensively and updated continuously since that time. This system consists of two programs used in sequence. The first is a data

preparation program, which makes various grid system transformation and other adjustments to the input data, and computes the free-vibration modes to be used as generalized coordinates. The second is the VGA program proper, which solves the equations of motion to give frequency response functions and from these computes power spectral densities and other pertinent response information. The VGA system was used in Task 1 of the NASA/Lockheed active controls program in the comparison of flight-measured with theoretical loads and accelerations due to oscillating control surfaces, Section 5.6. It was also used in the earlier Lockheed-funded program in which the active control system was synthesized, to predict the effect of the active controls on gust loads and accelerations.

The second program system, designated the GLP ("gust loads program") series, has been developed comparatively recently, with the intent that it would eventually supersede the VGA system. It is a modular system consisting of programs GLP-1, GLP-3, GLP-4, and GLP-6. GLP-1 is comparable to the data preparation program in the VGA system. GLP-3 computes, at a limited number of frequencies distributed over the frequency range of interest, the various coefficients appearing in the modalized equations of motion. It also computes at these same frequencies the coefficients needed to determine the various specific responses such as local accelerations, bending moments, etc. GLP-4 then interpolates to the many more individual forcing frequencies, solves for the frequency-response functions, and processes these to give the power spectral densities and other pertinent response information. GLP-6, an alternate to GLP-4, was completed early in 1978. It accounts for the three-dimensional nature of the gust structure — most importantly, the spanwise variation of the vertical gust velocity. The GLP series differs from the VGA series primarily in its use of interpolated aerodynamic coefficients, in its use generally of somewhat larger order grid systems, in its much greater flexibility with respect to such choices as the number of generalized coordinates to be used and the response quantities to be computed, and in its "3-D" gust analysis capability. In the present NASA/Lockheed program, the GLP system was used in both Task 1 and Task 3 to compare the reductions in gust loads and accelerations due to active controls as predicted theoretically with reductions actually achieved in flight (Section 5.7). The Task 1 comparisons utilized the traditional "one dimensional" treatment of the gust structure (GLP-4); in Task 3, comparisons were made on both 1-D and 3-D bases, using GLP-6. The GLP series was also used in the Task 3 comparison of flight measured with theoretical loads and accelerations due to oscillating control surfaces.

In gust loads analyses using either program system:

- Airplane mass data is provided to the programs in panel weight form on a "basic loads" grid consisting of 251 (261) points per half-airplane. (Values in parenthesis are for the extended-span configuration.)

- Elasticity data is defined in the form of structural deflection influence coefficient data ("SIC's") on a grid consisting of 333 (380) coordinates per half-airplane. (This grid is actually somewhat coarser than the basic loads grid, inasmuch as the 333 coordinates must provide separately for x, y, and rotational motions, as well as z motions, at many of the locations.)

- Aerodynamic data is defined in the form of aerodynamic influence coefficients ("AIC's"). These are determined by means of unsteady lifting surface theory using the kernel function approach. (The AIC's, accordingly, are functions of frequency.) However, adjustments are made to both lift and downwash such as to match wind tunnel force and pressure measurements at zero frequency. The kernel function solutions utilize an 81 (90)-point control grid for the wing and a 49-point control grid for the horizontal tail (per half airplane).

- Except in the 3-D gust analyses using GLP-6, the vertical gust velocity is assumed not to vary spanwise. Full account is taken, however, of the gradual penetration of the airplane into the gust in the direction of flight.

- The active control system characteristics are represented by means of control system transfer functions, which relate control surface positions to accelerations or rates sensed at particular locations in the airplane. Each transfer function is introduced in the form of a fraction consisting of a series of factors in both numerator and denominator, each factor of the form $(1 + as)$ or $(1 + as + bs^2)$, where s is the Laplace transform variable. This transfer function represents not only the control system computer, or "black box," but also the frequency-response characteristics of the sensors and of the control system servos. Provision is made for a separate transfer function for each combination of sensor and control surface.

- The equations of motion are formulated in terms of 22 generalized coordinates, consisting of the rigid-airplane plunge and pitch modes (in a moving-axis system) and the first twenty symmetric free vibration elastic modes. The 20 elastic modes cover a range of natural frequencies from about 1.3 to 16 Hz, varying somewhat with airplane weight. This range is considerably greater than the 0 to 7.5 Hz range (0 to 3.75 Hz for the flaps-extended gust flight tests) over which the equations of motion are solved to give transfer functions; the higher modes are needed to adequately account for the static aeroelastic effects, which can be significant in the vicinity of the short-period frequency (about 0.3 Hz). In the 3-D analysis, antisymmetric as well as symmetric modes are included. These consist of the rigid-airplane modes of lateral translation, yaw, and roll and the first 20 free vibration modes.

- In determining the response to an oscillating control surface, Section 5.6, the equations of motion are solved to give frequency-response functions

relating the various responses as outputs to the surface motions as inputs. These constitute the desired results.

In determining the response to random turbulence, Section 5.7, the equations of motion are solved to give frequency-response functions relating the various responses to the vertical gust velocity as the input. In the baseline tests in order to facilitate the machine plotting of the comparisons of theoretical with flight test data, these computations were made at frequencies chosen to coincide with those of the test data; accordingly, 192 frequencies were used, uniformly spaced at 0.0390625 Hz. In the extended span tests, 115 frequencies were used, spaced at .04 and .10 Hz. The square of the modulus of each frequency-response function is then multiplied by the gust input psd (power spectral density) to give the response psd, which is then integrated to give the corresponding $\bar{A}$ and N_o values. The Von Karman gust velocity psd is used, with a scale of turbulence, L, of 762 meters (2500 ft). $\bar{A}$ is the ratio of rms (root-mean-square) response to rms gust velocity, given by the square root of the area under the response psd curve (the rms gust velocity being unity); N_o is the characteristic frequency of the response, given by the radius of gyration of the response psd about zero frequency. (N_o is used in routine loads determinations to calculate frequency of load exceedance). These computations are performed as part of the VGA, GLP-4 and GLP-6 programs.

- The standard output of the VGA program includes frequency response functions, power spectral densities, and $\bar{A}$'s and N_o's, of

  - o 125 shears, bending moments, torsions and accelerations distributed over the half airplane.

  - o The 22 generalized coordinates used in the analysis.

  - o Separately, the airloads, inertia loads, and net loads acting on the wing-mounted and fuselage engines.

  - o Deflections and deflection rates of the three primary control surfaces i.e., the outboard aileron, the inboard aileron, and the horizontal stabilizer

The GLP series is flexible as to responses computed; in its use in the present study, the computed responses are generally confined to the particular responses included in the gust flight test data processing.

4.3 GFAM ACT SYNTHESIS/ANALYSIS PROGRAMS - FLUTTER

4.3.1 Introduction

Two aeroelastic analytical models are currently in use for the L-1011, one meeting the requirements for flutter analyses and the other the requirements for dynamic loads analyses. When the L-1011-CCV research study was initiated, the loads aeroelastic model was initially the basis for the L-1011 active control (ACT)

synthesis. It was recognized, however, that the loads model did not provide adequate representation of the higher order flutter sensitive modes. In view of this, active control synthesis tools using the flutter aeroelastic model definition were implemented in an interactive graphics system known as GFAM (Graphics Flutter Analysis Methods). Consequently, the flutter model for active control synthesis is also known as the GFAM model.

The ACT synthesis method (the method of constraints) available on GFAM was designed to satisfy requirements for gust loads as well as flutter. Maneuver loads, handling qualities requirements, ride quality, etc. may be integrated into the synthesis procedure.

4.3.2 GFAM

An interactive computer graphics system, Graphics Flutter Analysis Methods (GFAM), was developed by Lockheed-California Company to complement its general batch-process Flutter And Matrix Algebra System (FAMAS) and other computer programs in performing complex numerical calculations, using a fully integrated data management system. GFAM has many of the matrix operation capabilities found in FAMAS, but on a smaller scale, and is utilized when the analysis requires a high degree of interaction between the engineer and computer, and schedule constraints exclude the use of batch entry programs.

GFAM, using a matrix data base generated for batch flutter analysis in the FAMAS system, performs interactive flutter analysis, structural optimization to satisfy flutter requirements, control synthesis for CCV (Control Configured Vehicle) applications, dynamic gust loads, airplane response, decompression (vent) analysis, general matrix algebra operations, and the matching of structural dynamics analysis to ground vibration test data. GFAM supports test data correlation, flutter methods development, and quick analysis of a design for flutter and structural dynamic characteristics during preliminary and point design phases.

GFAM technology modules perform interactive calculations in a specialized format directed by the form of the equations requiring solution. Each program has its own display but all share in a common data base.

Of particular interest here are the GFAM modules used in ACT synthesis activity. GFAM's FLUTTER FEED module performs standard flutter analysis and generates gain and

phase data for flutter constraints required in the method of constraint synthesis process. GFAM's GUST FEED module performs standard dynamic gust loads analysis and generates gain and phase data for gust loads requirements. GFAM's BODE takes the gain and phase data from FLUTTER FEED and GUST FEED and other gain and phase constraint data from handling qualities, etc. and solves for the transfer function that best fits the gain and phase constraint data.

Typical gain and phase constraint boundaries for the active control function required to satisfy loads and flutter constraints are illustrated in Figure 4-1. The curve fit technique currently employed in BODE is based on least square fit to the gain and phase of the active constraint data. This method was primarily used during the initial ACT development stage and found to produce transfer functions of more complex form than was desirable.

Satisfying all gain/phase constraints by the least square method invariably results in a transfer function having higher order polynomials which usually have poles in the right hand plane. Realistic mechanization and reliability considerations require a more simple transfer function which is a compromise in satisfying the imposed constraints of the active control system. An updated version of FLUTBODE will permit inequality constraints to be imposed on the transfer function coefficients during the curve fitting process. This will give the engineer greater control over the final form of the transfer function.

The flutter and gust modules are sized to accept 50 generalized (modalized) coordinates and 24 control transfer function matrices.

4.3.3 ACT Synthesis - Method of Constraints

The methodology for active control synthesis is based on a concept in which the active control system is designed to specified active constraints. These constraints include requirements for flutter, gust, and handling qualities. The method, which is an outgrowth of work on structural resizing for flutter (Reference 10), makes extensive use of solving two equations for two unknowns in the flutter determinant and in the response equations.

The design-to-constraints general procedure includes many of the standard steps required in any synthesis procedure. The basic flow of the method is illustrated in Figure 4-2. First, for flutter and gust, the reference configuration must be

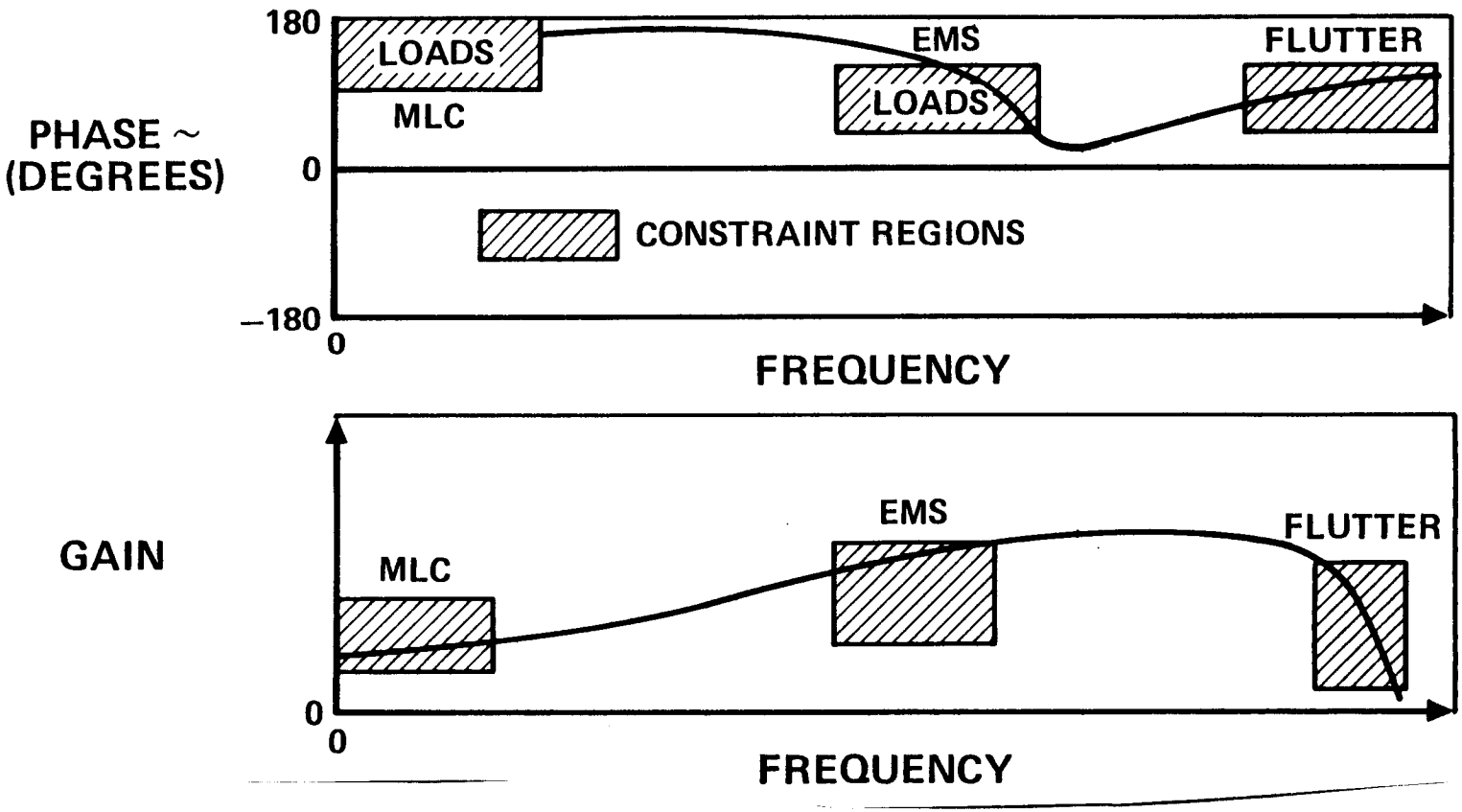

Figure 4-1. Bode Curve Fit

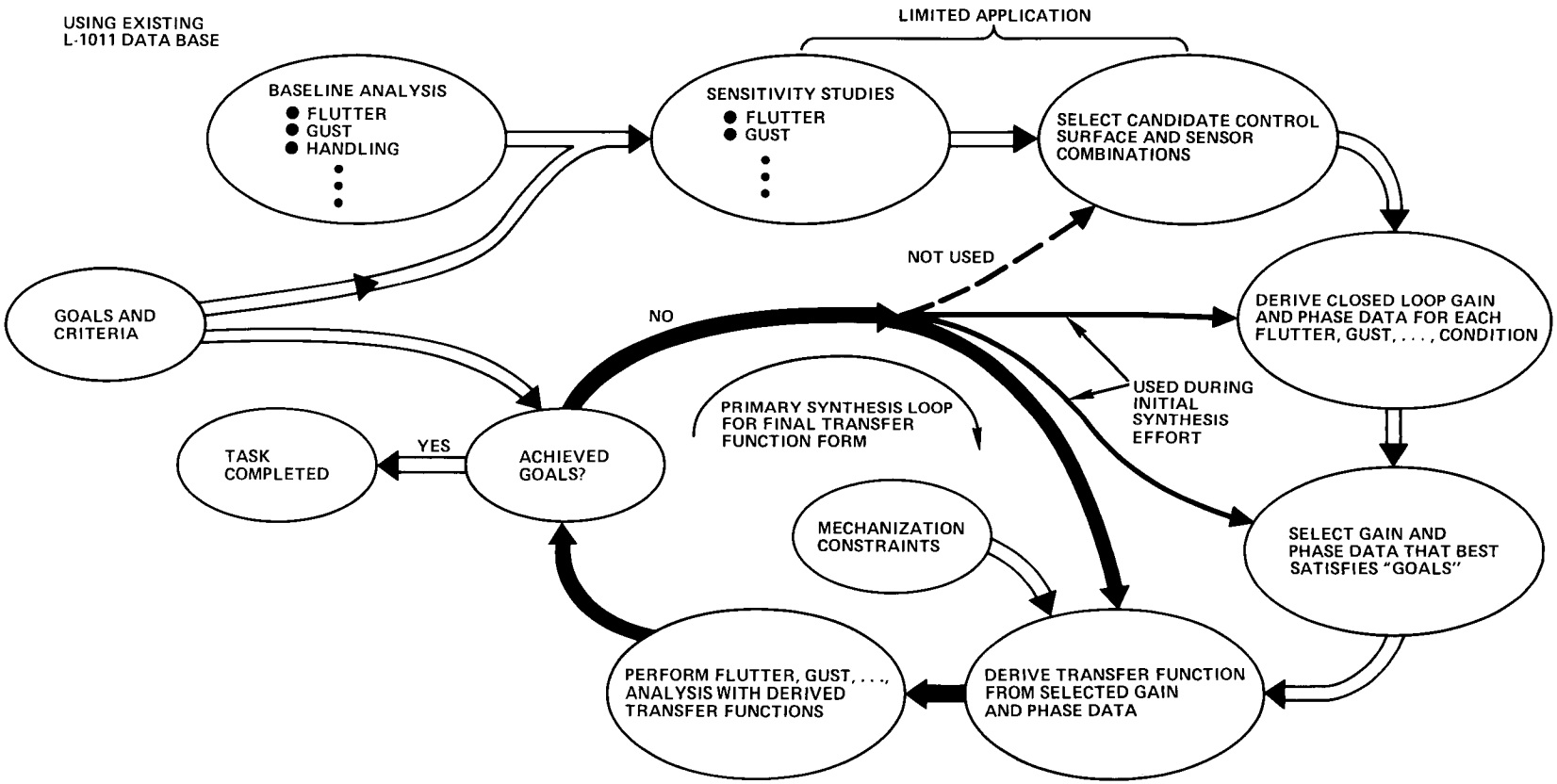

Figure 4-2. L-1011 ACT Synthesis - Method of Constraints

analyzed and design deficiencies determined for flutter and gust. Then, goals for flutter and loads relief must be established and the analysis criteria derived from the goals. The next step is a sensitivity study to establish an optimum combination of control surfaces and sensors. With the completion of the sensitivity study, the closed loop constraint gain and phase data for each of the flutter and loads deficiencies are then computed.

From the gain and phase constraint data, the data that best satisfy the objectives of the study are then compiled. The transfer function that most closely fits the constraint gain and phase data is derived with the additional consideration of mechanization or hardware constraints. Finally, the closed loop analyses for flutter and dynamic gust loads are performed to verify that the constraints made active during the synthesis completely satisfy the objectives of the study. If at this point the model is still deficient in flutter or loads some constraints made inactive may have to be activated and the analysis repeated.

4.3.4 GFAM L-1011 ACT Synthesis/Flutter Model

The GFAM L-1011 ACT synthesis/flutter model is a 117 structural degrees of freedom simple beam element representation. The structural model has been correlated with ground vibration and static deflection tests. The model uses unsteady kernel function aerodynamics adjusted for wind tunnel (steady) data. A set of 9 x 9 collocation points was used on the wing and horizontal tail and compensation for geared elevator on the horizontal tail was provided. Elevator aerodynamic effectiveness was also adjusted to reflect test data. The horizontal stabilizer control surface was force actuated using a complete model of the actuator. The inboard and outboard ailerons were displacement actuated.

The generalized coordinates for the basic airplane included 3 airplane rigid-body, one free pitch stabilizer, 35 full airplane vibration modes, 5 simply supported stabilizer modes and 6 unit modes which are associated with the aileron and stabilizer actuator attachment points degrees of freedom. For the extended span configuration, one full airplane vibration mode was deleted and a free pitch aileron and 4 simply supported aileron modes were added. The 6 unit modes were deleted by incorporation into the stabilizer and aileron modes. The aerodynamics were computed for 23 reduced frequencies and were interpolated for other reduced frequencies required for either flutter or gust analysis within the respective programs in GFAM. Twenty-five load quantities and 15 accelerations were computed during the ACT synthesis effort.

4.4 STATE SPACE/OPTIMAL CONTROL TECHNIQUES

State space techniques were used (1) to represent the elastic airplane in linear and non-linear simulation in the time plane, and (2) for control law derivations using optimal control techniques.

Control law studies based on the state-space optimization procedure originally utilized an algorithm based upon Potter's method to yield directly a full-state matrix solution for the optimal feedback gains. The performance index is of the quadratic form

$$\int_0^\infty \left(\sum_{k=1}^{n} \underline{h}_k' \, Q_k \, \underline{h}_k + \underline{u}' \, R \, \underline{u} \right) dt$$

Each of the terms 1 through n represents a group of variables to be minimized, such as a gust loads group, a maneuver loads group, a handling qualities group, etc. Within each group, the h's represent sets of equations defining variables to be minimized in accordance with the specified criteria. Each set is of the form

$$\underline{h}_j = a_j \dot{\underline{x}} + B_j \underline{x} + C_j \underline{u}.$$

where $\underline{x}$ is the vector of state variables and $\underline{u}$ is the vector of control variables in the system state space equation

$$\dot{\underline{x}} = F \, \underline{x} + G \, \underline{u}.$$

Q_j is a diagonal weighting matrix which determines the relative importance of each of the variables in $\underline{h}_j$. Adjustments of the weighting matrices are facilitated by man-in-the-loop evaluations made possible by a computer graphics terminal which permits the engineer's judicious placement of closed loop poles and his balancing of trade-offs among the various criteria (Reference 11).

Application of this optimization technique to a highly sophisticated mathematical model of the type used in loads and flutter analyses, requires that the model be converted to the state-space form (time domain) and that its complexity (matrix rank)

be reduced. An appropriately reduced model will describe the rigid-body dynamics and only that part of the structural dynamics necessary for the particular purpose at hand. An optimal control law is based upon tradeoffs among the various criteria and their relationships with the dynamic characteristics defined by the simplest appropriate model.

A 40 x 40 state space model of the baseline airplane was obtained from the sophisticated loads analysis model by modal truncation. It was represented in an inertial coordinate system. The representation of the unsteady aerodynamics in the time domain was based upon least square fits of kernel function aerodynamics at selected frequencies. The model included three controllers (inboard aileron, outboard aileron, and horizontal stabilizer), two rigid body modes (pitch and plunge), six structural modes, free stabilizer pitch, aileron actuator dynamics, and Dryden gust input. The free stabilizer pitch coordinate permitted special representation of the horizontal stabilizer control system dynamics. The quadratic optimization algorithm was successfully applied to this model to obtain a full-state optimal (though impractical) control law matrix of 120 feedback signals. Current independently funded research is underway to solve the partial state feedback problem.

A 27 x 27 model contained all of the modes that were in the 40 x 40 model, except that extraneous poles which resulted from the unsteady aerodynamic approximations were eliminated by a method of spectral decomposition. It should be noted that the "residue reflections" of the "unsteady aerodynamic poles" remained with the other twenty seven poles. This and other reduced models were transformed into a moving coordinate system.

A 12 x 12 reduced model obtained by still further spectral decomposition was used to represent the airframe in conjunction with the "iron bird," employing the real hardware (hydraulic servos and breadboard computer). This model had two rigid modes (short period and phugoid), three structural modes, and the Dryden gust input.

A 4 x 4 reduced model was modified to a 7 x 7 model by the addition of three unknown control lags to be optimized for phase control. The resulting state-space model contained the short period mode, the first wing bending mode, and three exponential lag terms (two in the aileron channel and one in the horizontal stabilizer channel). The quadratic optimization procedure yielded a full-state feedback matrix (seven state variable signals commanding two controllers), which was then mathematically transformed into a system with only three input signals: wing tip

acceleration, c.g. acceleration, and pitch rate. A Luenberger observor (Reference 12) was utilized in the transformation process to represent one of the state variables. This is an example of a technique for using optimal control theory with limited numbers of sensors. The combination of sensors must be able to "observe" all of the modes treated. A control system derived in this manner is "optimal" only for the modes considered, and must still be verified by the more complete flutter and gust loads programs.

The quadratic optimization procedure was also applied to rigid body models which included downwash and gust penetration effects. These were useful for comparing simplified results with those from the more sophisticated models.

Simulation for the extended-span configuration of Task 3 also started with a 40 x 40 model truncated from the larger gust loads model. The 40 x 40 was reduced by spectral decomposition to an 18 x 18 and a 14 x 14 for non-linear controls studies using CSMP (continuous system modeling program). The 14 x 14 was used for the VSS simulation. These models contained one and three more structural modes than the 12 x 12 used for the baseline tests.

4.5 CONTROL LAW DERIVATION

The control laws derived for the flight testing were formulated to achieve the system performance objectives previously identified in the Lockheed IRAD investigations. These objectives were 1) aileron deflection of -8.67° per incremental load factor for maneuver load control and 2) a reduction of approximately 25% of the wing gust load increment at a midspan station. Although these objectives were originally defined for an increased gross-takeoff-weight L-1011 derivative, it was expected that the requirements for the extended span configuration would be quite similar.

In order to accomplish the objectives as defined, active controls functions of maneuver load control (MLC) and elastic mode suppression (EMS) were implemented by means of the outboard ailerons, and the function of gust load alleviation (GA later GLA) was implemented utilizing the horizontal stabilizer. The initial effort to synthesize the required control laws utilized a 40 x 40 state-space mathematical model in a quadratic optimization procedure. Although the method in general exhibits a great deal of potential, serious difficulties were encountered in the specific application attempted: ill-conditioned matrices which had to be inverted, problems with the state-space representation of unsteady aerodynamics, sensitivity of the

results to the choice of merit function weighting factors and, most difficult of resolution, the lack of a reliable method of reducing the full-state feedback solution to a practicable configuration. Although most of these difficulties were resolved in the IRAD program and significant progress was made in resolving the remaining ones, schedule constraints dictated the use of alternate procedures for control law synthesis.

One such procedure, the method of constraints, was developed as a modification of an in-house procedure called Incremented Flutter Analysis (Reference 10) and implemented as part of the GFAM system (Section 4.3). In this method, the control system amplitude and phase characteristics are defined, at given flight conditions and at specified frequencies, which are required to satisfy a given set of constraints. Once these desired gain and phase characteristics are established for the design space of interest and the given control system characteristics identified, a best-fit control law is derived which approximates the desired characteristics. Unfortunately, a large number of constraints may be required in order to assure adequate behavior over the design space of interest, frequently resulting in overly-complex or ill-conditioned functions. In practice, it is also difficult to define constraints over a sufficiently broad design space to assure acceptable characteristics of the complete active control system. The gain and phase requirements generated by this method, however, provided a useful guide in the development of the actual control laws.

The control laws, then, were developed from the data available as a result of the application of these formalized methods, supplemented by engineering judgment. It was recognized, for example, that the EMS function derived from wing-tip acceleration must be compatible with the MLC function derived from body acceleration, in the quasi-static region. Further, the phase and gain requirements of the MLC and EMS functions were readily identified. These considerations led to the formulation of a single, blended MLC/EMS control law wherein the total quasi-static gain remains constant for a given airplane lift condition (high lift or clean), and the EMS gain is modulated by varying the proportion of wing tip and body acceleration inputs.

The synthesis of the gust load alleviation (GLA) function was a more difficult task, and the resultant control function produced only modest reductions in wing loads. After a large number of control functions was analyzed, with relatively disappointing results, a control law was selected which was modeled on the control

law used in the Lockheed C-5 Active Lift Distribution Control System (ALDCS) program. It should be noted, however, that the criteria applied to this function were quite stringent: the reduction of wing loads was to be accomplished with no increase in tail loads, and the gain of the GLA, which opposes the pilot's input if not compensated, was restricted to an equivalent of approximately 25% of the test airplane control capability. It is anticipated that the relaxation of one or both of these constraints may be required in order to achieve an acceptable GLA function on a production airplane.

The evolution of the control laws through this test series and into the production L-1011-500 with extended span and active load alleviation has resulted in a set of MLC/EMS aileron control laws similar to those of Task 3.

The GLA function has been deleted from the production system, however. Its use with the noted constraints and the existing stabilizer was not justified in a cost/benefits tradeoff. A GLA function can easily be incorporated in conjunction with the augmented stability (AS) function when a new smaller tail phases into production.

SECTION 5

RESULTS AND DISCUSSION

5.1 LABORATORY AND GROUND TEST RESULTS

The real output of a successful laboratory and ground test program is smoothly functioning flight. In this respect the ground programs were eminently successful. In detail, the VSS/VFS program developed a rapid pre-flight checkout tool, the Ground Test/Failure Detection (GT/FD) kit; determined detailed characteristics of the servos and computers and determined their compliance with the specified control laws; tested the systems in simulated flight and verified the non-critical nature of potential system failures. Examples of this work are given in this section.

5.1.1 Servo Characteristics

X-Y Plots, Hysteresis - Typical aileron displacements in response to simulated MLC/EMS signals are shown in Figures 5-1 (a) and (b). Figure 5-1 (a) indicates the specified slope of -8.7 deg/g over an authority range of $\pm$6.4 deg. Figure 5-1 (b) shows the technique of examining for minimum increment control. The scales are expanded 10- and 20 to 1. Command increments of order .05V to .08V are required to produce motions, and the motion increments are of order 0.2 deg. The hysteresis is attributed primarily to the aileron position feedback loop. Given the aileron gain of -8.7 deg/g, these results indicate little aileron response to steady acceleration increments below 0.01 g. The dynamic effects are discussed in Section 5.1.2.

The stabilizer minimum increment control, Figure 5-2, appears to be about 0.004V (0.002 deg) with a hysteresis of up to 0.015 deg. With the cruise gain of 0.1 deg/deg/sec, the stabilizer should respond to pitch rate changes as low as 0.02 deg/sec, corresponding to 0.01 g at M = 0.8.

Maximum Surface Rates - Figure 5-3 verifies the expected maximum aileron rates of order 60 deg/sec, and Figure 5-4 shows the maximum stabilizer rate at just over 8 deg/sec, in the Task 3 tests. The same aileron rates were obtained in the baseline Task 1 tests, but the stabilizer was originally limited to about 3.6 deg/sec by series servo rate limitations, as discussed in Section 2.3.2.

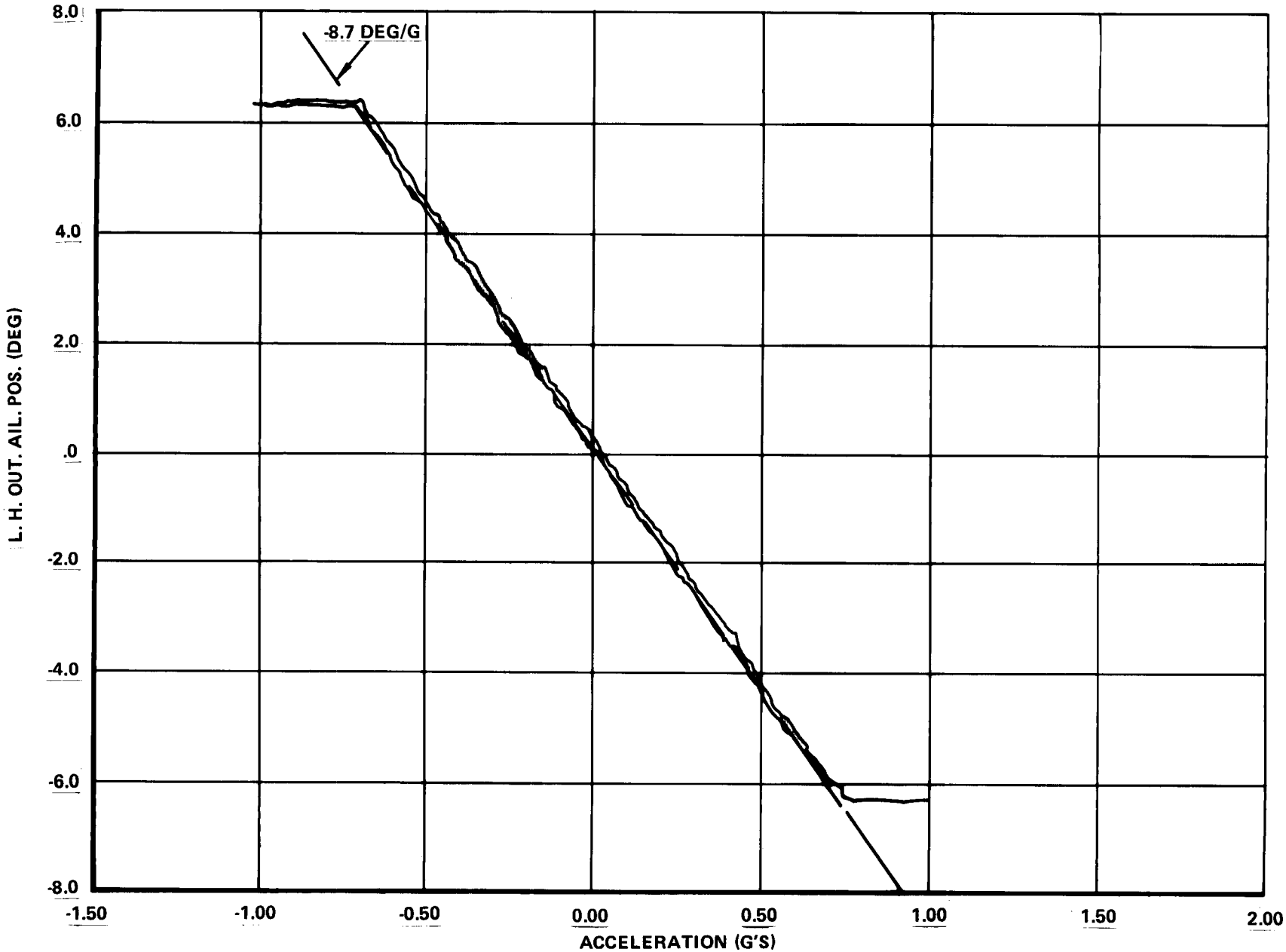

Figure 5-1. Left Aileron Displacement Characteristics
(a) Overall

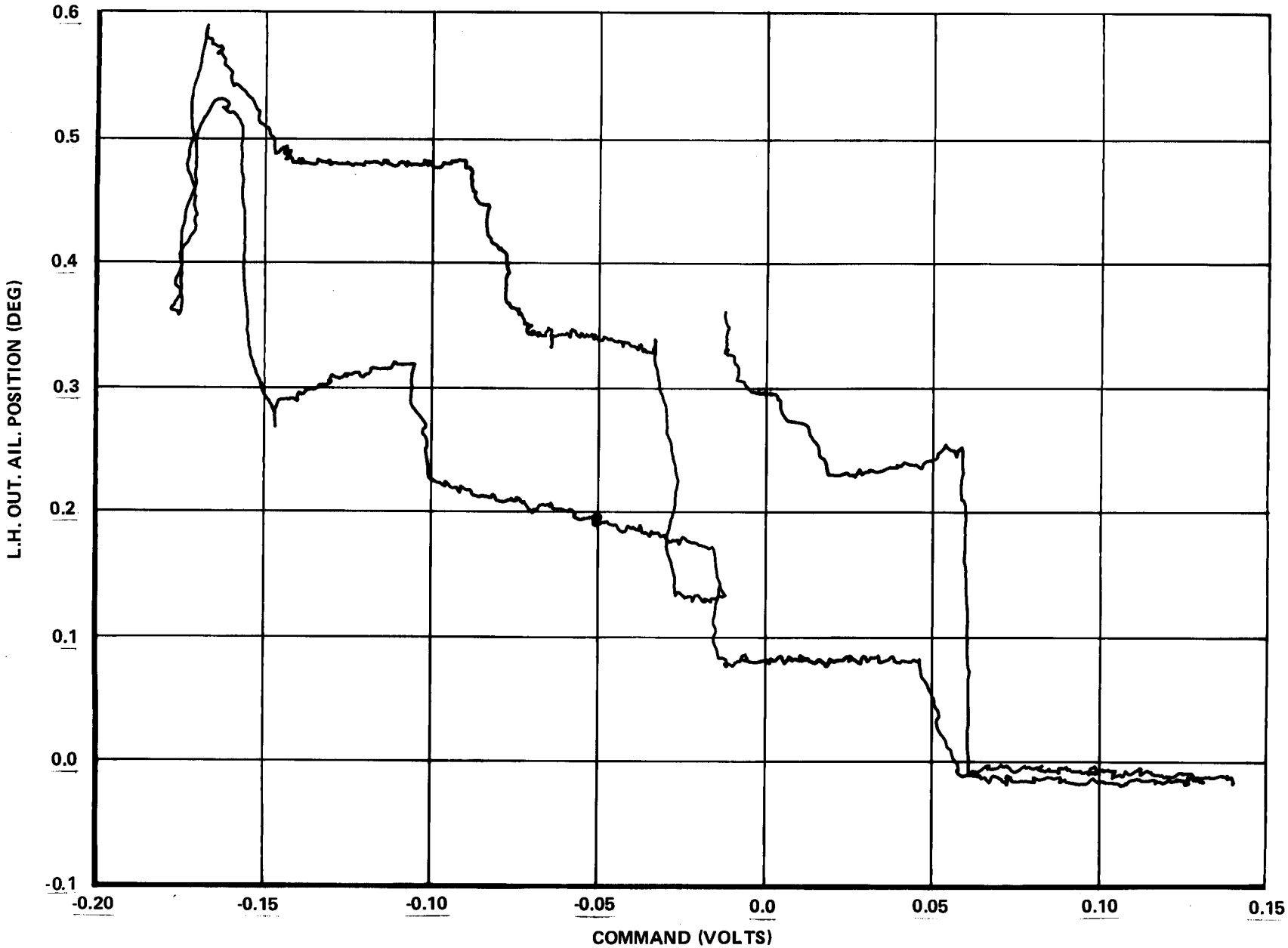

Figure 5-1. Concluded
(b) Aileron Fine Displacement

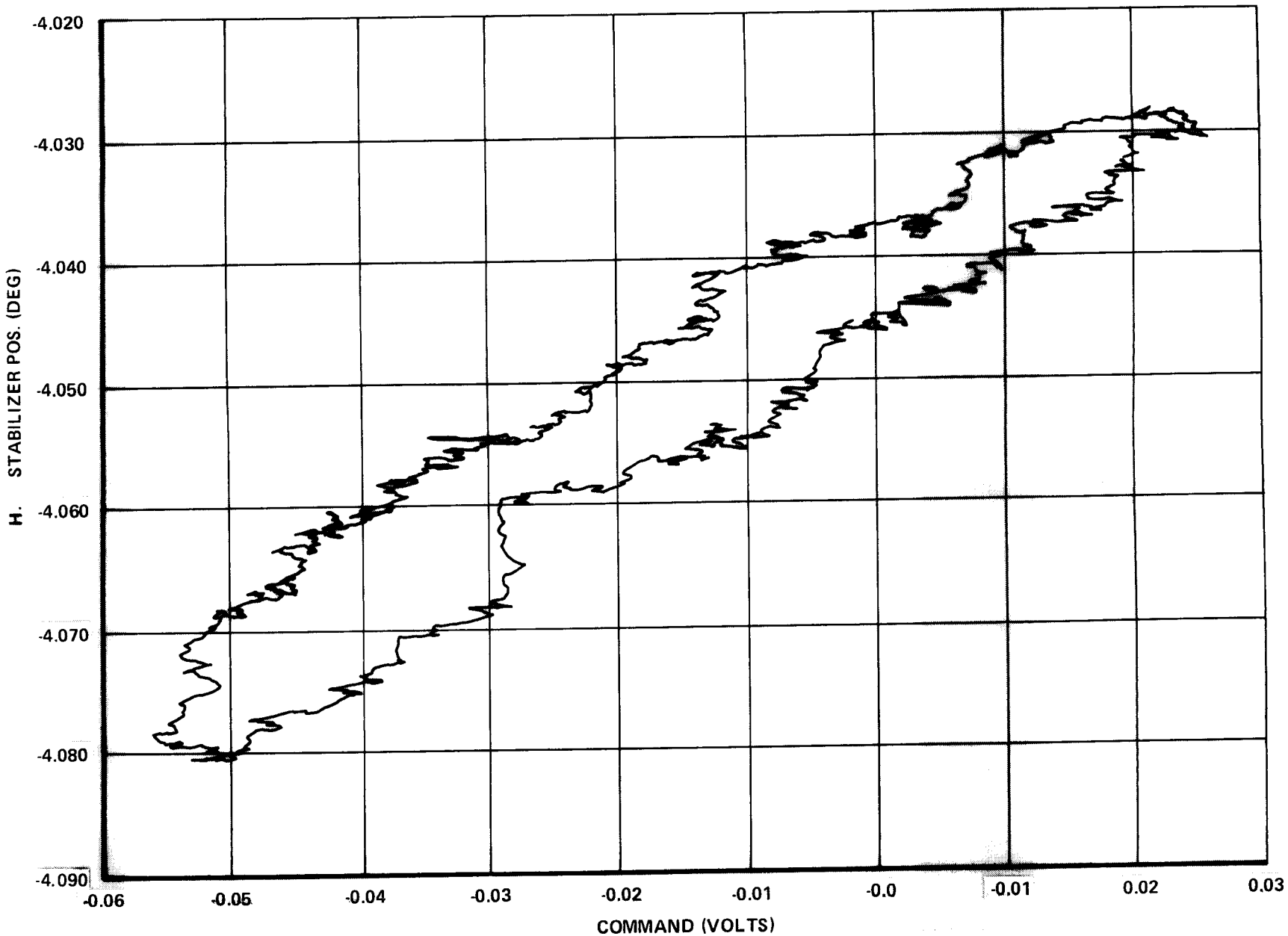

Figure 5-2. Stabilizer Fine Displacement

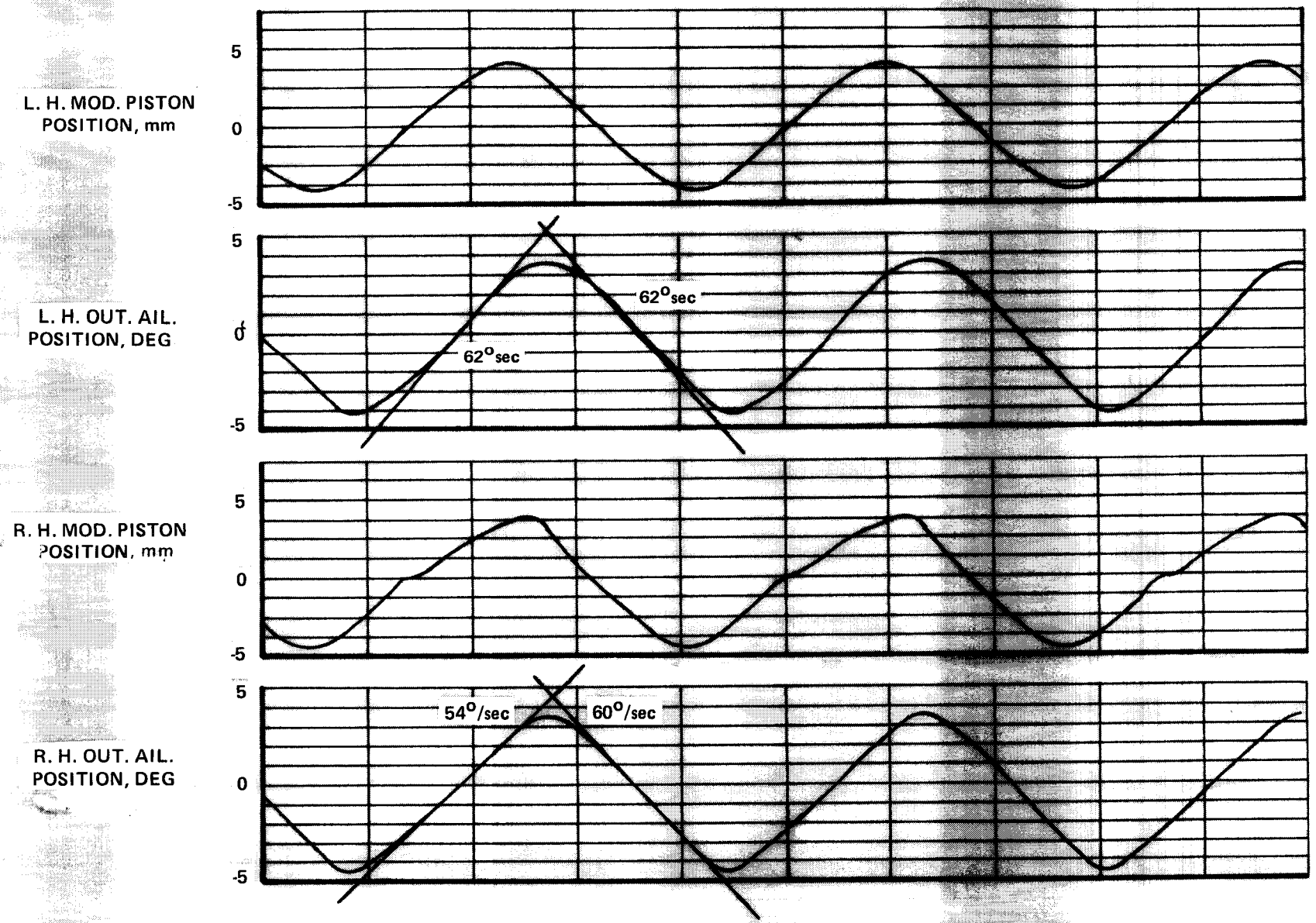

Figure 5-3. Aileron Max Rates - Oscillatory

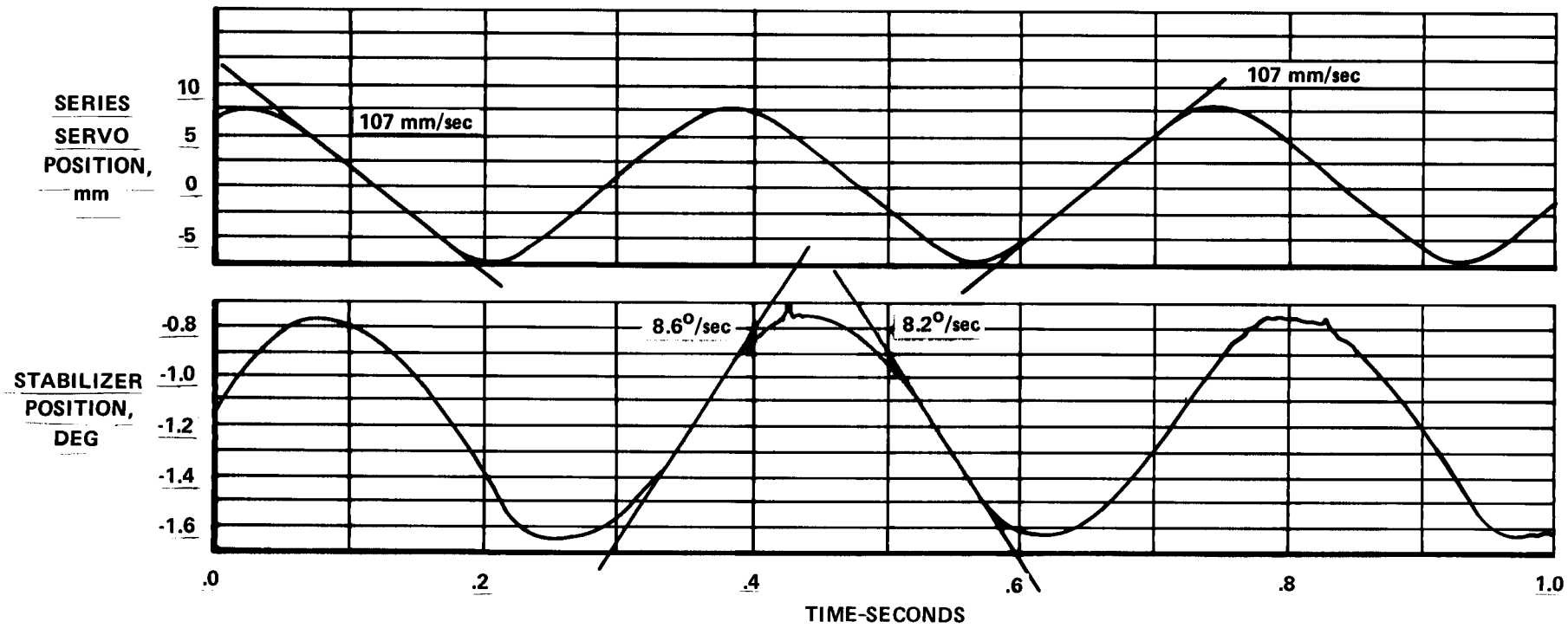

Figure 5-4. Stabilizer Max Rate - Oscillatory, Column Locked Extended Span Test

5.1.2 System Frequency Responses

A typical frequency response from simulated accelerometer output through the MLC/EMS computer to the ailerons is shown in Figure 5-5. The compliance to the specified control law is good. Note that the specified control law is based on the accelerometer output, and differs from that given in Figure 2-11 by the 1/(0.03S+1) filter built into the accelerometer.

The stabilizer gain-phase relationships, Figure 5-6, also show good agreement with the specified control law.

In the course of ground checkout in S/N 1001, the specific characteristics of the airplane servos were checked. These were the only items not transferred intact from the laboratory. Frequency response tests were made holding the output amplitude at $\pm$0.5 deg, $\pm$3 deg, and $\pm$6 deg. The response of the ailerons was degraded in both amplitude and phase angle at the 0.5 deg drive amplitude. At 1.5Hz, for example, the 0.5 deg results were down 1.2dB (15%) and had 20 deg more phase lag than the 3-deg and 6-deg amplitude data. This result is reasonably consistent with the laboratory finding of about 0.2 deg hysteresis in the aileron, Figure 5-1 (b). This non-linear response is not significant operationally, as a dead band of $\pm$0.5 deg is introduced deliberately in the digital system to minimize wear.

5.1.3 Simulated Flight Conditions

Once the servos and computers were checked out in the VSS, the VFS airplane simulation was coupled in to close the airplane response loop. A typical example of simulated flight test is shown in Figures 5-7 and 5-8, showing ACS off and on, with a step input into the aileron channel, for case LC-4 of the baseline tests. The input excited wing bending primarily. Closing the loop resulted in significantly improved damping of the wing bending with only small aileron motions, Figure 5-8.

An example of a simulated in-flight failure at cruise speed is given in Figure 5-9. The channel A accelerometer signal was disconnected. The monitor threshhold was 2 volts, corresponding to 1.4 deg symmetric aileron for cross-channel monitoring and 2.1 deg for left vs. right series servo monitoring. Inasmuch as the monitor will not be tripped unless the signal exceeds 2 volts, simulated air turbulence at a rms level of 3 m/s (10 fps) was introduced. The monitor level was reached

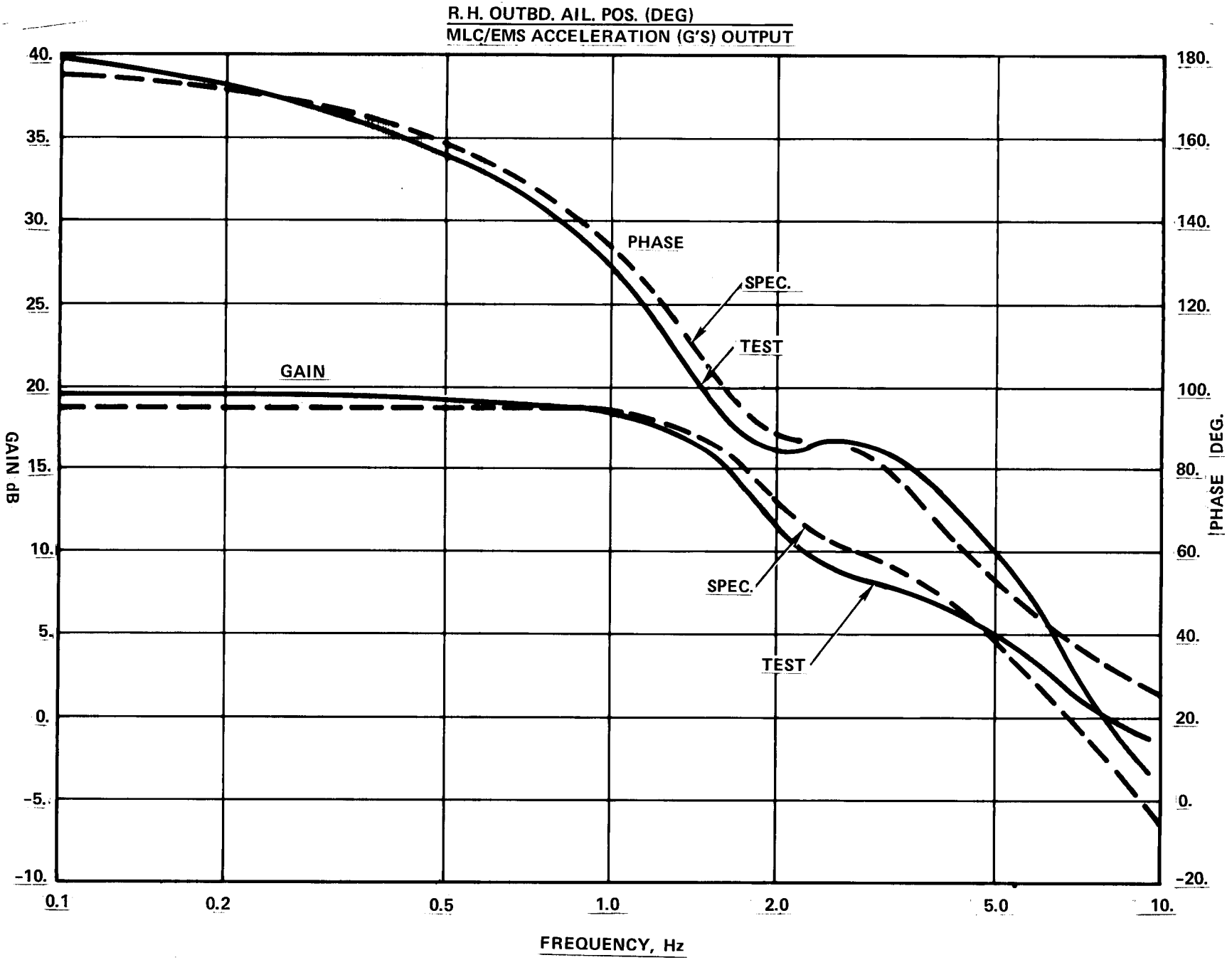

Figure 5-5. Right Aileron Bode Plot, Cruise. Extended Span Configuration

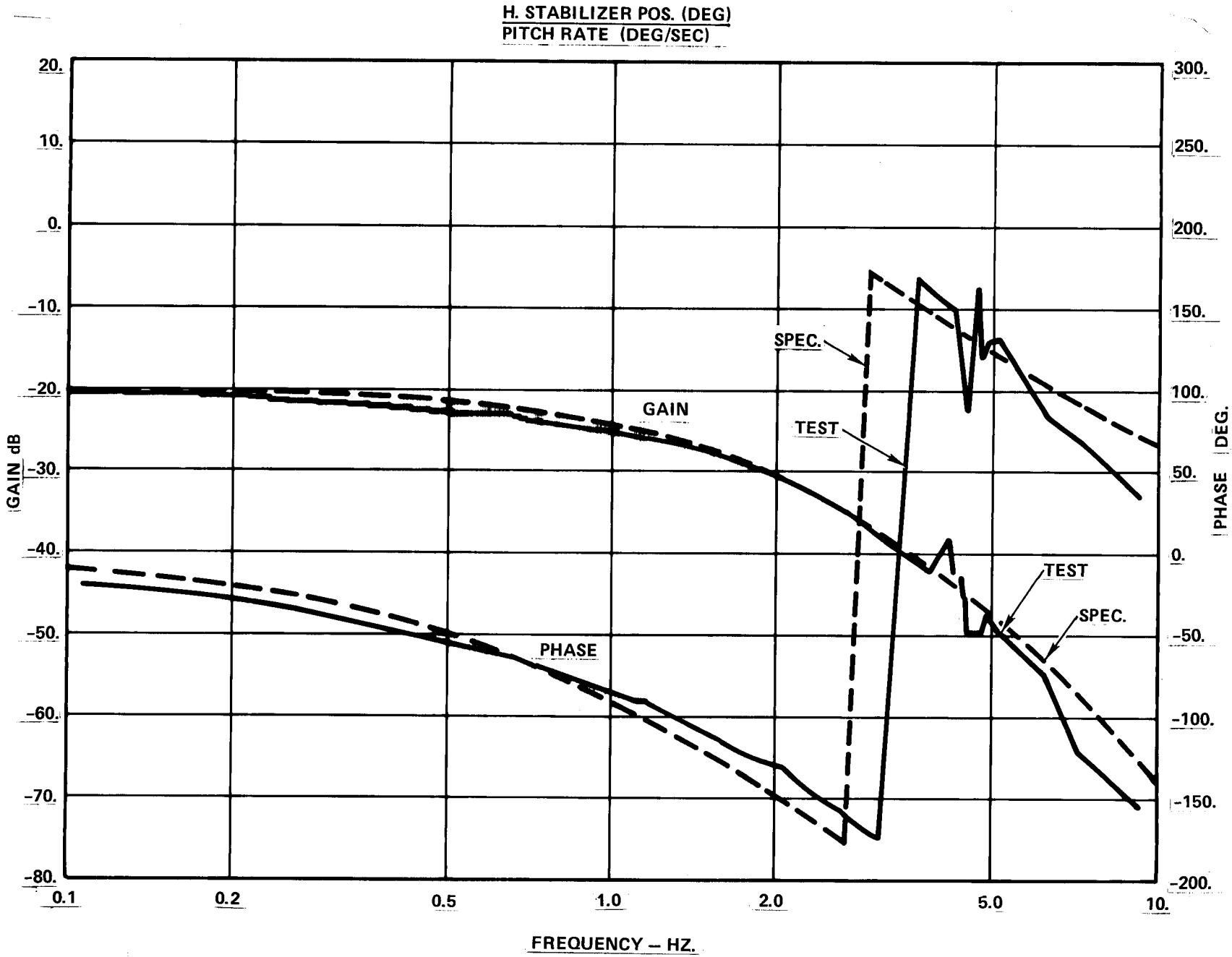

Figure 5-6. Stabilizer Bode Plot, Cruise. Extended Span Configuration

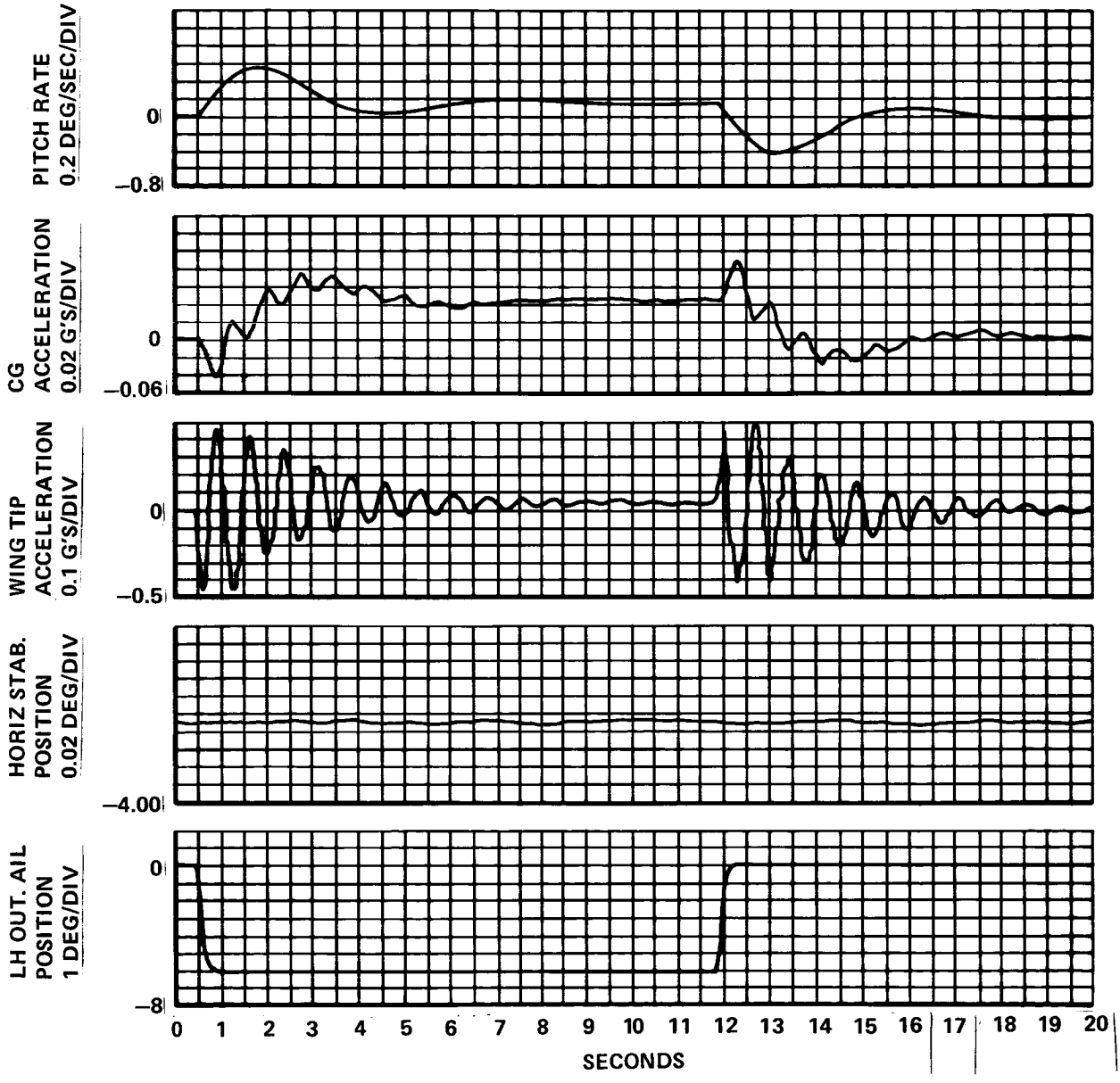

Figure 5-7. Open-Loop (ACS off) Response to Step Symmetric Aileron. VFS/VSS, Case LC-4 - Baseline
V = 225 KEAS, M = 0.50

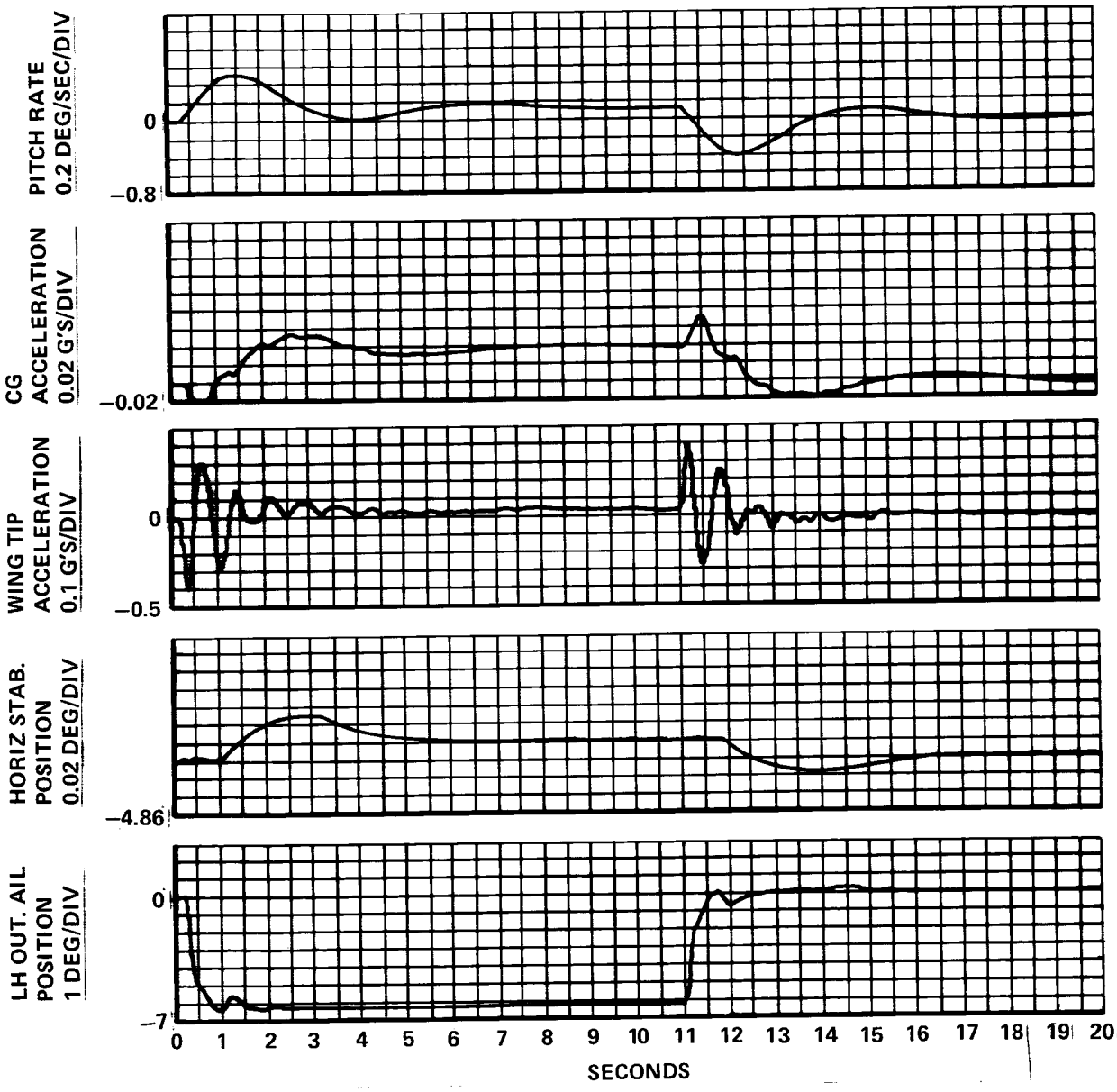

Figure 5-8. Closed-Loop (ACS on) Response to Step Symmetric Aileron Command. VFS/VSS, Case LC-4 V = 225 KEAS, M = 0.50

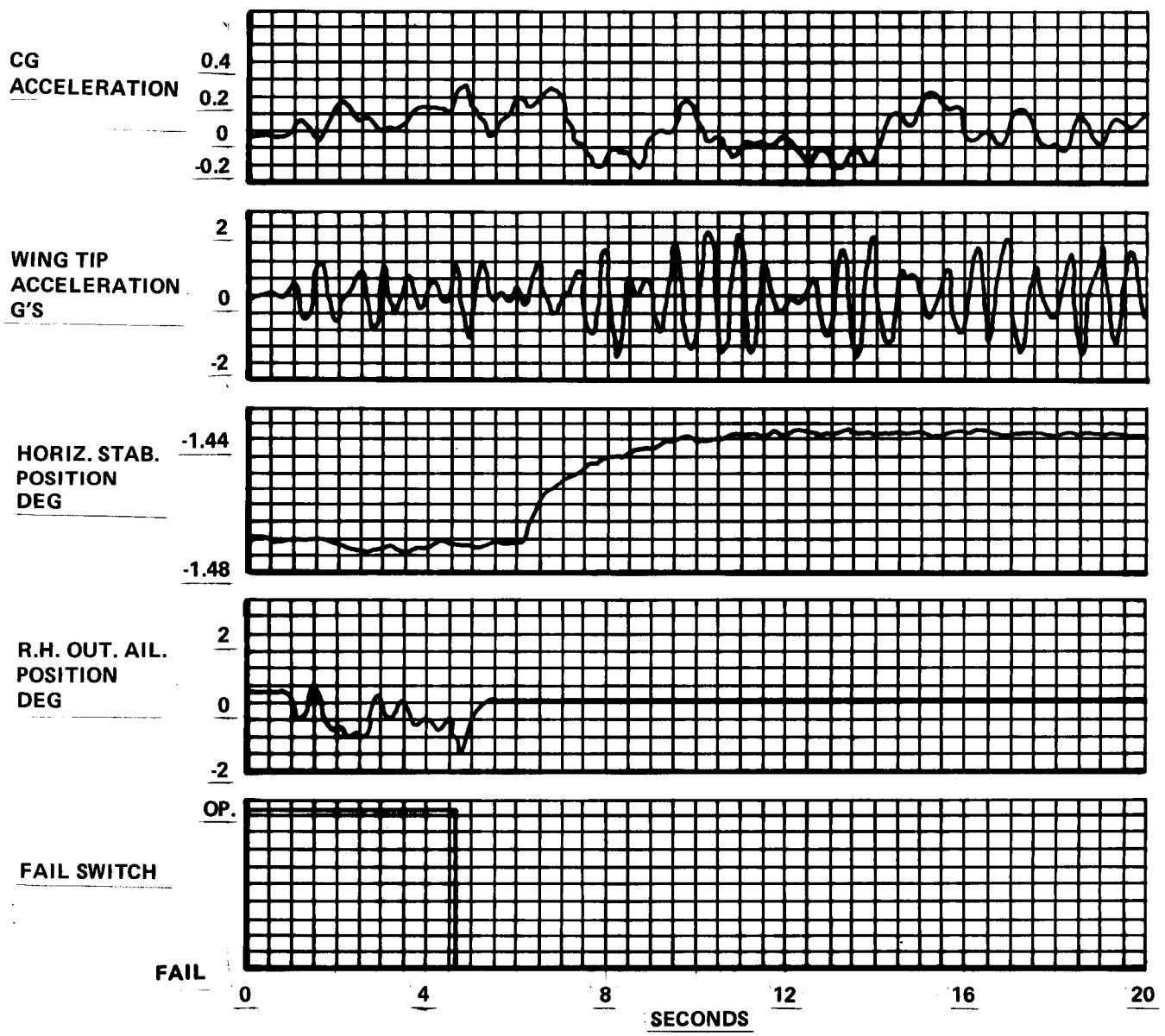

Figure 5-9. Loss of c.g. Accelerometer Signal, Channel A
Simulated Turbulence. Extended Span Configuration
V = 312 KEAS, M = 0.85

at about 4.5 seconds, when the fail switch tripped. All active systems went passive; this would represent a second failure in an operational dual-dual active control system. The failure is annunciated at the pilot station, and is only noticeable in some increase in c.g. acceleration and a marked increase in wing-tip motion. All other simulated operational-system second failures tested were similarly mild.

5.2 GROUND VIBRATION TEST RESULTS

Frequency sweep surveys were made at various shaker locations between 1 and 30 Hertz. Figure 5-10 presents a typical response plot.

The amplitude and phase angle of each surveyed point was punched on IBM cards and plotted by computer processes on a scaled isometric view of the airplane. The computer program was written such that the data were normalized to a unit vector at the point of maximum amplitude. A typical mode shape vector plot is presented in Figure 5-11. Table 5-1 presents a summary of the modes recorded during the July 1978 ground vibration test. Also included in the summary are the theoretical modal frequencies and the frequencies from the L-1011-385-1 FAA Certification Ground Vibration Test performed in 1971. A typical direct comparison summary plot for one mode is presented in Figure 5-12.

5.3 FLIGHT FLUTTER TEST RESULTS, EXTENDED SPAN

A flight flutter test program was conducted to verify the flutter integrity of the L-1011-385-1 with extended wing and aileron span, and active controls. Prior to the actual flight test, flutter analyses were conducted at and beyond the flight conditions to be evaluated. A description of the theoretical analysis method used is contained in Section 4.3 of this report.

As part of their basic function, the active controls effectively increased the damping of the wing first vertical bending mode.

The second wing engine mode, which is the most likely to be sensitive to the span extension and to the ACS, tends to couple with the wing first bending mode as described in Reference 13. Under the test conditions; i.e., with normal fuel and at 6.7 Km (22,000 ft) and speeds up to 440 KEAS, no significant change in modal stability was predicted analytically due to either the span extension or the ACS.

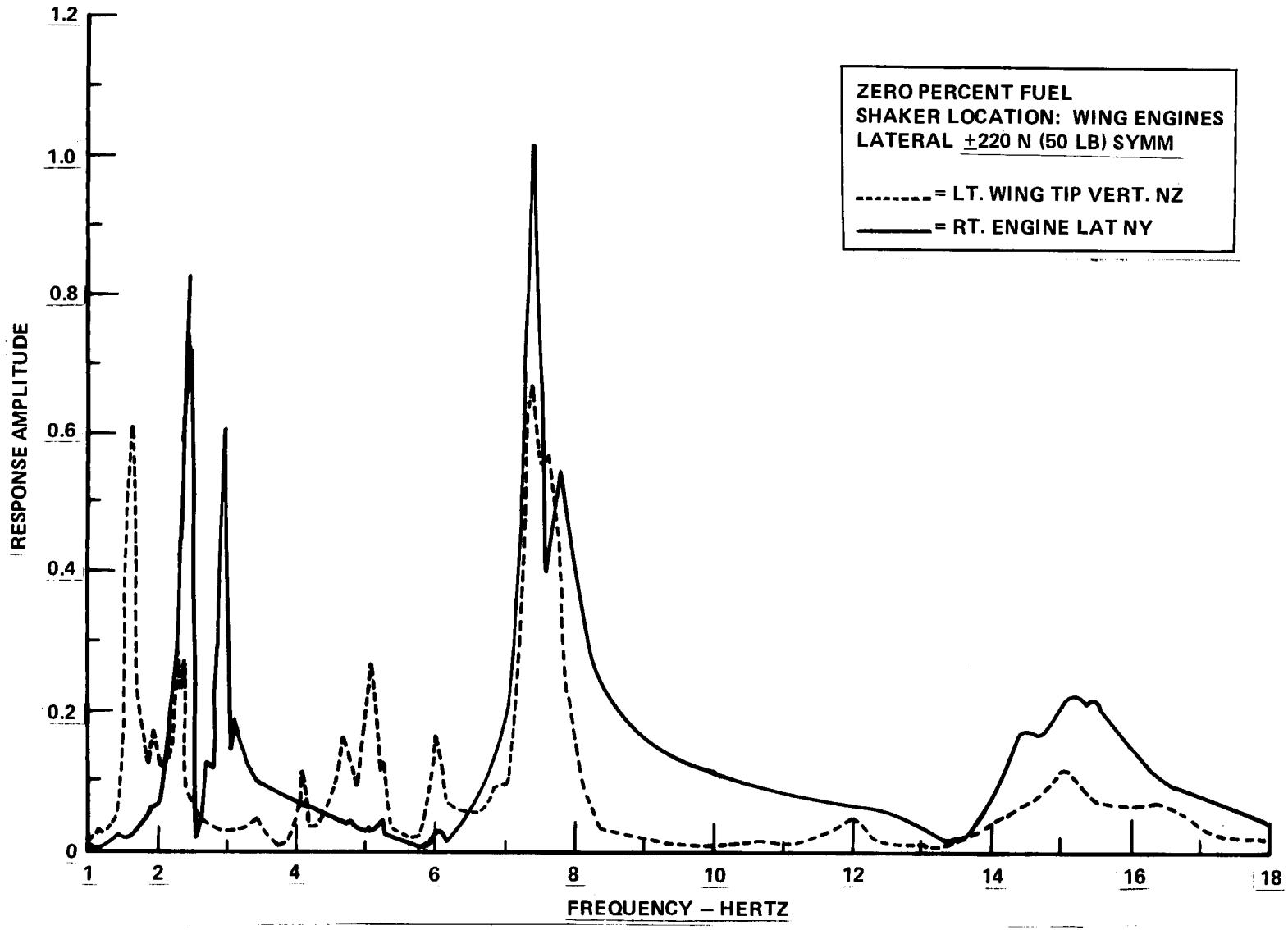

Figure 5-10. Relative Response Amplitude Vs Frequency for L-1011 with Extended Wing Tips - Ground Vibration Test Frequency Sweeps

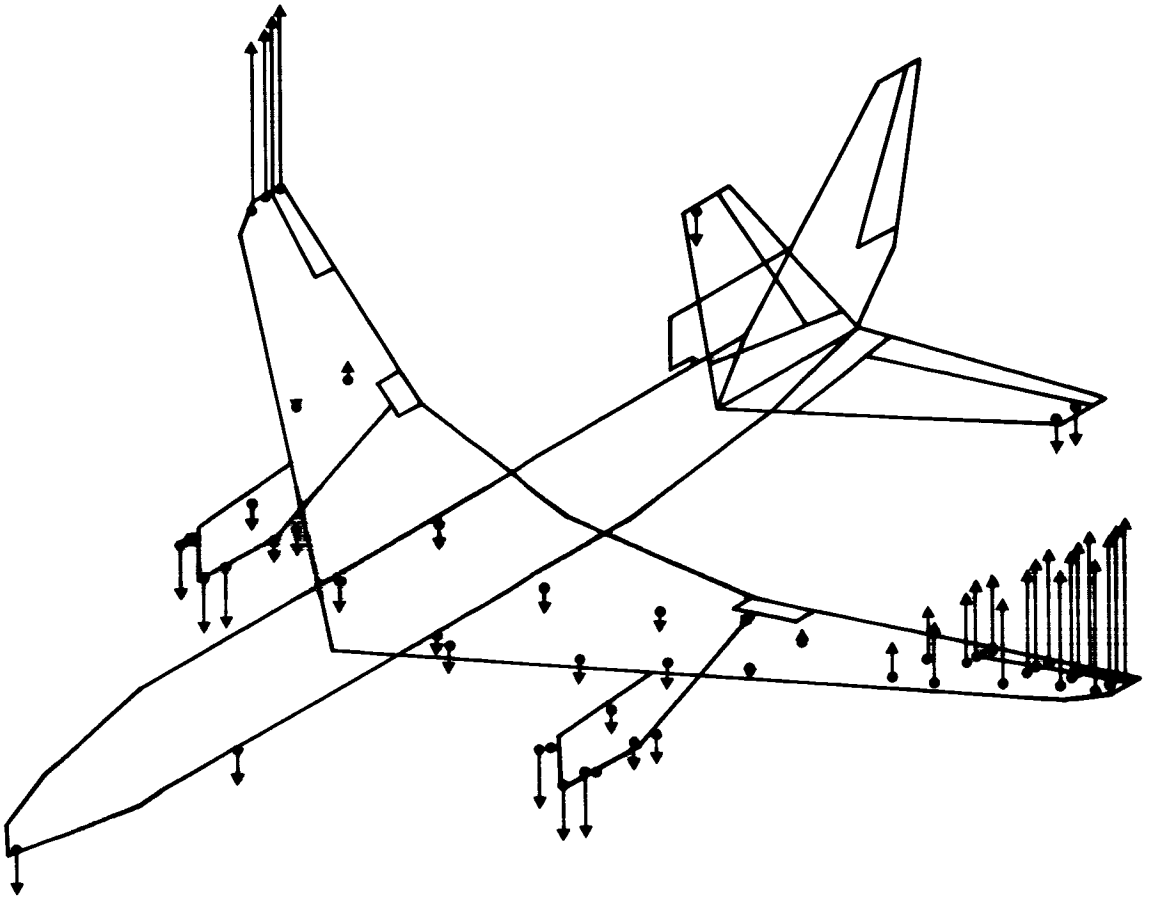

Figure 5-11. Mode Shape Vector Plot

TABLE 5-1. SUMMARY OF GROUND VIBRATION TEST MODAL FREQUENCIES

Mode Identification	Symmetry	Theoretical Analysis Freq. Hz	July 78 Test		1971 Test	
			Freq. Hz	Damping g	Freq. Hz	Damping g
Rigid Body Pitch	S	.95	.96	.057	1.00	N.M.
Rigid Body Plunge	S	1.53	1.59	.017	1.59	N.M.
Wing 1st Vertical Bending	S	1.73	1.80	.082	1.80	N.M.
Wing Engine Lateral Bending	S	2.36	2.35	.041	2.36	.08
Wing Engine Vertical Bending	S	2.90	2.87	.027	2.85	.06
Wing 2nd Vertical Bending	S	5.06	5.03	.015	5.00	.05
Wing 1st Torsion	S	11.33	11.31	.050	11.60	N.M.
Aileron Rotation	S	17.78	16.25	N.M.	N.M.	N.M.
Rigid Body Roll	A/S	N.A.	1.21	N.M.	1.23	N.M.
Wing 1st Vertical Bending	A/S	N.A.	2.08	N.M.	2.12	.018
Wing Engine Lateral Bending	A/S	N.A.	2.70	N.M.	2.57	N.M.
Wing Engine Vertical Bending	A/S	N.A.	3.36	N.M.	N.M.	N.M.
Wing 2nd Vertical Bending	A/S	N.A.	7.11	N.M.	7.50	.04
Wing 1st Torsion	A/S	N.A.	10.73	N.M.	11.60	.06

N.M. = Not Measured

N.A. = Not Available

MODE: WING-ENGINE LATERAL BENDING

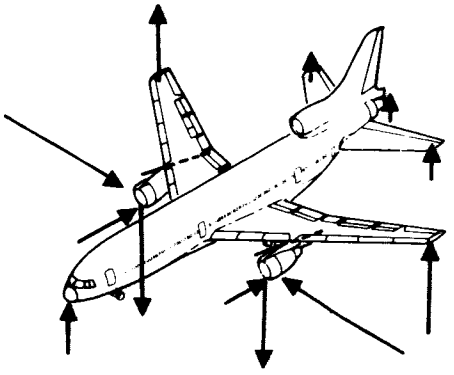

FREQUENCY 2.35 HERTZ
g = 0.041

GVT WITH EXTENDED WING TIPS TESTED JULY 1978

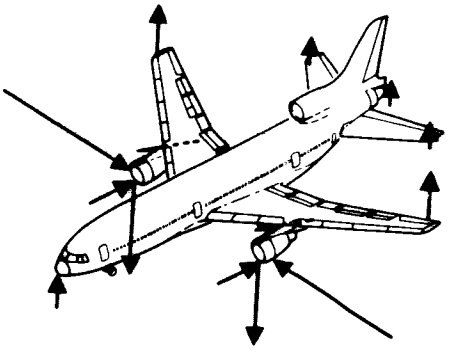

FREQUENCY 2.36 HERTZ

THEORETICAL ANALYSIS FOR A/C IN JULY 1978 GVT CONFIGURATION

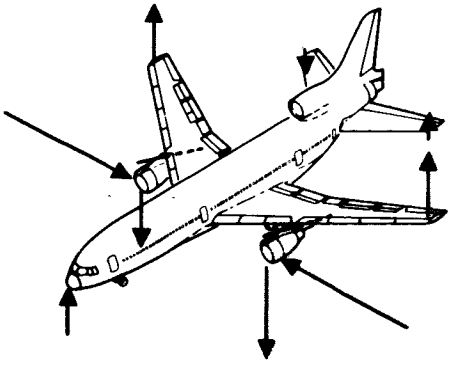

FREQUENCY 2.36 HERTZ
g = 0.08

GVT ORIGINAL L-1011-1 TESTED 1971 (STANDARD WING SPAN)

Figure 5-12. Comparison of Mode Shapes from L-1011 Ground Vibration Tests and Theoretical Analysis

The flight flutter tests were performed to assess possible modal stability changes with the addition of the extended wing tips, ailerons, and the active controls with zero, nominal, and twice nominal gain. Control column pulses and/or tuned quick stops using sinusoidal stabilizer or aileron input drives were performed at each of the flight conditions. The structural responses of the wing tipe, engines, stabilizers and aileron tips were monitored by telemetry to assess the stability of potential flutter modes.

These modes showed no observable reductions in stability, within test scatter, due to either the extended span or the active controls.

5.4 MANEUVER LOADS ALLEVIATION

5.4.1 Baseline Configuration

The objective of the baseline configuration maneuver load testing was to determine the MLC system effectiveness in reducing the baseline S/N 1001 wing loads and to compare the measured and predicted results to verify analytical methodology. Three nominal flight conditions were defined for the test and predictive analysis. These flight conditions, LC-1M, LC-2M, and LC-7M, are defined in Table 5-2. The predictive analysis was performed for the nominal test conditions as indicated in Table 5-2. The analysis was performed prior to the test to provide an indication of the magnitude of the load changes to be expected between system-on and system-off tests.

Two types of maneuvers were planned for each flight condition, wind-up-turns (WUT) and rapid "pull-and-hold" maneuvers. (The rapid "pull-and-hold" maneuvers turned out to be more of a roller coaster (RC) maneuver than the rapid transient FAR 25 design type maneuver.) The maneuvers were performed first with the MLC system off and then repeated with the MLC system on. A comparison of measured flight conditions and the nominal conditions is shown in Table 5-2. Since the objective of the analysis was to determine the effectiveness of the MLC system to reduce loads the analysis emphasized the change in load between system off and on and the slight to moderate variations between the nominal and measured flight conditions were deemed to be acceptable. This conclusion would not necessarily be valid when comparing the absolute value of the loads.

The measured stations analyzed are baseline wing semi-span stations, η = .20, .31, .38, .52, .75 and .85. Figure 5-13 shows both the baseline and extended span L-1011 wing geometry, load axis, and measured load station definitions.

TABLE 5-2. NOMINAL (PREDICTED) AND MEASURED FLIGHT CONDITIONS - BASELINE TESTS

CONDITION	GROSS MASS kg	GROSS MASS (LB)	C.G. % MAC	MACH NO.	VELOCITY KEAS	COMMENTS*
LC-1M						
a) Nominal (Predictive Anal.)	176,871	(390,000)	19.1	0.80	345	
b) Test Point, 3.101.800.01	177,460	(391,300)	22.3	0.82	351	RC - System OFF
c) Test Point, 3.111.800.01	176,553	(389,300)	22.3	0.81	356	RC - System ON
d) Test Point, 3.100.800.02	166,349	(366,800)	22.2	0.80	353	WUT - System OFF
e) Test Point, 3.110.800.03	165,079	(364,000)	22.1	0.80	350	WUT - System ON
LC-2M						(Flaps Extended 33°)
a) Nominal (Predictive Anal.)	154,195	(340,000)	27.5	0.28	155	
b) Test Point, 3.202.260.02	152,154	(335,500)	22.1	0.26	144	RC - System OFF
c) Test Point, 3.212.260.02	152,290	(335,800)	22.1	0.25	137	RC - System ON
d) Test Point, 3.200.260.01	155,057	(341,900)	22.1	0.26	146	WUT - System OFF
e) Test Point, 3.210.260.01	153,787	(339,100)	22.1	0.27	149	WUT - System ON
LC-7M						
a) Nominal (Predictive Anal.)	176,871	(390,000)	19.1	0.88	379	
b) Test Point, 3.701.900.01	168,163	(370,800)	22.2	0.87	373	RC - System OFF
c) Test Point, 3.711.900.01	167,846	(370,100)	22.2	0.88	376	RC - System ON
d) Test Point, 3.700.900.01	171,429	(378,000)	22.2	0.87	384	WUT - System OFF
e) Test Point, 3.710.900.02	170,068	(375,000)	22.2	0.88	388	WUT - System ON

*Note: RC = Roller-Coaster, WUT = Wind-Up-Turn

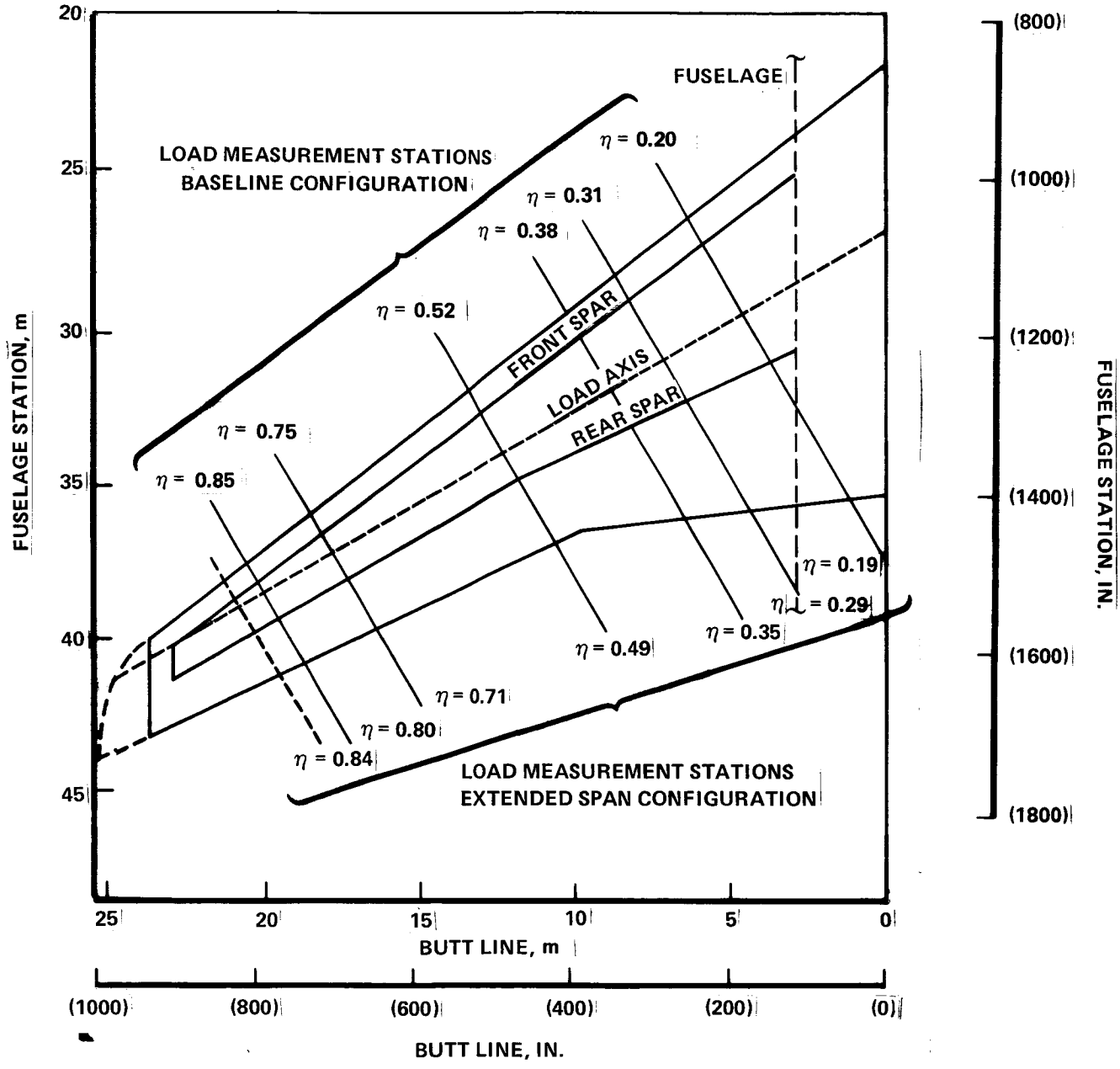

Figure 5-13. L-1011 Wing Geometry and Load Station Definition

The test data analyzed consists of time histories of the maneuvers. The time histories for each maneuver contain basic air data (e.g., Mach number, velocity, altitude, indicated angle of attack, c.g. normal acceleration, etc.), control surface positions, and load quantities. The time histories were examined carefully and suitable points were selected for detail loads analysis. The primary concern in selecting the points for analysis was to minimize the effect of extraneous conditions during the maneuver such as excessive speed variation, roll control inputs, buffet, etc. The time histories for the two high speed conditions, LC-1M and LC-7M, were relatively free of these extraneous conditions; however, the low speed flaps extended condition, LC-2M, contained significant amounts of speed variation and roll control inputs.

Extraneous conditions such as speed variations and roll inputs can be minimized during 1-g trimmed conditions so loads data was also obtained with the airplane in the following conditions:

- Trimmed at one-g, zero symmetric aileron from rigged position
- Trimmed at one-g, plus and minus approximately 4 degrees of symmetric aileron from rigged position
- Trimmed at one-g, plus and minus approximately 7 degrees of symmetric aileron from rigged position

This trimmed data provided the best indication of the aileron effectiveness for reducing loads.

Figure 5-14 shows comparisons of measured and pre-flight predicted spanwise distributions of shear, bending moment and torsion per unit aileron deflection for flight condition LC-1M. The measured data is for roller coaster, wind-up-turn, and 1-g trimmed flight and show considerable scatter about the predicted value; however, certain factors should be kept in mind when reviewing this comparison. Historically, the order of reliability of load measurement instrumentation has been bending moment, shear, and then torsion. Bending moment is primarily a measurement of axial stress in substantial tension and non-buckling compression members. Shear and torsion are related measurements of the strain in the front and rear beam webs; shear representing the sum of the two shears, while torsion represents their difference. Examination of previous load measurements for the L-1011 shows them to fit well into the historical pattern of confidence. It is noted that the bending moment data has

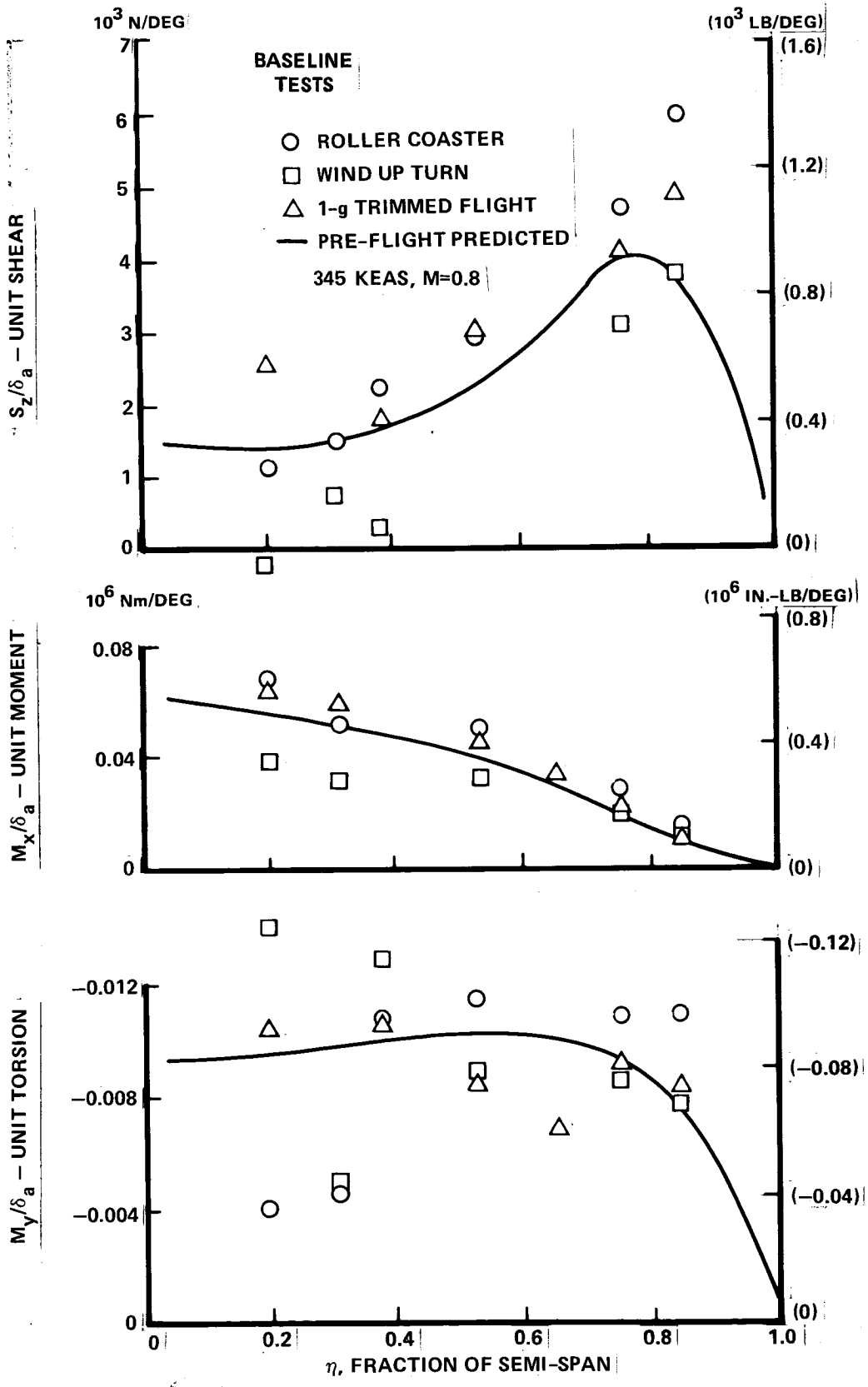

Figure 5-14. Comparison of Measured to Predicted Unit Incremental Wing Loads, LC-1M

less scatter than the shear and torsion. Also, the bending moment data shows the largest scatter for the inboard stations where the change in bending moment per unit aileron deflection is small compared with the absolute value of the bending ment. This is illustrated for LC-1M in Figure 5-15 where the ratio of the unit aileron bending moment to the 1-g bending moment (i.e., $M_x/\delta_a \div M_{x(1-g)}$) is presented. This ratio is equivalent to less than a 4 percent change in the 1-g load inboard of 0.5 semi-span (actually less than 2 percent at the wing root). Since the load measurement instrumentation was established to accommodate design loads of approximately 2.5 times the 1-g loads, it is not unexpected to find considerable scatter when measuring very small load increments.

The results of the baseline configuration tests and predictive analysis indicated the maneuvering bending moment reductions predicted for the active control system were being realized, the analytical methods and data base were entirely adequate, and a sound base was available for proceeding to the extended span configuration.

5.4.2 Extended Span Configuration

The extended span configuration wing geometry and load measurement stations are shown in Figure 5-13. The load measurement stations are indicated for both baseline and extended span configuration semi-span (η) stations. A new measurement was added at extended span $\eta = 0.84$ to provide additional load information in the tip region. This station was located as far outboard as possible with the limiting consideration being the ability to apply adequate calibration loads outboard of the station.

The test conditions for the extended span configuration are shown in Table 5-3. This table shows both the nominal specified condition and the actual test points. The maneuver conditions, M-1, M-2, and M-3, are essentially the same as the baseline conditions LC-1M, LC-2M and LC-7M respectively. The wind up turns were eliminated and only the roller-coaster maneuvers were performed since they had indicated less scatter in the baseline measurements. Since the baseline 1-g trimmed data provided the best indication of aileron effectiveness, this type of testing was expanded as indicated in Table 5-3. The initial test plan was to obtain data for conditions M-3 a) through e). During the testing, condition M-3 c) (M = 0.85, V = 400 KEAS) could not be maintained in level 1-g flight and the measurements were obtained in

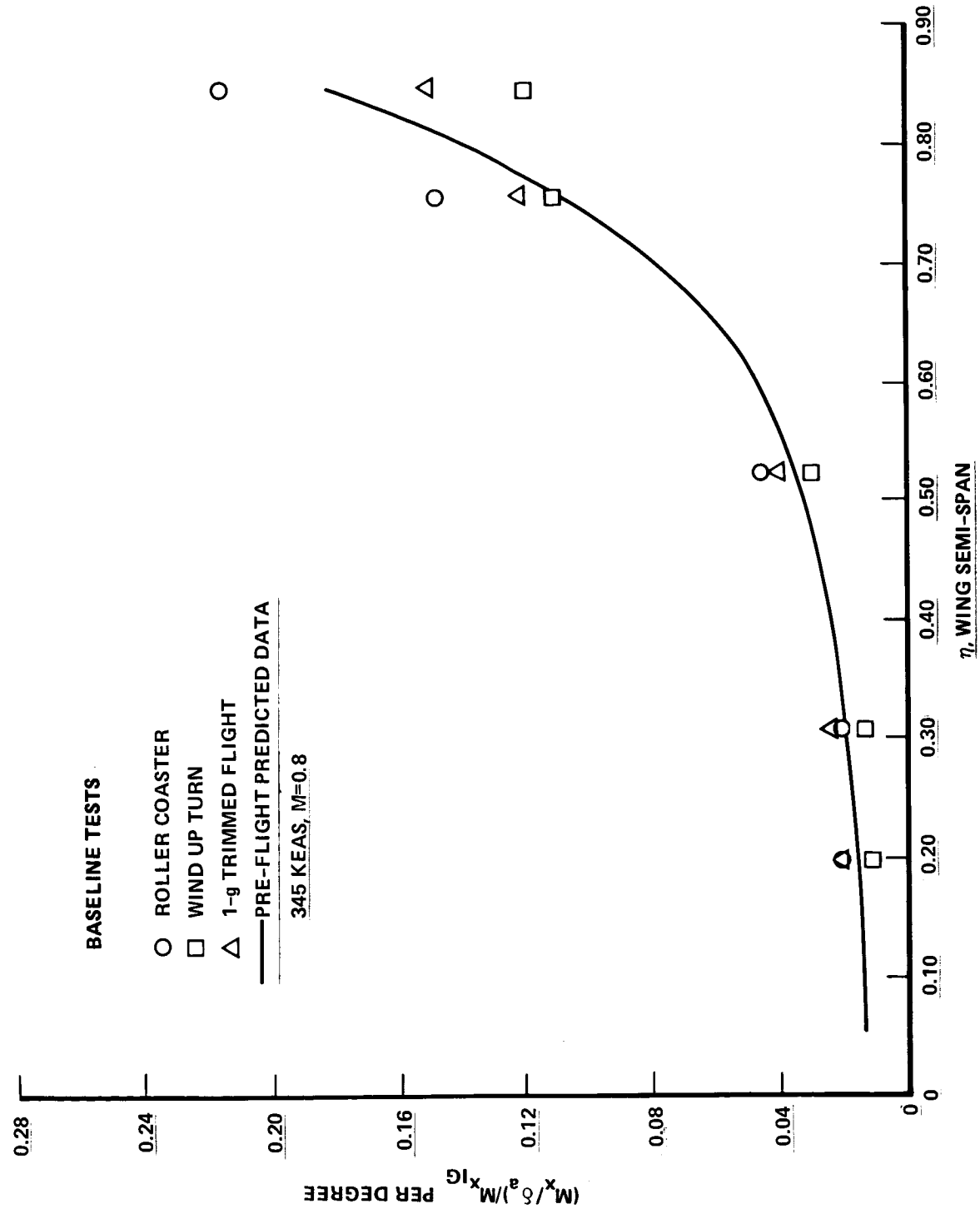

Figure 5-15. Comparison of Measured to Predicted Relative Wing Bending Moments, LC-1M

TABLE 5-3. NOMINAL (PREDICTED) AND MEASURED FLIGHT CONDITIONS - EXTENDED SPAN TESTS

CONDITION	GROSS MASS Kg	GROSS MASS (LB)	C.G. % MAC	MACH NO.	VELOCITY KEAS	COMMENTS
Maneuvers (Roller-Coasters)						
M-1						
a) Nominal (Predictive Analysis)	172,336	(380,000)	21.9	0.80	345	
b) Test Point, 22.323.360.03	167,574	(369,500)	24.7	0.80	344	System Off
c) Test Point, 22.323.360.03	167,574	(369,500)	24.7	0.81	351	System On
M-2						
a) Nominal (Predictive Analysis)	154,195	(340,000)	21.8	0.26	155	
b) Test Point, 15.323.30.03	145,306	(320,400)	24.9	0.32	159	System Off
c) Test Point, 15.323.30.03	145,306	(320,400)	24.9	0.31	155	System On
M-4						
a) Nominal (Predictive Analysis)	172,336	(380,000)	21.9	0.88	379	
b) Test Point, 22.323.398.03	166,122	(366,300)	24.9	0.88	375	System Off
c) Test Point, 22.323.398.03	166,122	(366.300)	24.9	0.89	380	System On
1-g Trimmed Flight						
M-3						
a) Nominal (Predictive Analysis)	172,336	(380,000)	21.9	0.85	320	
Test Point, 23.323.85.04		(355,800)	25.4	0.86	319	
b) Nominal (Predictive Analysis)	172,336	(380,000)	21.9	0.85	360	
Test Point, 23.323.85.04		(344,500)	26.1	0.86	356	
c) Nominal (Predictive Analysis)	172.336	(380,000)	21.9	0.85	400	
Test Point, 18.323.85.07		(333,600)	26.8	0.86	407	
d) Nominal (Predictive Analysis)	172,336	(380,000)	21.9	0.80	360	
Test Point, 20.323.80.07		(336,200)	26.6	0.80	359	

TABLE 5-3. NOMINAL (PREDICTED) AND MEASURED FLIGHT CONDITIONS - EXTENDED SPAN TESTS (Continued)

CONDITION	GROSS MASS Kg	GROSS MASS (LB)	C.G. % MAC	MACH NO.	VELOCITY KEAS	COMMENTS
e) Nominal (Predictive Analysis)	172,336	(380,000)	21.9	0.90	360	
Test Point, 25.323.90.07		(352,200)	25.6	0.90	346	
f) Nominal (Predictive Analysis)	172,336	(380,000)	21.9	0.80	320	
Test Point, 25.323.80.04		(349,000)	25.8	0.80	317	
g) Nominal (Predictive Analysis)	172,336	(380,000)	21.9	0.80	400	
Test Point, 15.323.80.07		(330,400)	27.0	0.81	403	

shallow dives. Since this data might have considerable scatter, it was decided during the test to add conditions M-3 f) and g) to provide three different velocity points at M = 0.80 where 1-g level flight could be maintained up to V = 400 KEAS.

The extended span maneuver loads data were analyzed in the same manner as the baseline test, i.e., suitable points were carefully selected from time histories of the maneuvers. The initial step in reducing the loads data, after the analysis points were selected from the time histories, was to plot the measured loads, both system on and system off, versus center of gravity load factor. These data (shear, bending moment, and torsion at η = 0.71) for test conditions M-1 and M-4 are shown in Figures 5-16 and 5-17, respectively. A linear regression line is shown for both the system on and off test data. It is noted that in general the trends with the MLC system on and off, e.g., reduced shear and bending moment and more positive torsion with MLC on, are as expected and that the quality of the test data is good. The predicted 1.6g incremental loads from system off to system on are plotted on the test results for comparison and indicate reasonable agreement.

The MLC function was checked by plotting the outboard aileron angle versus load factor. Figure 5-18 presents these data for both the M-1 and M-4 test conditions. A linear regression line is shown for both conditions. The data indicate the system was biased approximately 1 degree trailing-edge up during one g flight. (This is also indicated by the load measurements presented in Figures 5-16 and 5-17 where the system off and on loads tend to intersect at a C.G. load factor less than 1.0.) The gains of 8.4 degree per g for M-1 and 7.8 degree per g for M-4 agree favorably with the specified gain of 7.8 degree per g. (The maneuver tests were conducted with a gain of 0.9 times the nominal gain of 8.67 degrees per g.) The effects of the bias and gain variation are accounted for in the analysis and do not affect the conclusions concerning the effectiveness of the MLC system.

The loads data from the one g trimmed flight conditions, M-3, were analyzed to determine spanwise distributions of shear, bending moment, and torsion for a unit aileron. This unit data approach minimizes the effects of variation between the nominal predicted point and the flight test point, see Table 5-3, by eliminating the absolute values of the load quantities. The unit bending moment distributions for 3 velocities at M = 0.80 and M = 0.85 are shown in Figures 5-19 and 5-20, respectively. The M = 0.80 data in Figure 5-19 show very little scatter while the M = 0.85

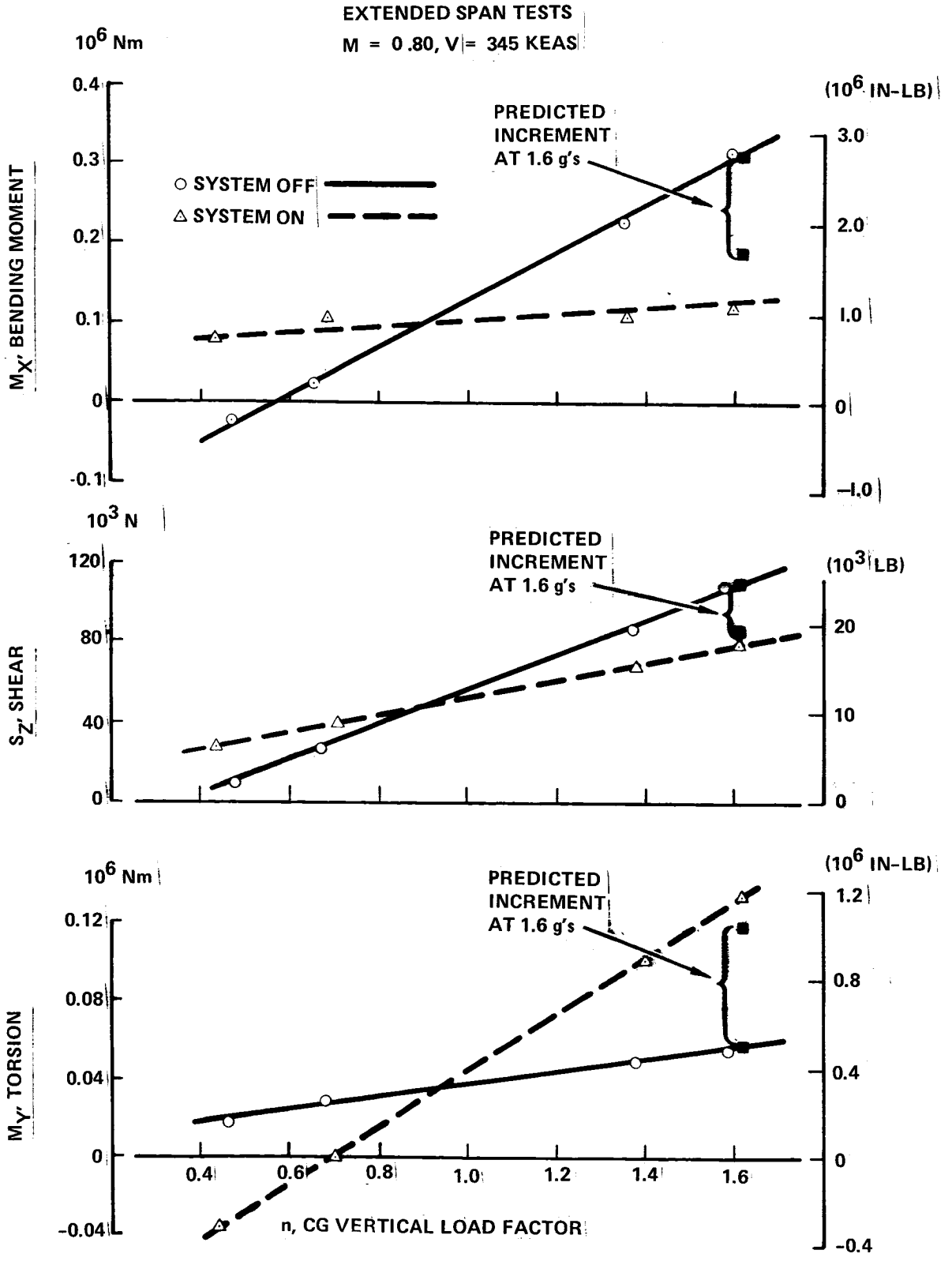

Figure 5-16 η=0.71 Bending Moment, Shear and Torsion vs. Load Factor, M-1

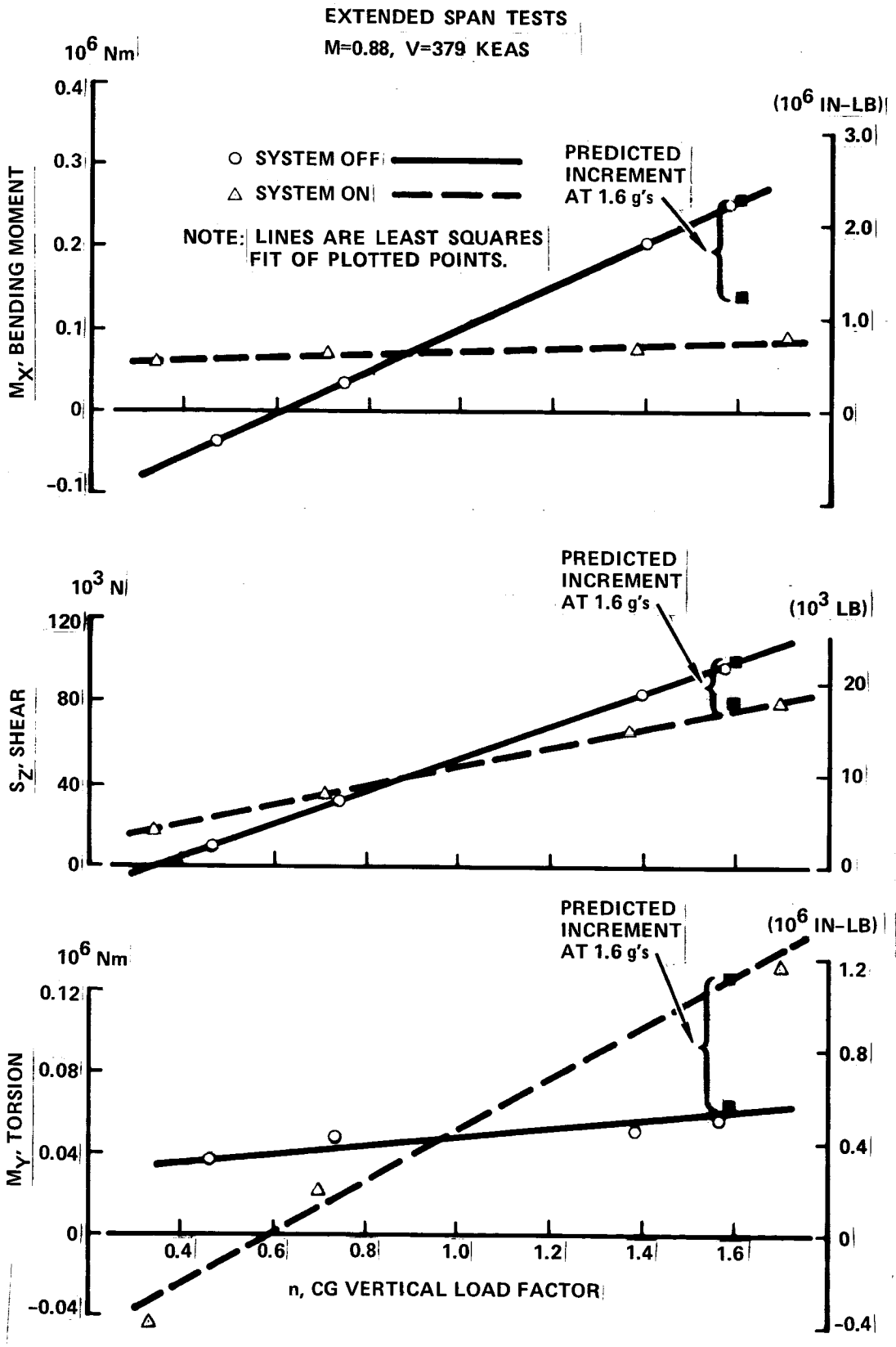

Figure 5-17 η = 0.71 Bending Moment, Shear and Torsion vs. Load Factor, M-4

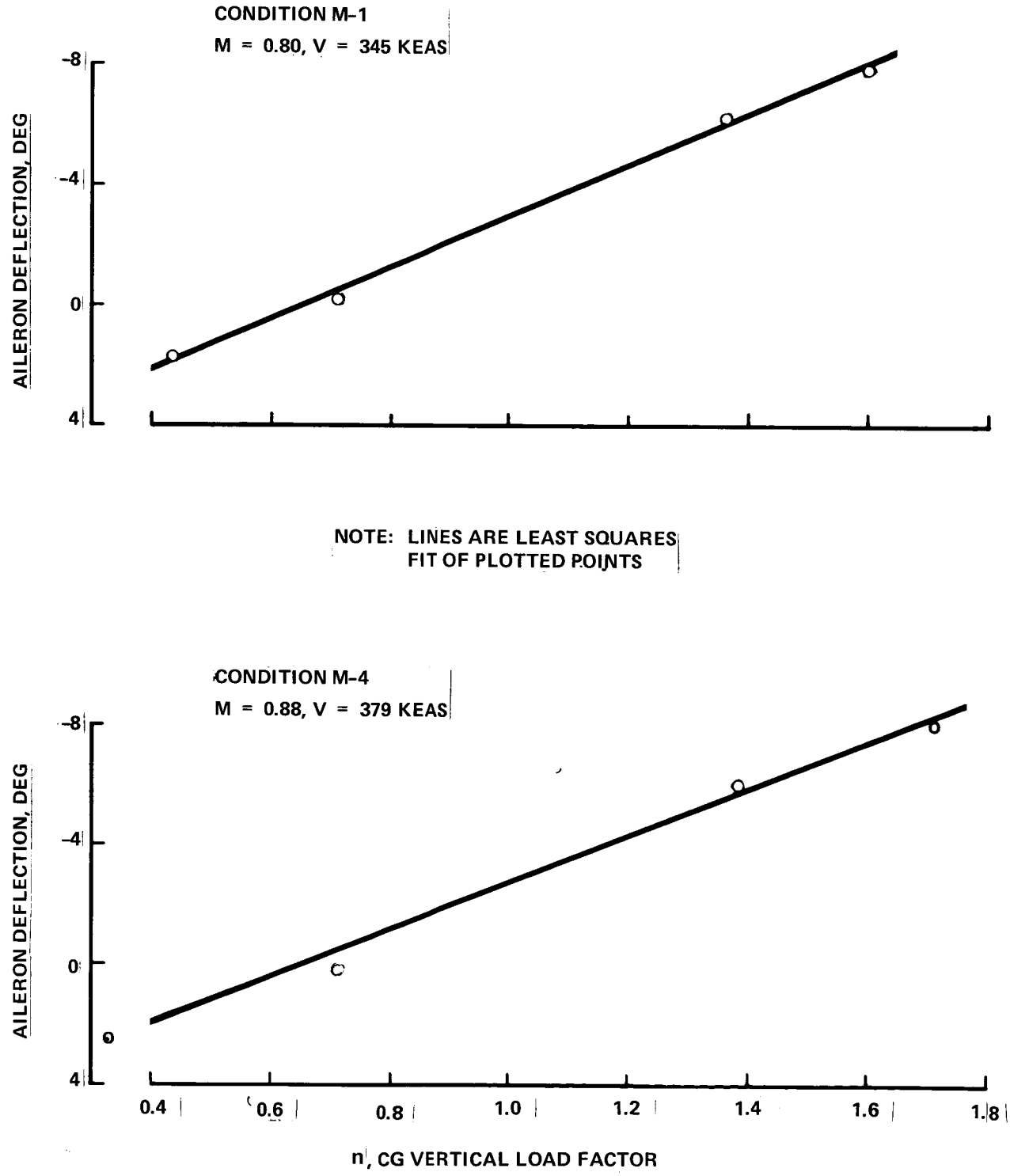

Figure 5-18. Left Outboard Aileron Deflections, M-1 and M-4

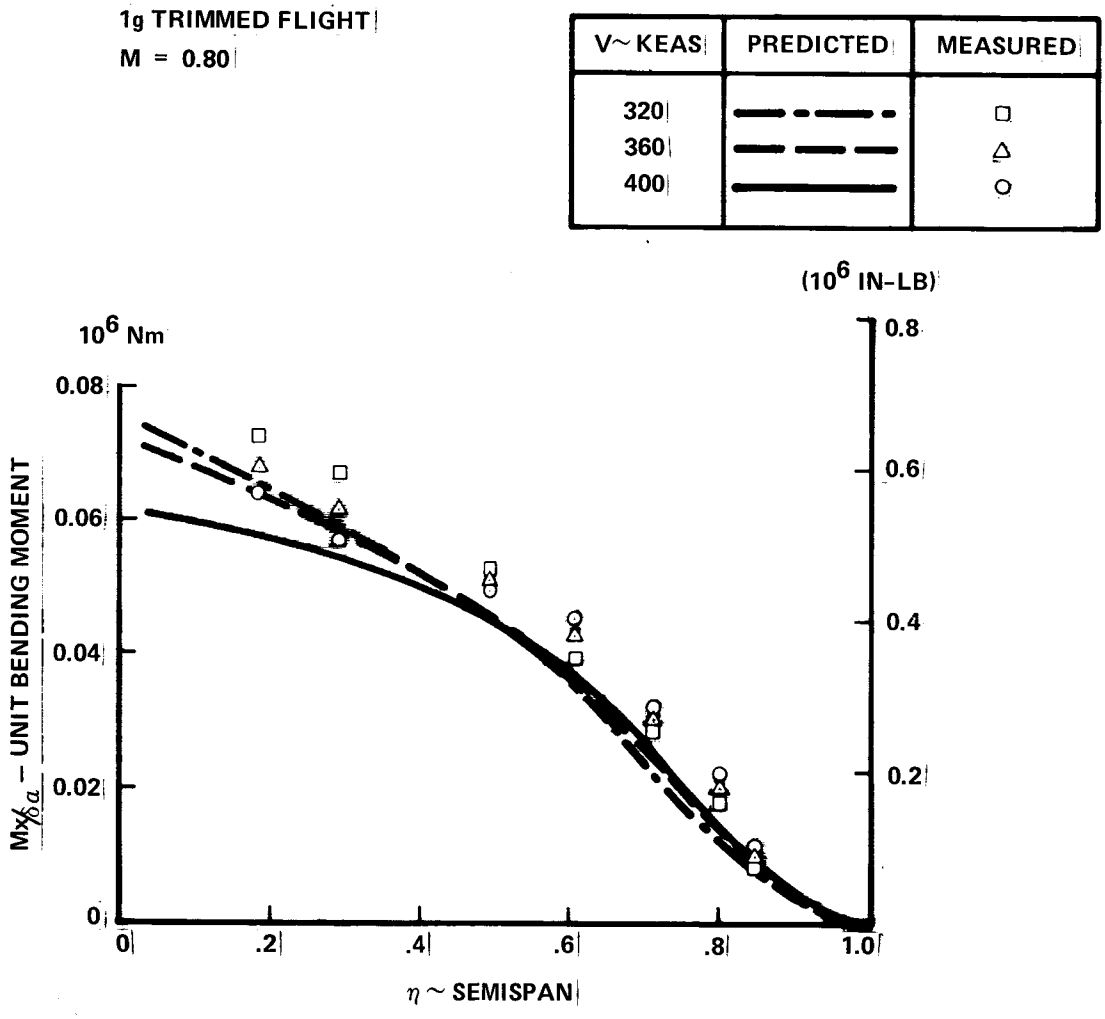

Figure 5-19. Comparison of Measured to Predicted Unit Incremental Wing Bending Moments M = 0.80

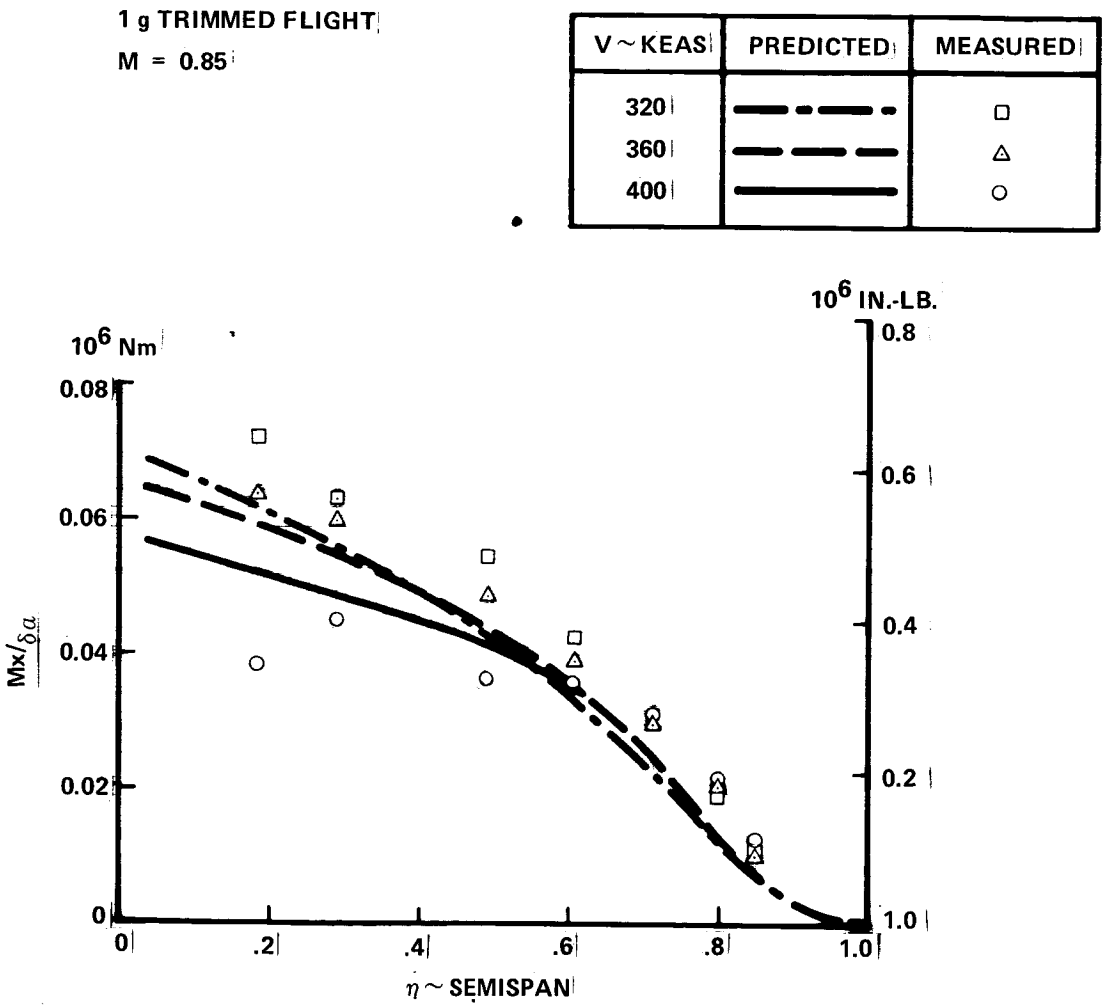

Figure 5-20. Comparison of Measured to Predicted Unit Incremental Wing Bending Moments M = 0.85

data at V = 400 KEAS show considerable scatter as was expected when the test point could not be maintained in level flight. The two lower velocity curves (V = 360 KEAS and V = 320 KEAS) show little scatter. The unit spanwise bending moment data in Figure 5-19 and 5-20 indicate that the extended outboard aileron remains effective at all velocities and confirms the predictions, although the measured effectiveness is even greater than predicted. The tendency for the outer wing moments to increase as the inner wing moments decrease, with increasing velocity, is confirmed.

The analysis and flight test data generated for the extended span configuration substantiate the effectiveness and feasibility of utilizing a MLC system to alleviate the loads induced by the 4.5 foot wing tip extension. In addition, the current L-1011 static aeroelastic loads programs adequately predict the loading effects of the system.

5.5 MOTION TRANSFER FUNCTIONS

Motion transfer function flight tests were conducted for conditions listed in Table 5-4. Transfer function test frequencies were specified to define short period mode, first wing bending mode, wing engine first and second modes and limited first fuselage bending and first stabilizer bending responses. There were six open loop flight tests (LC-1 through LC-6) and two closed loop flight tests (LC-1 and LC-2) for the baseline airplane (Task 1) and two open and closed loop flight tests (LC-11 and LC-12) for the extended span airplane (Task 3). Task 3 tests had large variations in gross weight between aileron and stabilizer excitation for the given flight condition (LC-11 or LC-12). However, the fuel in the outboard wing fuel tanks was fixed for both excitation tests.

Motion transfer function analyses were performed for all eight flight test conditions. The GFAM models and methods described in section 4.3 were used in the correlation of flight data with analysis. Model adjustments were made to fuel, payload and flight parameters (Mach, altitude) which were realized in the test flights.

The GFAM model correlations are examined critically in this section because the GFAM model was an important tool in determining the frequency-dependent portion of the control laws.

5.5.1 Open Loop Correlation

Open loop transfer function flight tests were conducted by commanding separately a symmetric sinusoidal oscillation of the outboard ailerons and a sinusoidal

TABLE 5-4. FLIGHT TEST PARAMETERS FOR LC-XX

BASE LINE

Parameter \ Condition / Exc.	LC-1		LC-2		LC-3		LC-4		LC-5		LC-6	
	Stab.	Ail.	Stab.	Ail.	Stab.	Ail.	Stab.	Ail.	Stab.	Ail.	Stab.	Ail.
Mass kg (lb)	161478 (356000)	166876 (367900)	155763 (343400)	159074 (350700)	151908 (334900)	153767 (339000)	176129 (388300)	177808 (392000)	160072 (352900)	167148 (368500)	148823 (328100)	150048 (330800)
c.g. % MAC	17.9	17.8	25.4	25.2	14.2	14.1	18.2	18.2	17.6	17.2	14.0	14.0
Fuel kg (lb)	38237 (84300)	44452 (98000)	31116 (68600)	34427 (75900)	28667 (63200)	30073 (66300)	52888 (116600)	54567 (120300)	35788 (78900)	42955 (4700)	25582 (56400)	26807 (59100)
h km (1000 ft)	6.7 (22)	6.7 (22)	3.0 (10)	3.0 (10)	6.7 (22)	6.7 (22)	6.1 (20)	6.1 (20)	6.7 (22)	6.7 (22)	3.0 (10)	3.0 (10)
Mach No.	0.80	0.80	0.26	0.26	0.80	0.80	0.50	0.50	0.88	0.88	0.38	0.38
V_{KEAS}	345	345	145	145	343	349	225	225	378	378	210	210

EXTENDED SPAN

Parameter \ Condition / Exc.	LC-11		LC-12	
	Stab.	Ail.	Stab.	Ail.
Mass kg (lb)	174590 (384900)	159890 (352500)	152950 (337200)	137440 (303010)
c.g. % MAC	23.4	25.1	22.9	26
Fuel kg (lb)	56790 (125200)	42180 (93000)	37470 (82600)	19600 (43200)
h km (1000 ft)	6.7 (22)	6.7 (22)	4.0 (13)	4.6 (15)
Mach No.	.71	.71	.30	.32
V_{KEAS}	305	305	156	159

oscillation of the horizontal stabilizer. For purposes of discussion, these tests will be referred to as aileron excitation and stabilizer excitation. The motions to be reviewed in this section are the wing tip acceleration, the wing engine accelerations, and CG acceleration. There are three types of figures which are used in comparing flight measured responses to theoretical responses. The first plot is the standard transfer function format giving amplitude ratio (modulus) versus frequency and phase versus frequency for a given flight condition. The second is a cross plot showing magnitudes of particular response peaks versus equivalent air speed. This type of plot is provided in order to show the variation of the response with flight conditions. As in the transfer function plot, it will contain both analysis and flight test data. The third type of plot shows analysis to test ratios and comparative phases. In this plot, the data can be easily assessed as to how closely the model correlates with the flight test. It should be noted, however, that the normalized plots weight the low amplitude responses on the same level as the more significant responses. The phases were compared with the peak amplitude response for both the analysis and the flight test. This compensated for shifts in frequency that may exist between the flight test and the theoretical analysis. Flight test data and analysis of the extended span airplane are included along with the baseline results. Each extended span analysis and data point is enclosed by a circle to distinguish the configuration.

Wing Tip Accelerations

Wing tip response in the first wing bending mode (1.6 to 1.9 Hz) is of particular interest here. Figure 5-21 to Figure 5-26 present comparisons of modulus and phase of the transfer function for the wing tip accelerometer between analysis and test for stabilizer and aileron excitation. The overall quality of the test and analysis correlation is excellent. An outstanding feature of the data is the excellent phase correlation across a broad frequency spectrum including the short period mode (~0.14 - 0.3 Hz) the first wing bending mode (~1.6 Hz), the first engine mode (~2.3 Hz), second engine mode (~2.7 Hz), the first fuselage bending mode (~3.5 Hz) and finally the first stabilizer bending and wing second bending modes (4 - 6 Hz). The response peak of the wing tip acceleration in the first wing bending mode is shown on Figure 5-27 for stabilizer and aileron excitation. The response peak data for the aileron excitation shows good correlation between tests and analysis.

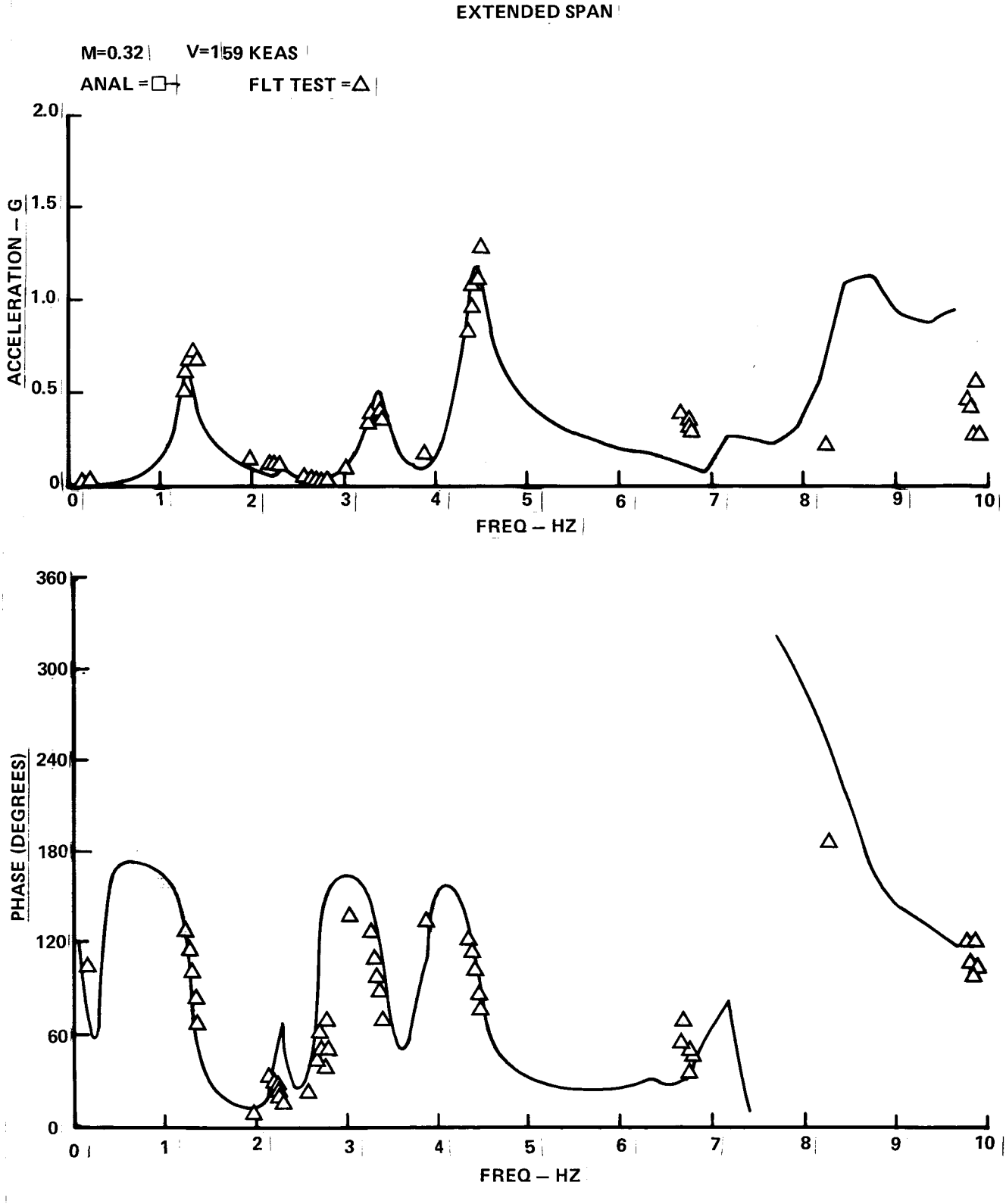

Figure 5-21. LC-12 Wing Tip Normal Acceleration/Degree Aileron Open Loop

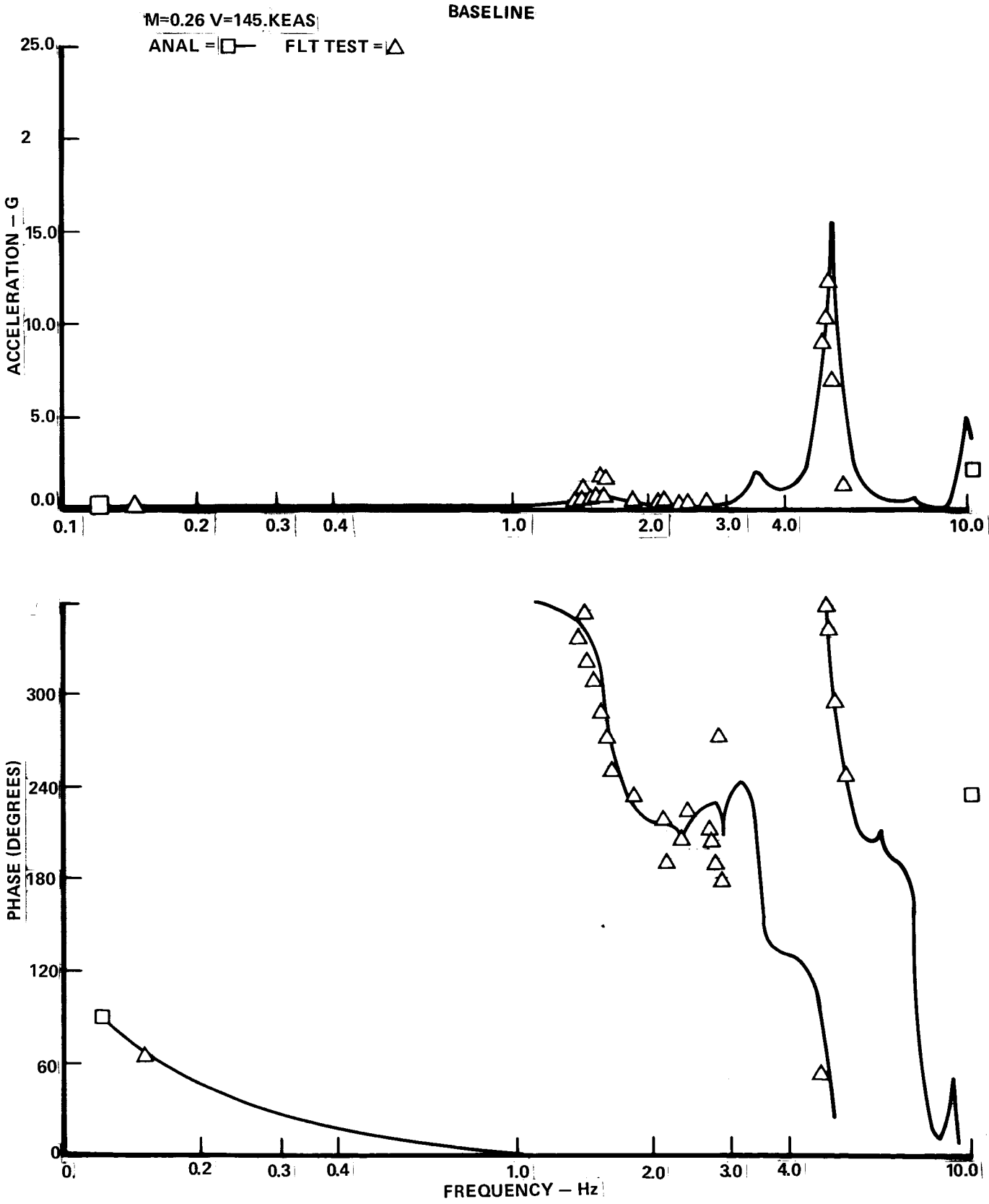

Figure 5-22. LC-2 Wing Tip Normal Acceleration/Degree Stabilizer Open Loop

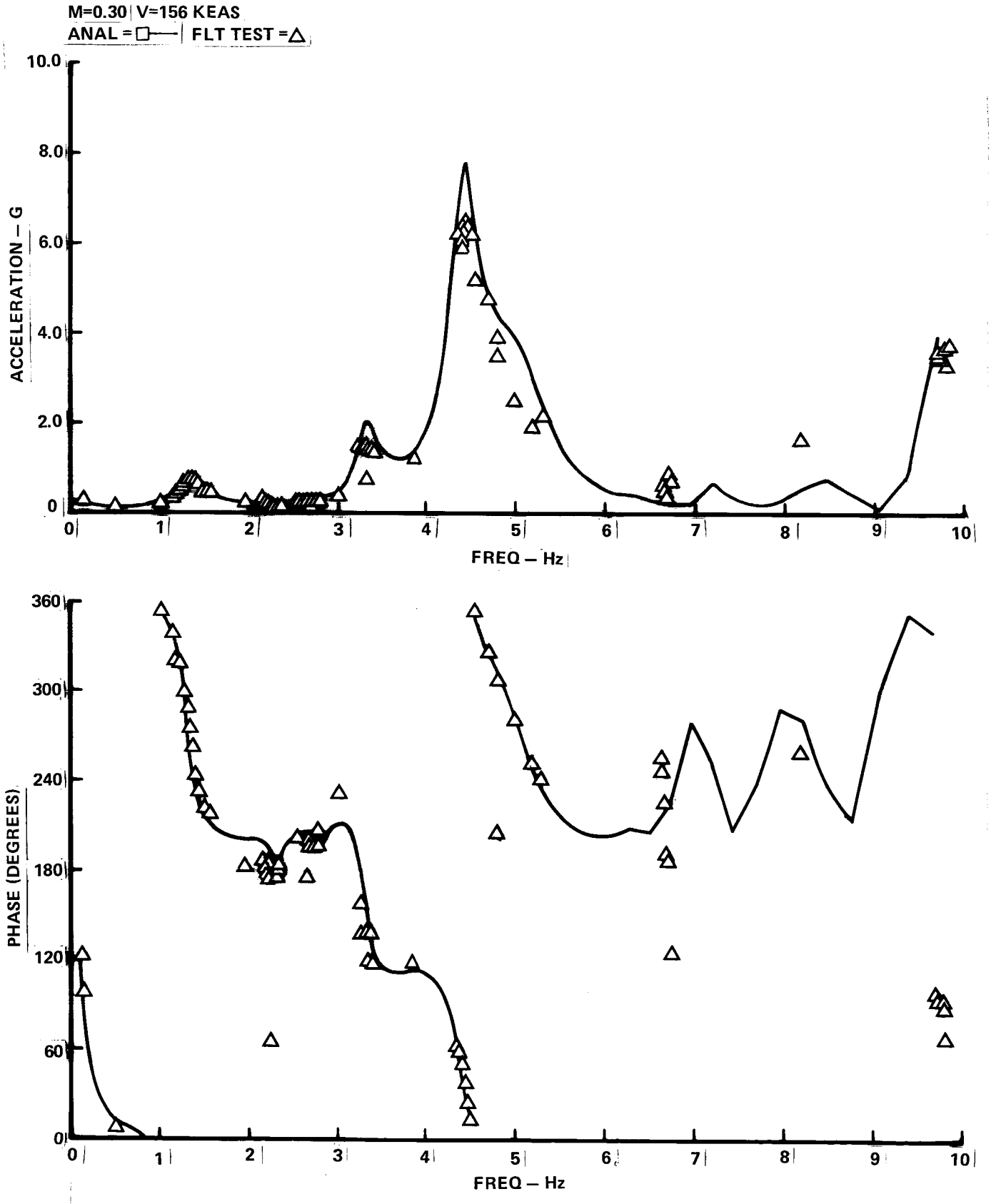

Figure 5-23. LC-12 Wing Tip Normal Acceleration/Degree Stabilizer Open Loop

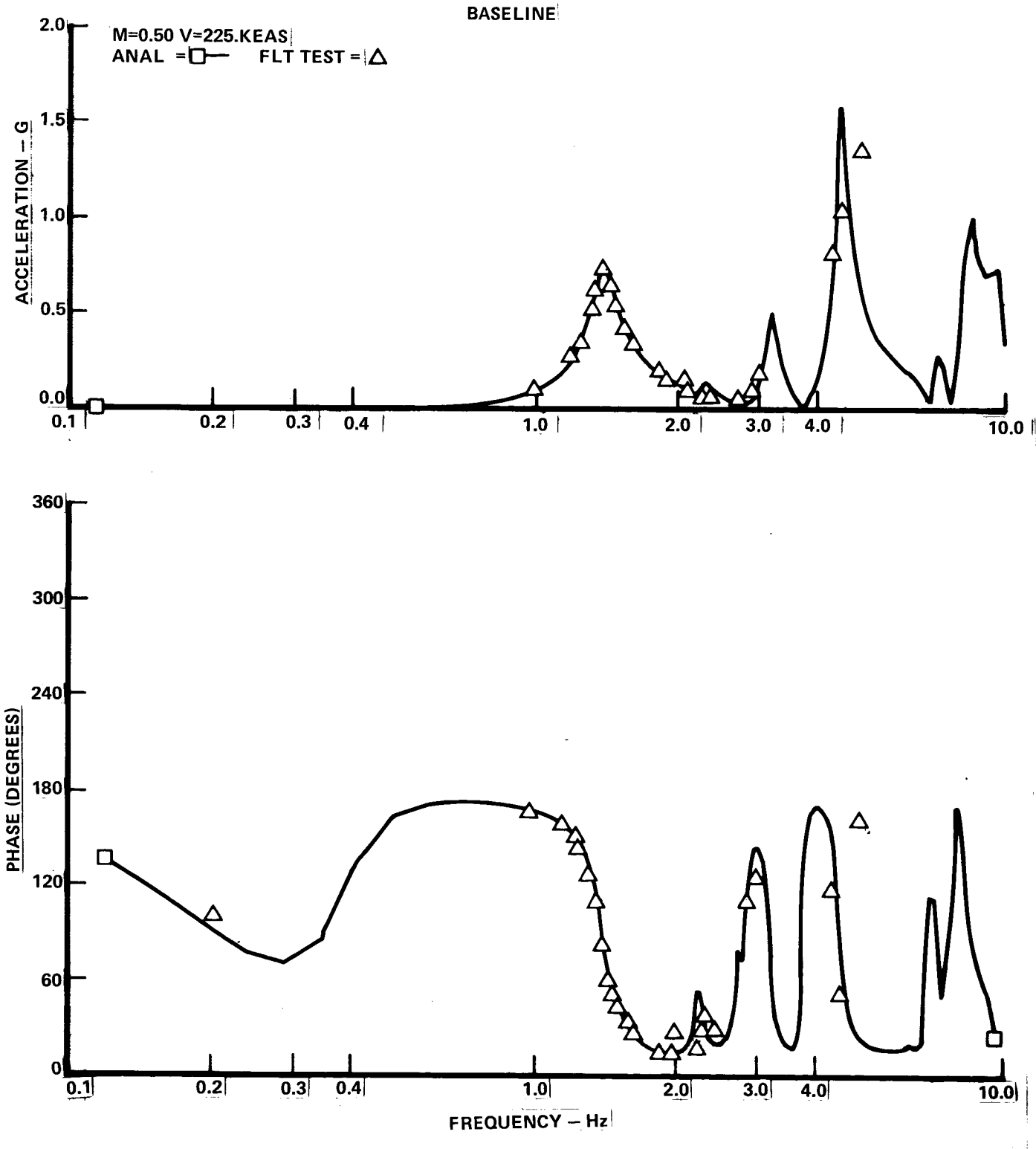

Figure 5-24. LC-4 Wing Tip Normal Acceleration/Degree Aileron Open Loop

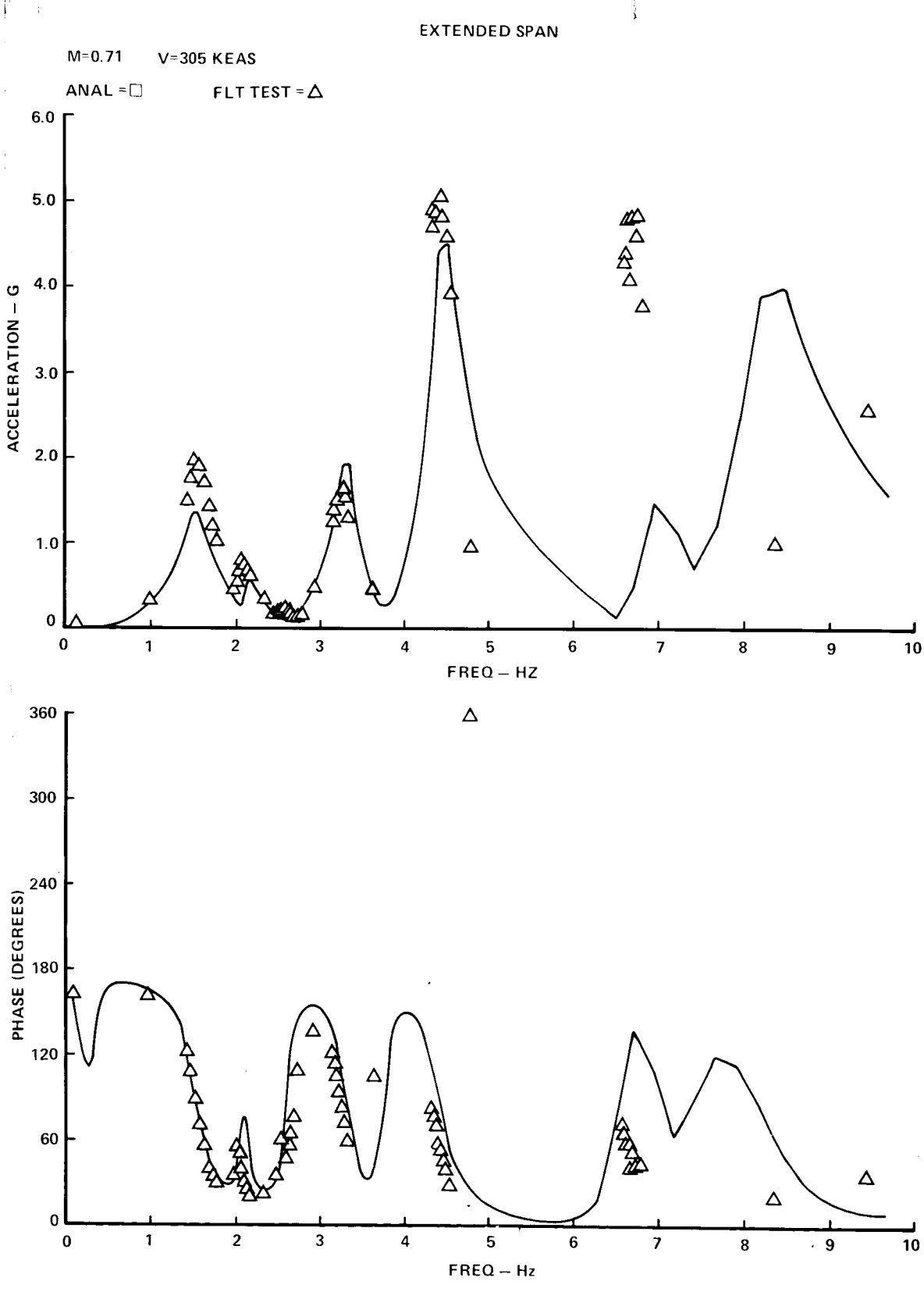

Figure 5-25. LC-11 Wing Tip Normal Acceleration/Degree Aileron Open Loop

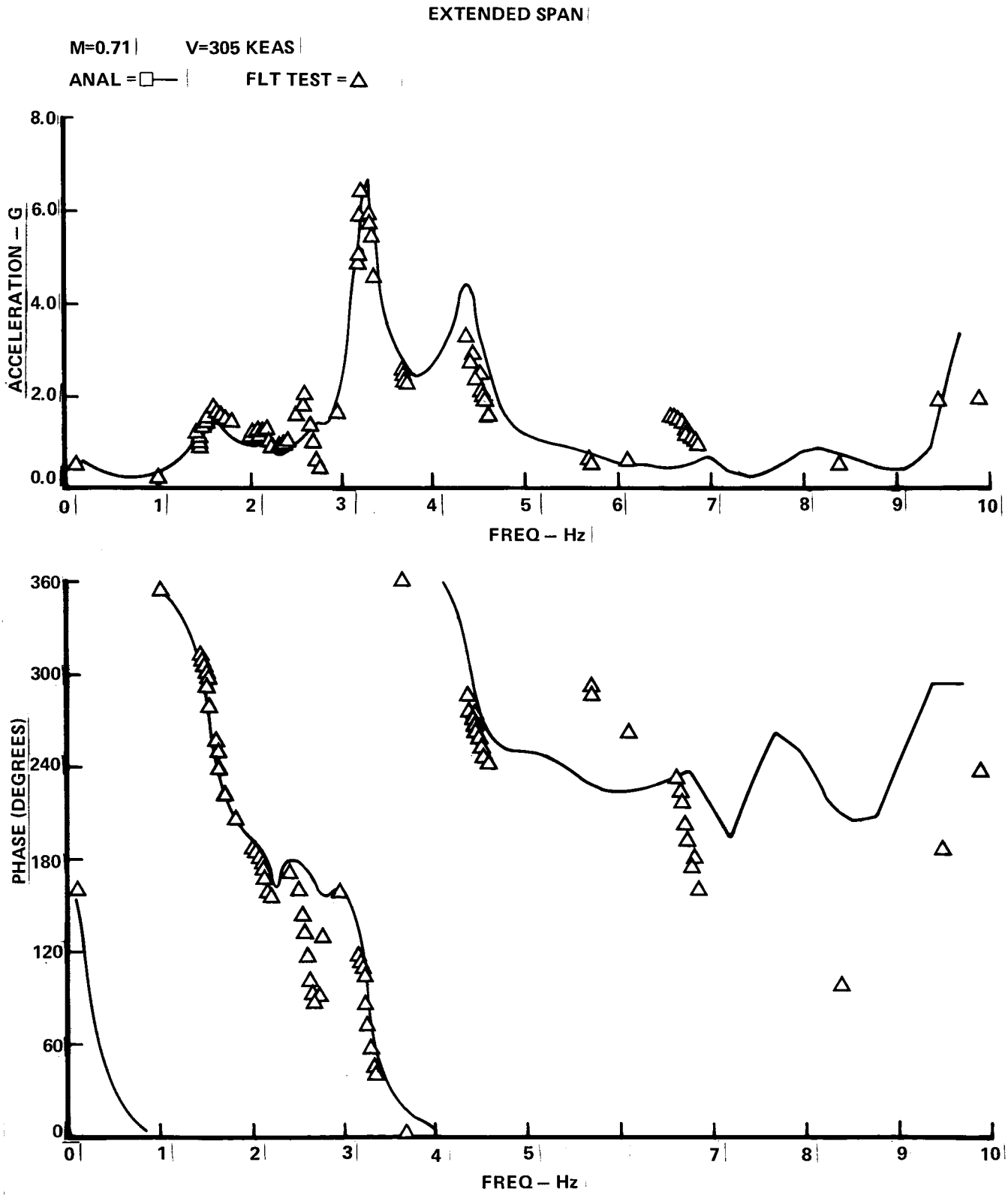

Figure 5-26. LC-11 Wing Tip Normal Acceleration/Degree Stabilizer Open Loop

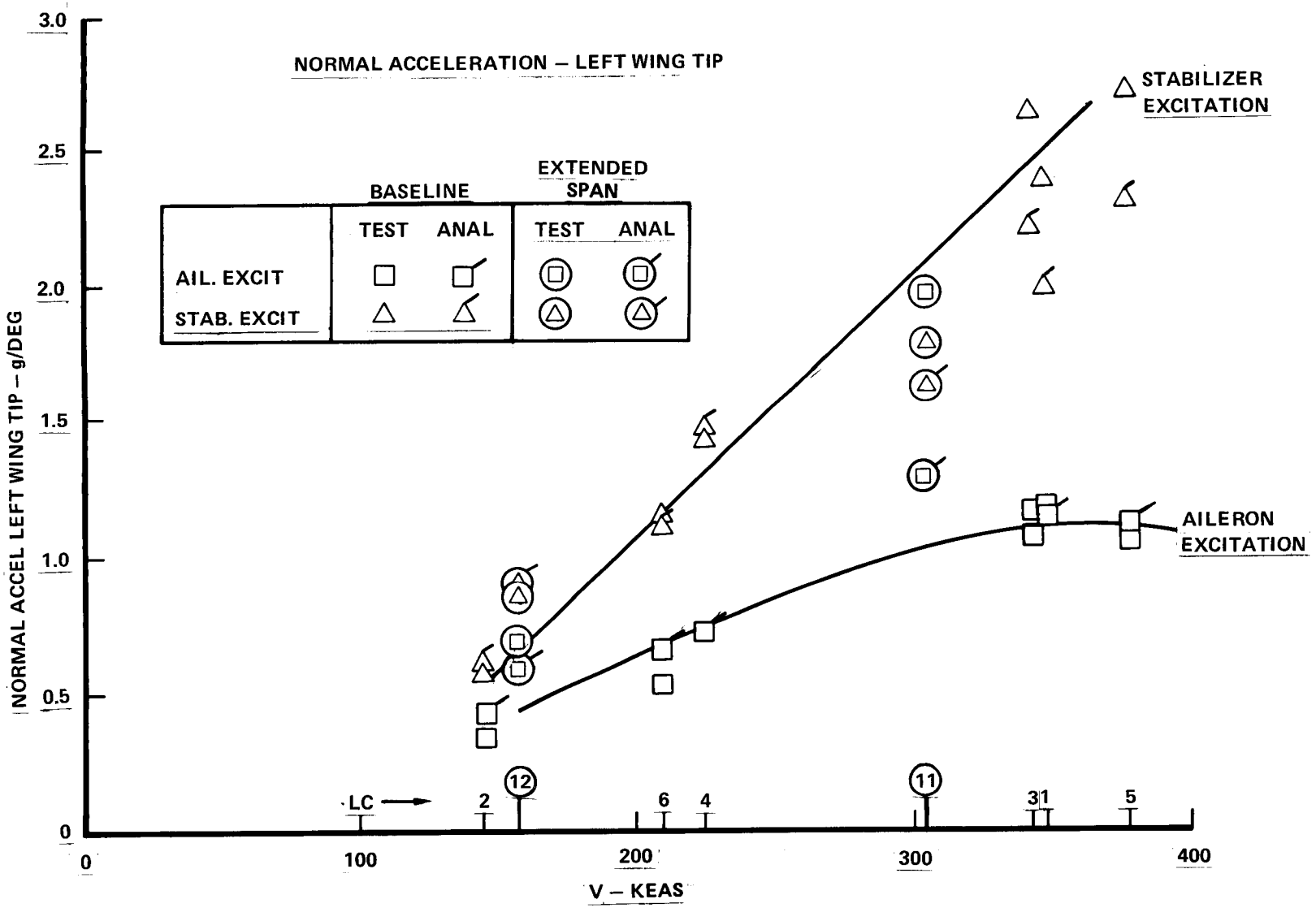

Figure 5-27. Wing Tip Normal Acceleration Peak Response for First Wing Bending Mode Open Loop

For the baseline, both the tests and analysis indicated a roll off of the response peak with higher dynamic pressure (q). For the extended wing airplane, the effectiveness of aileron inputs on wing tip accelerations increased over the baseline, as expected. However, the test data point for LC-11 shows peak responses 1.4 times greater than analysis. The wing tip response due to stabilizer correlates well at low q's but shows significant differences at the higher q's. The data scatter as shown in this figure for stabilizer excitation at the higher q becomes well-behaved in the same region in Figure 5-28 where the analysis peaks are normalized to test values. The analysis, however, is predicting 16 percent less response than was seen in flight. The data would indicate that the stabilizer aerodynamic loading in the analysis is not adequately represented in the range of q's that the test data covered. A possible explanation may be in the elevator aerodynamic effectiveness which was held constant in the analysis for low q and high trim angles as well as for high q and low trim angles of the horizontal stabilizer. The response due to aileron excitation was over-predicted by analysis as compared to flight tests at low q in the baseline. High q flight data had good correlation with analysis. The aileron excitation data for the extended span shows a parallel shift from the baseline data, again indicating higher-than-expected aileron effectiveness at all speeds. Some of this effect was found in the maneuver loads correlations, Section 5.4. The more pronounced test/analysis difference with the GFAM model is probably due to predicted aileron windup associated with use of a single aileron actuator at the most inboard hinge, whereas the airplane (and the maneuver loads model) has actuators at both inboard hinges.

Phase angle correlation between flight test data and analysis was made on the first wing bending mode. All points were within five degrees of the flight test points, and often much less as shown in Figure 5-28. Phase readouts were made at the response peak amplitude for both the analysis and the flight test data.

Wing Engine Accelerations

Wing engine dynamic characteristics are important to flutter and dynamic loads analyses. Normal accelerometers were installed on wing engines number one and number three while longitudinal and lateral accelerometers were available on engine number one. The wing engine motions in flight were generally asymmetric for baseline tests and symmetric for extended wing tip tests. This made lateral acceleration data difficult to interpret for the

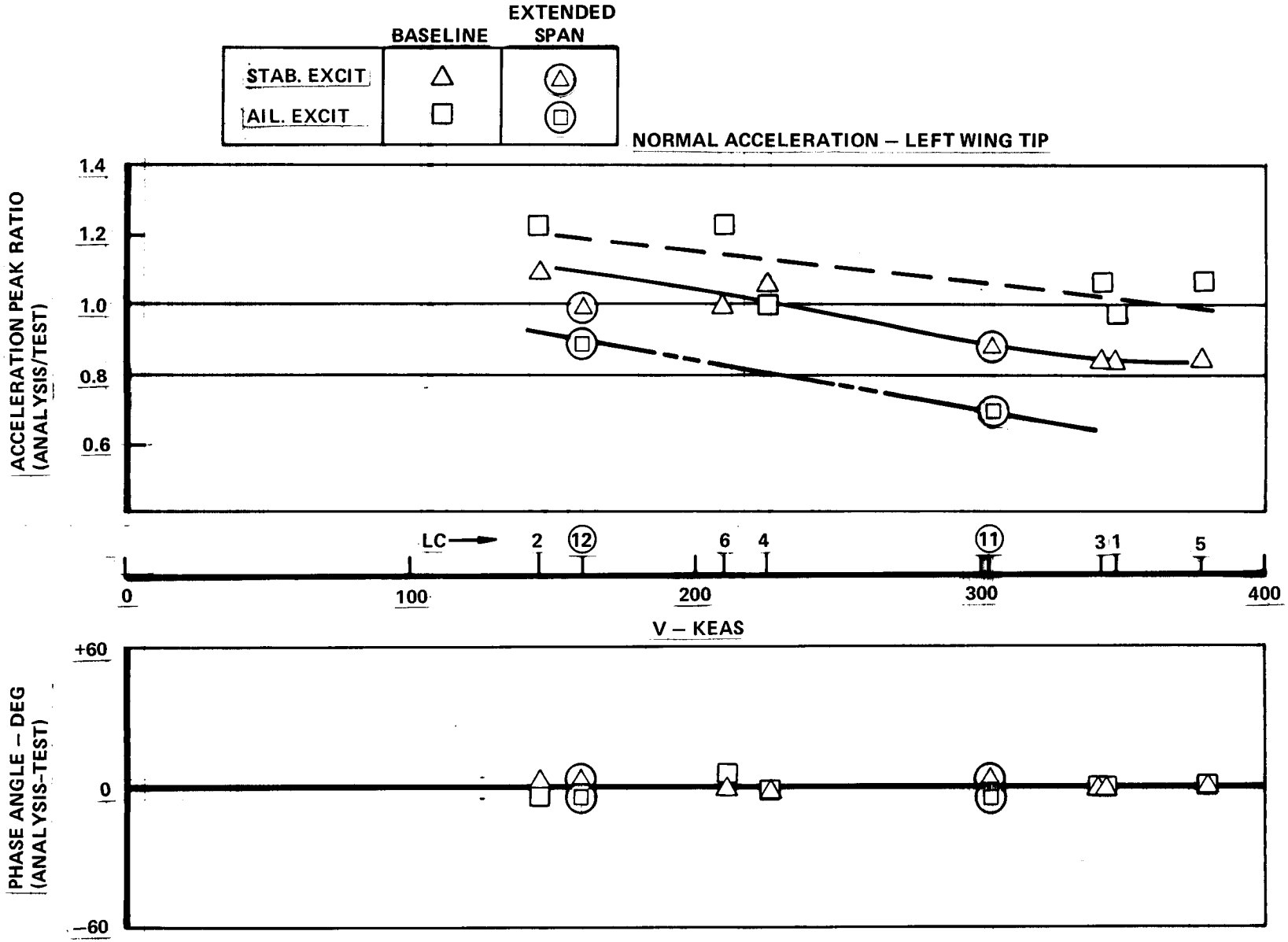

Figure 5-28. Wing Tip Normal Acceleration Peak Ratios for First Wing Bending Mode Open Loop

baseline tests. The severe engine environment may have been responsible for the normal accelerometer being inoperative during portions of the flight test program. The engine normal accelerometers were relocated on the engine fan ring aft of the baseline location (~25 inches). The wing engine normal acceleration flight data for the extended span configuration was generally symmetric and consistent. Figures 5-29 to 5-32 show representative engine normal responses due to stabilizer excitation. The analysis shows for the baseline case good phase and fair amplitude ratio correlation up through the second engine mode (2.7 Hz). Figure 5-29, however, shows poor amplitude and phase correlation between flight data and analysis for the fuselage first bending mode (3.5 Hz). The extended span analysis, Figure 5-30, shows poor amplitude ratio correlation especially for the second engine mode. The normalized data in Figure 5-32 show fair amplitude correlation for the second engine mode for the baseline and poor correlation for the extended wing tip. The first engine mode analysis to test correlation is marginal. The phase data show good correlation for both modes.

C.G. Accelerations

The response of the airplane center-of-gravity or some other representative fuselage location is important to active control systems because it is a primary input signal for the MLC function and influences the signal conditioning for the EMS function.

Figures 5-33 to 5-36 show representative responses of the C.G. accelerometer for stabilizer and aileron excitation. The quality of the correlation between analysis and test over the frequency spectrum is good.

The response peak amplitude plots and normalized correlation plots for the wing first bending mode are shown in Figure 5-37.

Overall, the correlation was good in amplitude and excellent in phase. The C.G. response due to stabilizer excitation at the first wing bending mode, as shown in Figure 5-37, is excellent. The correlation for aileron excitation is good considering the low levels of the response.

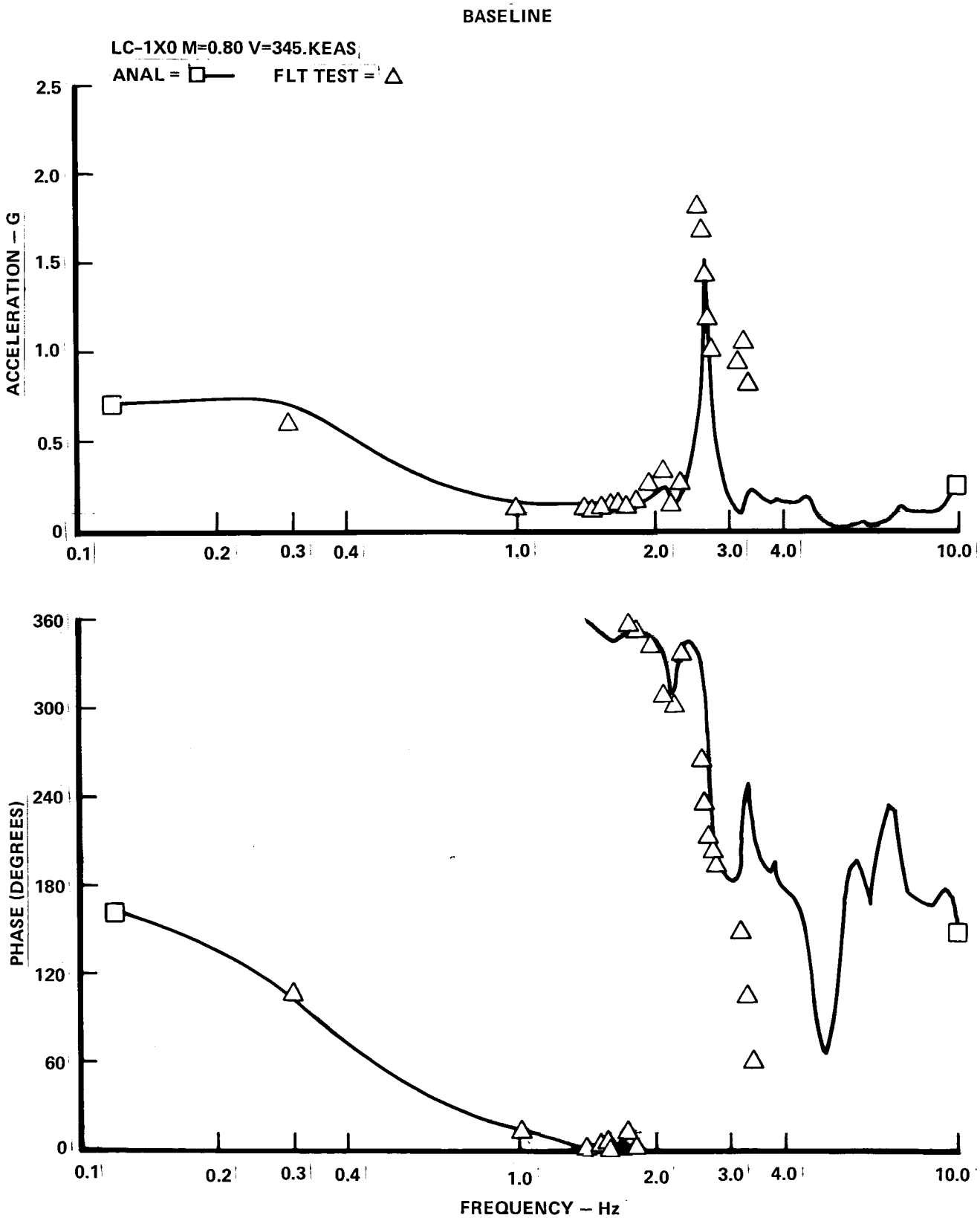

Figure 5-29. LC-1 Engine -1 Normal Acceleration/Degree Stabilizer Open Loop

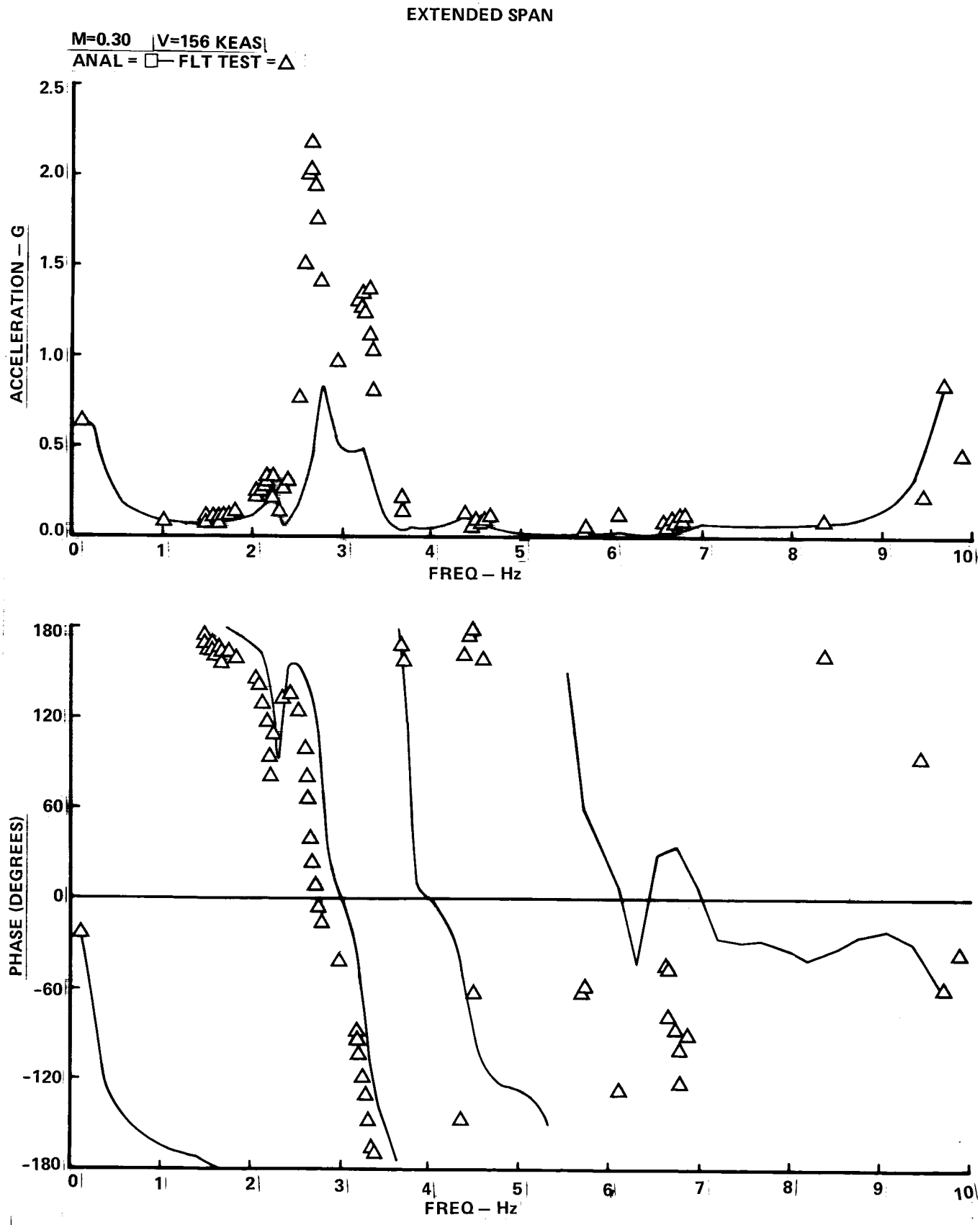

Figure 5-30. LC-12 Engine-1 Normal Acceleration/Degree Stabilizer Open Loop

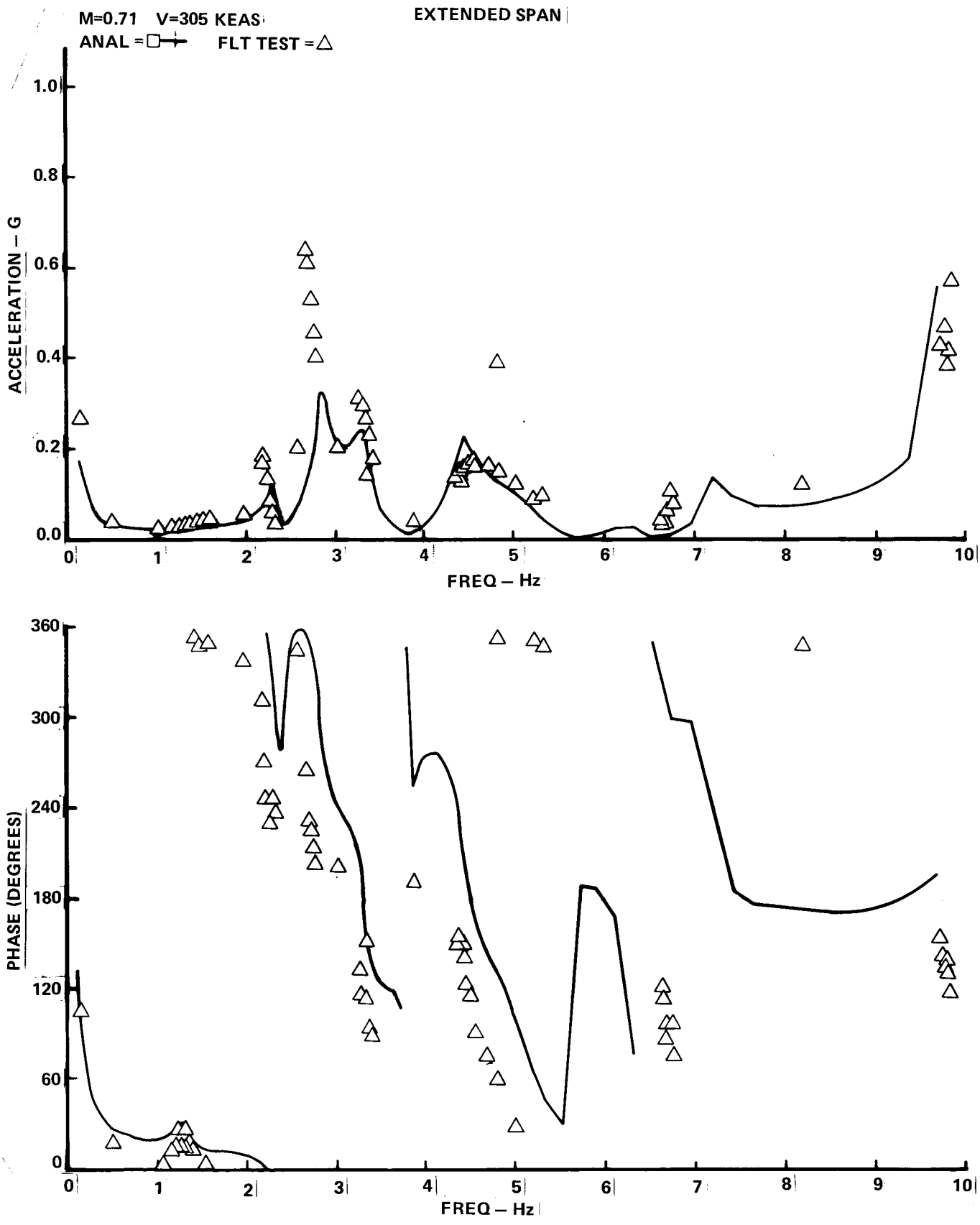

Figure 5-31. LC-11 Engine-1 Normal Acceleration/Degree Stabilizer Open Loop

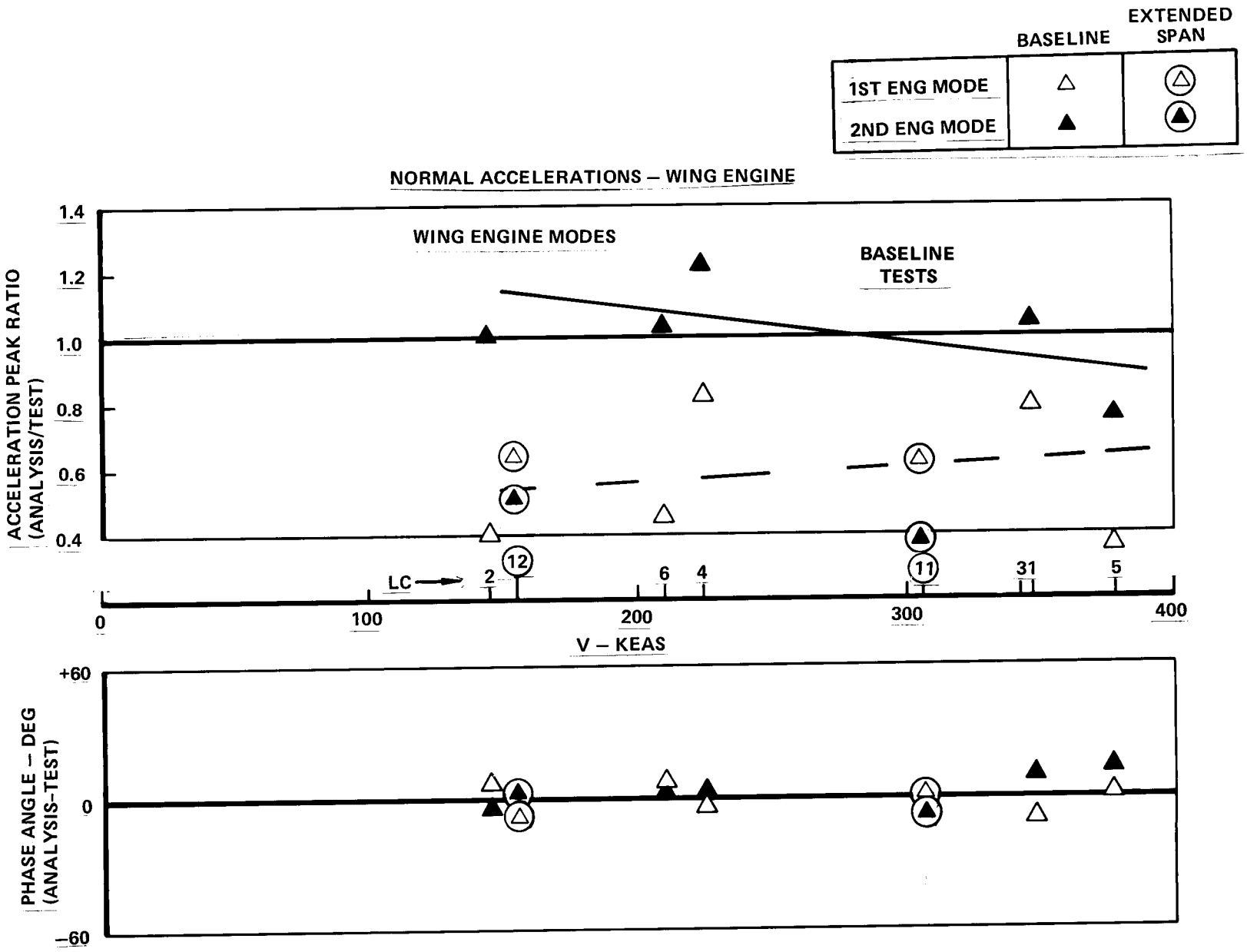

Figure 5-32. Wing Engine Symmetric Normal Acceleration Peak Ratios - Stabilizer Open Loop

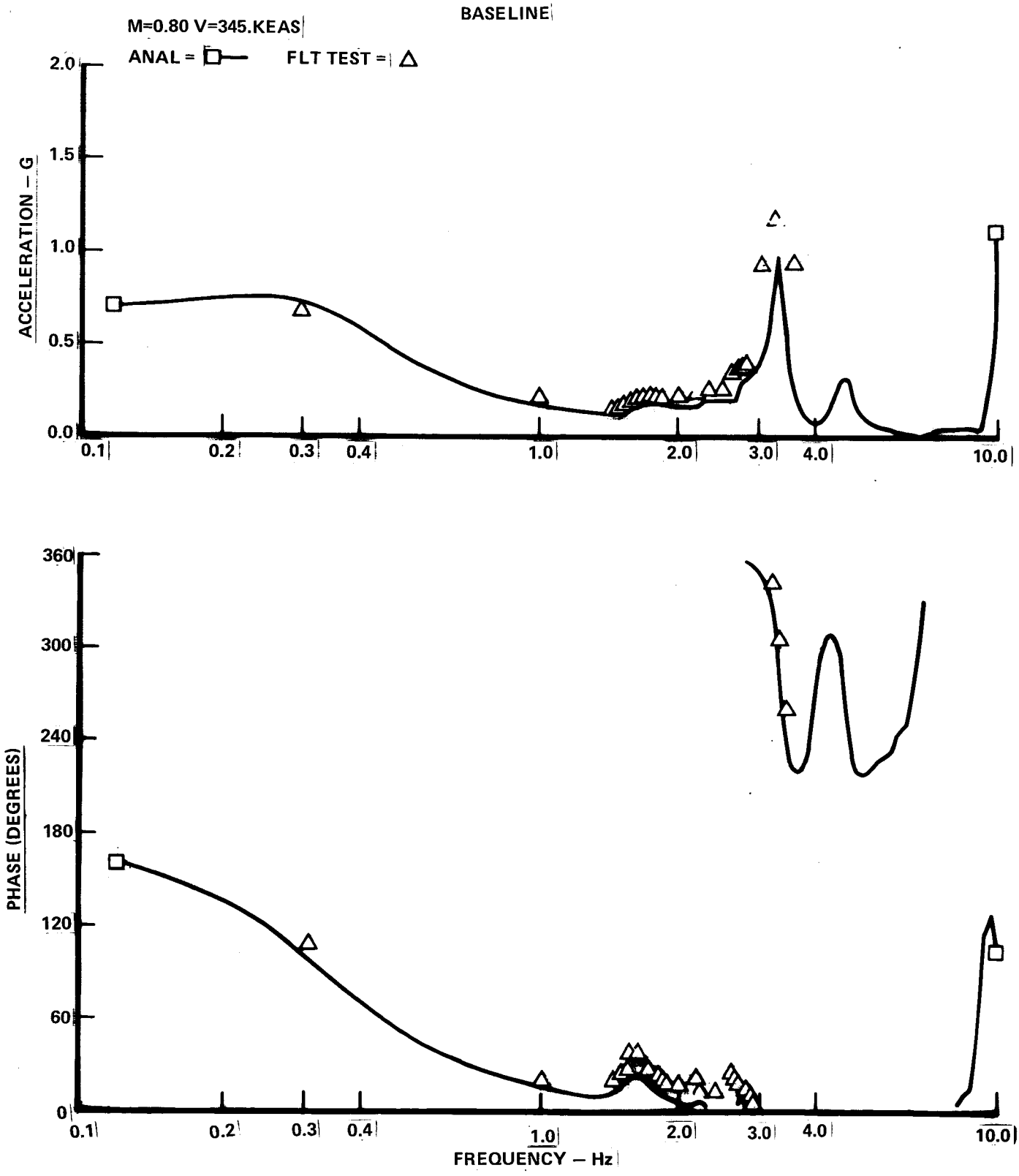

Figure 5-33. LC-1 C.G. Normal Acceleration/Degree Stabilizer Open Loop

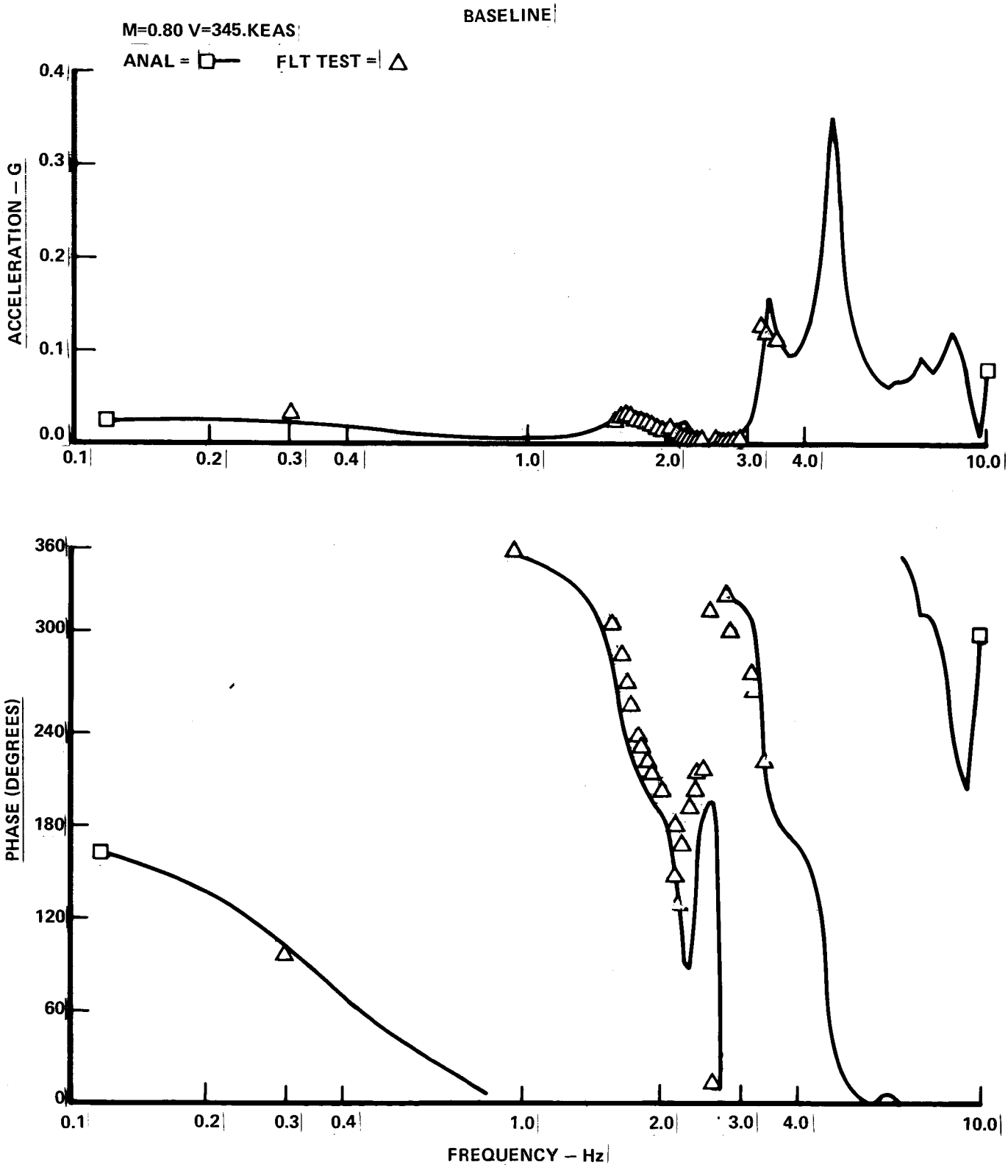

Figure 5-34. LC-1 C.G. Normal Acceleration/Degree Aileron Open Loop

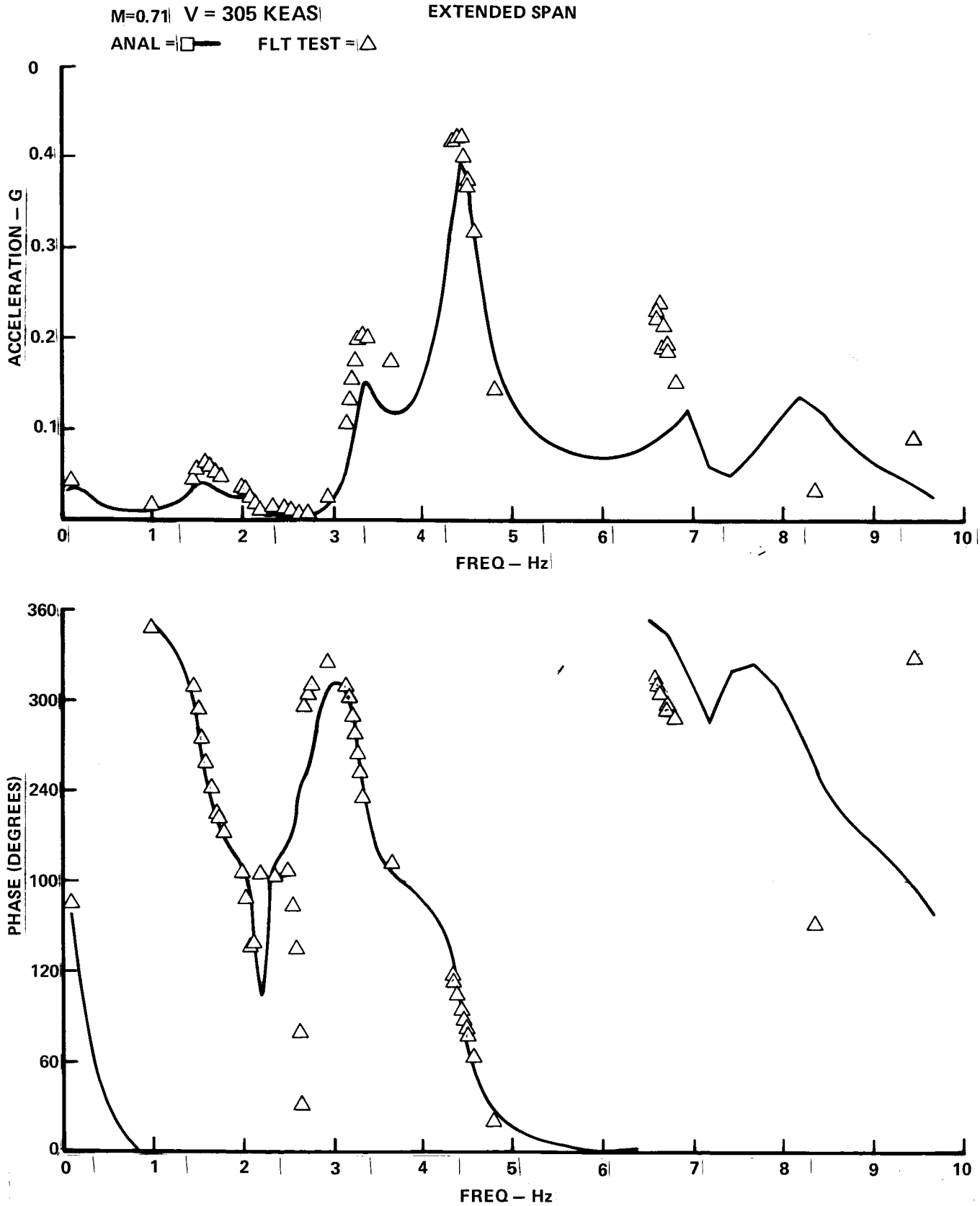

Figure 5-35. LC-11 C.G Normal Acceleration/Degree Aileron Open Loop

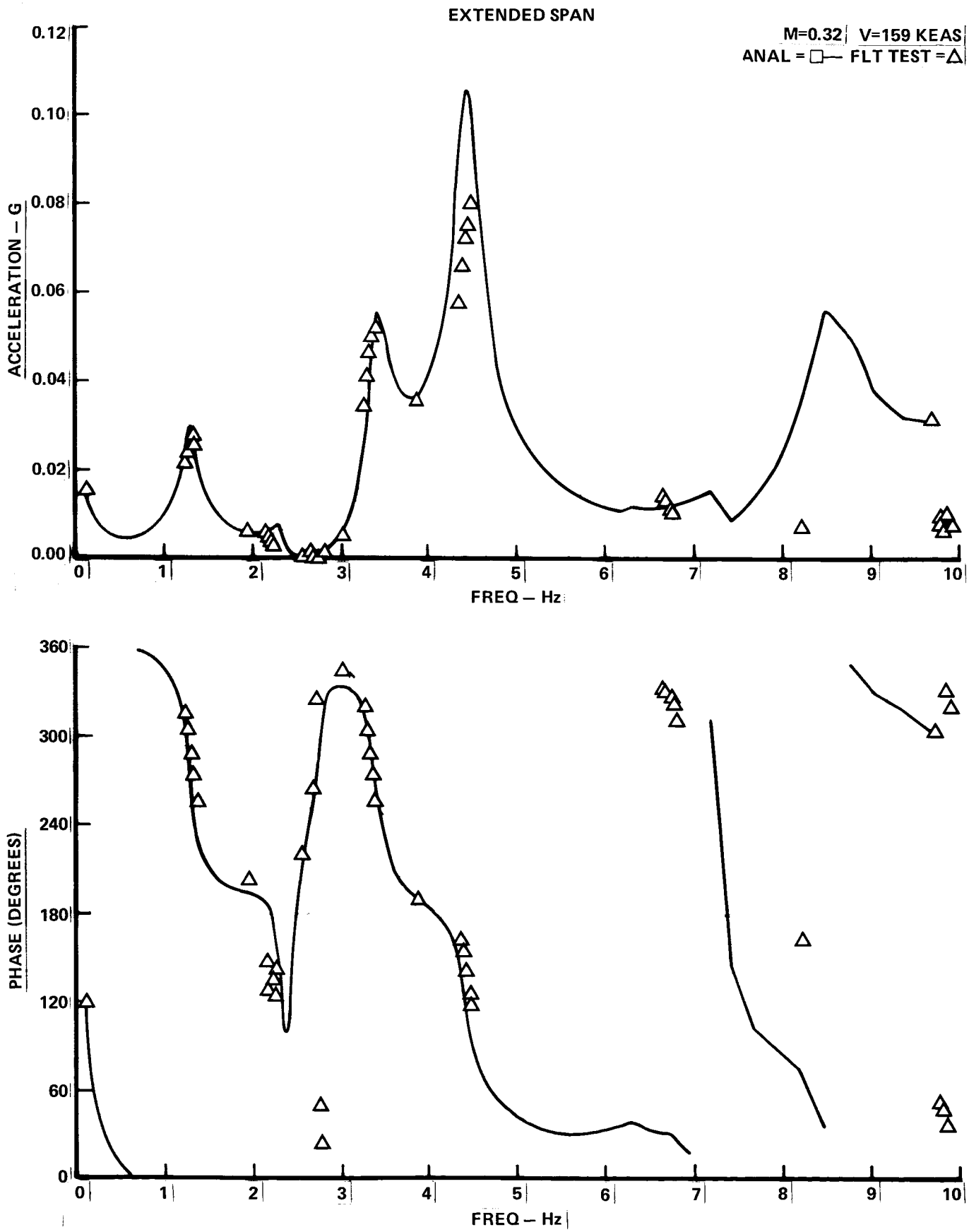

Figure 5-36. LC-12 C.G Normal Acceleration/Degree Aileron Open Loop

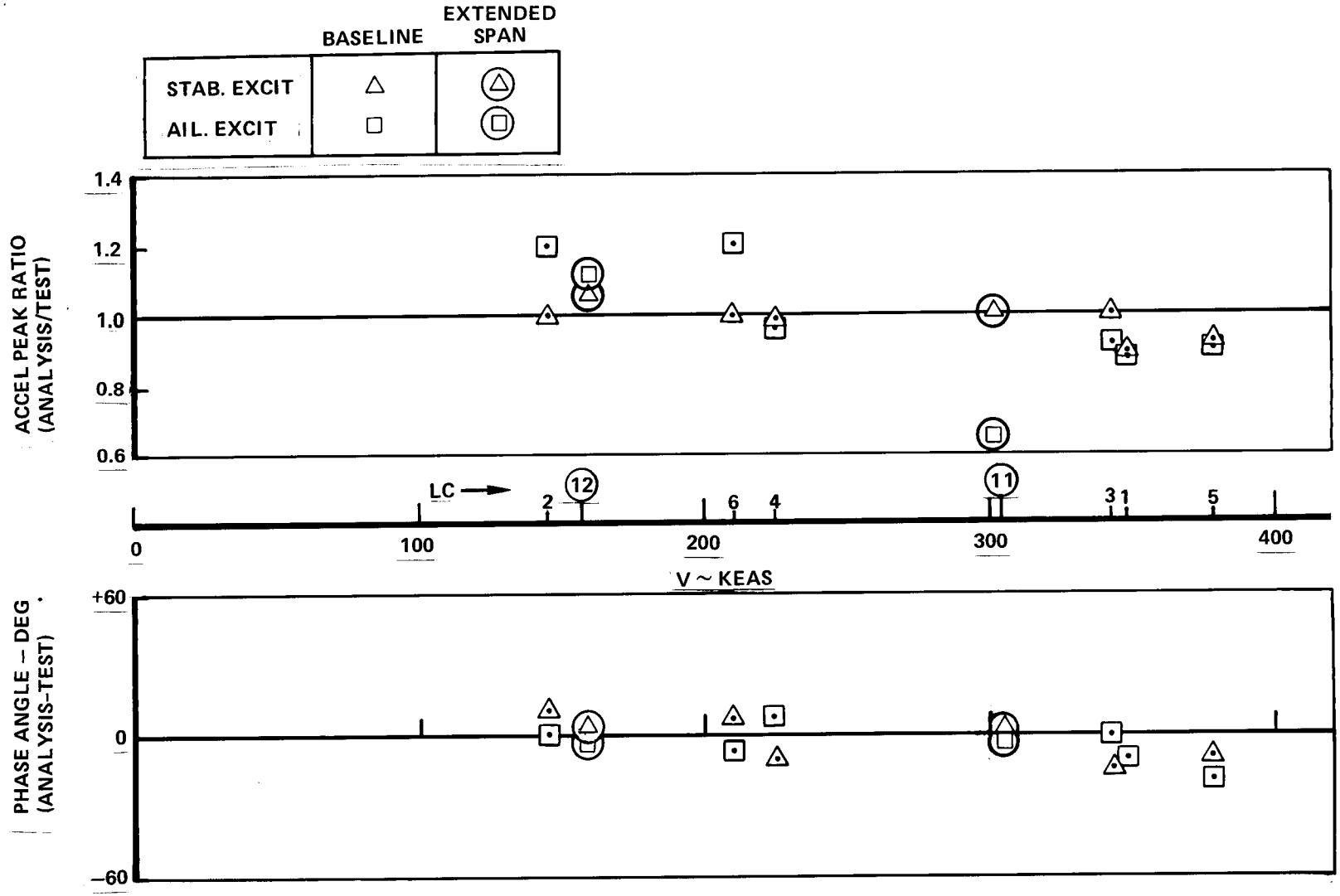

Figure 5-37. C.G. Normal Acceleration Peak Ratios for First Wing Bending Mode Open Loop

5.5.2 Closed Loop Correlations

The closed loop tests were conducted concurrently with the open loop tests by closing the ACS loop immediately after the open loop data were recorded. The oscillator amplitude and the frequency input to the control surface series servo were held constant during open and closed loop response tests. The open loop data plotted along with closed loop data permit evaluation of the effect of ACS on the various response parameters.

In order to facilitate engineering interpretation of the results of closed loop correlation studies, response data for both test and analysis were normalized to a command surface angle to replace oscillator command voltage. The command surface angle is simply the conversion of oscillator voltage into an equivalent surface angle.

The closed loop correlation between analysis and test is presented for wing tip accelerations in the form of transfer function plots (Figures 5-38 to 5-41). The data include aileron and stabilizer excitation for LC-1 (high q) for baseline configuration and aileron excitation for extended span LC-11 and LC-12. For reference the plots include open loop analysis and test results. The aileron excitation test data show ACS effectiveness in reducing wing tip response within the 1-2 Hz frequency band. The test responses closely follow the analysis results for open and closed loop cases. The stabilizer excitation data for the baseline, however, show the closed loop response data to be more attenuated below the first wing bending frequency than above the first wing bending frequency. The analysis response data gives the type of wing tip response reduction that was shown in the aileron excitation condition.

A possible explanation for the difference between closed-loop test and analysis for stabilizer excitation may be in the area of the transfer function for the aileron series and power servo for the low wing amplitudes produced by the stabilizer excitation. A servo lag of 30-40 degrees from the nominal, associated with the low amplitude, may be responsible for this result. For this reason, extended span closed loop stabilizer excitation data were not processed.

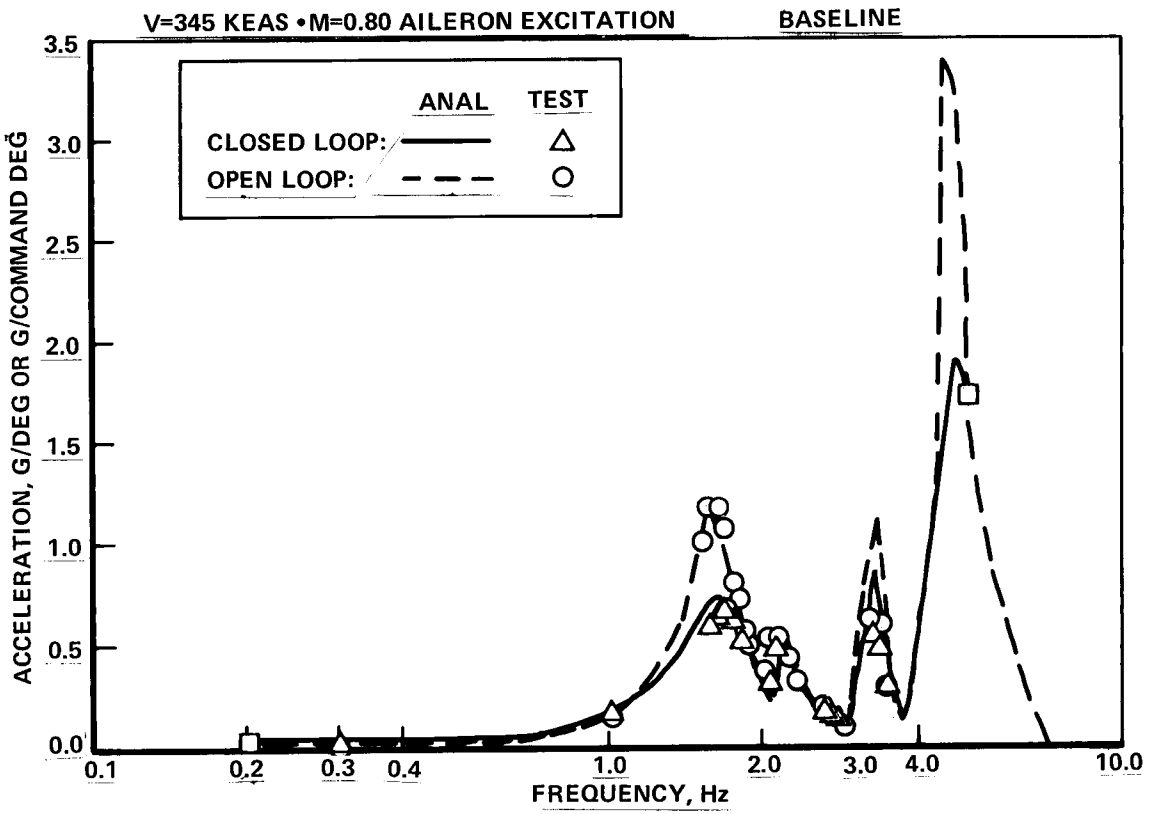

Figure 5-38. LC-1 ACS On/Off Response Comparison Wing Tip Acceleration/Degree Aileron

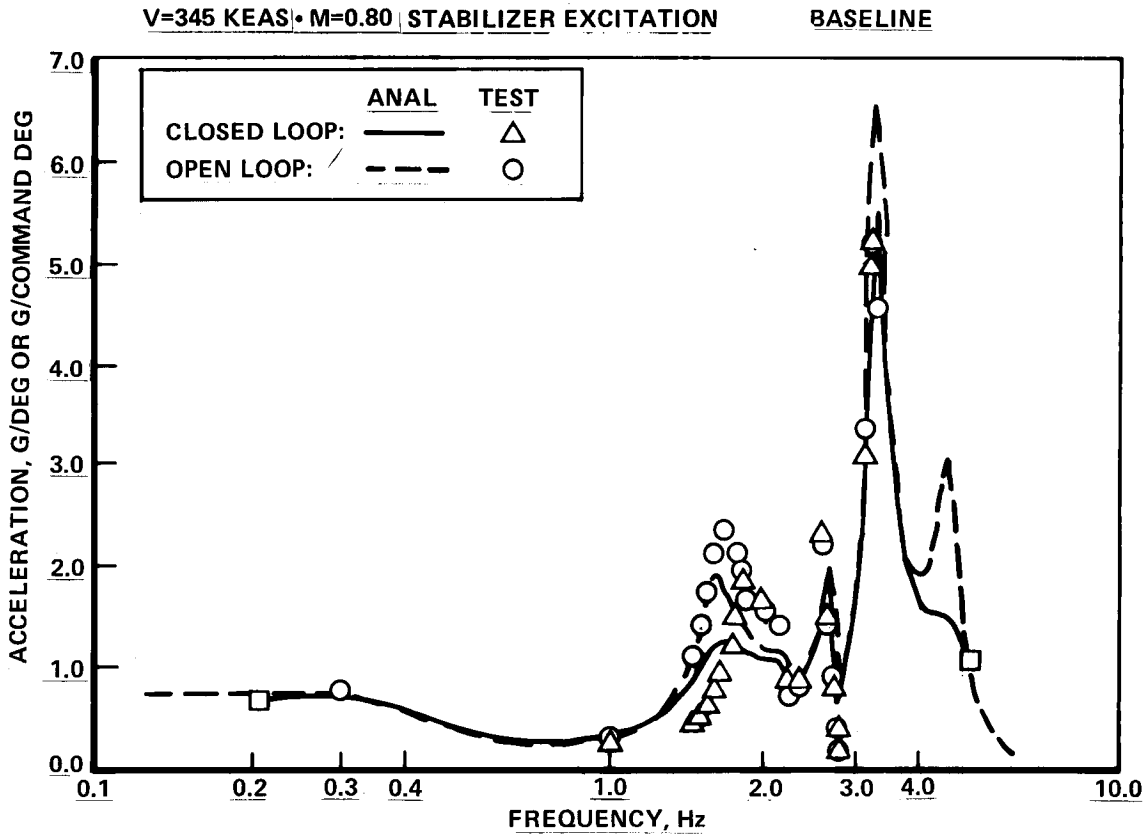

Figure 5-39. LC-1 ACS On/Off Response Comparison Wing Tip Acceleration/Degree Stabilizer

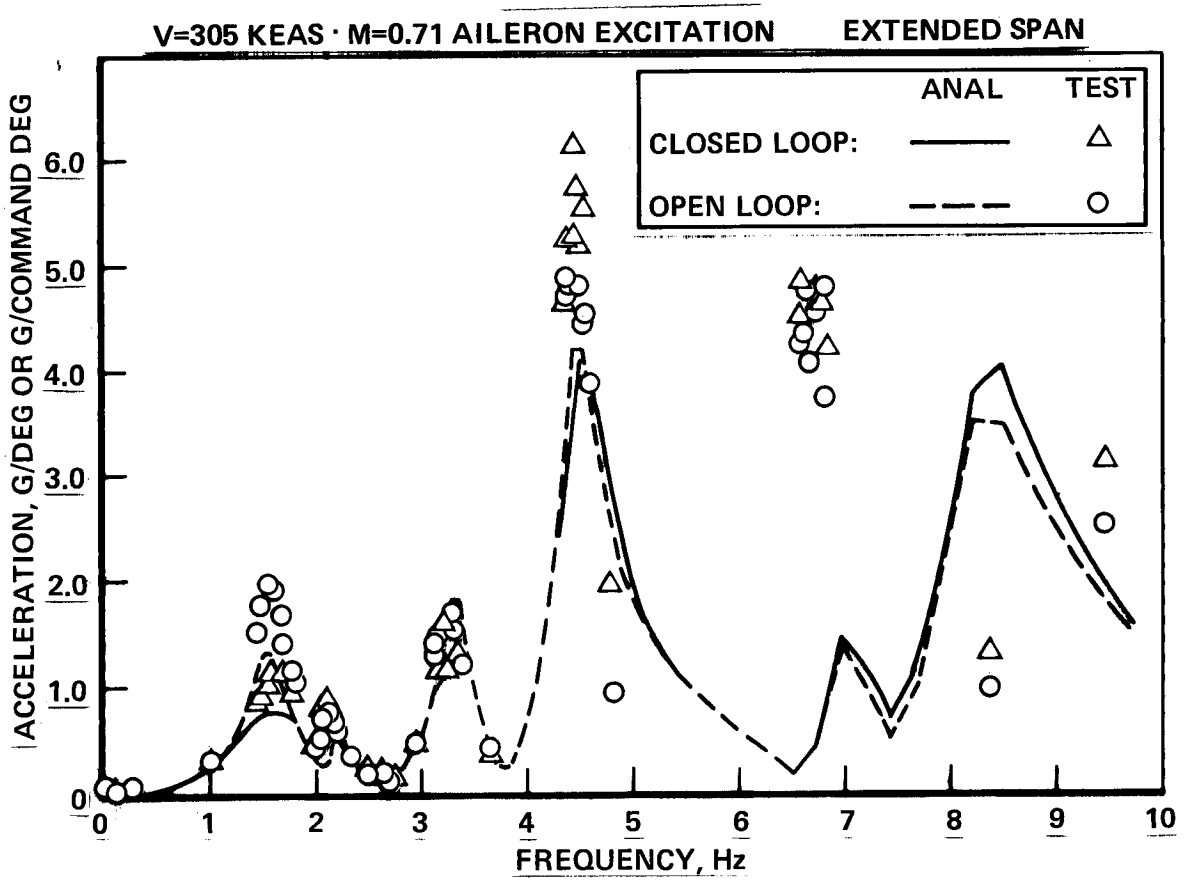

Figure 5-40. LC-11 ACS ON/OFF Response Comparison Wing Tip Acceleration/Degree Aileron

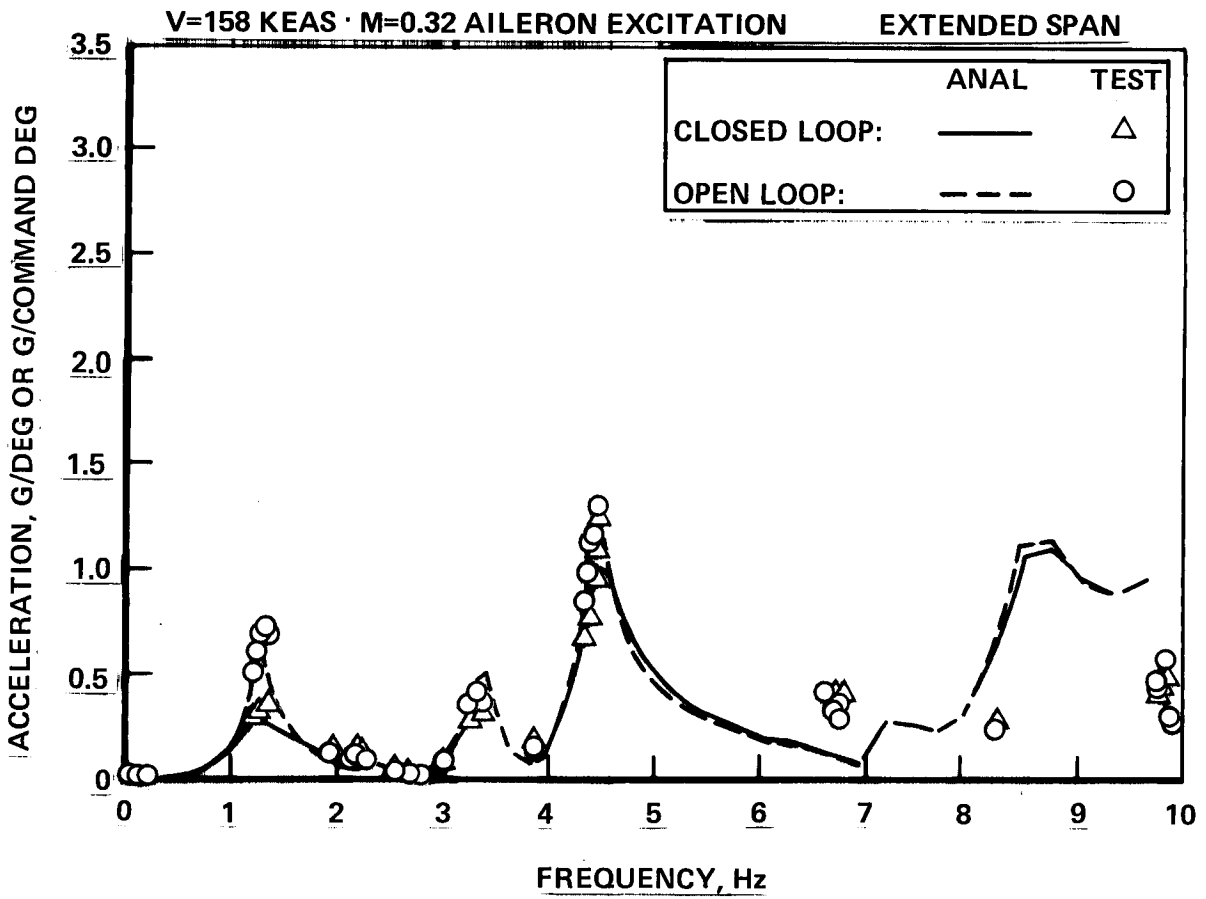

Figure 5-41. LC-12 ACS ON/OFF Response Comparison Wing Tip Acceleration/Degree Aileron

Figure 5-42 shows the closed loop peak amplitude response for the first wing bending normalized by the open loop peak amplitude response. Test ratios were plotted against analysis ratios. The measure of correlation is the distance from the 45 degree line. Overall, the correlation is acceptable.

All of the data points lie within ±20% of exact correlation values relative to test.

5.5.3 Conclusions, GFAM Model

The GFAM model for the conditions analyzed provided excellent correlation for the baseline airplane and good correlation for the extended span configuration with transfer function flight test data for both aileron and stabilizer excitation conditions for frequencies up through first wing bending (~1.9 Hz). Amplitude ratio correlations for the first and second engine modes were marginal.

Overall, the GFAM model demonstrated good correlation with flight data for frequencies including fuselage first bending, wing second bending and stabilizer first bending for both baseline and extended span configurations.

Amplitude ratio correlations for center of gravity accelerations were good for first wing bending mode. The closed loop correlation was limited to wing tip accelerations and found to be fair to good.

Based on these results, the GFAM model is fully qualified for active control synthesis work associated with MLC, EMS, and GA functions. Although not part of the current charter, the model is also fully qualified to synthesize ride quality functions.

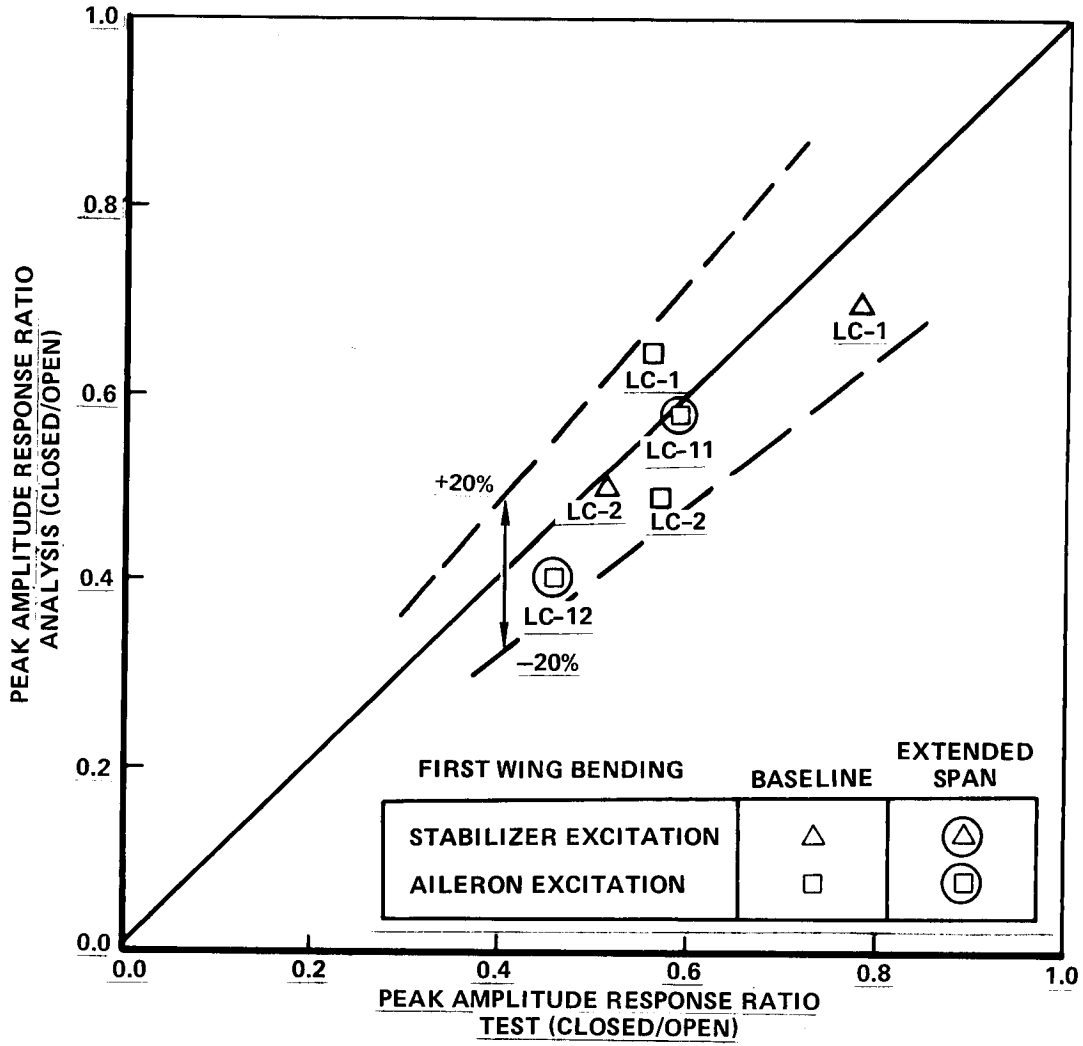

Figure 5-42. Wing Tip Acceleration Peak Response (ACS ON/OFF) Ratios

5.6 LOADS TRANSFER FUNCTIONS

5.6.1 Baseline Test Results

The baseline testing consisted of five flight conditions, summarized in Table 5-5, in which loads transfer functions were obtained separately for symmetrically oscillating ailerons and for oscillating horizontal tail. The VGA program, Section 4.2, was used in developing the baseline comparisons.

Figures 5-43 and 5-44 present representative data. They show comparisons of wing root (η = .20) bending moment per degree aileron and per degree stabilizer for the LC-1X (cruise) condition. Both figures show close agreement between test and analysis data at 0.3 Hz, the vicinity of the airplane short period mode. The response to aileron input, Figure 5-43, at the first wing bending frequency of approximately 1.6 Hz, agrees very well in magnitude, with the analysis frequency low by about 10%.

The wing root bending response to stabilizer input, Figure 5-44, shows the measured data at 1.6 Hz exceeding the theoretical, and the frequency as measured again about 10% higher than the theoretical prediction. The second evident elastic mode peak at about 2.7 Hz, reflecting the second wing engine mode, shows relatively good agreement in load level and frequency.

5.6.2 Extended-Span Loads Transfer Functions

The Task 3 loads transfer function comparisons were developed through the use of the GLP series of gust analysis programs. As noted in Section 4.2, the VGA and GLP series provide essentially the same results with respect to turbulence response (one-dimensional) and with respect to the theoretical loads induced by oscillating control surfaces. The GLP system was used in the Task 3 transfer function comparisons to be compatible with the turbulence flight testing analysis, reported in Section 5.7.

Three flight conditions were utilized in the Task 3 testing, described in Table 5-6.

TABLE 5-5. FLIGHT CONDITIONS FOR LOADS TRANSFER FUNCTION COMPARISONS - BASELINE TESTS

CONDITION PARAMETER	LC-IX		LC-2X		LC-3X		LC-4X		LC-5X	
	STAB.	AIL.	STAB.	AIL.	STAB.	AIL.	STAB.	AIL.	STAB.	AIL.
Mass, kg	161,450	166,850	155,750	159,050	151,900	153,750	176,100	177,800	160,050	167,100
(lb)	(356,000)	(367,900)	(343.4)	(350,700)	(334,900)	(339,000)	(388,300)	(392,000)	(352,900)	(368,500)
c.g. % MAC	17.9	17.8	25.4	25.2	14.2	14.1	18.2	18.2	17.6	17.2
Fuel, kg	38,230	44,440	31,110	34,420	28,660	30,070	52,880	54,560	35,780	42,950
(lb.)	(84,300)	(98,000)	(68,600)	(75,900)	(63,200)	(66,300)	(116,600)	(120,300)	(78,900)	(94,700)
h, km	6.7	6.7	3	3	6.7	6.7	6.1	6.1	6.7	6.7
(1000 ft.)	(22)	(22)	(10)	(10)	(22)	(22)	(20)	(20)	(22)	(22)
Mach. No.	.80	.80	.26	.26	.80	.80	.50	.50	.88	.88
V_{KEAS}	345	345	145	145	343	343	225	225	378	378

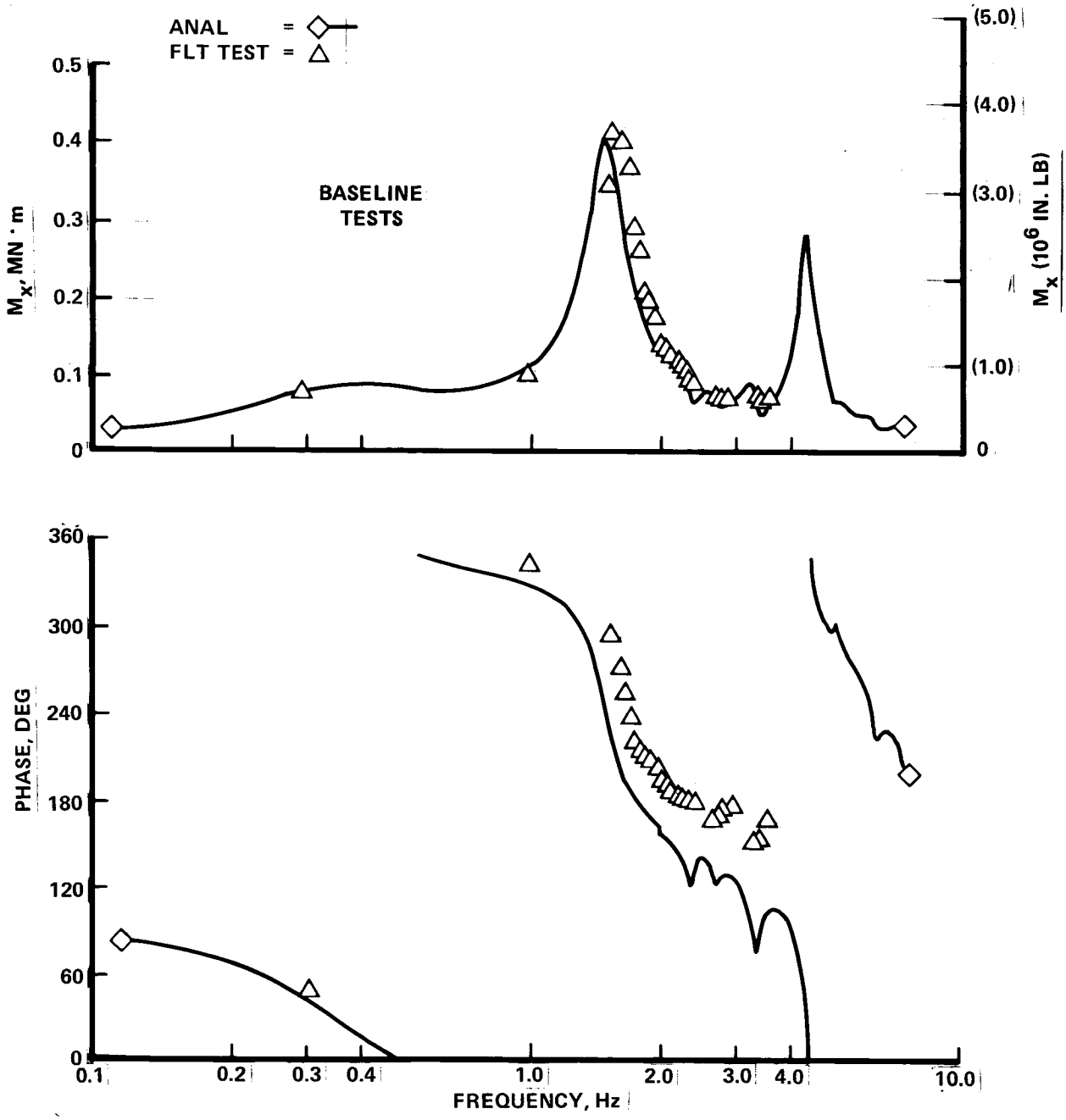

Figure 5-43. Wing Bending Moment/Degree Aileron
η = 0.20 345 KEAS M = 0.80

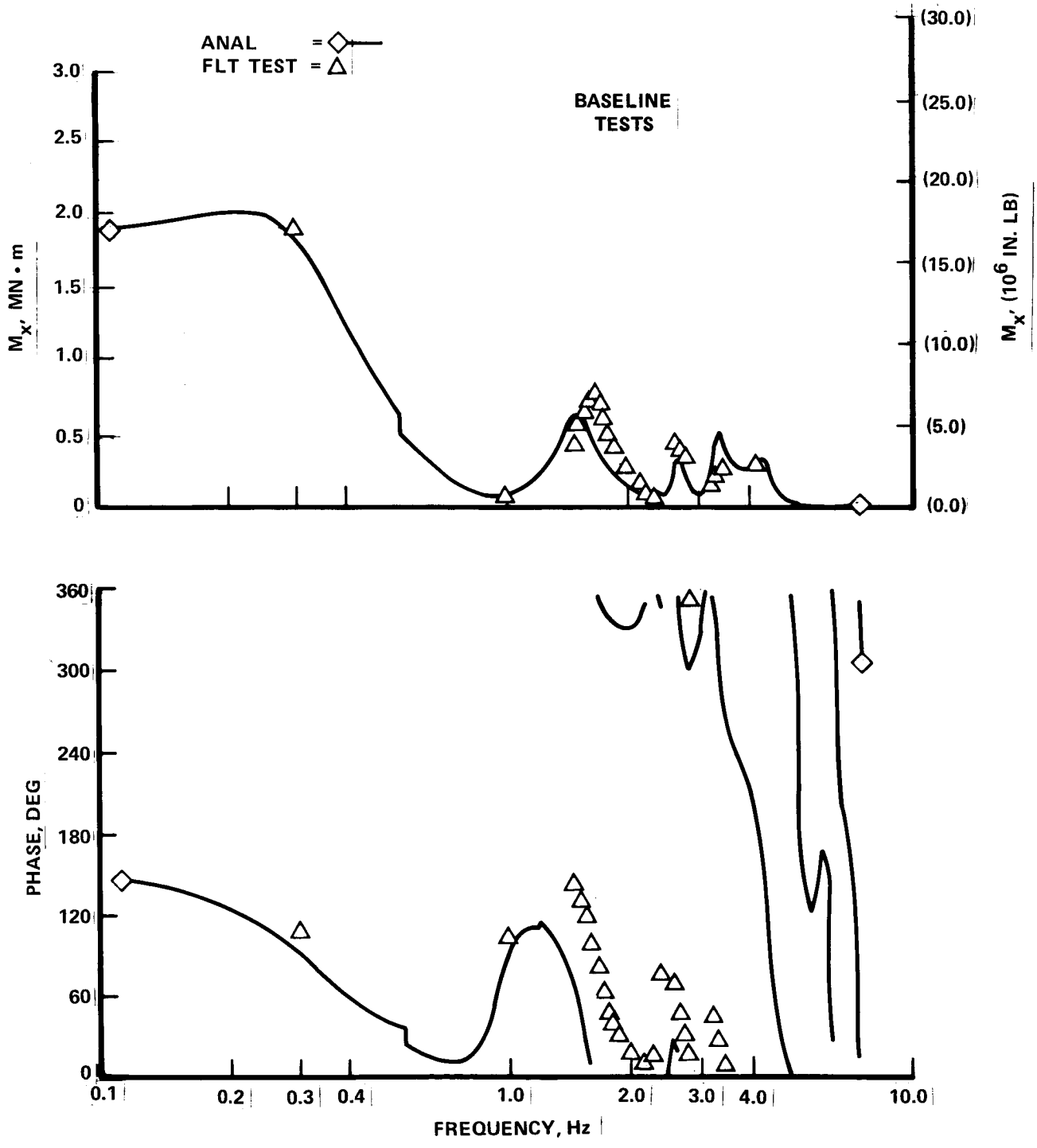

Figure 5-44. Wing Bending Moment/Degree Stabilizer
η = 0.20 345 KEAS M = 0.80

TABLE 5-6. FLIGHT CONDITIONS FOR LOADS TRANSFER FUNCTION COMPARISON - EXTENDED SPAN

CONDITION PARAMETER	1	2	2A
Mass, kg	141,500	158,300	169,800
(lb.)	(312,000)	(349,000)	(374,400)
c.g. % MAC	17.7	27.9	31.9
Fuel, kg	20,160	40,690	57,530
(lb.)	(43,200)	(87,200)	(123,300)
h, km	4.6	6.6	6.6
(1000 ft.)	(15)	(22)	(22)
Mach. No.	.32	.71	.66
V_{KEAS}	158	315	305

Fourteen figures are included herein to illustrate the comparison of theoretical and test results. Figures 5-45 to 5-51 reflect the low-speed, flaps-extended results for the symmetrically oscillating aileron. Good agreement is indicated at all locations in modulus and phase.

The peaks in the response, most noticeable in Figure 5-45 are identified with airplane response modes as per the following summary.

Frequency	Mode
.15	Airplane short period
1.25 - 1.3	Wing first bending
2.4, 2.7	Wing engine modes
3.3	Fuselage first bending
4.2 - 4.5	Wing second bending or horizontal tail bending.*

Figures 5-52 and 5-53 present wing loads (shear and bending moment) at η = .71, low speed, flaps extended, due to stabilizer oscillations. The

*Three structural modes exist in this frequency range. The character of the modes is similar, differing only in the amounts of wing and tail motions. Aerodynamic effects also alter the character of the modes, preventing precise identification.

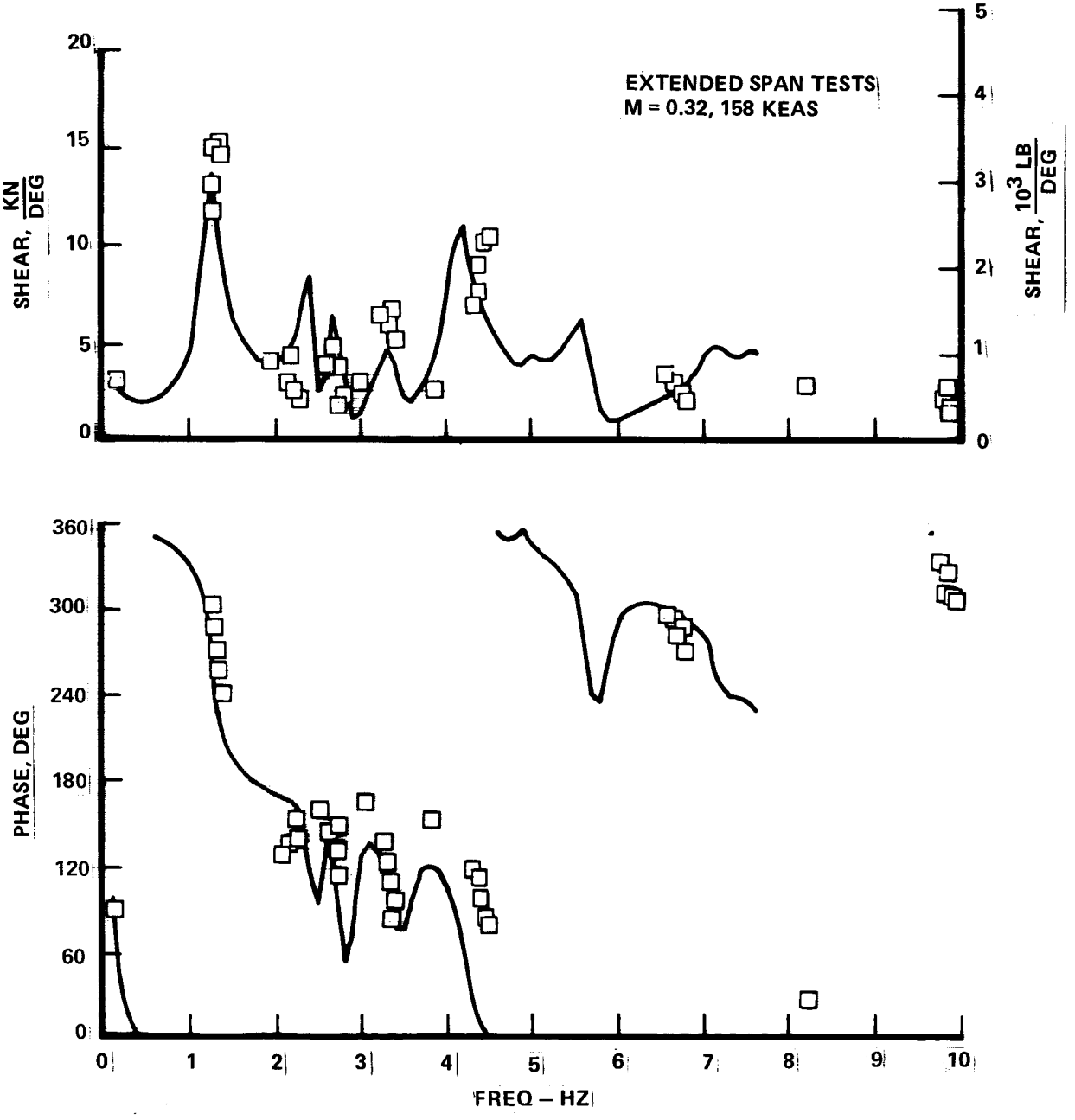

Figure 5-45. Test/Analysis, Shear at η = .19, Aileron Drive, Flaps Down

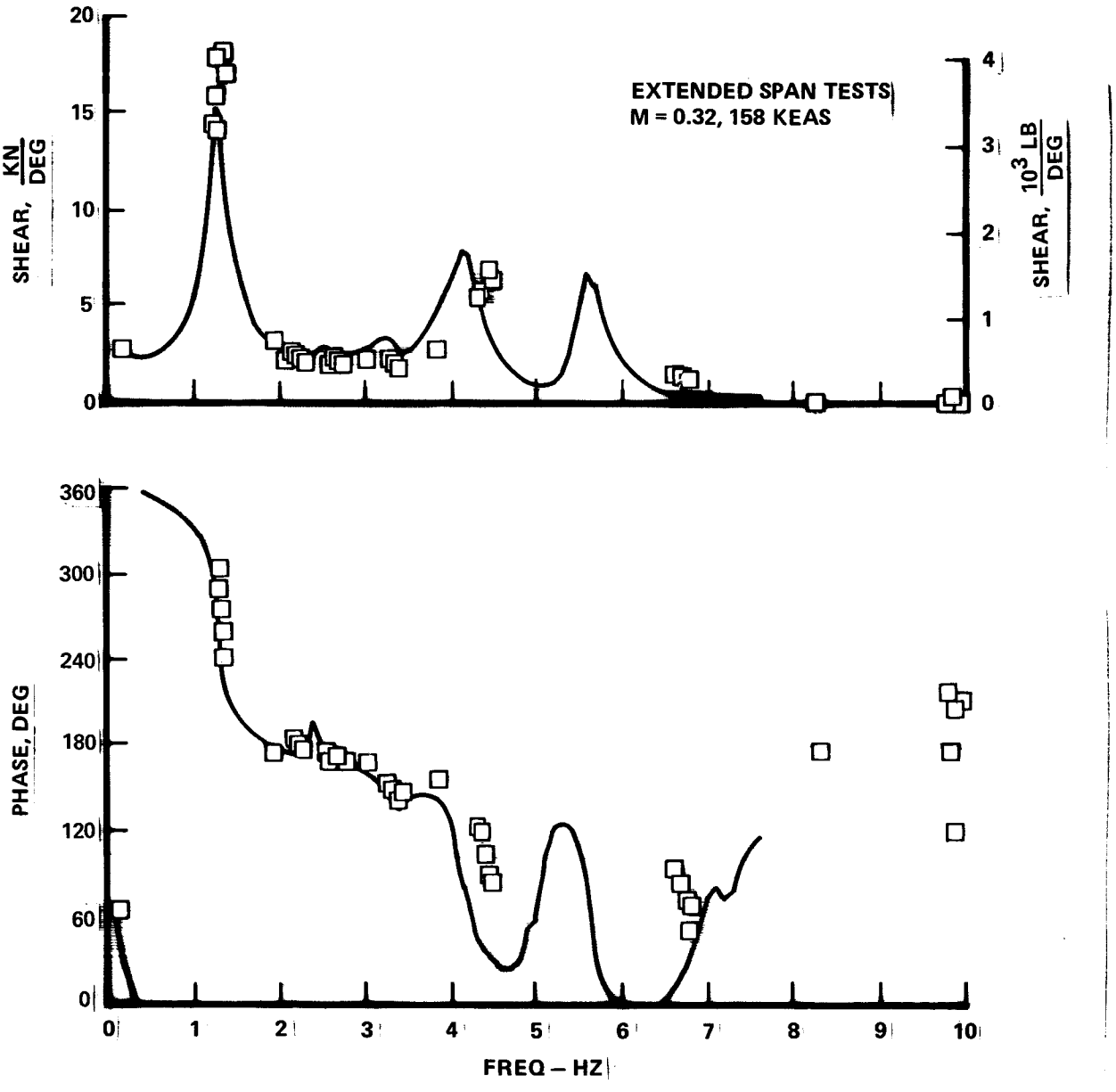

Figure 5-46. Test/Analysis, Shear at η = .49, Aileron Drive, Flaps Down

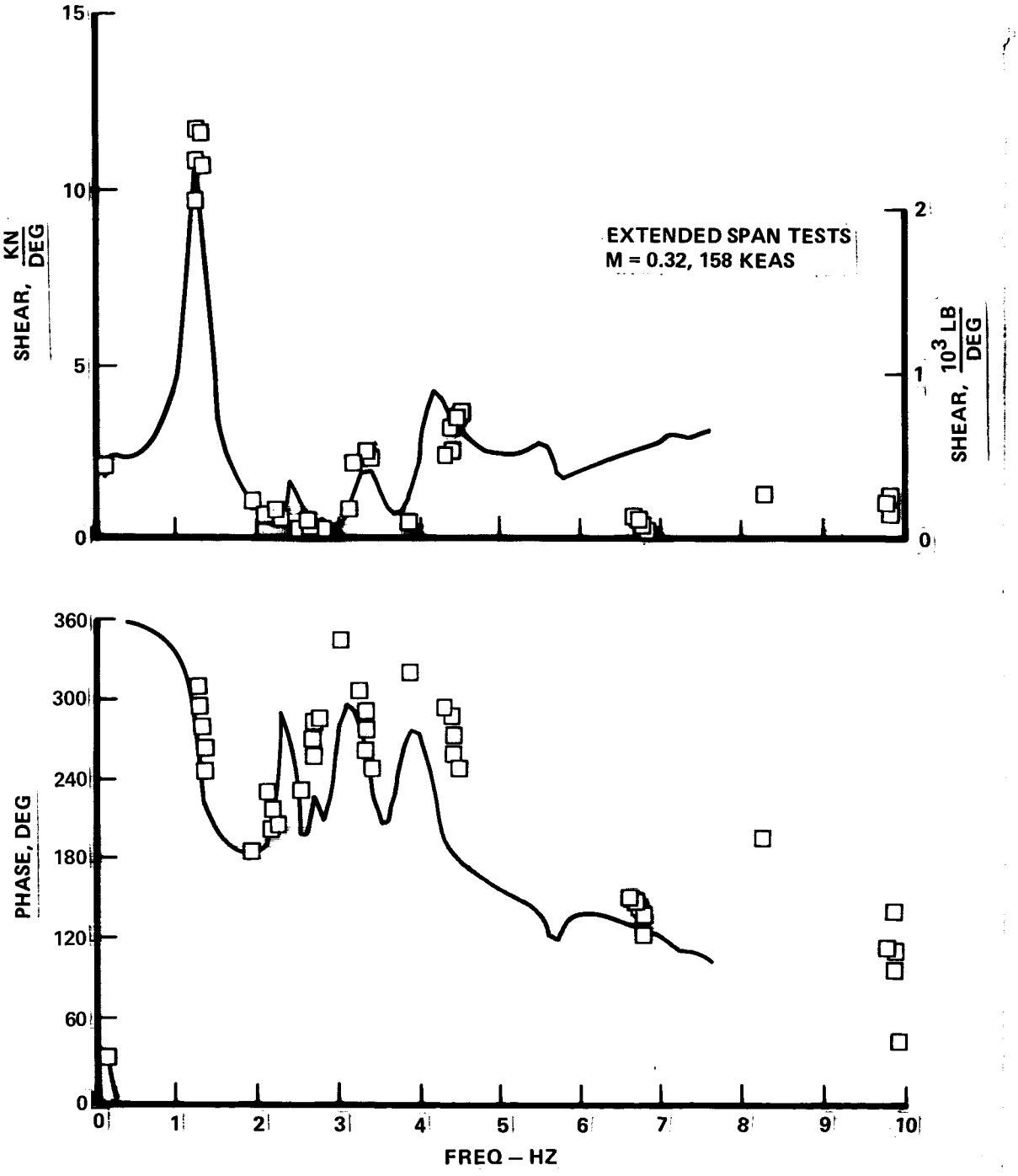

Figure 5-47. Test/Analysis, Shear at η = .71, Aileron Drive, Flaps Down

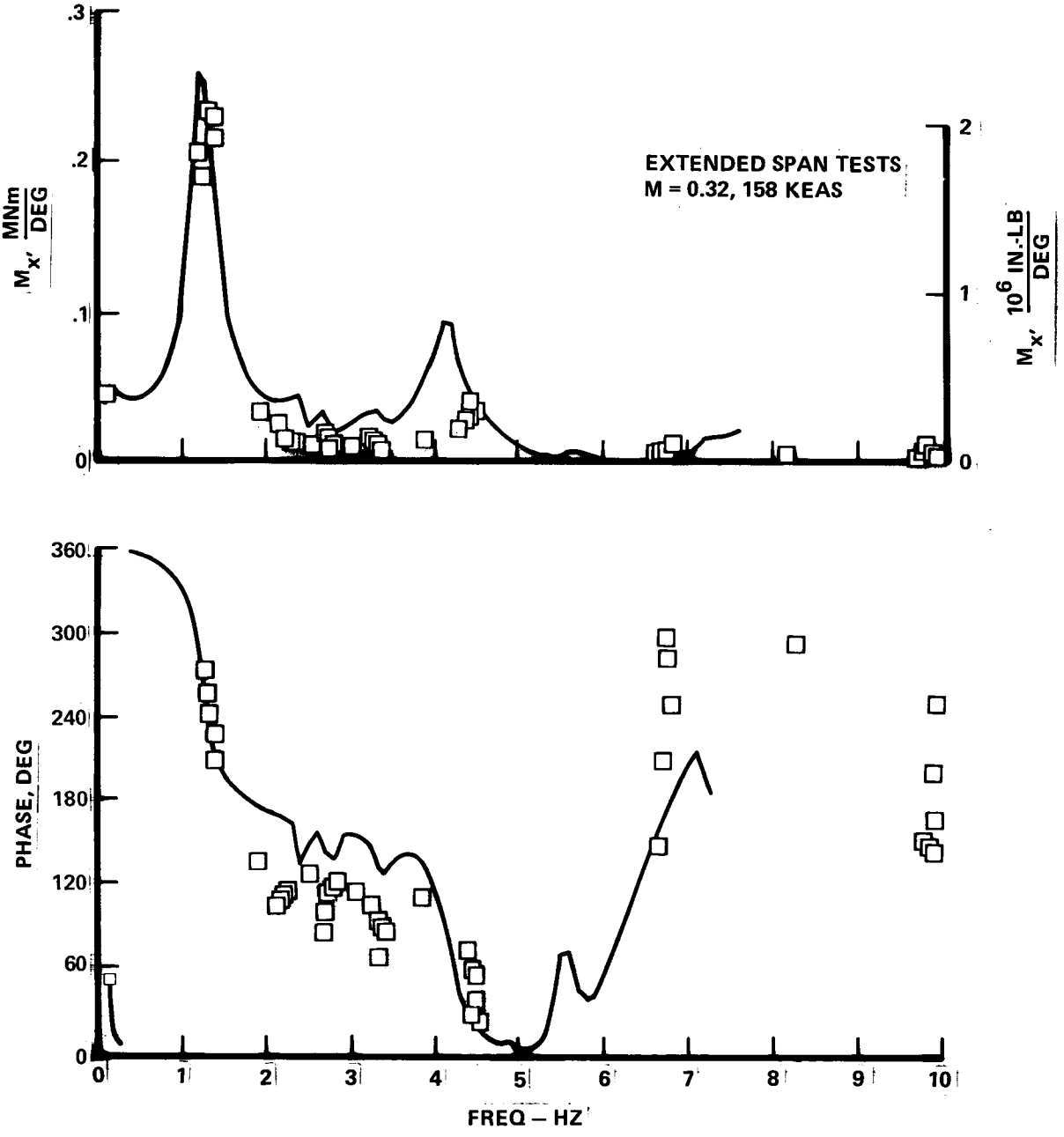

Figure 5-48. Test/Analysis, Bending at η = .19, Aileron Drive, Flaps Down

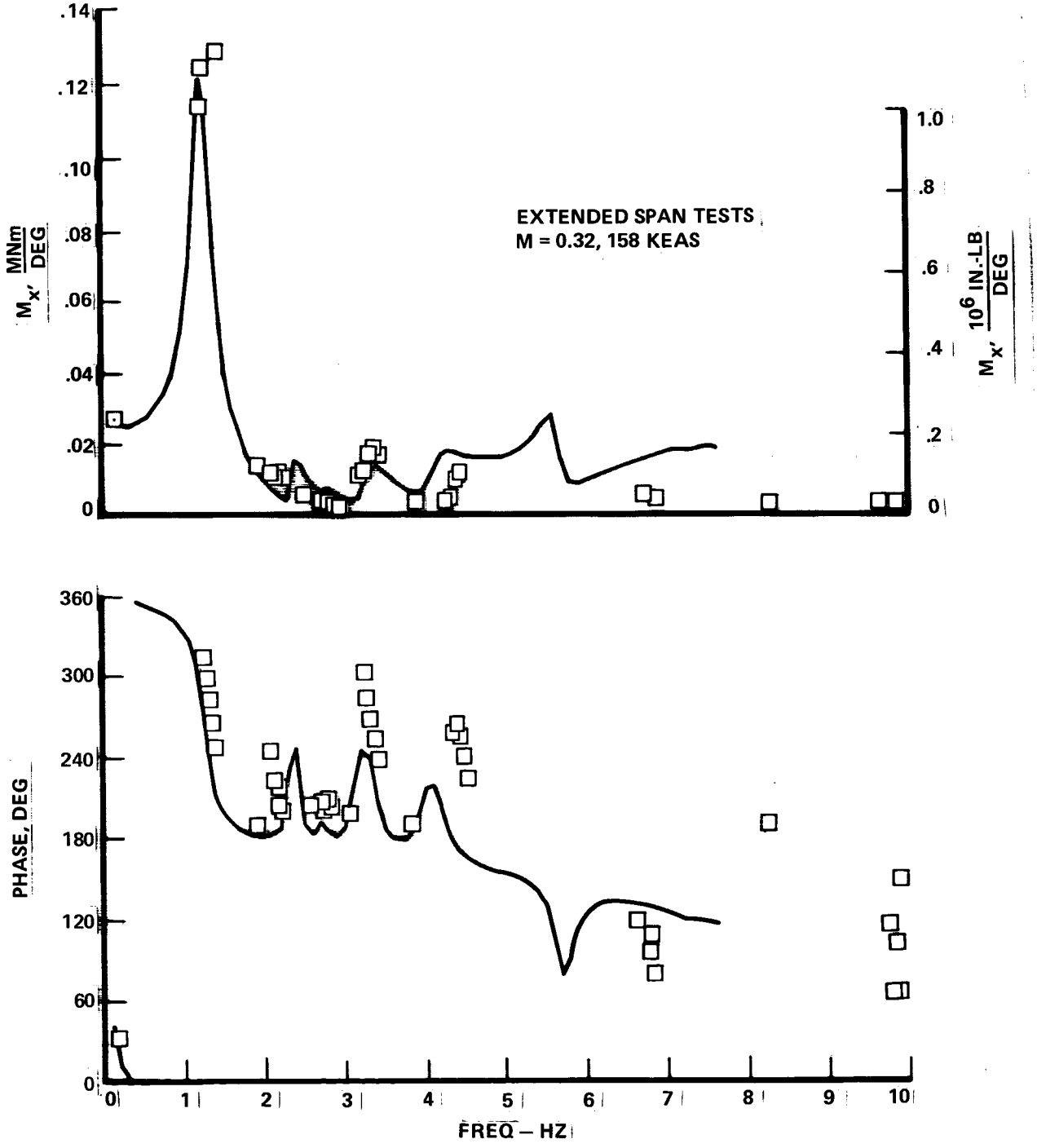

Figure 5-49. Test/Analysis, Bending at η = .49, Aileron Drive, Flaps Down

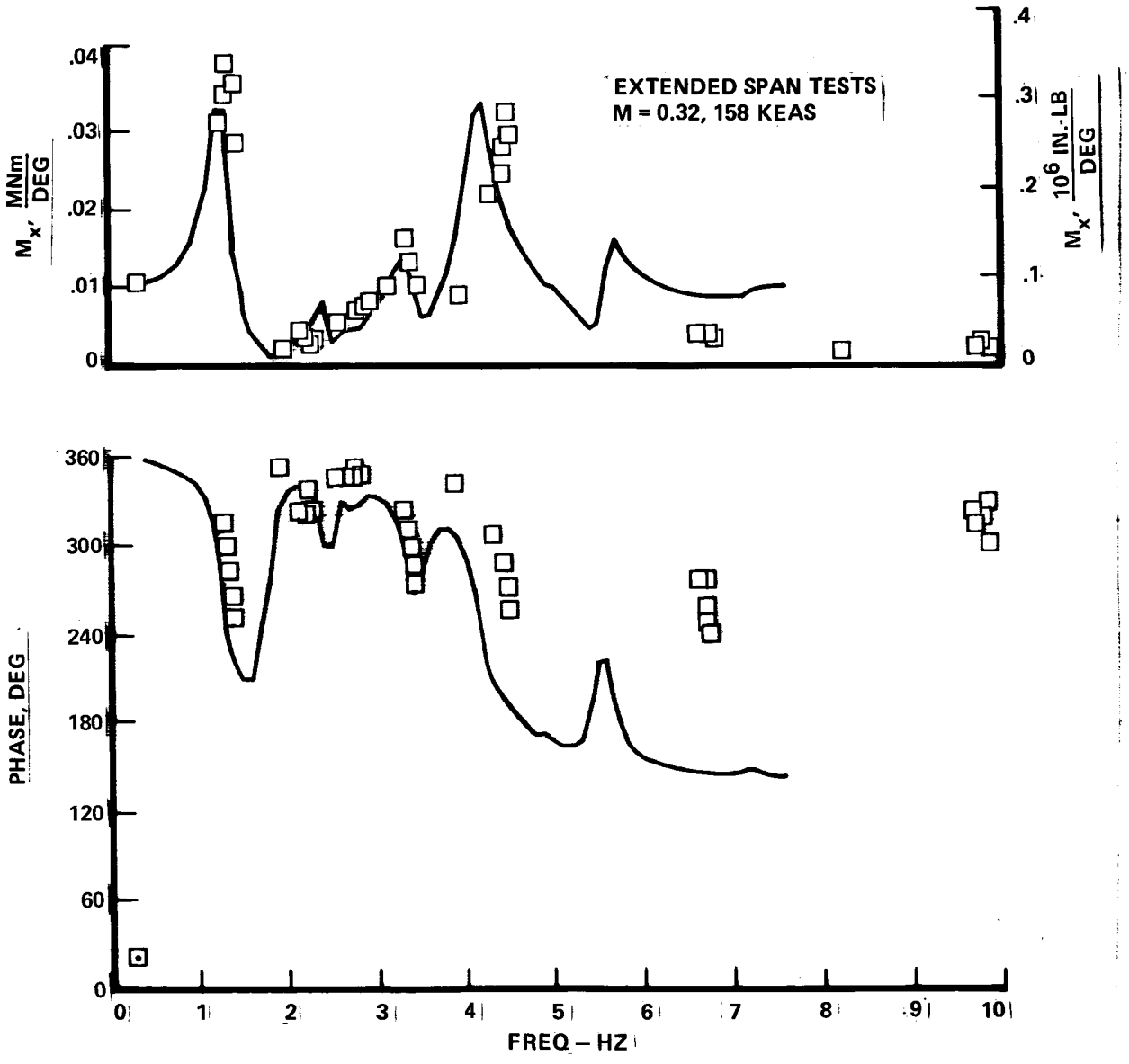

Figure 5-50. Test/Analysis, Bending at η = .71, Aileron Drive, Flaps Down

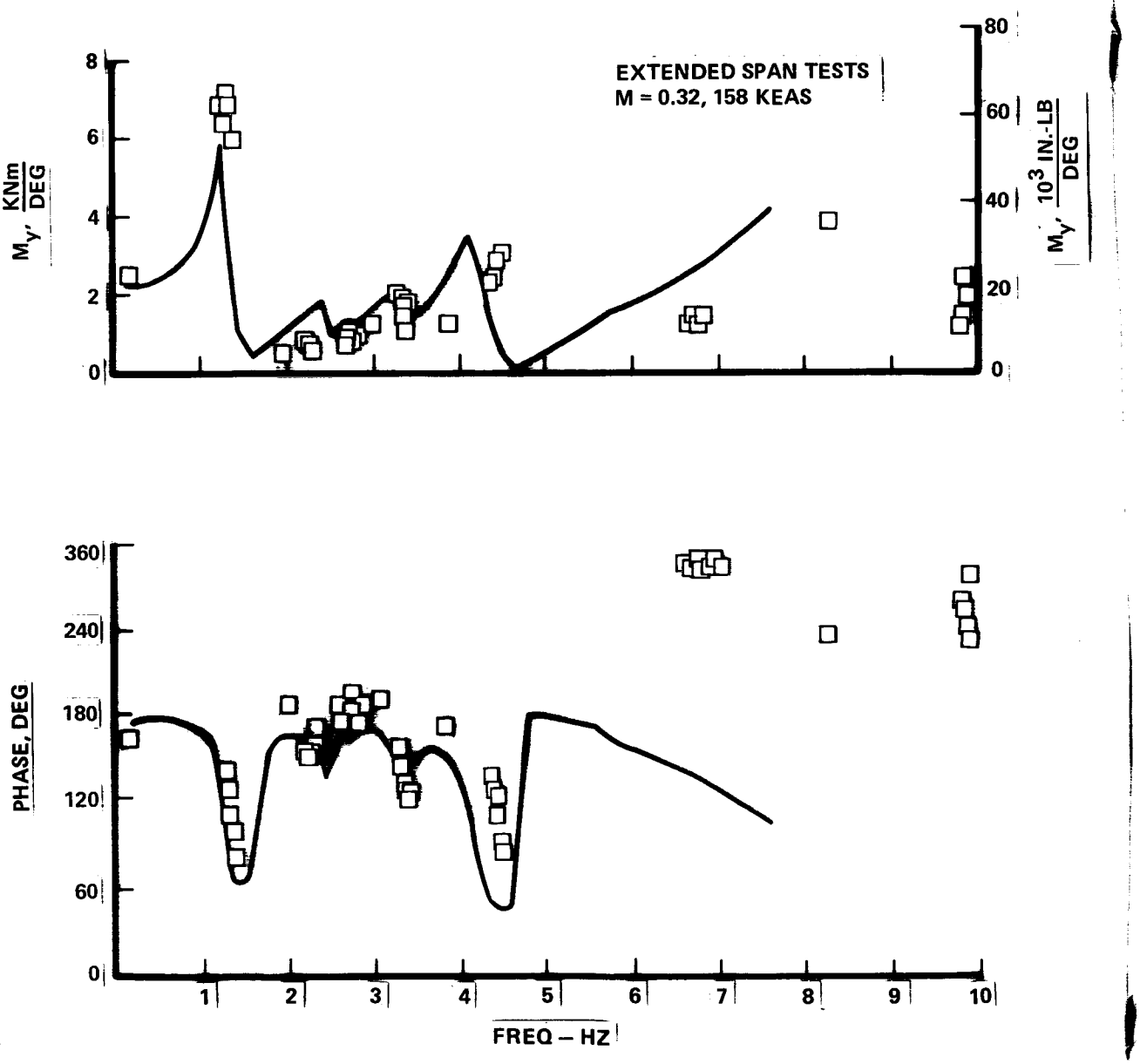

Figure 5-51. Test/Analysis, Torsion at η = .71, Aileron Drive, Flaps Down

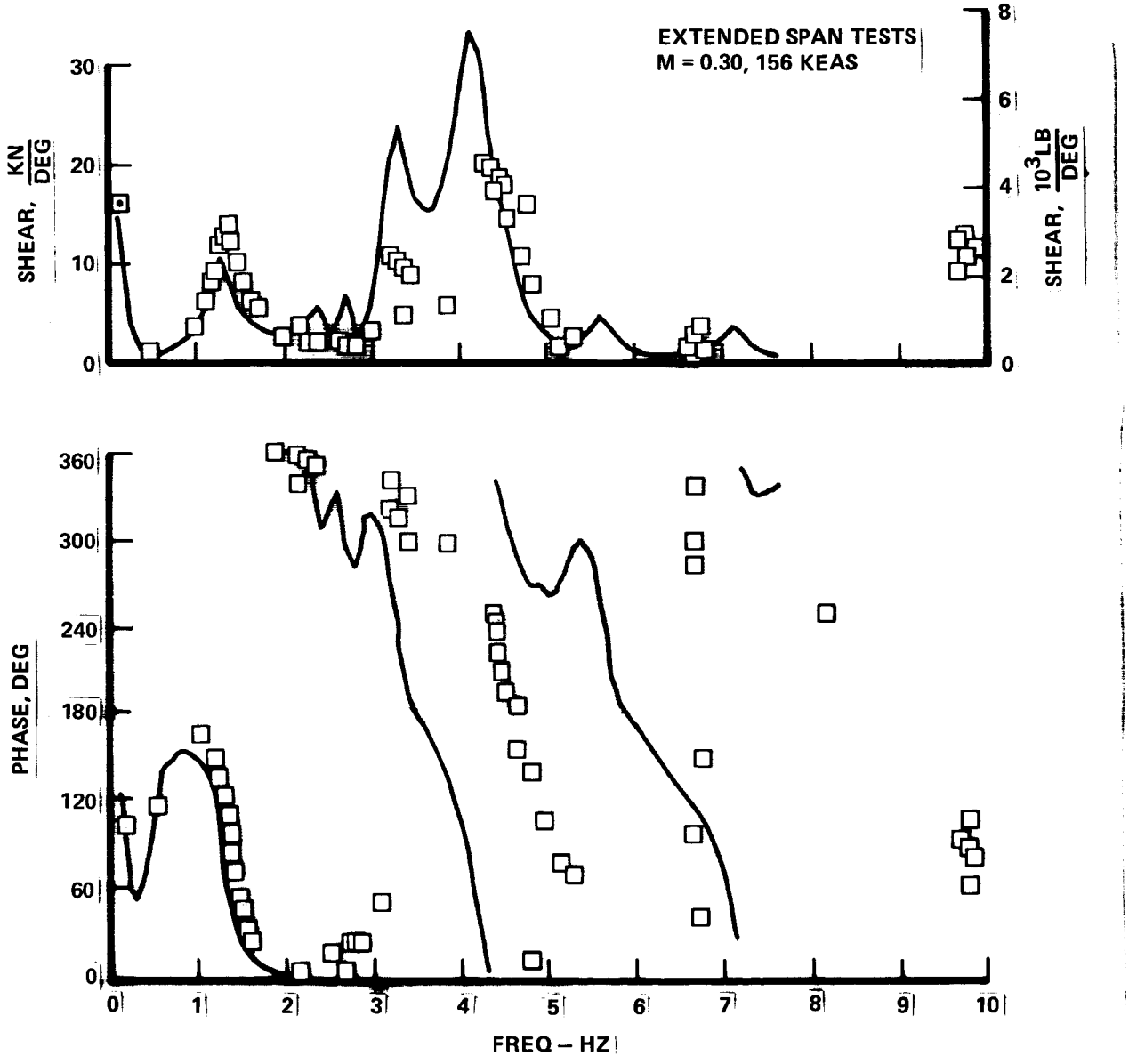

Figure 5-52. Test/Analysis, Shear at η = .71, Stabilizer Drive, Flaps Down

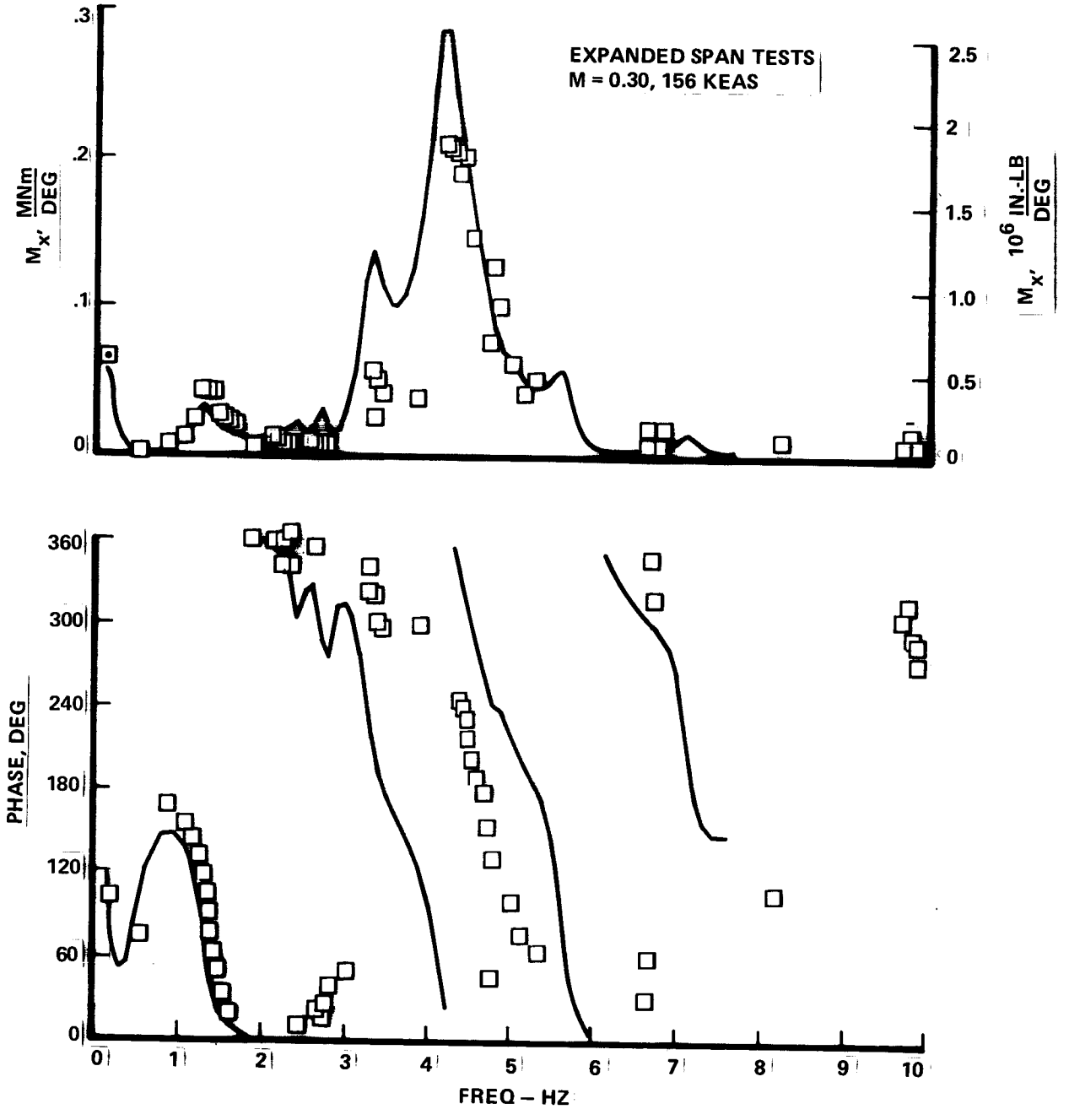

Figure 5-53. Test/Analysis, Bending at η = .71, Stabilizer Drive, Flaps Down

agreement in test and theory is seen to be very good for frequencies up to about 3 Hz. Above 3 Hz the theory tends to overpredict the airplane response. This result is typical of the stabilizer-oscillation results.

Figure 5-54 shows a cruise speed, aileron oscillation test-to-theory comparison. The theoretical frequency (1.4 Hz) is somewhat less than the measured value (1.5 Hz) but the magnitude of the modulus agrees quite well. The theory overpredicts the test results over the frequency range from about 2 Hz to 4.4 Hz, and identifies peak modal responses much more clearly than does the test data.

Figures 5-55 to 5-58 present typical data for the cruise speed stabilizer oscillation tests, comparing wing loads due to stabilizer oscillation. The loads at very low frequency (.10 - .15 Hz) agree very well in modulus and fairly well in phase. The first wing bending mode peaks at 1.5 Hz are somewhat higher than predicted.

The baseline and extended-span root bending moments are summarized in Figures 5-59 to 5-61, giving the magnitudes of the low-frequency and wing-bending frequency responses per degree aileron and per degree stabilizer. Responses at these frequencies are the primary determinants of the loads encountered in turbulence.

It may be seen from these figures that the baseline and extended-span test/analysis agreement is generally reasonable. It is concluded that gust loads predictions using the GLP program should give reasonable agreement with the test results.

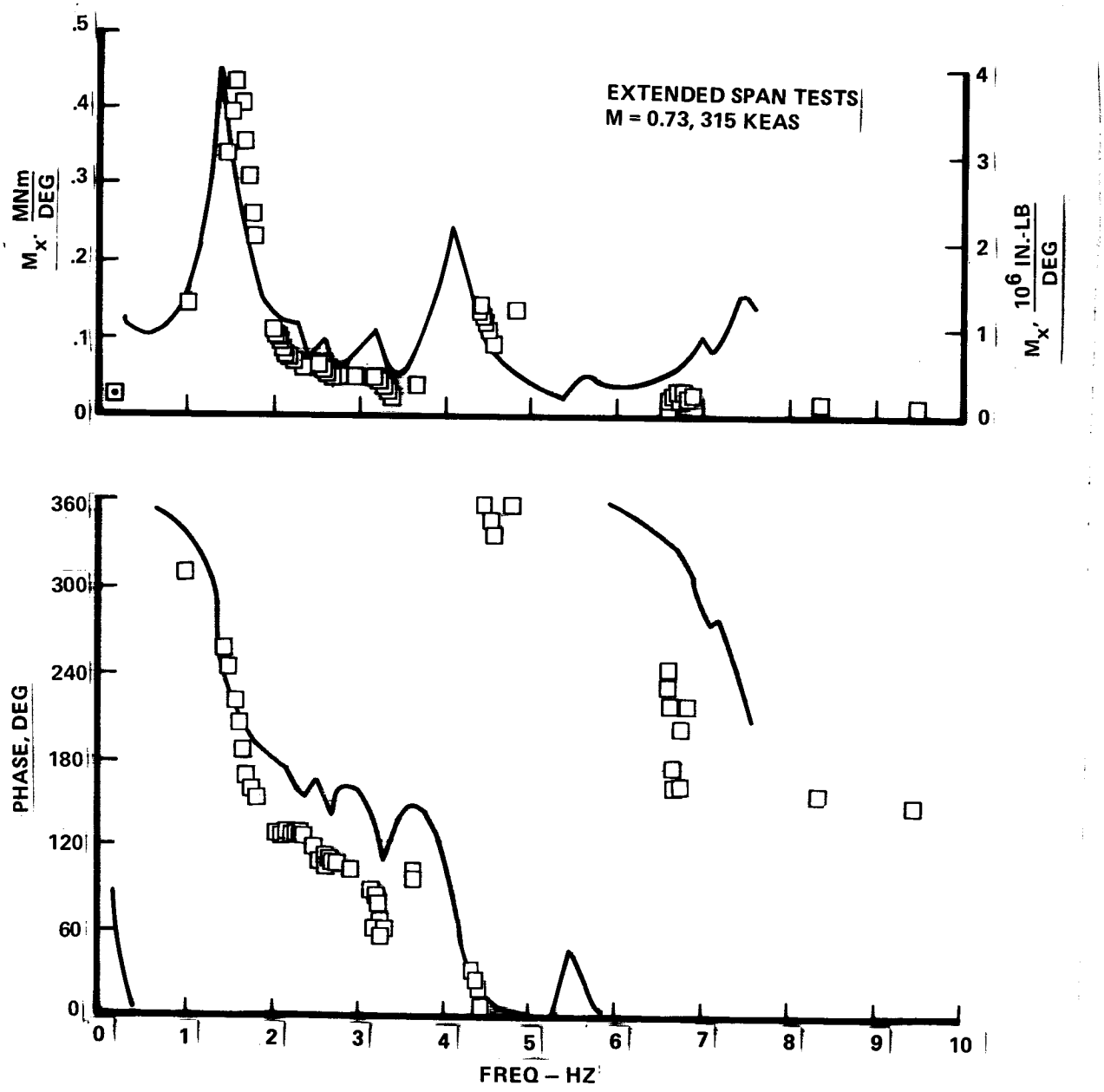

Figure 5-54. Test/Analysis, Bending at η = .19, Aileron Drive, Cruise

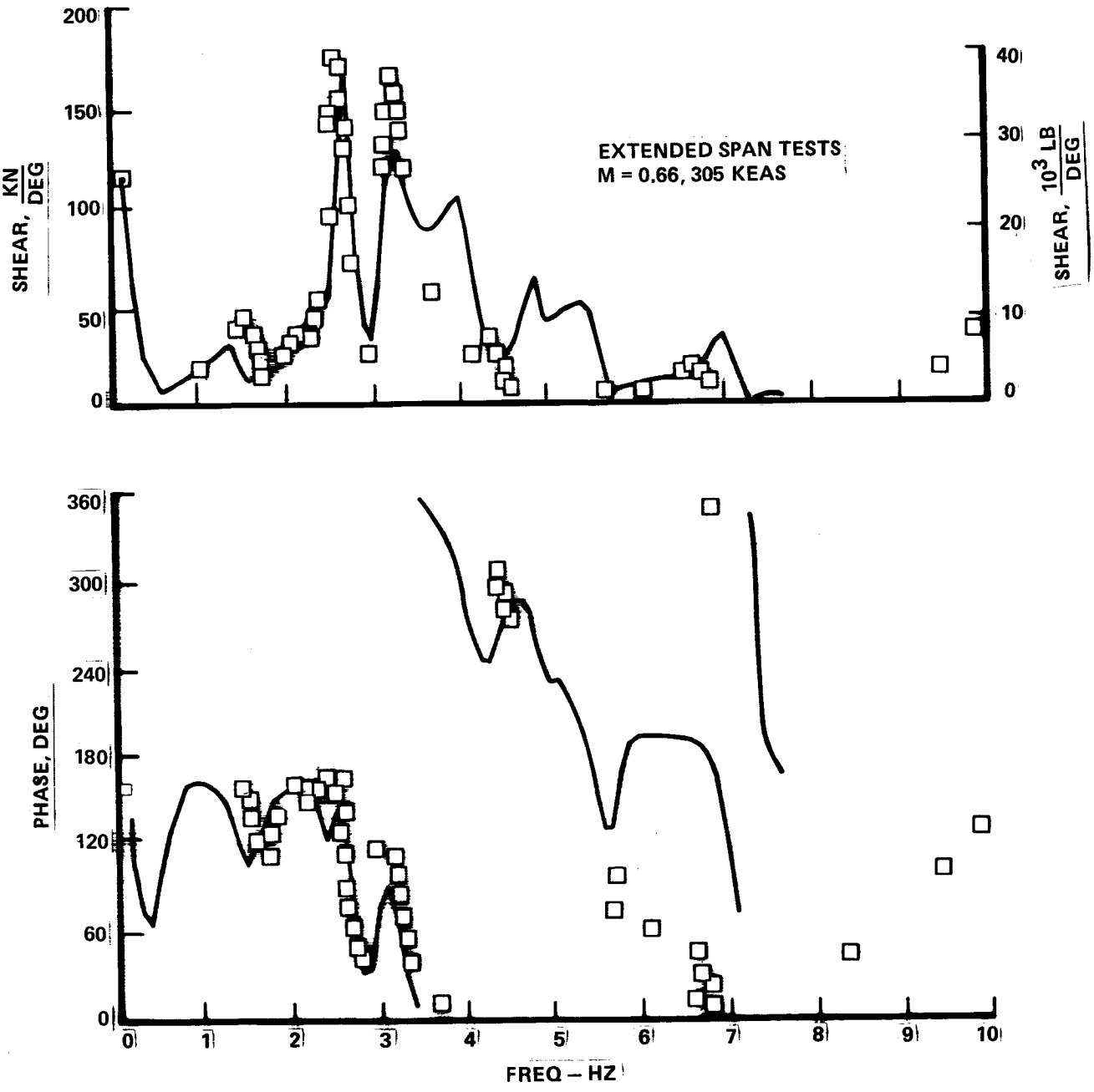

Figure 5-55. Test/Analysis, Shear at η = .19, Stabilizer Drive, Cruise

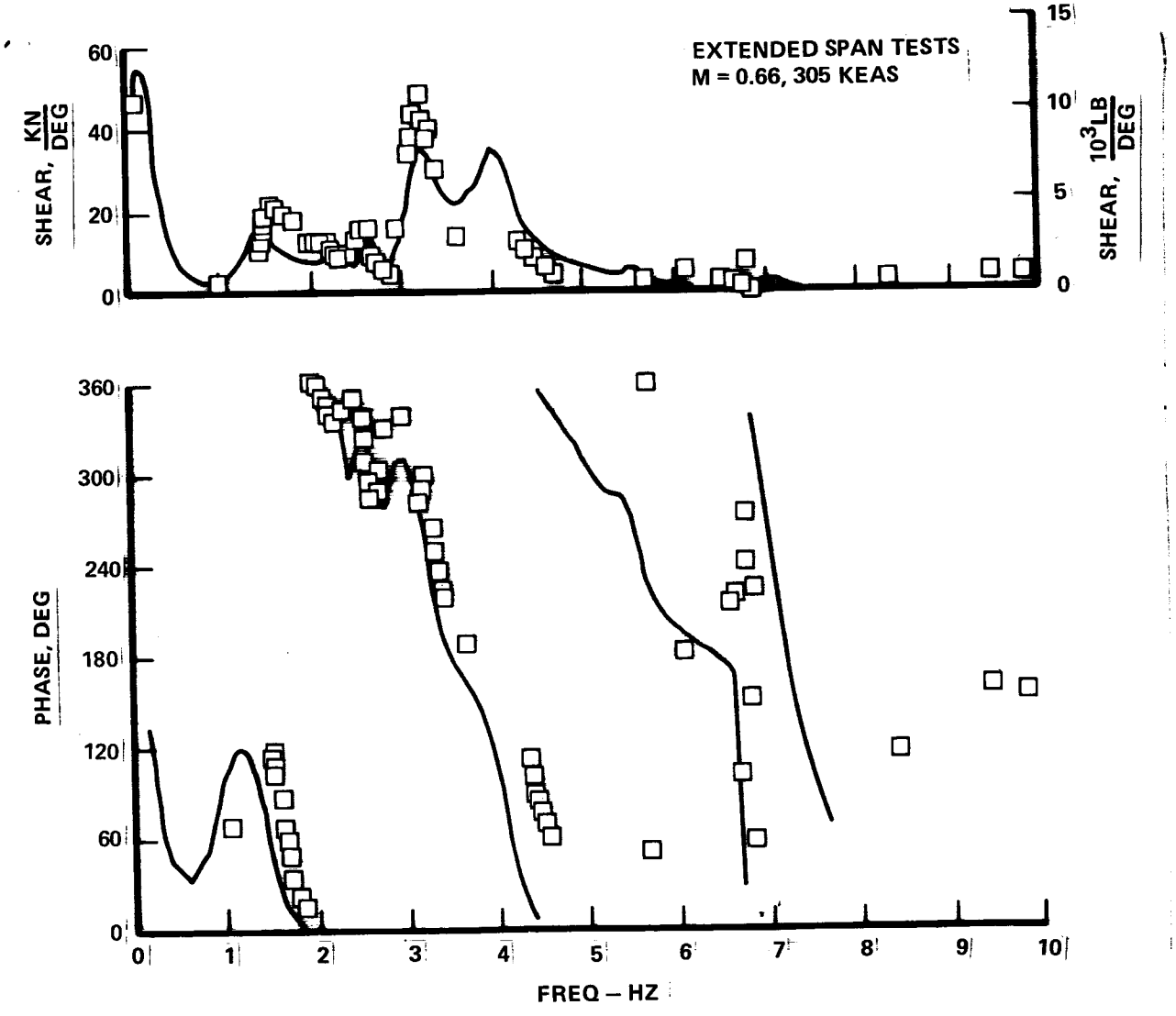

Figure 5-56. Test/Analysis, Shear at η = .71, Stabilizer Drive, Cruise

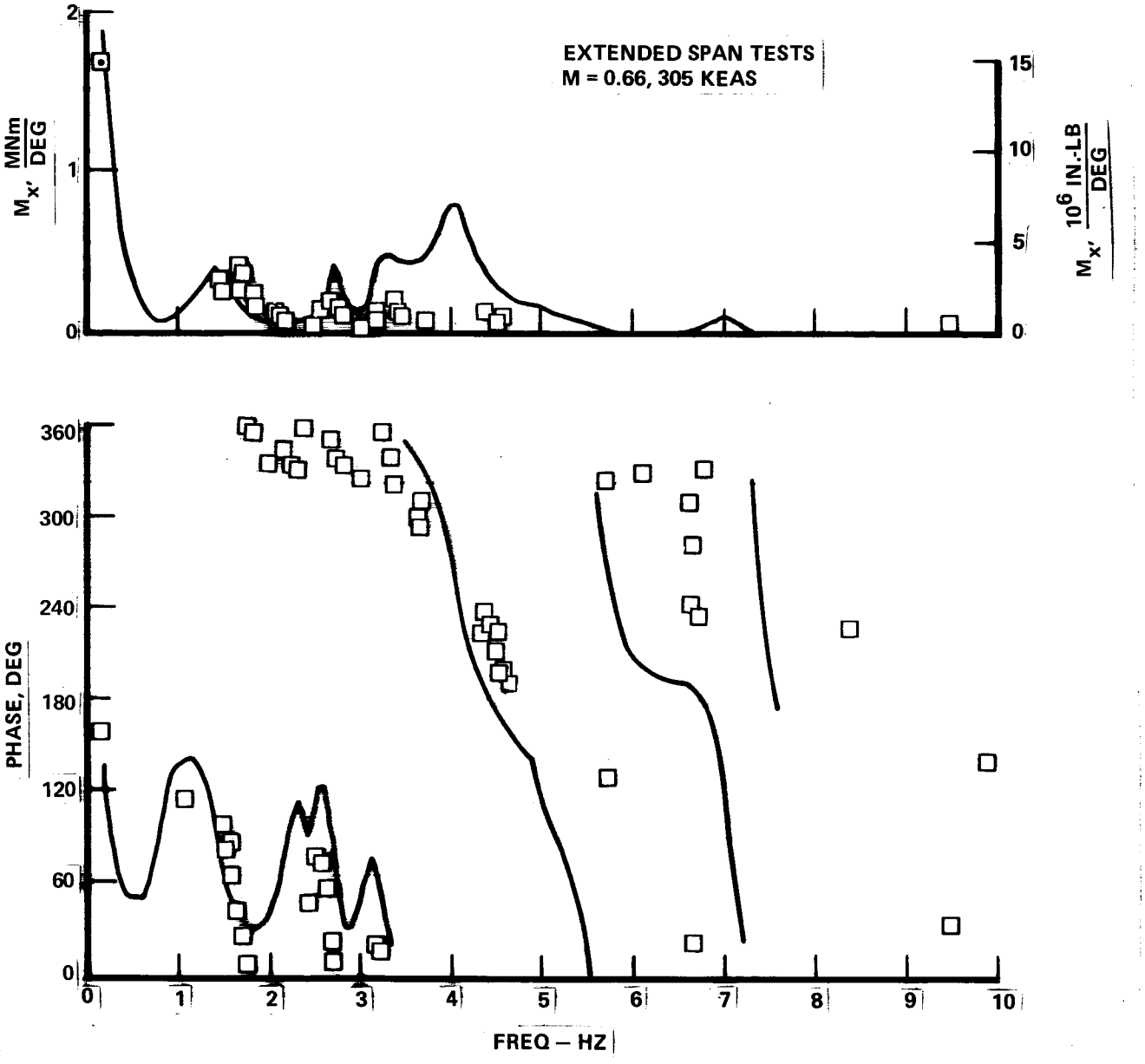

Figure 5-57. Test/Analysis, Bending at $\eta = .19$, Stabilizer Drive, Cruise

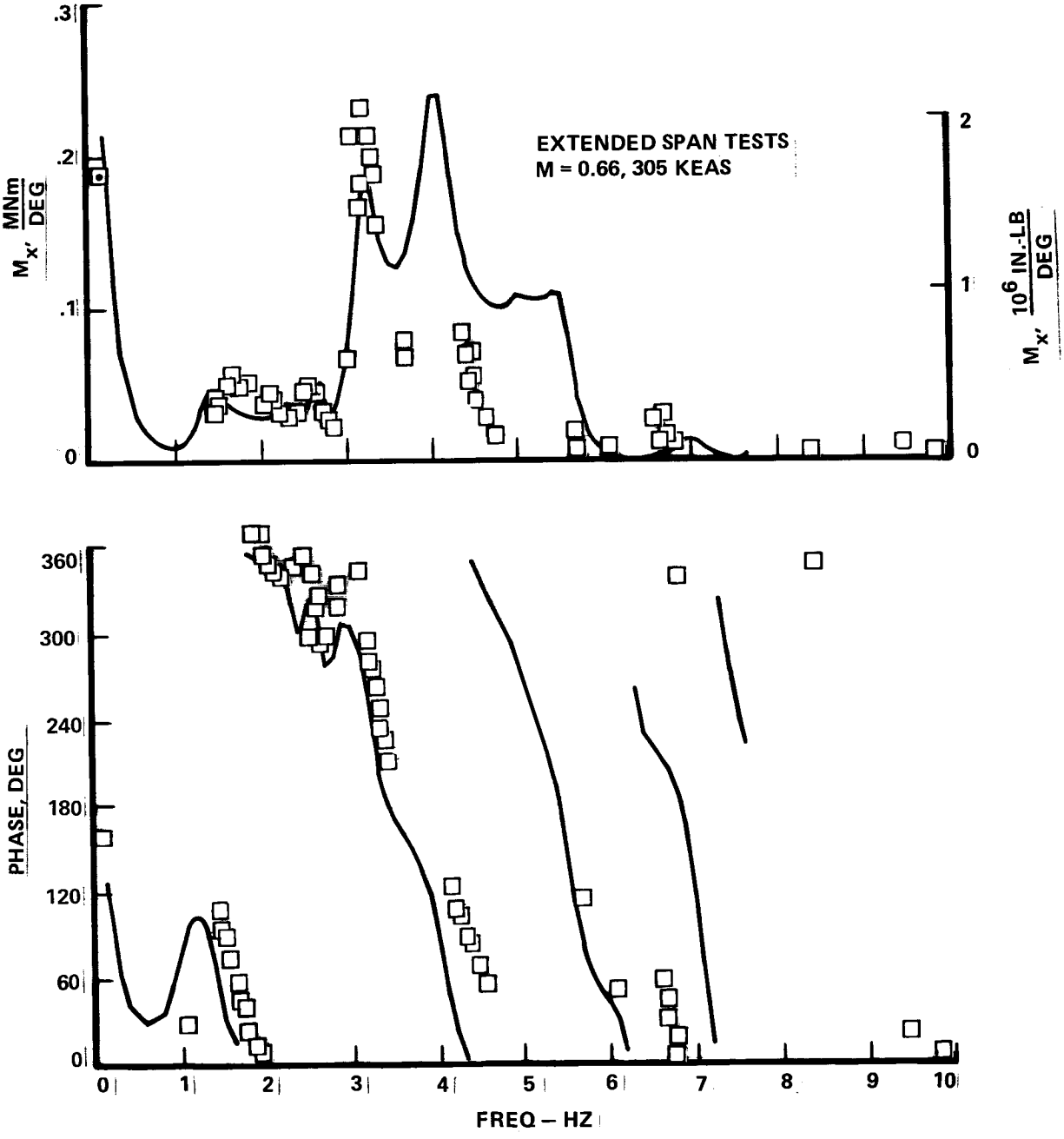

Figure 5-58. Test/Analysis, Bending at η = .71, Stabilizer Drive, Cruise

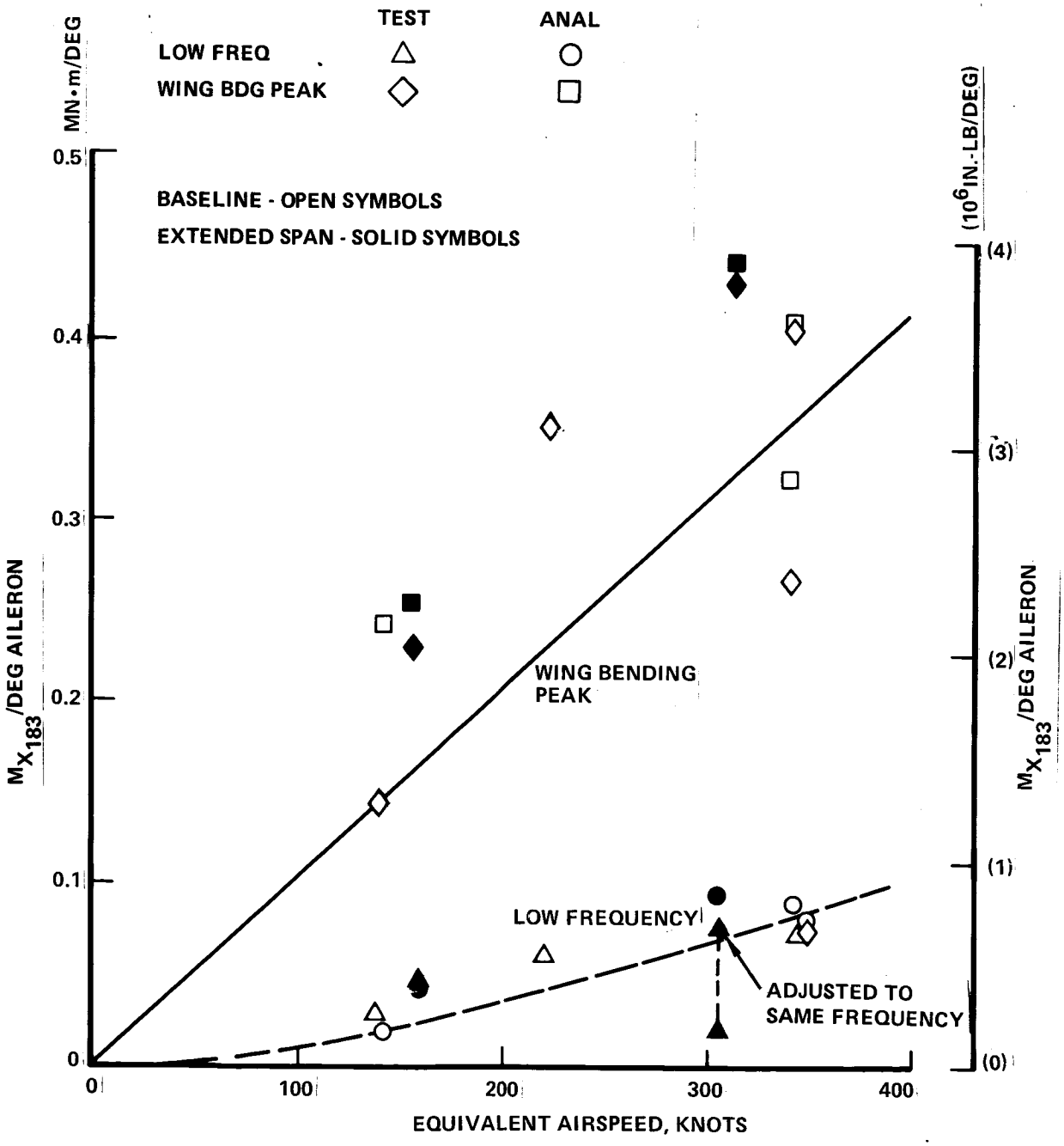

Figure 5-59. Wing Bending Moment per Degree Aileron Vs. Equivalent Airspeed, η = 0.20

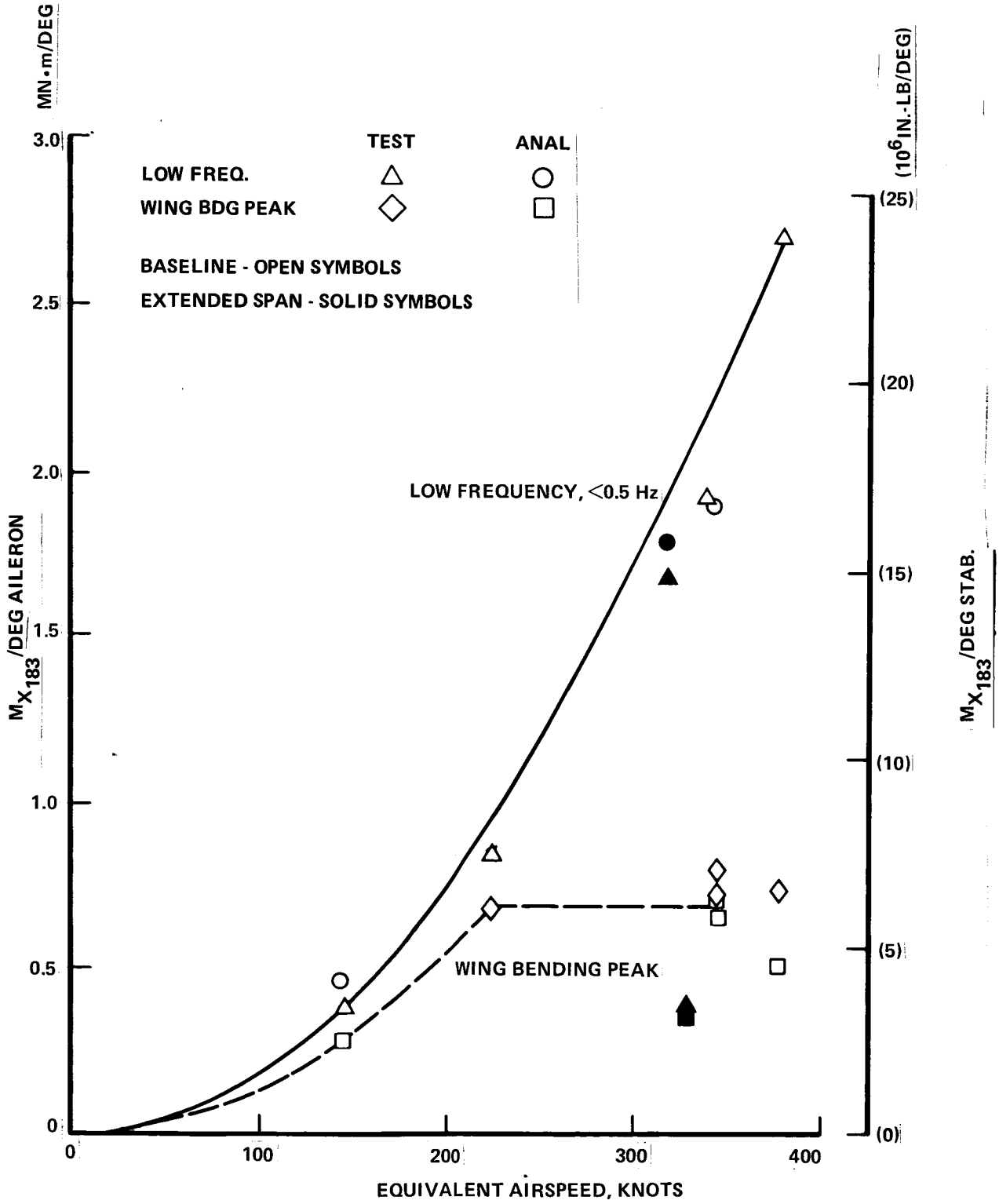

Figure 5-60. Wing Bending Moment per Degree Stabilizer Vs. Equivalent Airspeed, η = 0.20

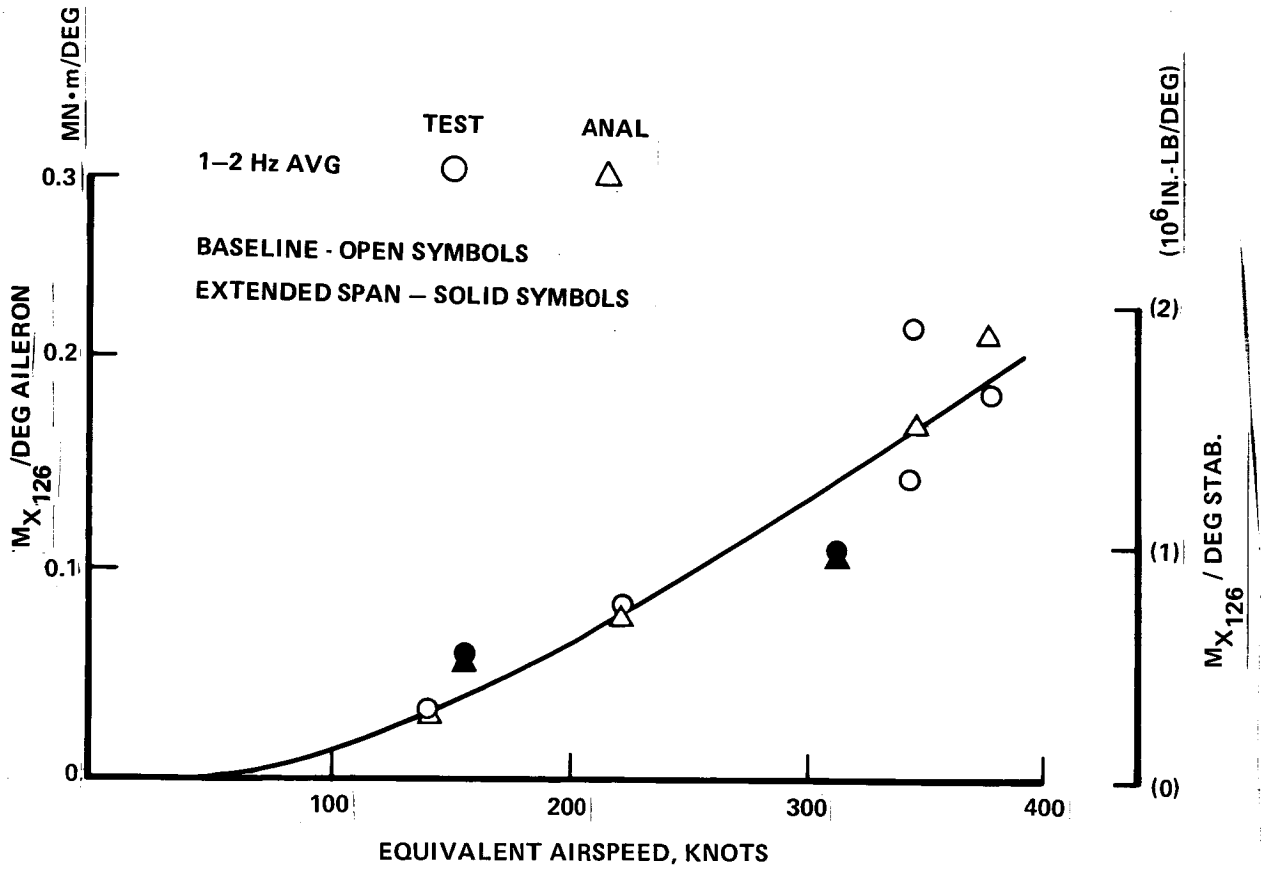

Figure 5-61. Stabilizer Bending Moment per Degree Stabilizer Vs. Equivalent Airspeed, η = 0.29

5.7 GUST LOADS

Gust loads flight tests were conducted in order to confirm that the active control system can produce the load reductions predicted by analysis.

The tests involved flying in continuous turbulence and measuring simultaneously the gust velocity and some 30 or more airplane responses - shears, bending moments, torsions, accelerations, etc. The data were processed on a power spectral basis.

5.7.1 Turbulence Samples and Flight Conditions

The tests were conducted for basically two flight conditions. The first was representative of cruise flight and consequently of conditions critical for limit design gust loads. The second was a flaps-extended condition representative of takeoff or landing approach. Such a condition is important for structural fatigue. For an airplane such as the L-1011, most of the fatigue damage is produced by the ground-air-ground cycle; the controlling flight loading occurs at low speed with flaps extended, because of the higher one-g level-flight loads.

The baseline tests were conducted on Aug. 11, 1977, in thunderstorm turbulence over Texas. Data were obtained only for the cruise condition.

Extended span tests were conducted first on October 14, 1978, in the lee of the Sierra crest in California, and on December 14 and 16, 1978, near mountain ridges in the Montana-Wyoming area. The October 14 tests involved only the cruise condition; inasmuch as the turbulence intensities were somewhat less than desired, no particular effort was made to secure stabilized flight conditions or to secure flaps-extended data. The turbulence for the December 14-16 tests was considerably more severe; cruise condition tests were conducted on December 14, and flaps-extended tests on December 16.

The particular turbulence samples for which data were processed are identified in Table 5-7, with pertinent flight condition data included. Each sample is identified by a burst number for later reference.* Also included in Table 5-7 are averages of pertinent bursts, weighted according to length of burst. A comparable but more extensive program of measuring loads in turbulence on the same L-1011 airplane was conducted by Lockheed in 1971. Burst 12e1 from that program is also included in Table 5-7 for reference.

*In earlier reporting, Burst 2a in the table was designated Burst 1c.

TABLE 5-7. TURBULENCE SAMPLES AND FLIGHT CONDITIONS

1	2	3	4	5	6	7	8	9	10	11	12	13	14	15	16
				Duration		Altitude					CG Δn, g's			RMS Gust Velocity	
Wing Span	Burst	ACS	Start Time	Sec	FFT Blocks	m	(ft)	V_E knots	V_T knots	M	Max Neg	Max Pus	RMS	m/s (fps)	Stationarity
Basic	1a	Off	1526:30	76.3	3	4850	(15,900)	343	451	.72	-.65	+.80	.196	2.39 (7.84)	Excellent
Basic	1b	Off	1548:57	153.6	6	5120	(16,800)	344	460	.71	-.75	+.70	.181	2.18 (7.16)	Excellent
Basic	1 aver.	Off		230.4	9			344	457	.71					
Basic	2a (1c)	On	1533:28	102.4	4	5150	(16,900)	344	462	.73	-.55	+.60	.180	2.12 (6.27)	Excellent
Basic	12e1	Off	-	290		1460	(4,800)	317	340	.53	-.40	+.40	.114	1.54 (5.06)	Excellent
Ext'd	3a	Off	1538:52	51.2	2	3470	(11,400)	336	410	.63	-.35	+.50	.125	1.88 (6.18)	Good
Ext'd	3d	Off	1542:40	25.6	1	2560	(8,400)	326	381	.58	-.20	+.30	.083	0.96 (3.16)	Good
Ext'd	3 aver.	Off		76.8	3	3170	(10,400)	333	400	.61				1.64 (5.37)	
Ext'd	4c	On	1559:58	51.2	2	2930	(9,600)	319	378	.57	-.35	+.40	.115*	1.57 (5.16)	Excellent
Ext'd	4g	On	1606:38	102.4	4	1800	(5,900)	318	358	.54	-.30	+.30	.097	1.26 (4.13)	Excellent
Ext'd	4 aver.	On		153.6	6	2160	(7,100)	318	365	.55				1.37 (4.50)	
Ext'd	5b	Off	1630:28	76.8	3	2440	(8,000)	313	352	.55	-.75	+.55	.154	2.21 (7.25)	Fair
Ext'd	5c	Off	1632:22	102.4	4	2410	(7,900)	313	353	.55	-.55	+.60	.155	1.69 (5.53)	Fairly Good
Ext'd	5 aver.	Off		179.2	7	2410	(7,900)	313	353	.55				1.93 (6.32)	
Ext'd	6a	On	1616:00	179.2	7	2380	(7,800)	316	354	.55	-.85	+.95	.179	2.69 (8.81)	Fairly Good
Ext'd	6b	On	1621:41	51.2	2	2410	(7,900)	321	365	.56	-.45	+.40	.188	1.89 (6.20)	Fairly Good
Ext'd	6 aver.	On		230.4	9	2380	(7,800)	317	355	.55				2.53 (8.30)	
Ext'd	9a	Off	1147:51	153.6	6	2010	(6,600)	161	176	.27	-.40	+.35	.110*	1.96 (6.42)	Good
Ext'd	9b	Off	1157:11	153.6	6	2190	(7,200)	161	177	.28	-.60	+.55	.120	2.60 (8.54)	Fair
Ext'd	9d	Off	1213:35	153.6	6	1950	(6,400)	159	173	.27	-.60	+.30	.100	2.02 (6.64)	Excellent
Ext'd	9 aver.	Off		460.8	18	2040	(6,700)	160	175	.27				2.21 (7.26)	
Ext'd	10a	On	1249:29	102.4	4	2530	(8,300)	155	175	.27	-.45	+.30	.106	1.74 (5.71)	Very Good
Ext'd	10b	On	1244:33	102.4	4	2470	(8,100)	158	177	.28	-.45	+.50	.151	2.71 (8.88)	Good
Ext'd	10c	On	1249:24	153.6	6	2530	(8,300)	161	180	.28	-.55	+.65	.158	2.70 (8.86)	Excellent
Ext'd	10d	On	1257:17	204.8	8	2590	(8,500)	156	176	.28	-.35	+.35	.056	1.36 (4.46)	Fairly Good
Ext'd	10 aver.	On		563.2	22	2560	(8,400)	158	177	.28				2.13 (6.99)	

*Instrument malfunction - value given inferred from other data

Note: Gross mass for all bursts was in the range 152,000 to 166,000 kg (335,000 to 365,000 lb). See Table 5-8 for actual masses.

Mass data are given separately in Table 5-8. Fuel tanks are all located in the wing. Approximate locations and capacities (per side) are:

Tanks 1 and 3	.12 to .41 semispan (baseline) 24550 kg (54,000 lb)
Tanks 2L and 2R inboard	.41 to .65 semispan (baseline) 7700 kg (17,000 lb)
Tanks 2L and 2R outboard	.65 to .93 semispan (baseline) 3930 kg (8,700 lb)

All tests were conducted with essentially no ballast or payload, although the operating empty weight for the flight test airplane is some 4000 kg (10,000 lb) above typical operating empty weights of airplanes in airline service. Over all of the tests, total weights of fuel stayed within a fairly narrow range, 33000 to 47000 kg (73,000 to 104,000 lb).

Experience and theory indicate that, to achieve desirable statistical reliability, a total of 200 seconds of data should be available separately for the controls-off and controls-on cases.

In the baseline tests (Bursts 1 and 2), it is seen that the controls-off samples total 230 seconds and the controls-on samples 102 seconds. The somewhat limited duration of the controls-on data should be borne in mind in drawing conclusions from the flight data.

The October 1978 extended span data (Bursts 3 and 4) also are of less than desirable duration, with only 77 seconds of controls-on data available. Fortunately these samples are augmented by the December 1978 data for essentially the same flight condition.

The December 1978 cruise condition samples (Bursts 5 and 6) approach or exceed the 200-second standard, with durations of 179 and 230 seconds respectively. Together with Bursts 3 and 4, the total duration of data controls-off is 256 seconds and, controls-on, 384 seconds. This should be more than adequate.

The flaps-extended samples (Bursts 9 and 10), at 461 and 563 seconds respectively, are far in excess of the 200-second standard.

In summary, for the baseline tests taken by themselves, the somewhat limited duration of the data requires that some care be taken in drawing conclusions. For the extended-span data and for the body of data as a whole, the duration is quite adequate.

TABLE 5-8. AIRPLANE MASS DATA

1	2	3	4	5	6	7	8	9
		Mass, (kg (lb))						
					Fuel per Side			
Wing Span	Burst	Gross Mass	Zero Fuel Mass	Fuel Mass	Tanks 1,3	Tanks 2L,2R Inboard	Tanks 2L,2R Outboard	CG % MAC
Basic	1a	156,000 (344,000)	119,000 (262,000)	37,250 (82,200)	12,660 (27,900)	2030 (4500)	3250 (8700)	23.4
Basic	1b	152,000 (336,000)	119,000 (262,000)	33,620 (74,100)	11,480 (25,300)	1380 (3000)	3950 (8700)	23.4
Basic	1 aver.							
Basic	2a (1c)	155,000 (341,000)	119,000 (262,000)	35,900 (79,100)	12,200 (26,900)	1780 (3900)	3950 (8700)	23.4
Basic	12el	152,000 (335,000)	119,000 (262,000)	33,300 (73,400)	11,070 (24,400)	1630 (3600)	3950 (8700)	18.0
Ext'd	3a	163,000 (360,000)	117,000 (259,000)	45,630 (100,600)	15,290 (33,700)	3670 (8100)	3860 (8500)	24.0
Ext'd	3d	163,000 (359,000)	117,000 (259,000)	45,180 (99,600)	15,150 (33,400)	3580 (7900)	3860 (8500)	24.0
Ext'd	3 aver.	163,000 (360,000)	117,000 (259,000)	45,500 (100,300)	15,240 (33,600)	3630 (8000)	3860 (8500)	24.0
Ext'd	4c	161,000 (354,000)	117,000 (259,000)	42,900 (94,600)	14,380 (31,700)	3220 (7100)	3860 (8500)	24.0
Ext'd	4g	160,000 (352,000)	117,000 (259,000)	42,000 (92,600)	14,060 (31,000)	3080 (6800)	3860 (8500)	24.0
Ext'd	4 aver.	160,000 (353,000)	117,000 (259,000)	42,270 (93,200)	14,150 (31,200)	3130 (6900)	3860 (8500)	24.0
Ext'd	5b	157,000 (346,000)	118,000 (260,000)	39,240 (86,500)	12,520 (27,600)	3220 (7100)	3860 (8500)	23.2
Ext'd	5c	157,000 (346,000)	118,000 (260,000)	38,870 (85,700)	12,380 (27,300)	3180 (7000)	3860 (8500)	23.2
Ext'd	5 aver.	157,000 (346,000)	118,000 (260,000)	39,000 (86,000)	12,430 (27,400)	3180 (7000)	3860 (8500)	23.2
Ext'd	6a	159,000 (351,000)	118,000 (260,000)	41,100 (90,600)	13,150 (29,000)	3540 (7800)	3860 (8500)	23.2
Ext'd	6b	158,000 (349,000)	118,000 (260,000)	40,460 (89,200)	12,970 (28,600)	3400 (7500)	3860 (8500)	23.2
Ext'd	6 aver.	159,000 (350,000)	118,000 (260,000)	40,960 (90,300)	13,110 (26,900)	3490 (7700)	3860 (8500)	23.2
Ext'd	9a	166,000 (365,000)	118,000 (260,000)	40,960 (104,300)	15,330 (33,800)	4450 (9800)	3860 (8500)	23.5
Ext'd	9b	164,000 (361,000)	118,000 (260,000)	45,860 (101,100)	14,830 (32,700)	4220 (9300)	3860 (8500)	23.5
Ext'd	9d	161,000 (355,000)	118,000 (260,000)	42,950 (94,700)	13,880 (30,600)	3760 (8300)	3860 (8500)	23.4
Ext'd	9 aver.	163,000 (360,000)	118,000 (260,000)	45,360 (100,000)	14,700 (32,400)	4130 (9100)	3860 (8500)	23.5
Ext'd	10a	157,000 (346,000)	118,000 (260,000)	39,280 (86,600)	12,610 (27,800)	3180 (7000)	3860 (8500)	23.4
Ext'd	10b	156,000 (345,000)	118,000 (260,000)	38,780 (85,500)	12,430 (27,400)	3080 (6800)	3860 (8500)	23.4
Ext'd	10c	156,000 (343,000)	118,000 (260,000)	37,500 (82,800)	12,110 (26,700)	2810 (6200)	3860 (8500)	23.4
Ext'd	10d	154,000 (340,000)	118,000 (260,000)	36,150 (79,700)	11,520 (25,400)	2680 (5900)	3860 (8500)	23.4
Ext'd	10 aver.	156,000 (343,000)	118,000 (260,000)	37,560 (82,800)	12,020 (26,500)	2860 (6300)	3860 (8500)	23.4

Experience also suggests that the turbulence encountered should be of at least moderate intensity and reasonably stationary (as judged by visual inspection of the time histories). The turbulence intensity is judged initially by the maximum incremental load factors recorded and, once psd's (power spectral densities) have been computed, by the rms (root-mean-square) gust velocity. RMS gust velocities shown in Table 5-7 were obtained as the square root of the area under the psd curve, with a lower limit of integration of 0.0391 Hz. (These can be converted to rms values corresponding to a Von Karman shape of gust psd with scale of turbulence L of 762 m (2500 ft) by multiplying by approximately 1.23 for V_T = 355 knots or 1.45 for V_T = 175 knots.) The data obtained are considered to be generally satisfactory from the standpoint of turbulence intensity although rms gust velocities below about 1.5 m/s (5 fps) might be considered marginal. The stationarity is somewhat variable from burst to burst, but is considered adequate in all cases for the data to be usable.

5.7.2 Quantities Measured

Table 5-9 lists the various response quantities for which measurements were made and data processed. These are in addition to the various quantities needed to determine the three components of gust velocity, which included gust probe pressures together with accelerations and angular rates at the gust boom.

Shears, bending moments, and torsions were measured with respect to arbitrary load axes, such as shown for the wing in Figure 5-13, page 5-20. The horizontal tail load axis is comparable. The fuselage load axis is a horizontal line on the airplane center line. For the wing and horizontal tail, subscripts indicate directions as follows: x and y axes are in a horizontal plane; the y axis is the projection of the load axis onto this plane, and the x axis is perpendicular thereto; the z axis is vertical. For the fuselage, the x axis is parallel to the fuselage reference line; the y and z axes are perpendicular thereto, with the z axis vertical and the y axis horizontal.

Locations of the various load measurements are also indicated on Figure 5-13. Locations on the wing and horizontal tail are defined by the intersection of the indicated butt line (BL) with the load axis.

Certain of the quantities listed in Table 5-9 were not available for particular bursts because of instrument or data system malfunction. L wing S_z at η = 0.29 was not available for Bursts 5 and 6. L wing M_x at η = 0.19 was not available for

TABLE 5-9. LIST OF LOADS AND OTHER RESPONSES MEASURED

	Baseline Tests	Extended Span Tests	Baseline and Extended Span Tests
L Wing S_z	η = .20	η = .19	n_z Fuselage (FS 123)
		η = .29	n_z Pilot Seat (FS 185)
	η = .38	η = .36	n_z ACS Body (FS 719)*
	η = .52	η = .49	n_z cg (FS 1216)
	η = .75	η = .71	n_z Aft Body (FS 1600)**
		η = .80	
		η = .85	
			L Wing Engine n_z
L Wing M_x	η = .20	η = .19	L Wing Engine n_y
	η = .31	η = .29	
	η = .52	η = .49	L Wing Tip n_z
		η = .61	R Wing Tip n_z
	η = .75	η = .71	Sym. Wing Tip n_z
		η = .80	
		η = .85	L Stabilizer Tip n_z*
			R Stabilizer Tip n_z*
L Wing M_y	η = .20	η = .19	Sym. Stabilizer Tip n_z*
		η = .29	
	η = .38	η = .36	$\dot{\theta}$ (Airplane Pitch Rate)
	η = .52	η = .49	
	η = .75	η = .71	L Aileron Deflection
		η = .80	R Aileron Deflection
		η = .85	Sym. Aileron Deflection
			Aileron Series Servo Command*
Fus S_z	FS 939	-	Horiz. Stab. Series Servo
	FS 1428		Command*
L HT S_z	η = .29	η = .29	
M_z	η = .29	η = .29	
M_x		η = .60	
M_x			
M_y	η = .29	η = .29	

*Extended-span tests only
**Extended span; baseline, FS 1535

Bursts 5, 6, 9, and 10; R wing M_x at $\eta = 0.19$ was substituted. Fuselage n_z at FS 719 (ACS accelerometer) was not available for Bursts 3 and 4 although operation of the ACS was not affected. Cg n_z was not available for Bursts 4 and 9a. R stabilizer tip n_z was not available for Bursts 3, 4, 6, and 10c. L wing M_y at $\eta = 0.19$ was not available for Bursts 5, 6, 9, and 10. In addition, the following were not available for Burst 9a only: L wing S_z at $\eta = 0.80$, HT S_z at $\eta = 0.29$, n_z pilot seat, and n_z at FS 719 (ACS accelerometer).

5.7.3 Flight Data Processing

Gust Velocity Time History Determination

Time histories of the three components of gust velocity were obtained by means of a differential pressure probe mounted ahead of the airplane nose (described in Section 2.5). Corrections were made for airplane motions utilizing the following measurements at the gust boom: n_z, θ, $\dot{\theta}$, n_y, ψ, $\dot{\psi}$, ϕ, $\dot{\phi}$, n_x. Accelerations were integrated to give velocities. In the baseline tests, only, angular rates were integrated to give angles, in preference to using the measured angles. Gust velocities as computed were in an earth-fixed, rather than an airplane, axis system.

Basic Processing of Flight Data

The basic processing of the flight data involved determination of power spectra and cross spectra, which were then used to determine transfer functions and coherencies.

Power spectral densities were obtained for each of the three components of gust velocity and each response quantity. Cross spectra were obtained relating each response quantity to the vertical component of gust velocity. Cross spectra were also obtained relating particular pairs of response quantities.

The power spectra and cross spectra were obtained using the Fast Fourier Transform technique.

Theory and previous flight testing have indicated that no response of significance occurs above 7.5 Hz. Consequently, a frequency range of 0 to 7.5 Hz was selected for the spectral calculations. (For the low speed tests, Bursts 9 and 10, the psd calculations were actually performed, and results plotted, only to 3.75 Hz.) With the frequency restricted to a maximum of 7.5 Hz, the sample rate of 40 samples per second at which the data were originally digitized could be reduced to 20 per

second for the spectral calculations. The resulting Nyquist frequency was 10 Hz. In order to prevent aliasing, the time histories as originally sampled at 40 samples per second were appropriately low-pass filtered. A Martin-Graham digital filter (Reference 14, NASA TR R-179) was used for this purpose, with "cutoff" and "termination" frequencies of 7.5 and 10 Hz respectively. By removing all frequency components above the Nyquist frequency of 10 Hz, aliasing was prevented, yet the contributions below 7.5 Hz were preserved.

The FFT (Fast Fourier Transform) technique involves dividing each burst into a number of time blocks, each consisting of L time points, where L must be a power of 2. The frequency spacing is related to L by the expression

$$\Delta f = \frac{1}{L\Delta t}$$

where Δt is the sample spacing, or the reciprocal of the sample rate, here 1/(20 per second) = 0.05 second.

A frequency spacing of about 0.05 Hz was considered the maximum acceptable to achieve adequate frequency resolution in these tests. For a sample rate of 20 samples per second (Δt = 0.05 sec.), available values of Δf in the vicinity of 0.05 Hz are:

L	Δf
256	0.078125 Hz
512	0.0390625 Hz

An increase in resolution (smaller value of Δf) results in a decrease in statistical reliability, which shows up most conspicuously as a lack of smoothness in the computed psd curves due to a random variation from frequency to frequency. Consequently the largest value of Δf that is acceptable from a resolution standpoint should be selected. The value 0.078125, associated with L = 256, was considered not to give adequate resolution of the static response peak at about 0.3 Hz; accordingly, the next larger value of L (512) was selected, giving Δf = 0.0390625 Hz.

With L = 512, the length of block is (512) (0.05) = 25.6 seconds. Bursts must then be defined so that the length of each is an integer multiple of 25.6 seconds - i.e., 25.6, 51.2, 76.8, 102.4, 128, 153.6,...seconds. The bursts defined in Table 5-7 are seen to satisfy this requirement. Inasmuch as the beginning and end of a turbulence patch is often not sharply defined in the test data, it was not

as difficult as might have been expected to adjust the burst lengths to these values.

After low-pass filtering, the linear trends were removed from the gust velocity time histories, and the means were removed from the various response time histories. All time histories were then prewhitened, by the usual procedure described in Appendix E of NASA TR R-199 (Reference 15). The resulting spectra were then post darkened so as to reflect the original non-prewhitened data. Prewhitening has been an accepted technique, for valid reasons, in obtaining psd's of gust velocity. It is not clear, however, whether it is actually beneficial in a program such as the present one, where the objective is to obtain airplane transfer functions. Fortunately, however, comparisons made using the L-1011 1971 data showed virtually no difference between psd's obtained with and without prewhitening. A similar indication is reported in NASA TN D-8288 (Reference 16).

The power spectrum and cross spectrum values given by the FFT computations were smoothed by the "Hanning" procedure - i.e.,

$$\phi_{i_{smoothed}} = \left[.25\phi_{i-1} + .5\phi_i + .25\phi_{i+1}\right]$$

Flight-Measured Transfer Functions and Coherencies

In comparing theoretical with measured airplane response characteristics, or the response characteristics with and without active controls, a basic measure of these characteristics is the frequency-response function. This is an especially appropriate measure when the design gust load determination is on a power-spectral basis and the flight data are obtained in continuous turbulence. The frequency-response function indicates, as a function of frequency, the relation between output and input in terms of the amplitude ratio (modulus) and phase angle, for a steady state sinusoidal input and output. In the gust response analysis, the gust velocity is the input; the many responses include accelerations, shears, bending moments, etc.

The frequency-response function is sometimes expressed alternately in terms of the real and imaginary parts of a complex quantity. This complex quantity represents a vector in a plane; the magnitude of this vector and its angle relative to the real axis define the modulus and phase angle respectively, of the frequency response function.

In this report, the term "transfer function" is used, for convenience, interchangeably with "frequency-response" function.*

Two methods are in common use for determining the transfer function relating two quantities, one considered the input (x) and one the output (y), from time histories of these quantities measured during flight through continuous turbulence.

The first is the "spectrum method" designated as "Option 1" in the computer programs used to process the L-1011 flight data. It computes the modulus of the transfer function from the expression

$$\left|H_s\right| = \sqrt{\frac{\phi_y}{\phi_x}} \tag{1}$$

where ϕ_y and ϕ_x are the psd's of output and input, respectively. Using this method, only the modulus is obtained.

The second is the "cross spectrum method," designated as "Option 2" in the L-1011 computer programs. In this method, the transfer function is computed as

$$H_c = \frac{\phi_{xy}}{\phi_x} \tag{2}$$

where ϕ_{xy} is the cross spectrum between input and output and ϕ_x is the psd of the input.

Inasmuch as the cross spectrum, ϕ_{xy}, is a complex quantity, the phase angle as well as the modulus is given. In addition, the cross spectrum method provides a transfer function that reflects only that part of the output that is linearly related to the input. It thus eliminates the contaminating effects of other sources of loading, such as pilot activity and the other components of gust velocity, and of noise in the output instrumentation.

*Actually "frequency-response function" is the more precise term in the present application. As noted, it expresses a relation between steady state input and output. On the other hand, the transfer function is an output-input ratio that arises in the operational or Laplace transform solution of transient response. However, the mathematical expressions for the two functions are essentially identical, the frequency-response function being obtained by substituting $i\omega$ for s in the mathematical expression for the transfer function. Consequently, the distinction is largely academic.

The expression,

$$\gamma^2 = \frac{|\phi_{xy}|^2}{\phi_x \phi_y} \tag{3}$$

defines the coherency function (of frequency), γ^2, or simply coherency. This is a measure of the degree to which the x and y quantities are linearly related. If the two quantities are in perfect linear relation, $\gamma^2 = 1$ for all frequencies. If they are linearly independent, or incoherent, $\gamma^2 = 0$. It can be shown readily from expressions (1), (2), and (3) that

$$\gamma^2 = \frac{|H_c|^2}{|H_s|^2} \tag{4}$$

Thus if $\gamma^2 = 1$, the spectrum and cross spectrum transfer functions are identical.

A useful related concept is that an output psd, ϕ_y, can be considered to be the sum of several parts, each coherent with a different independent input. The psd of that part of the output, y, coherent with a given input, x, is given by

$$\gamma^2 \phi_y$$

where γ^2 in this case is the coherency between x and y. Further, if all of the inputs are independent, the various parts of ϕ_y must add to give the total,

$$\gamma_1^2 \phi_y + \gamma_2^2 \phi_y + \ldots = \phi_y$$

where the subscripts 1, 2, ... denote the various inputs. From this expression it follows that

$$\gamma_1^2 + \gamma_2^2 + \ldots = 1$$

For the reasons indicated earlier, the cross-spectrum method might be considered the preferred method for obtaining experimental transfer functions for airplane loads in turbulence. In particular, this method would appear ideal to evaluate the mathematical modeling of the airplane as a dynamic system, inasmuch as it considers only that part of the output induced by a measured input.

On the other hand, one may also wish to determine from the test data whether a given response is in fact significantly affected by inputs not accounted for explicitly in the criteria. In such a situation, the spectrum method transfer function provides a useful tool.

Furthermore, even in evaluating the mathematical modeling, the cross-spectrum method transfer function must be used with caution. Gust load measurements almost invariably result in coherencies that are fairly close to unity over a frequency range from perhaps 0.25 to 1.50 Hz, then drop off rapidly with increasing frequency, and remain virtually zero above perhaps 5 or 6 Hz. The primary cause of this dropoff appears to be the variation of gust velocity across the wing span at the higher frequencies or shorter wavelengths. At these shorter wavelengths, the gust velocities at the various spanwise locations are no longer coherent with the gust velocity on the centerline, where the gust-measuring probe is located. Consequently, the loads produced are no longer coherent with the centerline gust velocity. Accordingly, the cross-spectrum transfer function is small. But the turbulence is still there, everywhere across the wing; and the loads it produces are still comparable in magnitude to those that would be produced by a gust velocity uniform across the span. For example, if engine loads were produced solely by the gusts striking the engines, these loads would be identical regardless of spanwise variation of gust velocity, even if the gust velocities at the engines and at the centerline were completely incoherent. If design loads were to be established by means of measured transfer functions, use of the cross spectrum transfer function clearly would result in loads that are unrealistically low.

With theoretical transfer functions available only from the traditional one-dimensional gust analysis, there seems to be no satisfactory way to resolve this dilemma. At the higher frequencies, one probably should expect the one-D theory to agree more closely with the spectrum method transfer function than with the cross spectrum method transfer function. But the spectrum method transfer function is bound to be too high by some unknown amount, because of the effect of other inputs such as lateral gust.

Fortunately, this dilemma has been largely resolved, for analysis of the extended-span data, by availability of a three-dimensional gust analysis computer program, as noted in Section 4.2. (The term "three-dimensional," or "3-D," in this context refers to the number of position coordinates upon which the gust velocity is assumed to depend.) This program was developed utilizing the basic

formulations presented by Eichenbaum in Reference 17. One of its outputs is a theoretical "cross transfer function," which corresponds closely to the measured cross-spectrum-method transfer function, or cross transfer function. Like the measured cross transfer function, the theoretical cross transfer function reflects only that part of the output that is linearly related to the input — here the vertical gust velocity at the probe. In particular, the theory accounts rationally for both the spanwise variation of the gust velocity and the particular location of the probe.* Accordingly, the measured and theoretical cross transfer functions are directly comparable. The value of the measured cross transfer function is thus greatly enhanced.**

The spectrum-method transfer function is still of value, however, in calling attention to the possible effect of other inputs. Accordingly, in the present study, both cross-spectrum method and spectrum method transfer functions were obtained, for the extended span data as well as the baseline data.

5.7.4 Theoretical Analysis

Theoretical transfer functions for comparison with the flight-measured transfer functions were computed using the GLP series of gust-loads computer programs, described in Section 4.2.

---

*In applying the 3-D theory to the flight test data, it is necessary to assume that the gust velocities at all spanwise locations have the same psd, even though their mutual coherencies might be relatively low, and to assume further that these coherencies are consistent with a standard gust psd shape. These assumptions, however, should be fairly realistic as applied to a reasonable turbulence sample.

**A potential limitation of any approach utilizing comparisons of measured with theoretical cross transfer functions should be noted. As mentioned earlier, a situation may exist in which, as a result of the spanwise variation of gust velocity, the coherency between a given response and the gust velocity at the probe approaches zero. The cross transfer functions - both measured and theoretical - will then also approach zero, even though the response itself may be substantial. Comparison of these two essentially zero transfer functions will, then, tell nothing about the validity of the theoretical loads. On the other hand, it may be possible to develop a procedure in which the measured response psd's can be compared with theoretical psd's computed using 3-D theory with the measured vertical and lateral gust psd's as inputs. Such a procedure was not available for use in the present program, nor would it necessarily have provided a more valid evaluation of the effect of the active control system.

In addition to the adjustments to the aerodynamic influence coefficients mentioned in Section 4.2, aerodynamic forces due to outboard aileron angle were multiplied by the following factors:

Baseline tests:	1.00
Extended-span tests, cruise speed	1.07
Extended-span tests, flaps extended	1.11

The factors for the extended-span tests reflect the increased aileron effectiveness shown by the one-g trimmed flight data discussed in Section 5.4.2.

The active control system was represented generally as indicated in Sections 2.3.4 and 2.3.5.

As discussed in those sections, the control laws differed somewhat between the baseline and extended-span tests. In addition, a change was made between Bursts 4 and 6 of the extended-span tests in the control law governing feedback to the ailerons. (All of the extended-span gust response testing was conducted with the digital ACS computer.)

The control system transfer functions used in the gust response analysis for each test condition are plotted in Figures 5-62 - 5-64. For Burst 2 (baseline tests), the aileron gains (Figure 5-62) include an increase of 14 percent over that defined in Section 2.3.5, to reflect VSS test results; the airplane test data, however, showed aileron gains to be equal to or less than the specification values. For the extended-span tests, the analysis used essentially the specification values in all cases.

The only significant transfer function differences from test to test, from the standpoint of their effect on gust response, are seen to be the following:

(a) At the first wing bending natural frequency of about 1.5 Hz, the aileron gains for feedback from the wing tip accelerometer (Figure 5-62) are substantially lower for the extended-span tests (Bursts 4, 6) than for the baseline tests (Burst 2). This difference tends to be offset by the larger aileron in the extended-span tests.

(b) In the extended span tests, the GLA system was modified by deleting the cg acceleration feedback to the horizontal stabilizer and increasing, by a factor of more than 5, the $\dot{\theta}$ (pitch rate) feedback. With respect to overall horizontal tail activity, the increase in $\dot{\theta}$ feedback far more than makes up for the deletion of the acceleration feedback.

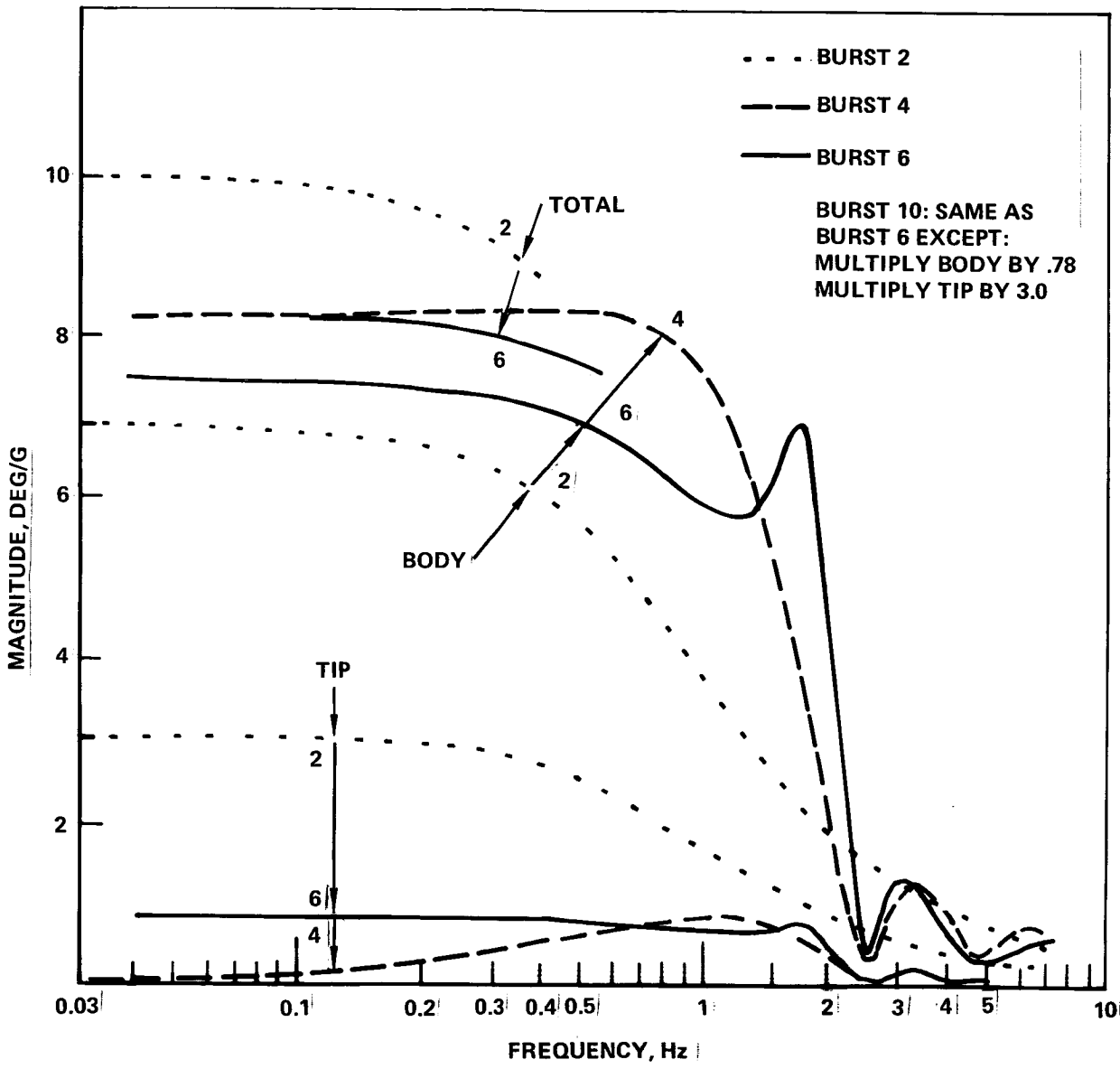

Figure 5-62. Active Control System Transfer Function - Aileron - Magnitude

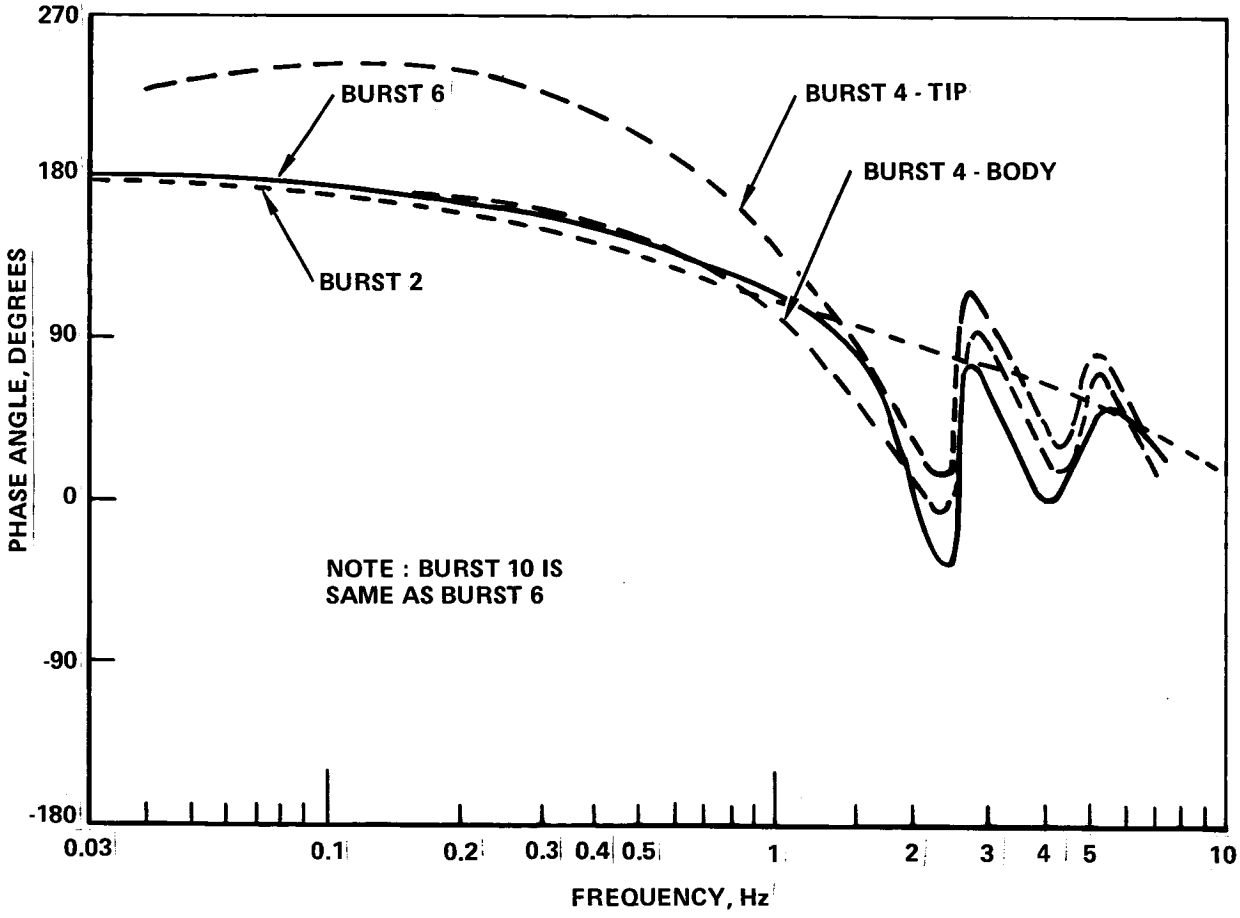

Figure 5-63. Active Control System Transfer Function - Aileron - Phase Angle

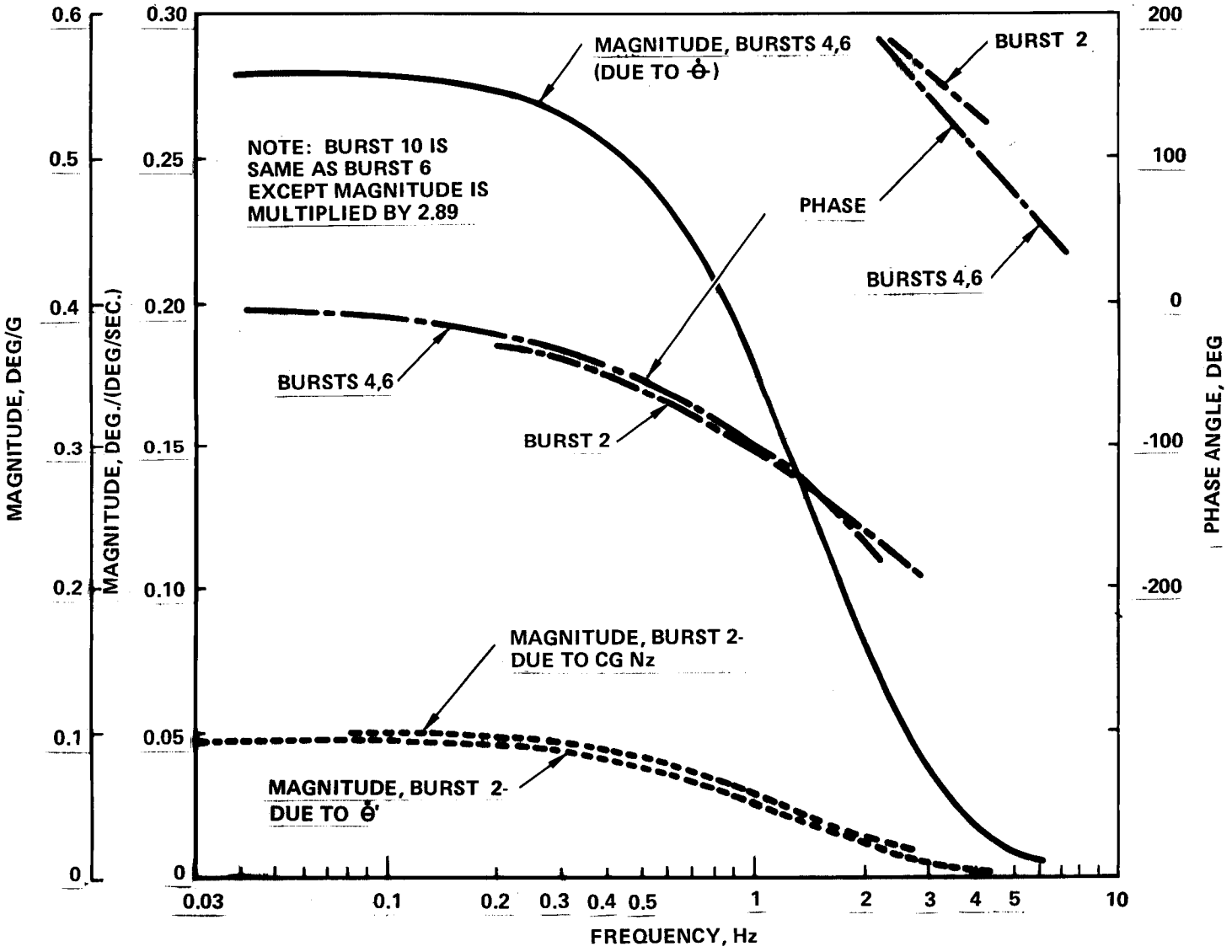

Figure 5-64. Active Control System Transfer Function - Horizontal Stabilizer

For the baseline tests, analyses were made separately for Bursts 1a, 1b, and 2a. Theoretical transfer functions for the average of Bursts 1a and 1b were obtained by averaging the transfer functions obtained for each burst, weighting by length of burst.

For the extended-span tests, analyses were made only for the "average" flight conditions indicated in Table 5-7 - that is, "3 aver," "4 aver," "5 aver," etc., using appropriately averaged input data.

5.7.5 Merge-and-Plot Computer Program

To assist in evaluating the effect of the active control system on gust loads, an extensive set of plots and tabulations was obtained.

In order to superimpose measured and theoretical data on the same computer-prepared plots, a merge-and-plot computer program, previously prepared for this purpose, was used. In this program the pertinent flight-measured and theoretical data are first merged onto a single magnetic tape. The data utilized are the flight-measured and theoretical transfer functions and the flight-measured coherencies. Response psd's corresponding to the respective transfer functions are then computed by squaring the modulus of the transfer function and multiplying by the Von Karman gust psd. For this purpose, the Von Karman psd, with frequency argument in radians per foot, is first converted to a frequency argument in cycles per second; this conversion depends upon the true airspeed for the particular burst. The psd's thus obtained are then integrated to give values of $\bar{A}$ and N_o, which are printed out in tabular form. All of these operations are performed separately for transfer functions given by the cross-spectrum method, the spectrum method, and "one-dimensional" theory. The measured coherency functions are also plotted. In addition, the program was expanded (under independent research funding) prior to its use with the extended-span data to utilize also cross transfer functions given by three-dimensional theory. Provision was also made to superimpose on the coherency plots a theoretical coherency given by the three-dimensional analysis.

The merge-and-plot program also makes provision for averaging the flight-measured transfer functions and coherencies for up to four separate bursts. This capability not only minimizes the number of plots to be made, examined, and stored; it also vastly simplifies studying the data to draw conclusions, and it smooths out

the irregularities in the flight data plots which are inherent in the statistical nature of the data. The flight-measured transfer functions are averaged by converting modulus and phase to real and imaginary parts, averaging, and reconverting to modulus and phase. This approach avoids, for example, averaging phase angles of +177 degrees and -179 degrees and getting -1 degree, where obviously the correct average is +179 degrees. Average coherencies are obtained by recomputing from the averaged transfer functions, using equation 4. Any desired weighting factors can be used. In the present work, weighting was according to the duration of the bursts. A single average theoretical transfer function and a single average theoretical coherency function are input to the program in each case. These were obtained as described in the preceding section; they are consistent with the flight-data averages computed in the merge-and-plot program.

Use of the averaging procedure requires, of course, that variations in flight condition (speed, altitude, weight) over the bursts which it is desired to average be relatively small. It is evident from Tables 5-7 and 5-8 that this requirement is met wherever averages were taken.

5.7.6 Data Presentation

Samples of the plots obtained are shown in Figures 5-65 through 5-74. Inasmuch as these are samples of computer outputs, they retain the customary system of units in which the computations were performed. Figures 5-65 through 5-67 resulted from the basic test-data psd computations. The samples shown are taken from Bursts 3a and 5c; similar plots were obtained for all 18 bursts. Figures 5-68 through 5-74 were produced by the merge-and-plot program. The samples shown are for the average of Bursts 3a and 3d and Bursts 5b and 5c; similar plots were obtained for all eight of the "average" bursts listed in Table 5-7 (1a and 1b, 2a, 3a and 3d, etc.) and also for Bursts 1a and 1b separately. All of the plots except the gust velocity psd's are associated with particular response quantities. The samples shown are for wing bending moment at 0.29 semispan. Similar plots were obtained for each of the quantities listed in Table 5-9 - 31 quantities for the baseline tests and 45 for the extended-span tests. A total of 4018 plots was obtained.

Gust Velocity PSD's

A sample gust velocity PSD is shown in Figure 5-65. Both vertical and horizontal scales are logarithmic. The horizontal scale is a spatial frequency in

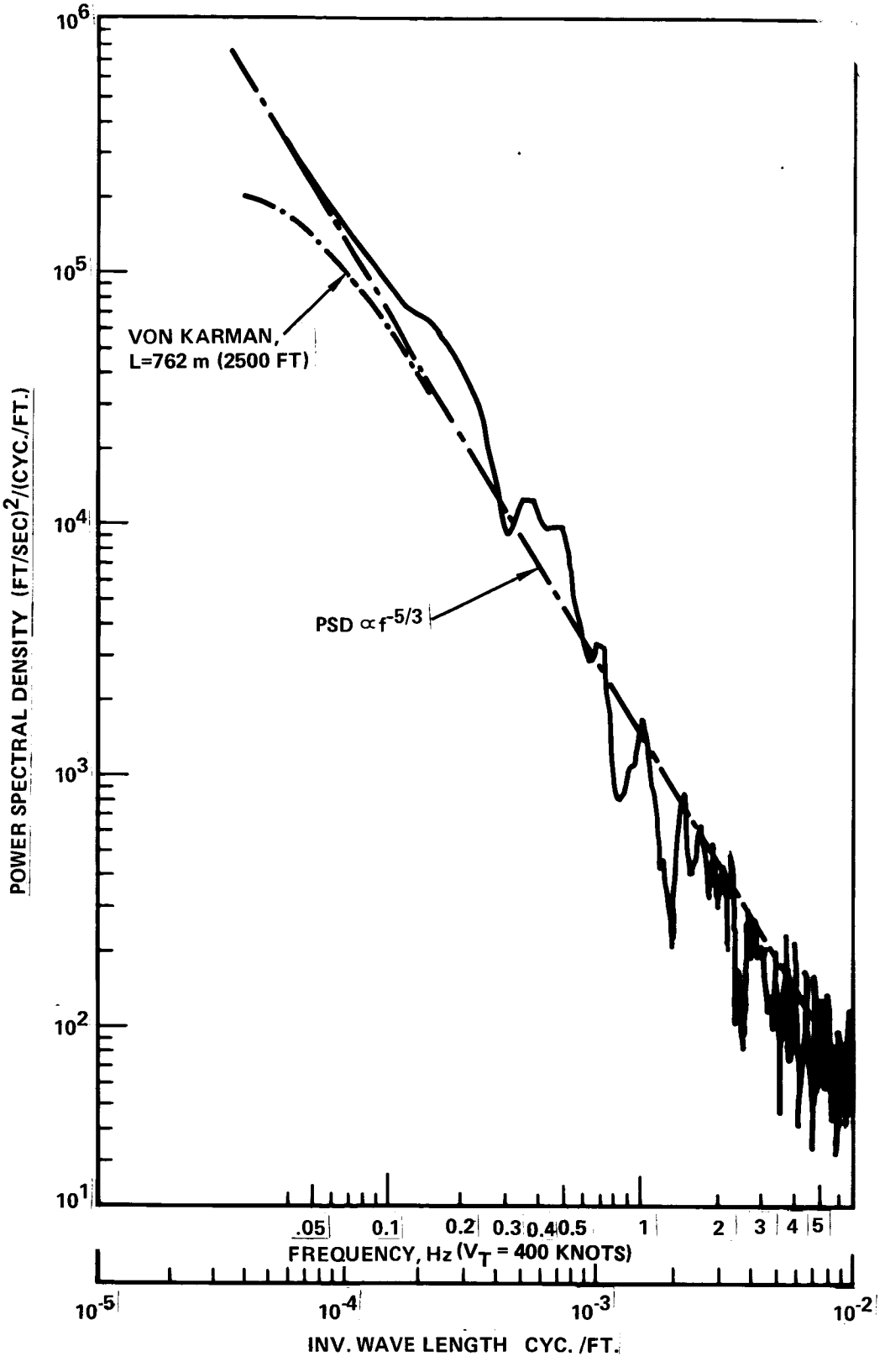

Figure 5-65. Gust Velocity PSD, Burst 3A (Computer Output)

cycles per foot. A frequency scale in cycles per second (Hz) has been added corresponding to a true airspeed representative of this burst (460 knots). The curve is seen to follow closely the -5/3 trend characteristic of the Von Karman spectrum used for design.

Response PSD's

A sample response psd is shown in Figure 5-66. The vertical scale is logarithmic, but the frequency scale is linear, as in all the remaining plots. This psd is of wing bending moment at 0.29 semispan, for Burst 3a. The airplane longitudinal short-period peak is evident at about 0.25 Hz and the wing bending peak at about 1.6 Hz. An additional elastic mode is indicated at about 4.2 Hz.

A second sample is shown in Figure 5-67. This, too, is of wing bending moment at 0.29 semispan. It is for a very similar flight condition, Burst 5c. Figure 5-67 is similar to Figure 5-66 except for the presence of the narrow spike below about 0.15 Hz. Such a spike is not unusual, and indeed an incipient spike can be seen in the previous Figure. Such a spike apparently reflects pilot maneuver inputs, either in roll or in pitch. The spike in Figure 5-67 is so substantial as to partially obscure the short-period peak.

The measured psd's are used, first, to give an early indication of the reasonableness of the data and, second, as a first step in the computation of transfer functions. (For the purpose of reasonableness checks early plots were also obtained of coherencies and transfer functions.)

The measured psd's were also routinely integrated to give rms (root-mean-square) values. (The rms value of the variable is equal to the square root of the area under the psd curve.) Rms values were obtained separately for four different lower limits of integration — 0.0390625 Hz and frequencies corresponding to gust wavelengths of 1220, 610, and 305 meters (4000, 2000, and 1000 ft). Rms values for representative wing bending moments based on the 0.0390625 Hz lower limit, are listed for each burst in Table 5-10. Rms values of gust velocity, obtained similarly, are also shown; these are the same as listed in Table 5-7.

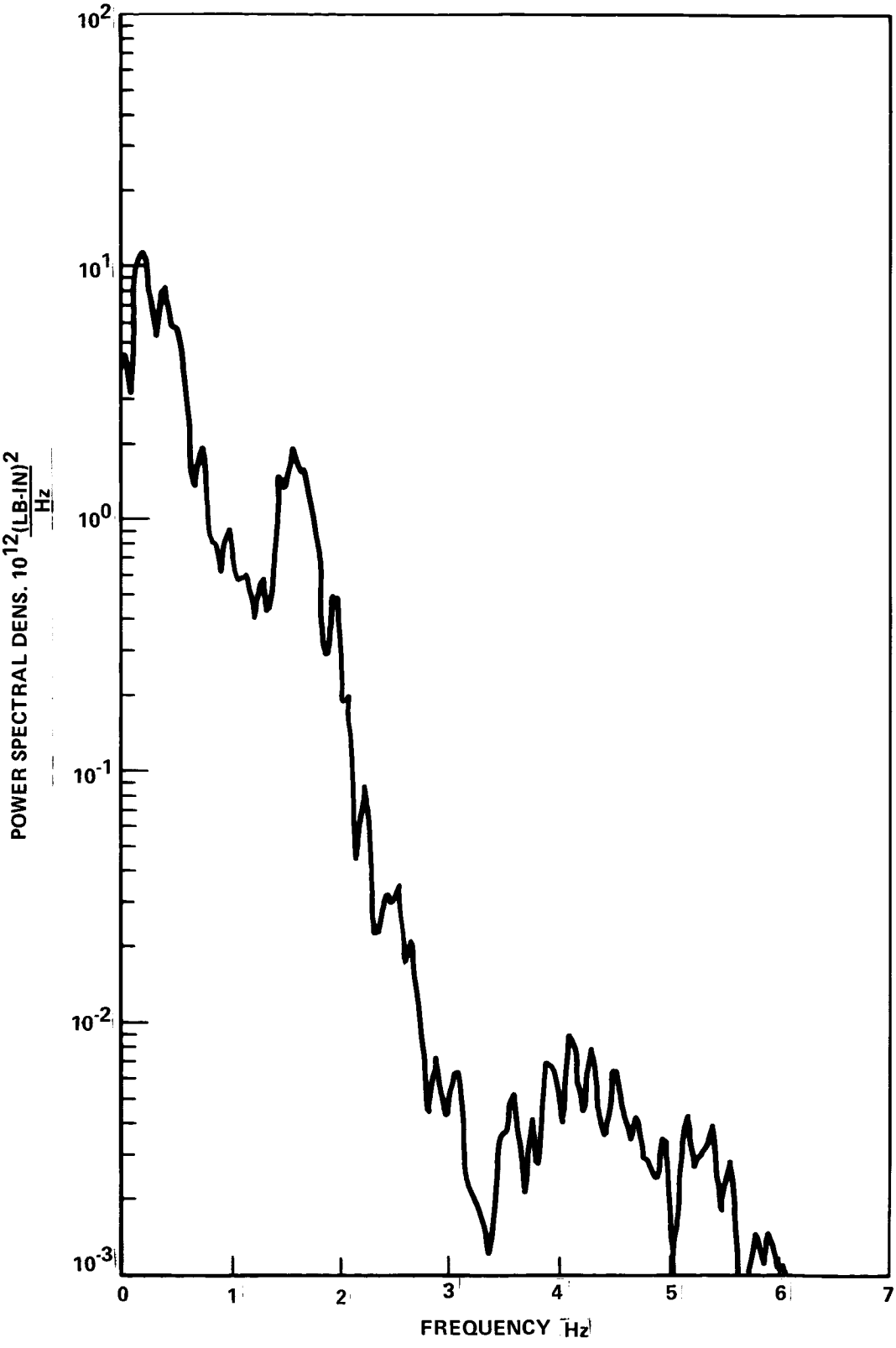

Figure 5-66. PSD Wing Bending at η = .29, Burst 3A (Computer Output)

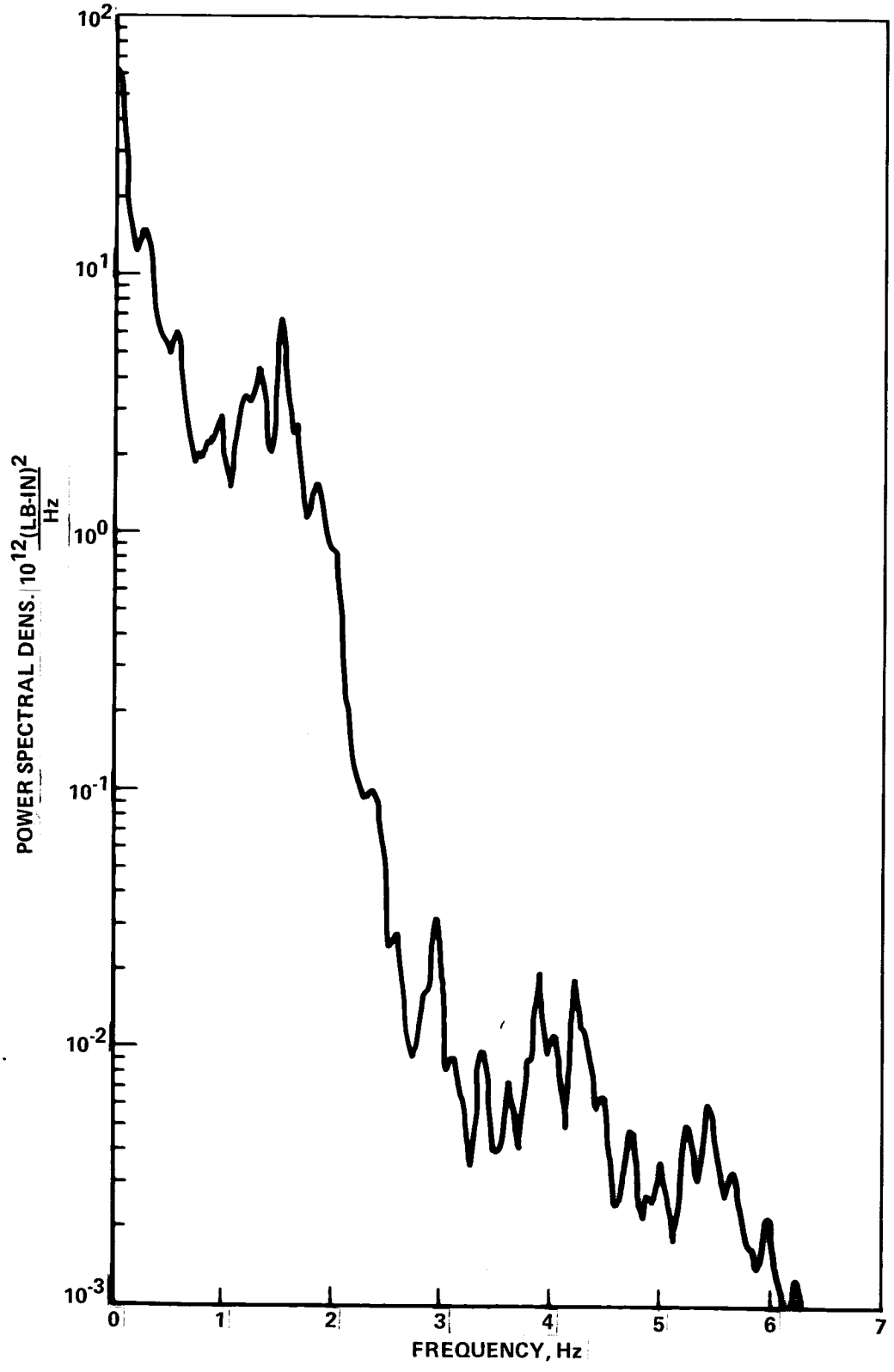

Figure 5-67. PSD Wing Bending at η = .29, Burst 5C (Computer Output)

TABLE 5-10. RMS VALUES OF MEASURED WING BENDING MOVEMENTS

1	2	3	4	5	6	7	8	9	10
Wing Span	Burst	ACS	RMS Gust Velocity	RMS Wing Bending Movement, MN·m (10^6 in. lb)					
			M/S (fps)	η = .19	η = .29	η = .49	η = .71	η = .80	η = .85
Basic	1a	Off	2.39 (7.84)	.712 (6.30)	.366 (3.24)	.289 (2.56)	.0516 (.457)		
Basic	1b	Off	2.18 (7.16)	.451 (3.99)	.365 (3.23)	.168 (1.49)	.0537 (.475)		
Basic	2a	On	2.12 (6.27)	.333 (2.95)	.258 (2.28)	.106 (.940)	.0433 (.383)		
Ext'd	3a	Off	1.88 (6.18)	.331 (2.93)	.262 (2.32)	.117 (1.04)	.0324 (.287)	.0152 (.135)	.0075 (.066)
Ext'd	3d	Off	0.96 (3.16)	.209 (1.85)	.172 (1.52)	.0811 (.718)	.0229 (.203)	.0107 (.095)	.0053 (.047)
Ext'd	4c	On	1.57 (5.16)	.277 (2.45)	.211 (1.87)	.0871 (.771)	.0191 (.169)	.0088 (.078)	.0044 (.039)
Ext'd	4g	On	1.26 (4.13)	.223 (1.97)	.176 (1.56)	.0696 (.616)	.0172 (.152)	.0086 (.076)	.0047 (.042)
Ext'd	5b	Off	2.21 (7.25)	.590 (5.22)	.447 (3.96)	.249 (2.20)	.0803 (.711)	.0329 (.291)	.0167 (.148)
Ext'd	5c	Off	1.69 (5.53)	.502 (4.44)	.375 (3.32)	.184 (1.63	.0663 (.587)	.0327 (.289)	.0172 (.152)
Ext'd	6a	On	2.69 (8.81)	.441 (3.90)	.355 (3.14)	.165 (1.46)	.0566 (.501)	.0297 (.263)	.0152 (.135)
Ext'd	6b	On	1.89 (6.20)	.494 (4.37)	.362 (3.20)	.147 (1.30)	.0533 (.472)	.0298 (.264)	.0156 (.138)
Ext'd	9a	Off	1.96 (6.42)	.374 (3.31)	.271 (2.40)	.139 (1.23)	.0473 (.419)	.0216 (.191)	.0123 (.109)
Ext'd	9b	Off	2.60 (8.54)	.588 (5.20)	.391 (3.46)	.197 (1.74)	.0670 (.593)	.0304 (.269)	.0178 (.158)
Ext'd	9d	Off	2.02 (6.64)	.357 (3.16)	.249 (2.20)	.128 (1.13)	.0442 (.391)	.0203 (.180)	.0117 (.104)
Ext'd	10a	On	1.74 (5.71)	.351 (3.11)	.236 (2.09)	.114 (1.01)	.0407 (.361)	.0191 (.169)	.0112 (.0992)
Ext'd	10b	On	2.71 (8.88)	.451 (3.99)	.313 (2.77)	.151 (1.34)	.0541 (.479)	.0259 (.229)	.0152 (.135)
Ext'd	10c	On	2.70 (8.86)	.511 (4.52)	.333 (2.95)	.157 (1.39)	.0530 (.469)	.0238 (.211)	.0147 (.130)
Ext'd	10d	On	1.36 (4.46)	.255 (2.26)	.170 (1.50)	.0854 (.756)	.0311 (.275)	.0149 (.132)	.0087 (.077)

Note: η values in column headings are for extended span airplane. For baseline airplane (Bursts 1a, 1b, 2a), values are .20, .31, .52, and .75 respectively.

Transfer Function Modulus

The transfer function modulus for the same quantity is shown in Figure 5-68. This figure is a merge-and-plot output and shows both measured and theoretical data, for the average of Bursts 3a and 3d.

The spectrum method and cross spectrum test curves are shown by the two solid lines. The spectrum method curve is always the higher of the two.

The two theoretical curves are indicated by the short-dash and dotted lines. The short-dash line is given by the traditional one-D (one-dimensional) theory. The dotted line is the theoretical cross transfer function given by the 3-D theory.

The agreement in trend between the theoretical cross-transfer function curve (dotted line) and the test cross-spectrum-method curve is excellent up to about 3 Hz and fairly good at least to 5 1/2 Hz. In magnitude, in the important range from 0.3 to 1.5 Hz, the test curve is seen to be consistently lower than the theoretical curve by some 10 to 20 percent. Also, the measured first bending mode resonance, although not precisely defined, seems to occur at a slightly higher frequency than the theoretical resonance at 1.5 Hz. This frequency difference agrees with that observed in the transfer function tests described in Section 5.6.2 (Figure 5-54).

PSD Given by Design Gust PSD Times Square of Modulus of Transfer Function

In comparing loads obtained in flight with and without the active control system in operation, it is necessary to account for the fact that the gust inputs - in particular the gust psd's - will be different for the various bursts. To compare response psd's controls-on and controls-off, the flight measured psd's must, in effect, be adjusted to a common gust input psd. This adjustment is made by taking as a standard the Von Karman gust psd with an appropriate scale of turbulence - ordinarily the usual design value of 762 m (2500 ft) - and multiplying this gust psd by the square of the transfer function modulus. Comparison of measured with theoretical response psd's is accomplished in the same way.

Psd's obtained in this way are shown in Figure 5-69. Again the two test curves are distinguished by the fact that the cross spectrum method curve is always the lower of the two. Both scales are linear, so that the areas under the respective curves are undistorted.

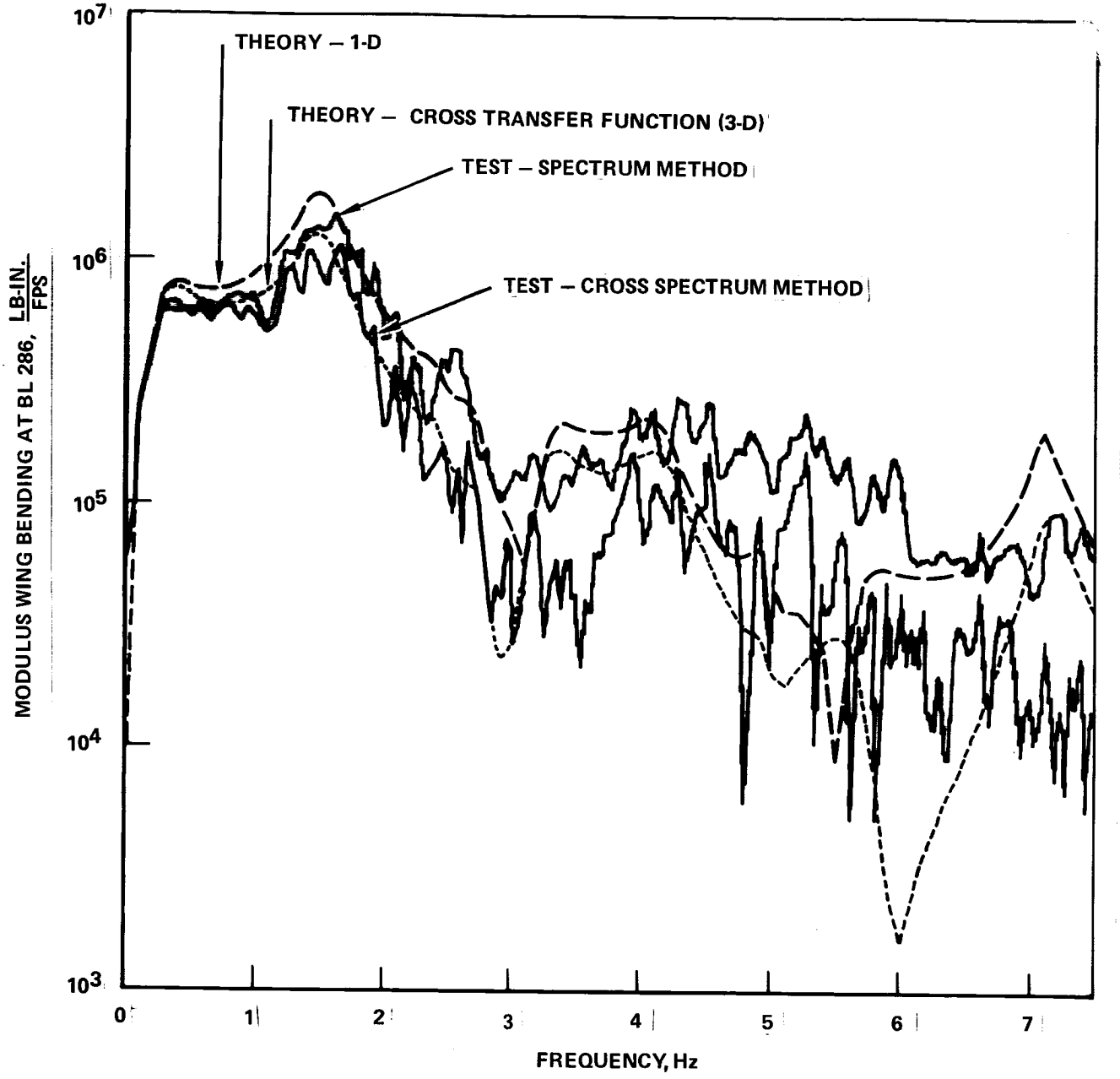

Figure 5-68. Transfer Function Modulus, Wing Bending at η =.29. Burst 3. (Merge/Plot Output)

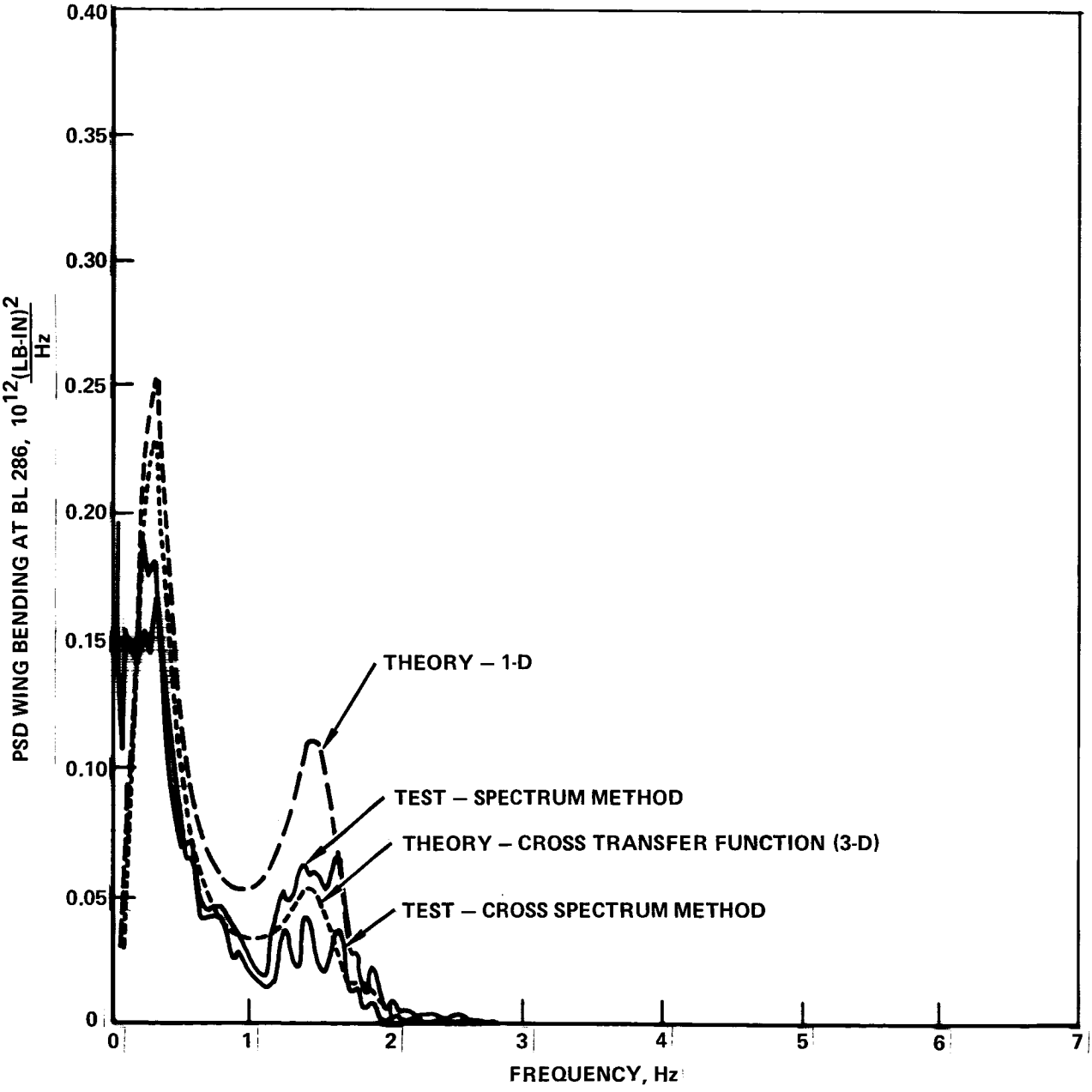

Figure 5-69. PSD Wing Bending at $\eta = .29$. Burst 3. (Merge/Plot Output)

Inasmuch as the rms value of the load is given by the square root of the area under the psd curve, this type of plot places in proper perspective the differences that occur, varying over the frequency range, between theory and test, between cross spectrum and spectrum methods of treating the test data, and between controls-off and controls-on. One might expect from the transfer function curves of Figure 5-68, for example, that the large difference between spectrum method and cross spectrum method curves between 3 and 4 Hz would introduce a major uncertainty in interpreting the results. But when the transfer function modulus is squared and multiplied by the gust psd, which drops off rapidly with increasing frequency, the contribution to load in either case is virtually zero. Figure 5-69 makes it immediately apparent that, for this particular response, what happens above 2.5 Hz has no effect whatever.

The corresponding curves for Burst 5 are shown in Figure 5-70. The spike that appeared below 0.15 Hz in the flight-measured psd in Figure 5-67 now dominates the plot. The spike is more conspicuous in this plot first because of the linear instead of logarithmic scale, but also, in part, because the gust psd in Bursts 5b and 5c falls away from the -5/3 power asymptote at low frequencies more rapidly than does the Von Karman spectrum with L = 2500 ft. In this case, reducing the scale of turbulence L to 305 m (1000 ft) gives a somewhat better fit to the measured gust psd's and reduces the psd value at 0.04 Hz, relative to its value at 0.3 Hz, by a factor of 3.5. Accordingly, for Bursts 5 and 6, the merge-and-plot program was run for L = 305 m (1000 ft) as well as L = 762 m (2500 ft). At the same time, the frequency scale in the plot was expanded by a factor of two for greater clarity. The result is shown in Figure 5-71.

Transfer Function Phase Angle

The transfer function phase angle for the same quantity is shown in Figure 5-72. The phase angle ordinarily has been considered of secondary importance in comparing theoretical with measured loads, because information on phase angle is lost when loads are expressed in psd form. Nevertheless, the phase angle can provide a useful additional tool in evaluating the basic accuracy of the theoretical modeling. Further, accuracy in predicting phase relations becomes vital in synthesizing an active control system to modify the response characteristics.

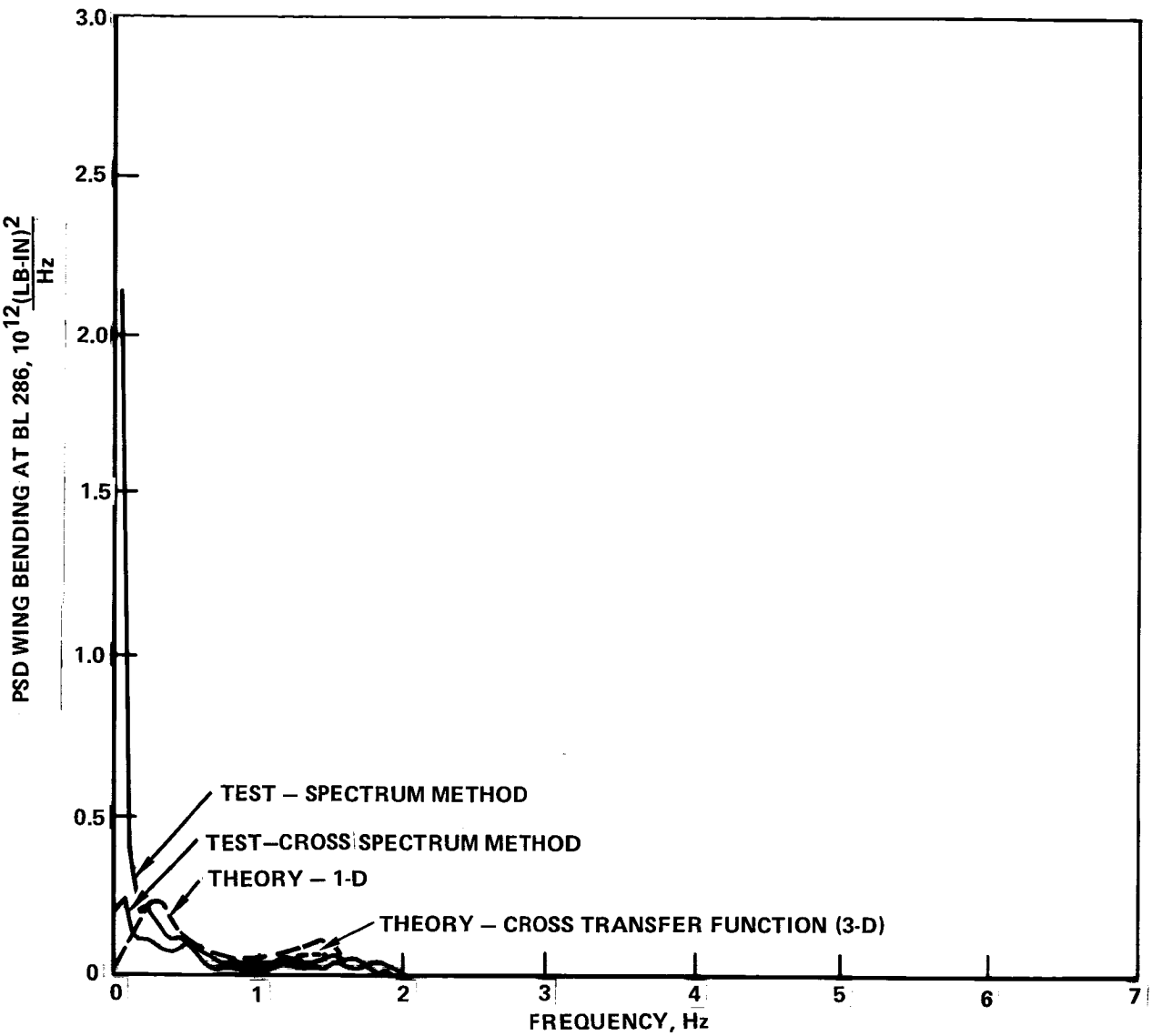

Figure 5-70. PSD Wing Bending at η = .29. Burst 5, L = 762 m. (2500 ft.)
(Merge/Plot Output)

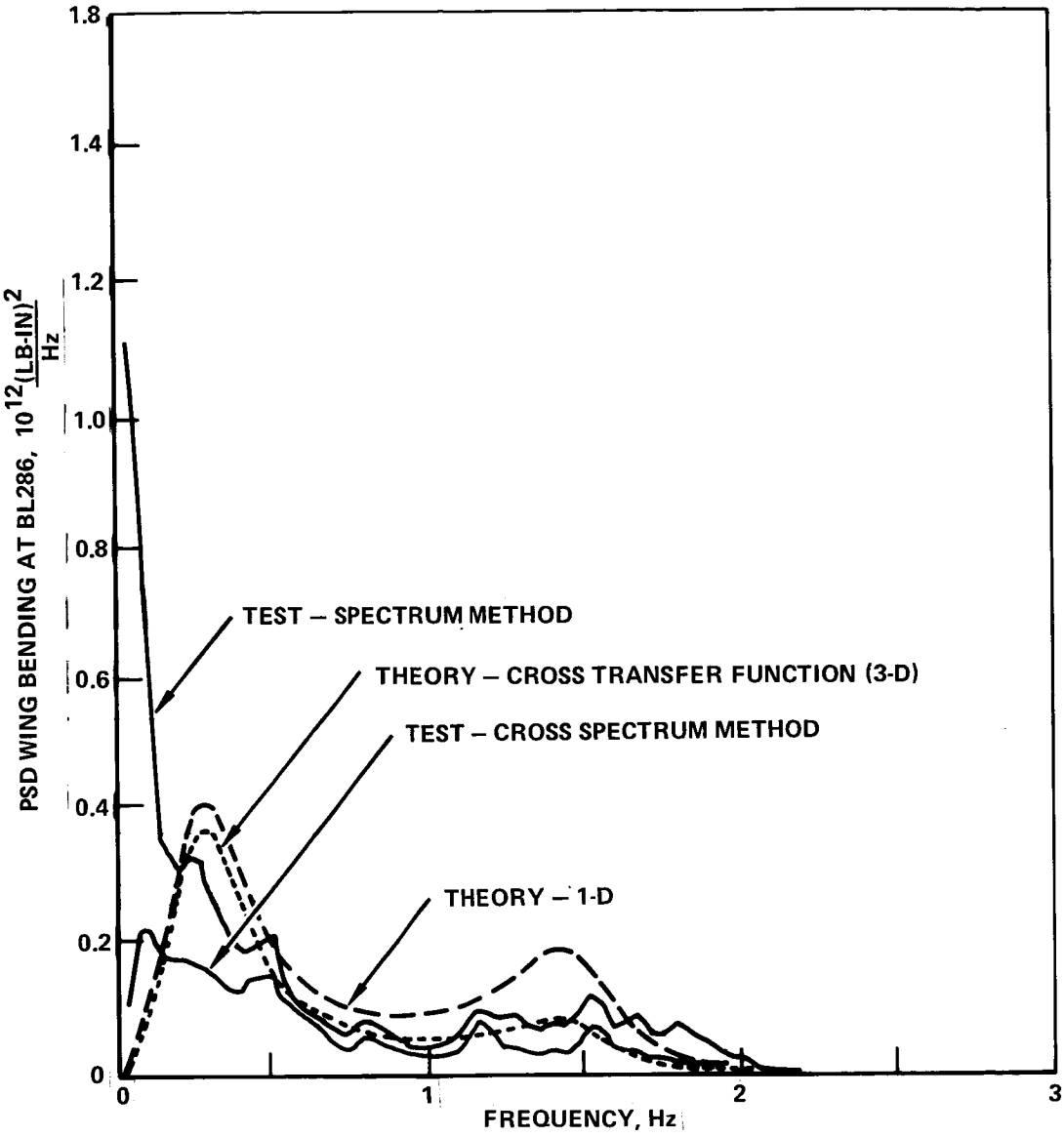

Figure 5-71. PSD Wing Bending at η = .29. Burst 5, L = 305m (1000 ft.) (Merge/Plot Output)

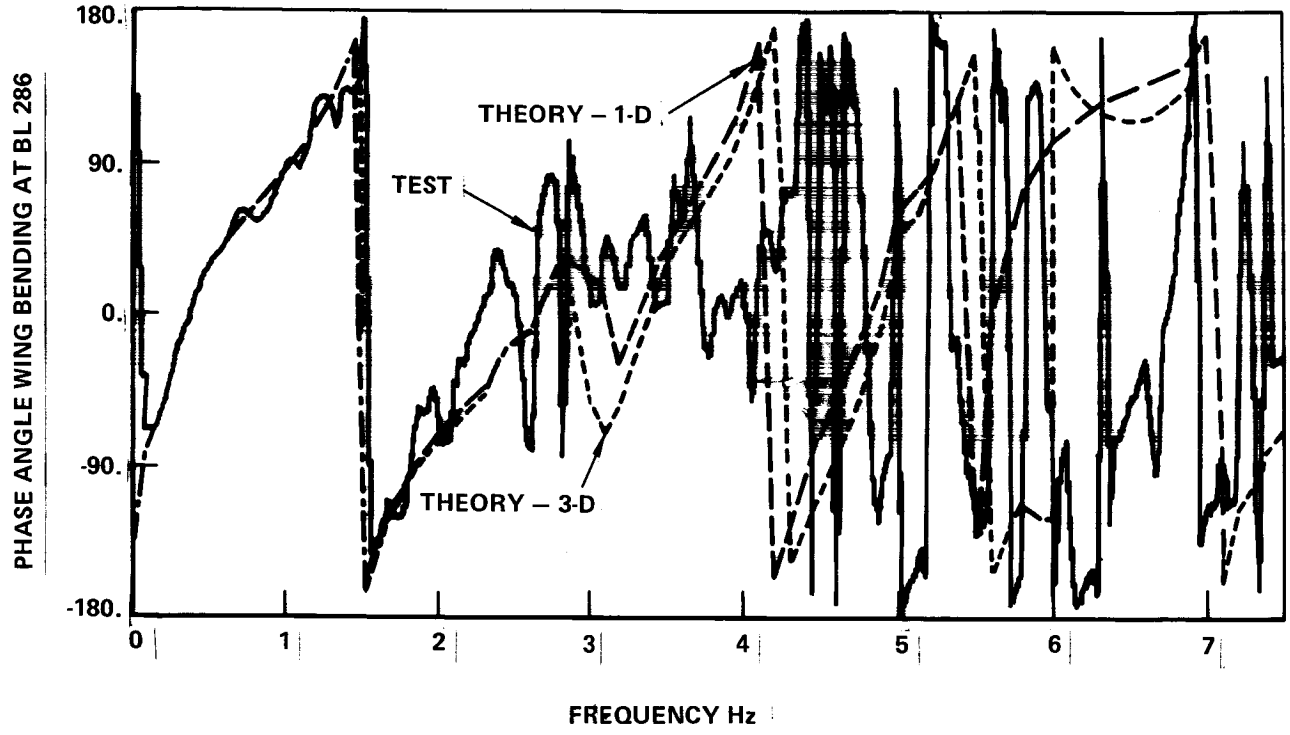

Figure 5-72. Phase Angle Wing Bending at η = .29. Burst 3.
(Merge/Plot Output)

The phase angle shown is the angle by which the response lags behind the gust - as encountered at the gust probe. This is a natural definition for the flight-measured phase angle; but it required a modification to the computation of the theoretical phase angle, which ordinarily is defined relative to the gust velocity at the airplane CG. The relation between phase angles relative to the gust at the probe and relative to the gust at the CG is:

$$(\text{Phase angle})_{\text{rel. to gust at CG}} = (\text{Phase angle})_{\text{rel. to gust at probe}} - \frac{\ell f}{V} 360$$

where ℓ is the distance from probe to CG (34.7 m, 114 ft), V is the true airspeed (in units consistent with ℓ and f), f is the frequency in Hz, and the phase angles are in degrees.

It may be remarked that the gust at the CG (which is roughly where the gust is felt by the airplane) lags the gust at the probe (where it is measured) by a phase angle in degrees of $(360\,\ell/V)f$. For a true airspeed of 206 m/s (400 knots), typical of the present data, the lag in phase angle due to this cause is 61f, or 61 degrees per Hz. Accordingly, this much of the phase angle can be thought of not as lag of the response relative to the input, but of the gust in moving from the probe to the CG.

Coherency Function

The coherency function for the same quantity is shown in Figure 5-73. The measured coherency (solid line) exhibits the typical characteristics noted in the discussion at the end of Section 5.7.3. It starts low, increases rapidly to a value of about 0.90 in the vicinity of 0.50 Hz, and then beginning at about 1.0 Hz drops off erratically to a value close to zero at about 6 Hz. (It has been found that experimental coherencies between quantities that theoretically should have zero coherency generally tend to oscillate between zero and some positive value, when plotted vs frequency; this positive value, for a burst of the duration of Bursts 3a and 3d combined, is about 0.3. See further discussion in Section 5.7.8.)

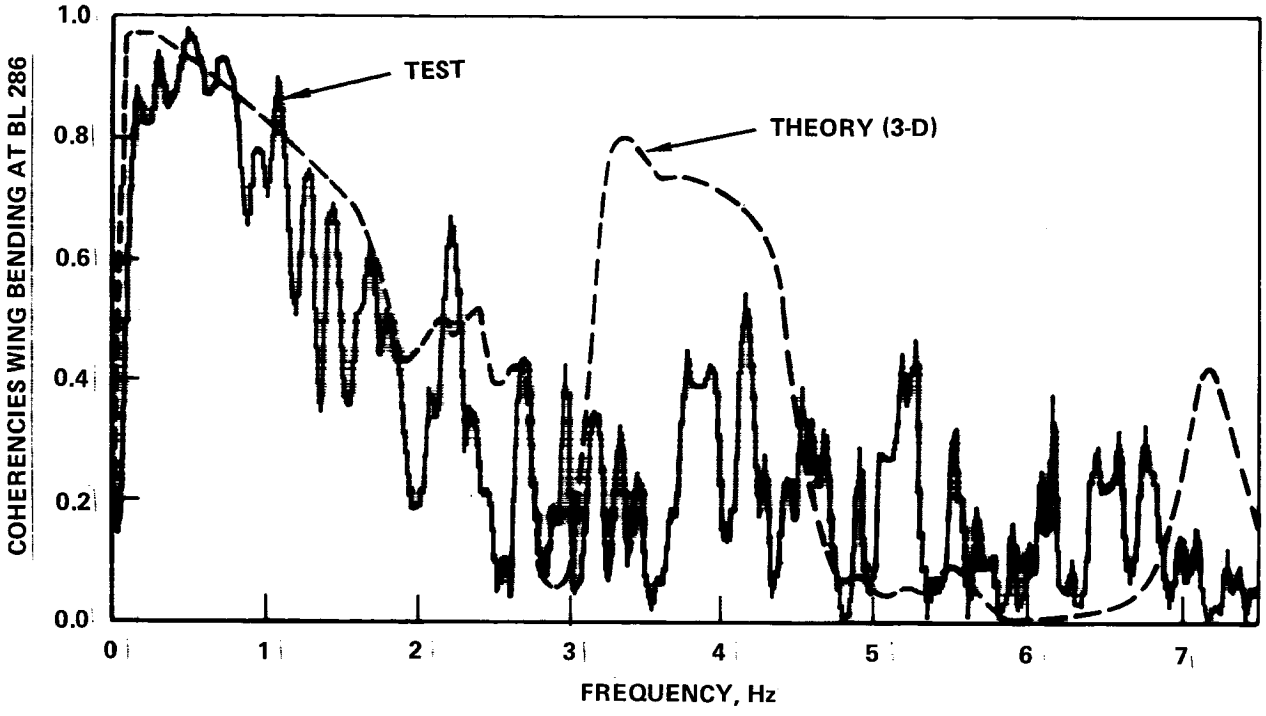

Figure 5-73. Coherencies Wing Bending at η = .29. Burst 3.
(Merge/Plot Output)

The theoretical coherency, based on 3-D gust analysis, is shown by the dash line. It differs from unity because of the spanwise variation of vertical gust velocity and because of lateral gust inputs. It represents an approximate upper limit to the measured coherency. The difference between the two reflects other inputs such as maneuvers, noise in the instrumentation, or extraneous inputs due to instrumentation malfunction. The availability of the theoretical coherency, as an upper limit, can be very helpful in providing perspective when the coherency is used to indicate quality of data. In Figure 5-73, the dropoff in measured coherency from 1.0 to 3.0 Hz is thus seen to be very much as predicted by theory. The principal cause is undoubtedly the spanwise variation of gust velocity, although the presence of lateral gust as a second input would also have some small effect. The small but distinct dropoff in the measured coherency below 0.5 Hz is evidently due to maneuver inputs. The large increase in theoretical coherency between about 3 and 4.5 Hz is believed to be due to response in elastic modes (such as fuselage bending) that are excited primarily by gust-induced aerodynamic forces acting close to the airplane centerline - on the inner part of the wing, the horizontal tail, and the fuselage itself.

The corresponding coherency plot for Burst 5 is shown in Figure 5-74. This figure differs from the preceding one primarily in the much greater dropoff in measured coherency below about 0.5 Hz. This is consistent with the large low-frequency spike appearing in Figures 5-67 and 5-70.

The three heavy dotted lines in Figure 5-74 indicate how average coherencies over the range 0.5 - 1.5 Hz were estimated, for presentation later in the report.

Integrated Data - $\bar{A}$ Values

In addition to plots vs. frequency, it is desirable to obtain, for each load quantity for each burst, a single number that will indicate the magnitude of that load quantity corresponding to a standard gust input. Such a number is $\bar{A}$, the ratio of the rms of the response to the rms gust velocity. The standard gust psd for this purpose is ordinarily the Von Karman gust psd with L = 762 m (2500 ft) and unit rms value. Inasmuch as the various psd curves from which A's will be obtained,

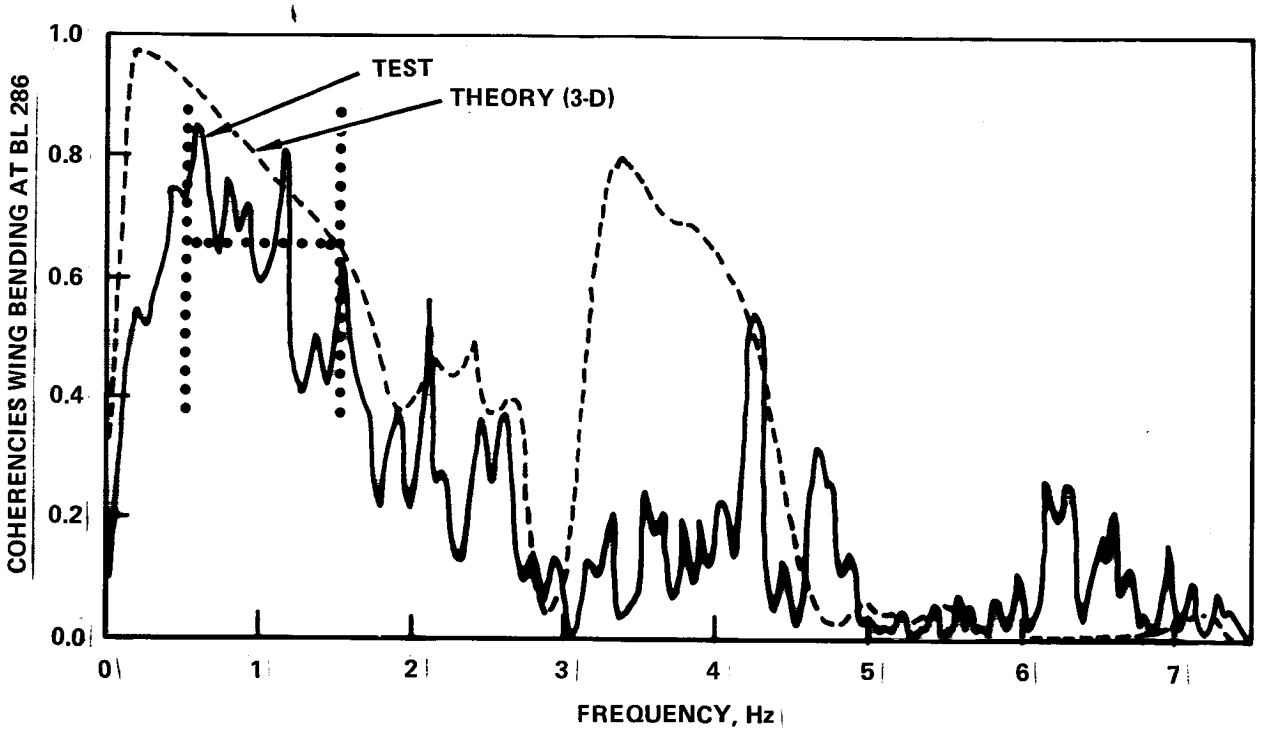

Figure 5-74. Coherencies Wing Bending at η = .29. Burst 5. (Merge/Plot Output)

such as shown in Figures 5-69, 5-70 and 5-71, are already based on such a gust input, A is given simply by the square root of the area under this curve. As noted earlier, the psd curves for Bursts 5 and 6 were obtained also for L - 305 m (1000 ft); A's for these bursts were obtained for both gust inputs. It might be remarked that the A values for L = 305 m (1000 ft) are generally larger than for L = 762 m (2500 ft) approximately in the ratio $\sqrt[3]{762/305} = 1.357$. Psd's likewise are larger, except at very low frequencies, approximately in the ratio $1.357^2 = 1.842$. (1.842 is the value approached by the ratio of the psd's as frequency increases and each gust psd approaches its respective -5/3-slope asymptote. The ratio decreases to about 1.66 at 0.25 Hz and 0.53 at 0.04 Hz.)

The computation of $\bar{A}$'s is carried out for the one-D theoretical psd's in the GLP-4 and GLP-6 programs, and for all theoretical and test psd's (corresponding to the Von Karman input spectrum) in the merge-and-plot program. (Theoretical psd's based on the 3-D cross transfer functions are not computed in GLP-6 and consequently are available only through the merge-and-plot program.)

5.7.7 Evaluation of Flight Data

Gust Power Spectral Densities

The nature of the turbulence encountered in terms of its power-spectral density is shown in Figures 5-75 through 5-78. Separate curves are shown for all three bursts of the baseline tests. For the extended-span tests, each curve is the average of individual bursts.* All of the curves are seen to follow closely the Von Karman

*In obtaining these averages, the psd's of the individual bursts were first ratioed so that the resulting rms gust velocity for each burst would be equal to the overall rms gust velocity for the several bursts, given by

$$\sigma_{\text{overall}} = \sqrt{\frac{\sigma_1^2 t_1 + \sigma_2^2 t_2 + \cdots}{t_1 + t_2 + \cdots}}$$

where the t's are the burst durations. In obtaining the average psd's, the individual bursts were weighted by duration of burst.

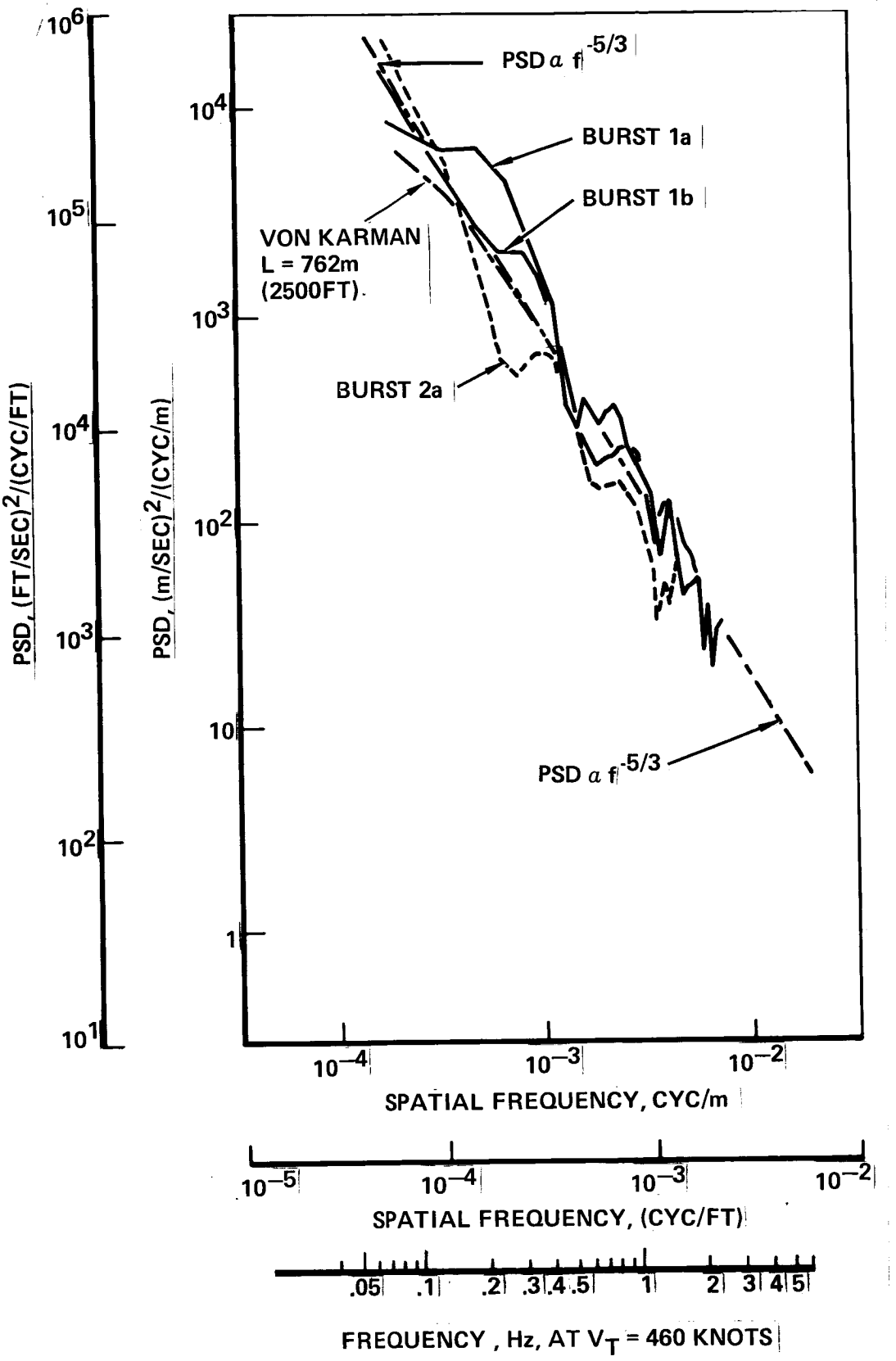

Figure 5-75. PSD's of Vertical Gust Velocity, Bursts 1 and 2

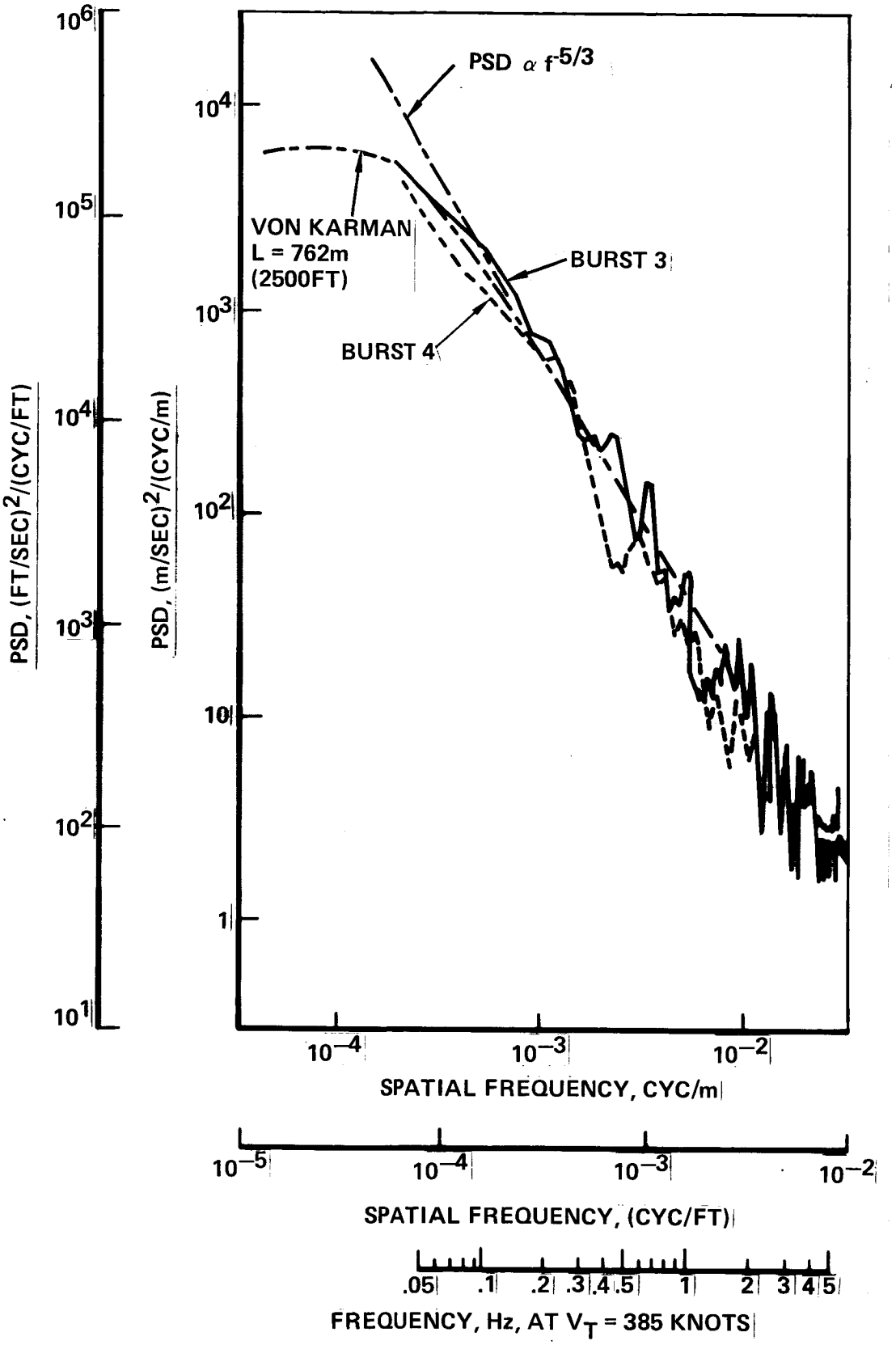

Figure 5-76. PSD's of Vertical Gust Velocity, Bursts 3 and 4

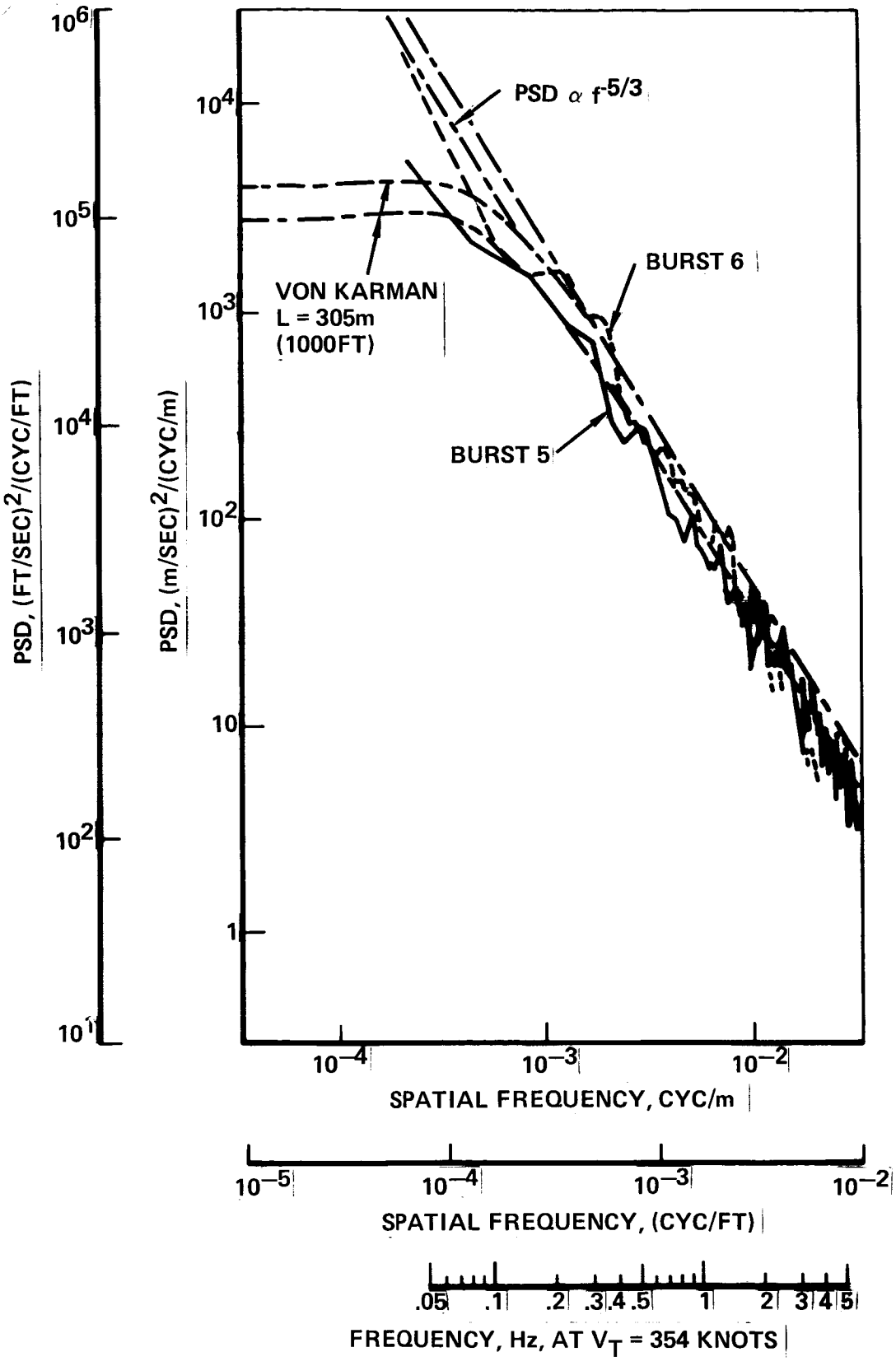

Figure 5-77. PSD's of Vertical Gust Velocity, Bursts 5 and 6

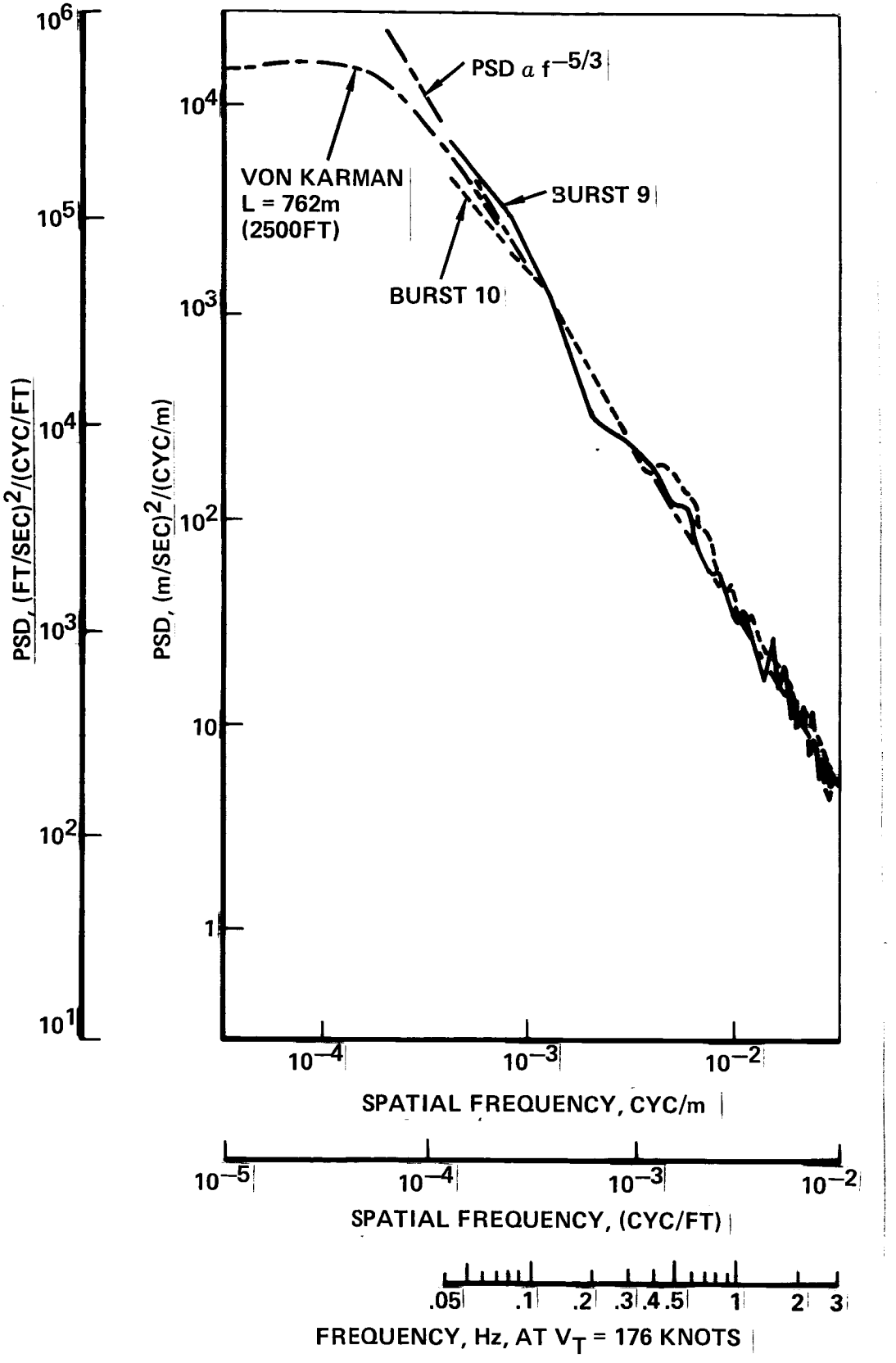

Figure 5-78. PSD's of Vertical Gust Velocity, Bursts 9 and 10

shape, especially with respect to the -5/3 exponent above the lowest frequencies. The best-fit scale of turbulence appears to be 762 m (2500 ft) or more for Bursts 1 and 2, 3 and 4, and 9 and 10. In Bursts 5 and 6, the measured curves drop away more conspicuously from the -5/3 exponent straight line at the lower frequencies and are better represented with a scale of turbulence of 305 m (1000 ft).

Coherencies

Measured coherencies have often been found useful in evaluating the quality of data in continuous turbulence gust response testing. Coherencies less than about 0.70 to 0.80 in the range of 0.5 - 1.5 Hz would suggest either faulty instrumentation, excessive maneuver inputs, nonlinearities in the system, or perhaps inadequate stationarity. In the present program, plots of measured coherencies for individual bursts served to identify several time segments which had to be discarded, due to instrumentation malfunction, in establishing the final bursts that would be analyzed as listed in Table 5-7.

Average Coherencies of Key Response Quantities. A comparison of all of the retained bursts in terms of coherencies of a few key response quantities is shown in Figure 5-79. The coherencies shown are averages over the frequency range 0.5 to 1.5 Hz for the cruise-speed bursts and 0.25 to 1.00 Hz for the low speed bursts. Early examination of the coherency plots indicated the coherencies generally to be highest over these ranges and fairly constant within these ranges. The averages were estimated from the plots as indicated by the heavy dotted lines in Figure 5-74.

Coherencies are shown in the figure for one or more body accelerations and for wing root bending moment. The CG acceleration (FS 1216) would ordinarily have been considered the pertinent body acceleration; however it was not available for all bursts, so the ACS body acceleration (FS 719) or the aft body acceleration (FS 1600) was shown instead or in addition for several bursts.

Generally the coherencies are comparable for all of the cruise speed bursts (1 through 6); they are also comparable, although somewhat lower, for the two low speed bursts (9 and 10). The bending moment coherencies are consistently lower than the acceleration coherencies.

Theoretical Coherencies. The reasons for these differences, as well as others to be noted later, are evident from an examination of the theoretical coherencies shown in Figures 5-80 and 5-81.

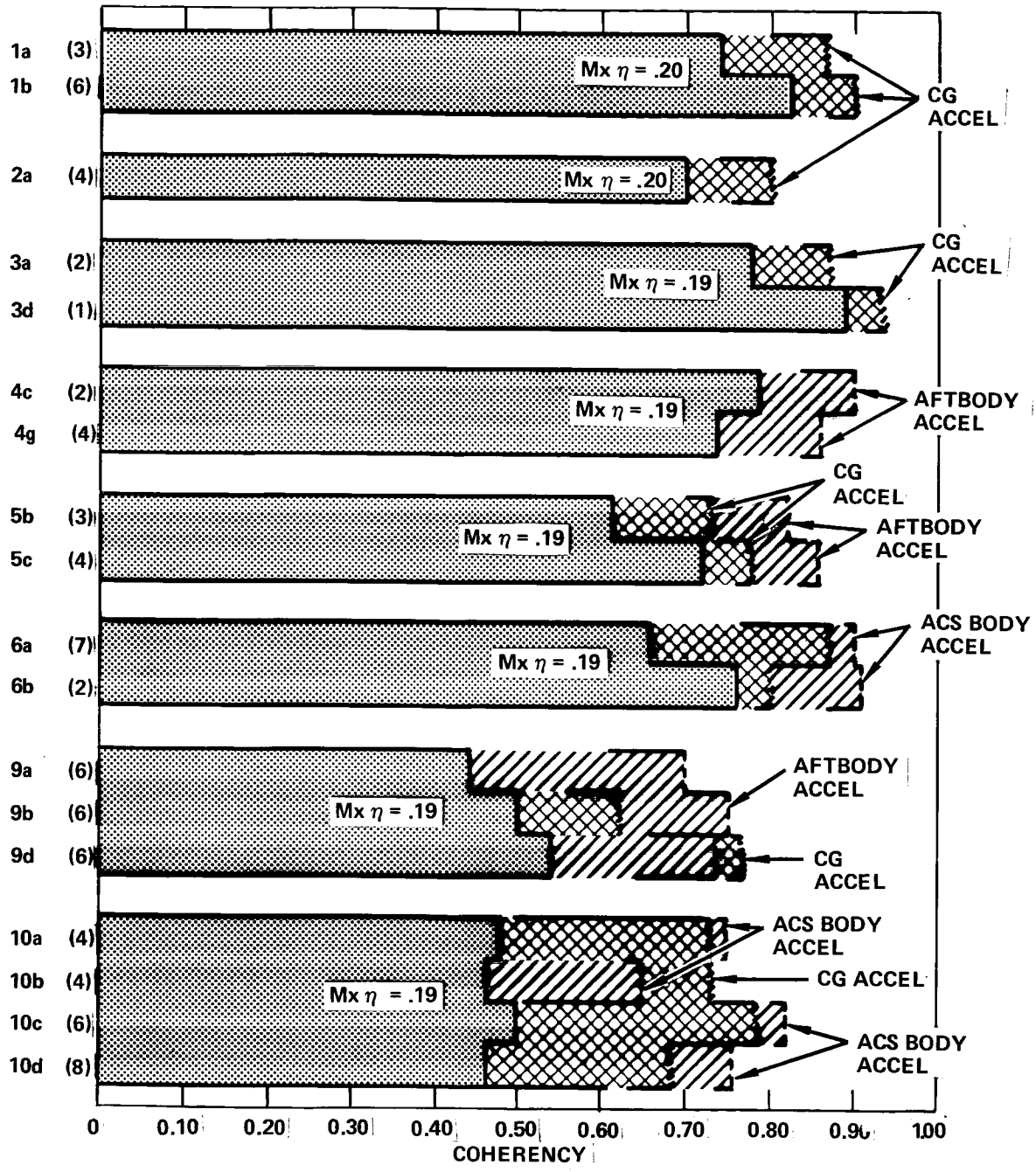

FIGURES IN PARENTHESES AFTER BURST NUMBER ARE LENGTH OF BURST IN BLOCKS OF 25.6 SECONDS

COHERENCIES SHOWN ARE AVERAGE OVER FREQUENCY RANGE 0.5 - 1.5 Hz FOR BURSTS 1 THROUGH 6, 0.25 - 1.0 Hz FOR BURSTS 9 AND 10

Figure 5-79. Quality of Test Data as Indicated by Average Coherencies of Key Response Quantities

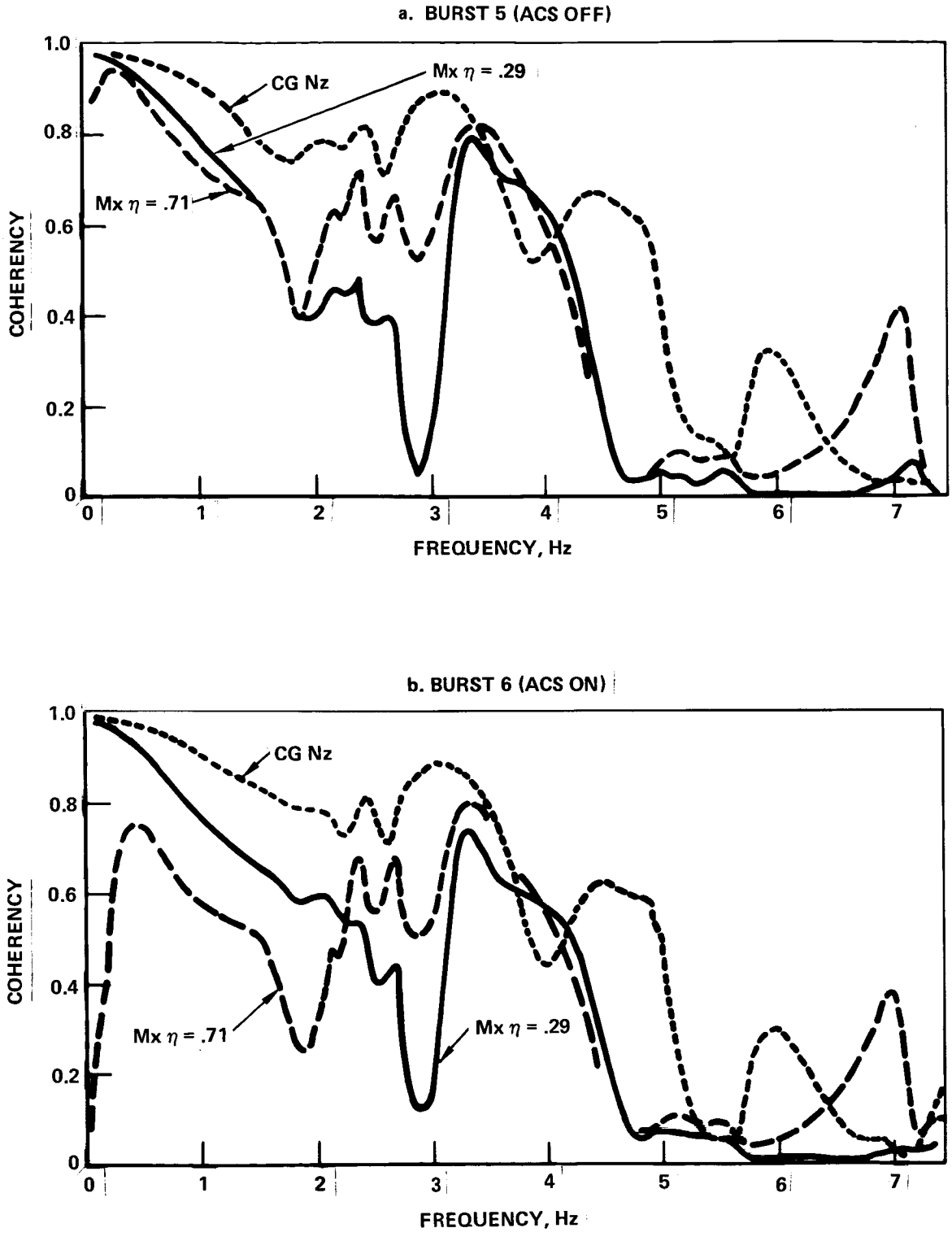

Figure 5-80. Comparison of Theoretical Coherencies for Various Responses

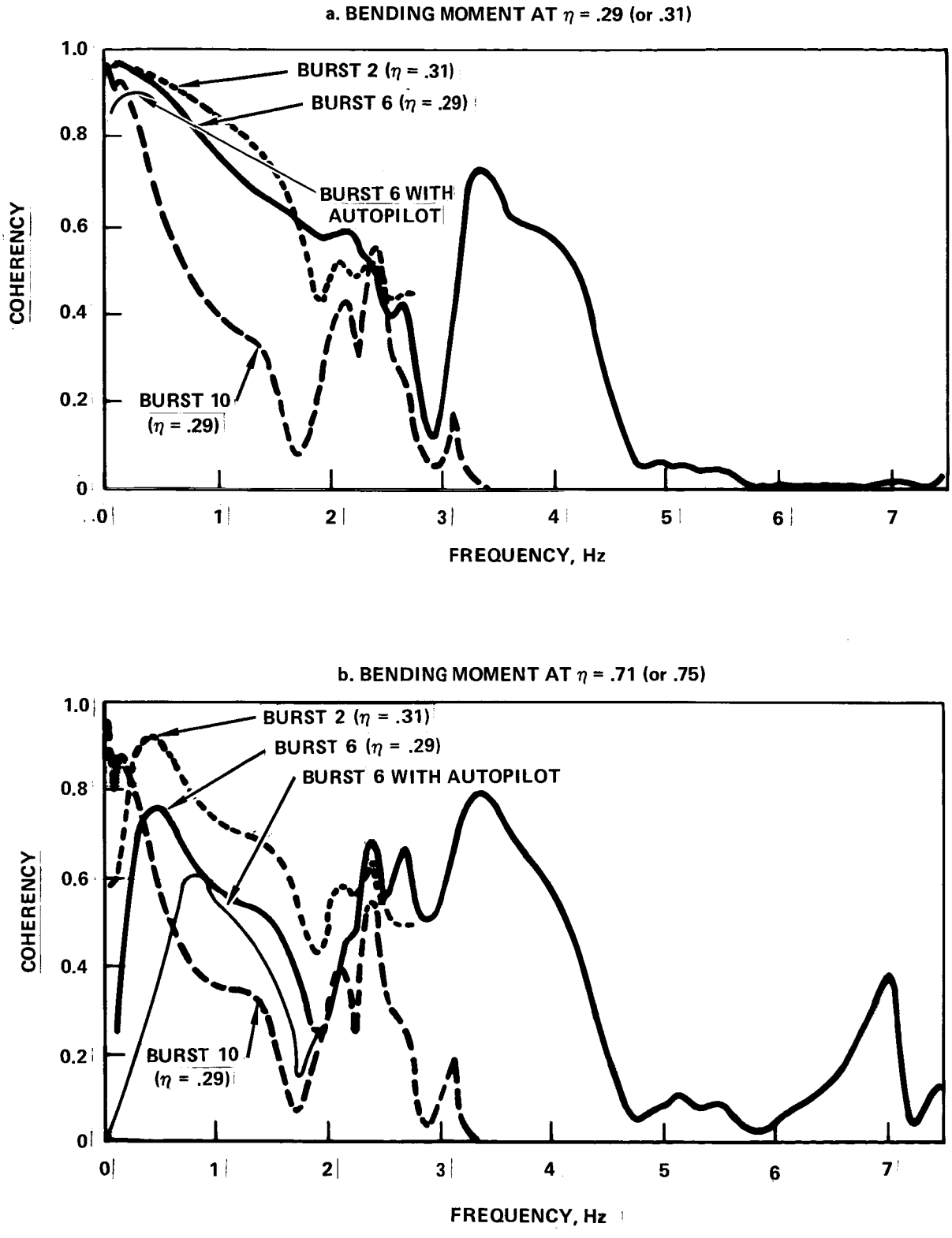

Figure 5-81. Comparison of Theoretical Coherencies for Various Bursts (ACS ON)

In both Figure 5-80(a) (ACS off) and 5-80(b) (ACS on), it is seen that the theoretical coherency in the region around 1 Hz is distinctly lower for root bending moment ($\eta = 0.29$) than for CG acceleration. This is reasonable, inasmuch as lift in the outer part of the wing, where the coherency of the gust velocity relative to that at the probe is least, contributes more heavily to the wing bending moment than to the CG acceleration.

In both figures, the coherency is lower for bending moment at $\eta = 0.71$ than at $\eta = 0.29$, in part for the same reason, although the difference is more conspicuous with ACS on.

Comparing Figures 5-80(a) and (b) it is seen that the ACS has virtually no effect on the coherency for CG acceleration and root bending moment, but substantially reduces the coherency at the more outboard location.

The large dropoff below 0.5 Hz in the curve for wing bending at $\eta = 0.71$ with ACS on is due to the lateral gust input, which with the vertical gust loads vastly reduced at this outboard location by the ACS, now predominates. The reason why this curve is lower in the region above 0.5 Hz than with ACS off is less clear. It may be related to the fact the bending moment at this location is, in effect, a rather small difference between two larger quantities, each with its individual incoherency. The first of these quantities is the bending moment due directly to the gust loading outboard of $\eta = 0.71$; the second is opposing bending moment due to an aileron deflection which depends primarily upon acceleration at the airplane CG.

The effect of flight condition on coherency is indicated in Figure 5-81.

For bending moment at $\eta = 0.29$ (or 0.31) Figure 5-81(a), the coherencies are seen to be comparable for Bursts 2 and 6, but much lower for Burst 10. The lower coherency for Burst 10 is due primarily to a difference in true airspeed, which is lower for Burst 10 than Burst 6 by a factor of two. The effects of spanwise variation of gust velocity depend upon gust wavelength, which is given by V_T/f. With a lower V_T, a given coherency should therefore occur at a correspondingly lower f. Accordingly, one would expect the coherency curve for Burst 10 to be given approximately by dividing the horizontal coordinates of the Burst 6 curve by 2. The actual factor, for Burst 6 frequencies below about 2 Hz, is more like 3; the reason for this additional difference is not evident.

The smaller differences between Bursts 2 and 6 could be due to two causes - the difference in wing span, and a further difference in true airspeed, 30 percent

higher for Burst 2 than Burst 6. Both of these effects are in the direction to increase the coherency for Burst 2 relative to Burst 6, which is the trend indicated by the curves.

A similar comparison for bending moment at $\eta = 0.71$ (or 0.75) is shown in Figure 5-81(b). The relationships shown here are not identical to those shown in Figure 5-81(a), but are comparable. The much increased difference between Bursts 2 and 6 would appear to be due to the larger aileron on the extended-span wing.

It is evident, therefore, that the following trends generally observable in the bar chart of Figure 5-79 are consistent, at least qualitatively, with the predictions of 3-D gust theory:

- Lower coherency for bending moment than for CG acceleration.
- Much lower coherency for Bursts 9 and 10 than Bursts 1 through 6.
- Somehwat lower coherency for Bursts 5 and 6 than for Bursts 1 and 2. (The greater coherency for Bursts 3 and 4, counter to the theoretical coherencies, is shown later to be due to much smaller pilot control inputs for these bursts.)

A fourth curve shown in Figures 5-81(a) and (b) is also illuminating. This is the curve labeled "Burst 6 with autopilot." This curve reflects the use of the L-1011 autopilot in its turbulence mode. The pitch feedback has negligible effect on coherency; but the effect of roll feedback to the ailerons is significant. The roll motion, which the autopilot acts to control, is due primarily to the lateral gust velocity and secondarily to the spanwise variation of the vertical gust velocity. Both of these inputs are uncorrelated with the vertical gust velocity on the centerline; consequently, any response which they produce reduces the coherency. For bending moment at $\eta = 0.29$, the effect is small but distinct. At $\eta = 0.71$, the effect is much greater, inasmuch as the outboard as well as the inboard ailerons are used for roll control. Roll control inputs by a pilot, as contrasted to an autopilot, have been found to differ substantially from pilot to pilot; but rms (root-mean-square) aileron angles due to autopilot control seem to be fairly representative of roll control by pilots. In addition to the reduction of coherency due to roll control, which is predictable qualitatively by 3-D theory, there is also, in actual flight, a reduction due to pitch control. This is not predictable by 3-D theory.

Comparisons of Measured With Theoretical Coherencies. Sample comparisons of measured with theoretical coherencies are shown in Figure 5-82, for wing bending moment at $\eta = 0.29$. In all cases, the measured coherencies have been heavily faired to facilitate the comparison. The comparisons for Bursts 3 and 5 were shown earlier (without fairing - Figures 5-73 and 5-74); here these are repeated and Bursts 4, 6, 9, and 10 added. Note the expanded frequency scale for Bursts 9 and 10. In all cases, the agreement in trend over the range from 0.5 Hz out to about 3 Hz is remarkable, and the measured coherencies are close enough to the theoretical to leave little doubt that the quality of the data is adequate. The departure of the measured coherencies from the theoretical below 0.5 Hz is, of course, due to pilot control inputs, as noted earlier.

Average Coherencies of All Response Quantities. A more comprehensive view of the measured coherencies is provided by Table 5-11. Here as in Figure 5-79, the coherencies are represented by average values over a pertinent frequency range. This range, again, is generally 0.5 - 1.5 Hz for the cruise-speed data and 0.25 - 1.00 Hz for the low speed data. Two quantities, wing tip symmetric n_z, and wing engine $|n_y|$, respond negligibly at these lower frequencies; their coherencies are averaged, therefore, over the range 1.0 - 3.0 Hz.

Several specific observations regarding the tabulated values are appropriate. First the coherencies for both shear and bending moment are seen to decrease generally going outboard. This decrease is in accordance with the decreasing coherency between the gust velocity producing the load and the gust velocity as measured on the center line. The torsions are more erratic. The generally very low coherencies at $\eta = 0.38/0.36$ and at $\eta = 0.75/0.71$ are consistent with the 12e1 (1971) data. Studies of the 1971 data indicated that the low coherencies at these locations, just inboard of the inboard and outboard ailerons respectively, are related to a high coherency between the torsions and the aileron angles. In other words, pilot input to the ailerons is an especially significant contributor to these loads. The variations of coherency from burst to burst tend to follow the pattern suggested by the earlier discussion of the theoretical coherencies. The listed coherencies are generally lower for Bursts 9 and 10 than for the cruise speed bursts; and in the outer part of the wing, coherencies for shear and bending moment are generally lower with ACS on than off (Burst 2 vs 1, 4 vs 3, 6 vs 5, and 10 vs 9.)

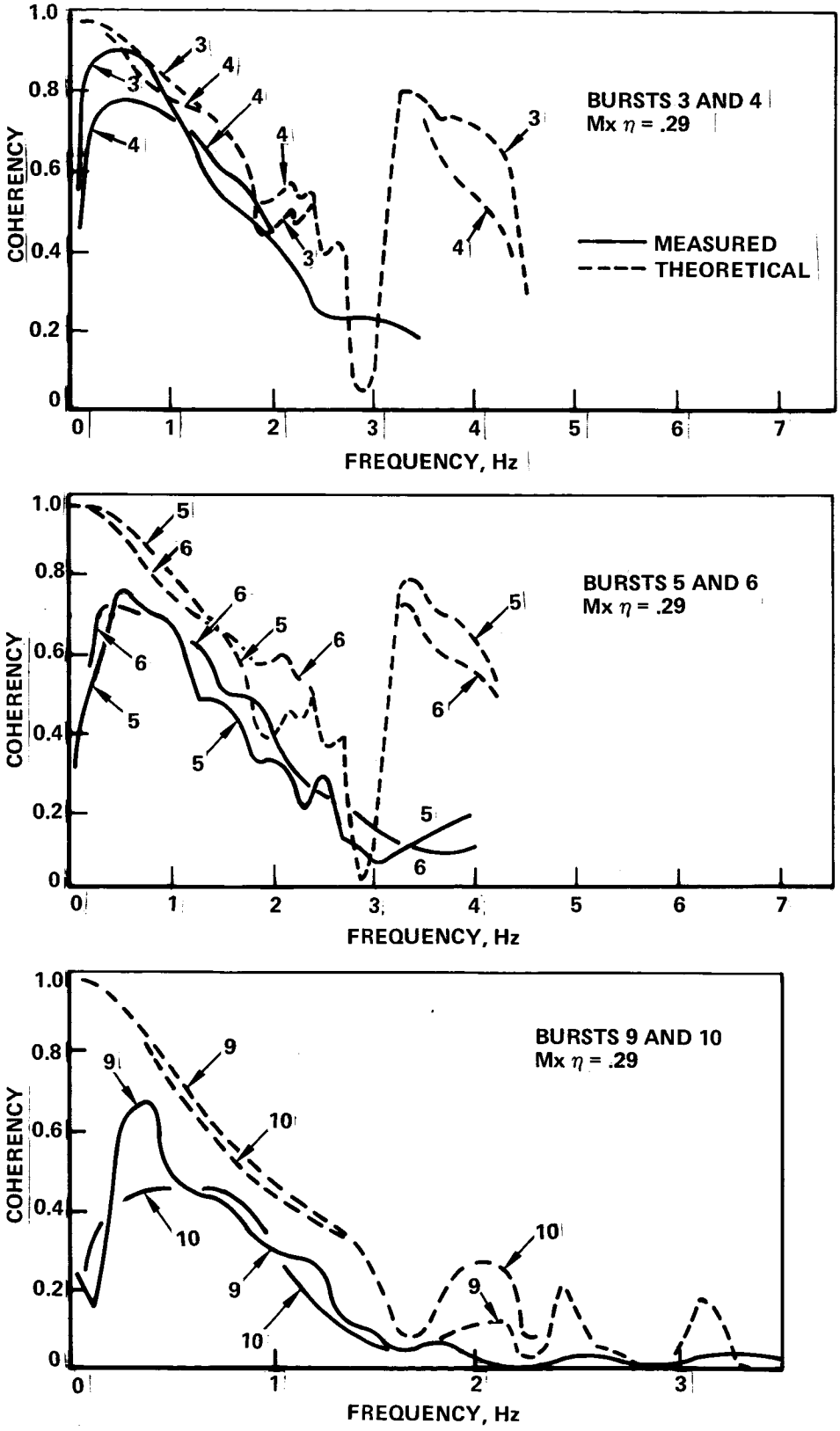

Figure 5-82. Comparison of Measured With Theoretical Coherencies - Bending Moment at η = .29

TABLE 5-11. QUALITY OF TEST DATA AS INDICATED BY AVERAGE COHERENCIES

Quantity	Baseline	Ext'd Span	Average Coherency Over the Specified Frequency Range for the Burst Indicated								
			1	2	12e1	3	4	5	6	9	10
W S_z	η= .20	.19	.84	.80	.79	.79	.80	.69	.75	.52	.42
	.31	.29			.79	.80	.81	.65	.72	.56	.56
	.38	.36	.81	.77	.76	.79	.77				
	.52	.49	.79	.71	.75	.77	.74	.66	.70	.48	.44
	.75	.71	.68	.46	.69	.73	.57	.58	.47	.34	.28
		.80				.59	.44	.50	.25	.30	.24
		.85				.56	.50	.47	.20	.30	.22
W M_x	η= .20	.10	.66	.72	.75	.79	.74	.65	.65	.48	.42
	.31	.29	.77	.66	.75	.76	.72	.65	.65	.46	.42
	.52	.49	.56	.52	.70	.73	.60	.58	.50	.38	.33
		.61						.56	.40	.35	.29
	.75	.71	.90	.25	.60	.67	.47	.49	.24	.31	.22
		.80				.65	.44	.42	.12	.26	.16
		.85				.61	.44	.40	.12	.27	.18
W M_y	η=.20	.19	.65	.57	.73	.70	.64				.12
	.31	.29			.25	.33	.33	.12	.15	.18	.17
	.38	.36	.12	.14	.15	.24	.23	.12	.08	.07	.05
	.52	.49	.30	.32	.52	.55	.45	.23	.32	.45	.44
		.61						.20	.27	.36	.29
	.75	.71	.19	.24	.30	.42	.53	.19	.19	.15	.18
		.80				.46	.50	.22	.13	.04	.08
		.85				.53	.49	.20	.12	.03	.05
Fus S_z	FS 239		.89	.87	.86						
	1426		.84	.80	.59						
HT S_z	η = .29		.65	.41	.74	.61	.57	.65	.71	.25	.26
M_x	.29		.66	.41	.72	.80	.64	.63	.67	.28	.27
M_x	.60					.76	.64	.59	.63	.32	.27
M_y	.29		.81	.56	.78	.80	.80	.79	.69	.63	.54
Nz nose FS 123	123		.87	.83	.93	.97	.84	-	-	.76	.65
pilot	185		.88	.83		.74	.79	.81	.88	.74	.67
ACS	719					-	-	.82	.90	.76	.72
CF	1216		.88	.80	.90	.87	-	.76	.85	.68	.72
aftbody	1535	1600	.86	.74		.85	.87	.78	.86	.72	52
W engine n_z				.42	.65	.52	.48	.40	.43	.33	.30
n_y			.43	.33	.22	.31	.32	.30	.36	.10	.08
W tip sym n_z			.63	.56		.55	.52	.50	.47	.13	.14
Stab tip sym n_y						-	-	.69	.73	.44	-
Sym δ_a			.12	.57		.25	.52	.10	.72	.02	.33
δ_H				.14	.03	.34	.07	.05	.06	.07	.08
$\dot{\theta}$ (pitch rate)				.38	.86	.73	.56	.61	.61	.62	.43

Note: Averages are over the range 0.5-1.5 Hz for Bursts 1-6, 0.25-1.0 Hz for Bursts 9 and 10, except for wing engine n_y and wing tip sym n_z for which the range is 1-3 Hz for all bursts.

The general consistency of the various coherencies listed in the table, in the context of the foregoing discussion, imparts confidence in the adequacy of the complete body of data.

5.7.8 Results and Discussion

Overall Results

An overall evaluation of the adequacy of the active control system to give the load reductions predicted by theory is provided by Figures 5-83 through 5-93. Figures 5-83 through 5-91 compare measured with theoretical reductions in wing shears and bending moments, while Figures 5-92 and 5-93 compare the measured with theoretical effect of the active controls on wing torsions. In this section of the report, the various figures are introduced and discussed briefly and conclusions indicated. Additional backup discussion and analysis is deferred to later sections.

In Figures 5-83 to 5-93, the horizontal scale is the ratio of $\overline{A}$ values ACS-on to ACS-off, as given by theory. The $\overline{A}$ values forming this ratio were obtained in all cases by running both the ACS-on and ACS-off analyses for the ACS-on flight condition; thus the controls-off $\bar{A}$ is for exactly the same flight condition as the controls-on value.

The vertical scale is the same ratio based on the flight data. This ratio cannot be computed directly as the ratio of two available $\overline{A}$'s, however, inasmuch as the ACS-on and ACS-off $\bar{A}$'s are always for slightly different flight conditions. Instead, the test $\bar{A}$ ACS-off is adjusted for the small difference in flight

condition by multiplying by the ratio of theoretical A's for the two flight conditions, both ACS-off. Thus, for Bursts 1 and 2, for example, where Burst 1 is with ACS off and Burst 2 with ACS on,

$$\left(\frac{\bar{A}\ \text{ACS on}}{\bar{A}\ \text{ACS off}}\right)_{test} = \frac{(\bar{A}\ \text{Burst 2})_{test}}{(\bar{A}\ \text{Burst 1})_{test}\ \dfrac{(\bar{A}\ \text{Burst 2 ACS off})_{theory}}{(\bar{A}\ \text{Burst 1 ACS off})_{theory}}}$$

The same result can also be thought of as given by

$$\left(\frac{\bar{A}\ \text{ACS on}}{\bar{A}\ \text{ACS off}}\right)_{test} = \frac{\left(\dfrac{(\bar{A}\ \text{ACS on})_{test}}{(\bar{A}\ \text{ACS on})_{theory}}\right)}{\left(\dfrac{(\bar{A}\ \text{ACS off})_{test}}{(\bar{A}\ \text{ACS off})_{theory}}\right)} \left(\frac{\bar{A}\ \text{ACS on}}{\bar{A}\ \text{ACS off}}\right)_{theory}$$

in which the last ratio is computed for the ACS-on flight condition.

In Figures 5-83 to 5-91, points below the 45-degree "test = theory" line indicate the ACS to be more effective than predicted, and above the line, less effective.

Cross Spectrum Method and 1-D Theory. In the first five figures, the test values were obtained using cross-spectrum-method transfer functions, and the theoretical values were based on traditional 1-D theory.

In these figures, the theoretical reduction ratios are seen to range approximately as follows:

Baseline tests, cruise	0.62 - 0.93
Extended span tests, cruise	0.50 - 0.90
Extended span tests, low speed	0.71 - 0.88

In all cases, the greatest reductions occur at the more outboard locations. The greater reductions for the extended-span tests are due to the larger aileron. The smaller reductions for the low speed tests (flaps extended) are related to the large reduction in dynamic pressure, only partially offset by changes in the system gains. It might be remarked that, for critical design conditions, load

reductions due to the ACS are only about 75 percent of those indicated here, as a result of the difference in airplane weights. Accordingly, a reduction factor of 0.60 for the flight test flight condition would become 0.70 for the design condition. Also, these ratios apply, of course, only to the gust increment. Inasmuch as the one-g part of the load, unaffected by the ACS, is roughly 1/3 of the total for gust conditions, the percentage reduction in net load is only about 2/3 of the percentage reduction in the gust increment. A reduction factor of 0.70 for the gust increment would thus become 0.80 for net load.

Results of the baseline tests are shown in Figure 5-83. These results are highly gratifying. With only one exception, all of the points lie very close to the "test = theory" line, and average slightly below. The only point significantly above the line is for bending moment at $\eta = 0.75$. The departure of this point from the line is believed to be due to the nature of the psd determinations from the test data, rather than any actual ineffectiveness of the ACS. This is discussed more fully later, under "Response PSD's".

Cruise condition results for the extended-span tests are shown in Figures 5-84, 5-85, and 5-86. In these figures, too, the test points generally fall close to the line, averaging slightly above the line for Bursts 3 and 4 and slightly below for Bursts 5 and 6. It might be remarked that the close similarity between the two figures for Bursts 5 and 6, one for L=762 m (Figure 5-85) and one for L = 305 m (Figure 5-86) indicates insensitivity of the results to the selection of the scale of turbulence, which involved some degree of judgment. The 305 m (1000 ft) case, however, is considered to be the more valid of the two.

All three of these figures display a consistent trend in the small departures of the test data from the 100%-effective line. Indeed, the detailed consistency of Bursts 3 and 4 with Bursts 5 and 6 tends to confirm the adequacy of the burst durations with respect to reliability of the $\overline{A}$ data.* Test points tend to lie slightly above the line for theoretical reduction ratios in the region 0.7 to 0.9, and slightly below in the region below 0.7. This trend may be real, as it is consistent with data in Figures 5-19 and 5-20 on bending moments due to static aileron deflections. In those figures, the test data for M_x/δ_a can be seen to exceed the theory by a larger percentage in the region $\eta = 0.6$ to 0.8 than farther inboard.

*The statistical reliability of the psd's at individual frequencies, however, will be much less. If n random quantities, each having the same mean and standard deviation, are added, simulating in a crude way the integration of psd's to give $\overline{A}$'s, the ratio of standard deviation to mean for the sum is equal to this ratio for a single term, divided by $\sqrt{n}$.

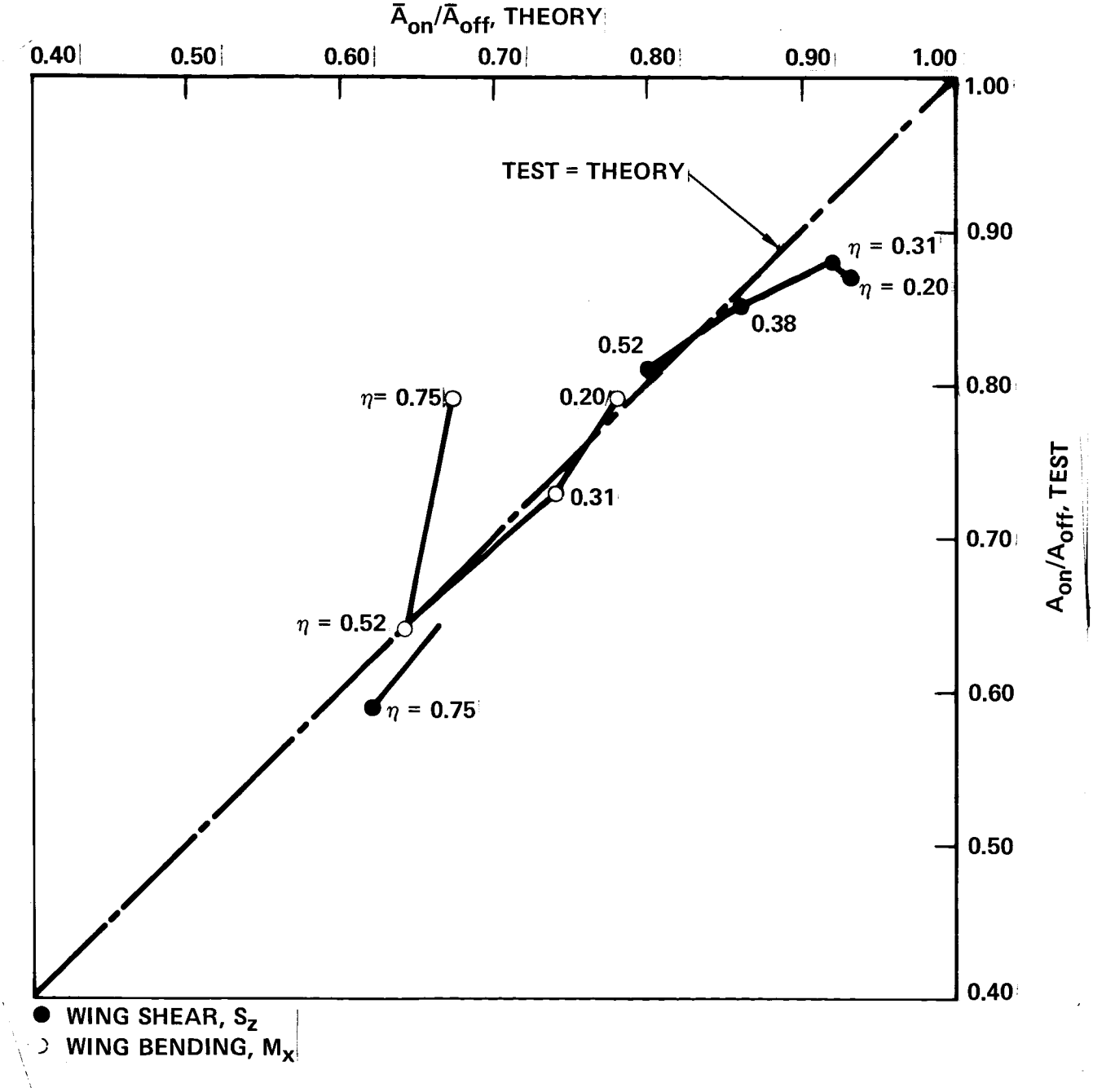

Figure 5-83. Load Reduction Due to Active Controls - Cross Spectrum Method, 1-D Theory - Bursts 1 and 2

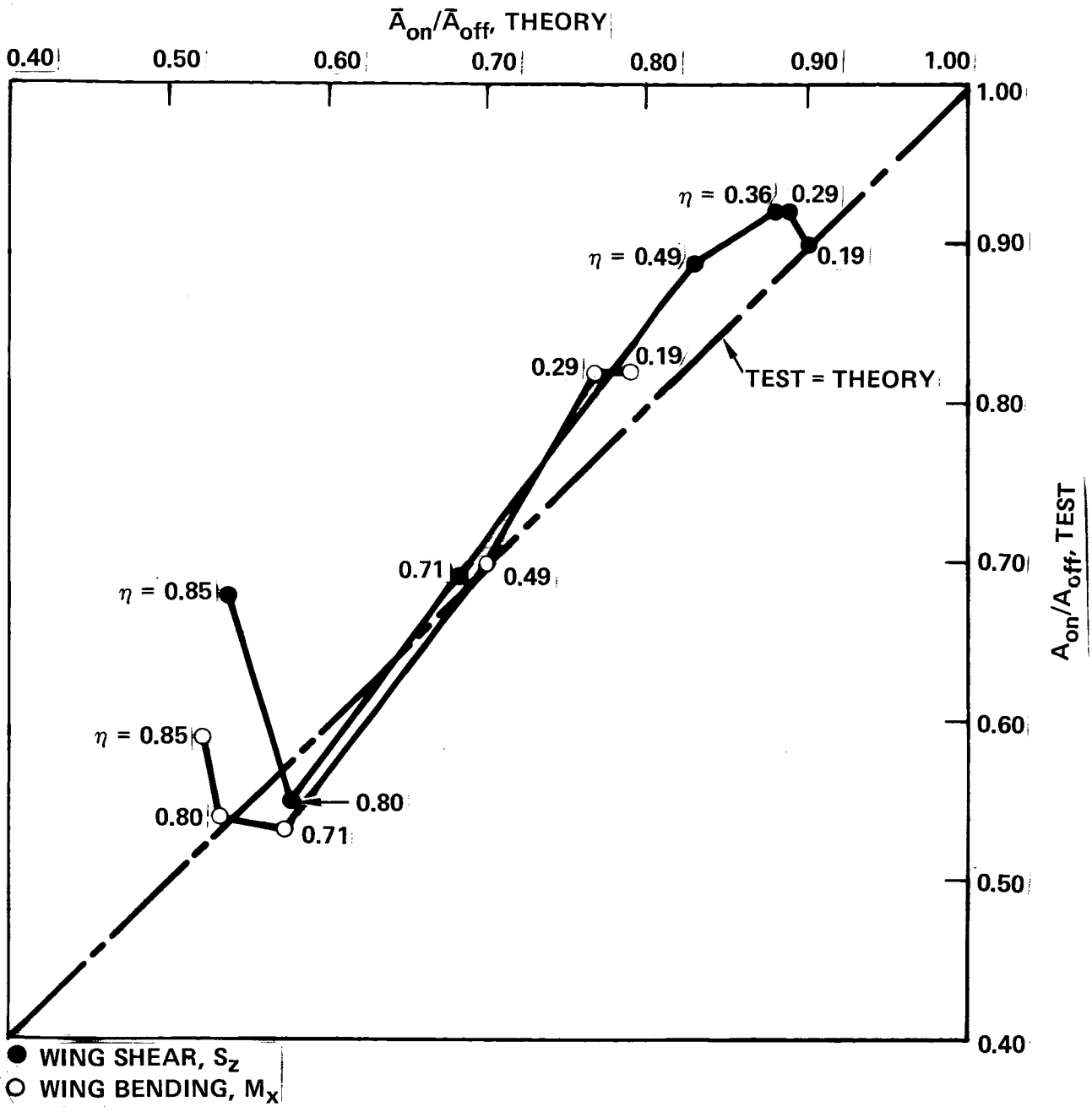

Figure 5-84. Load Reduction Due to Active Controls - Cross Spectrum Method, 1-D Theory - Bursts 3 and 4

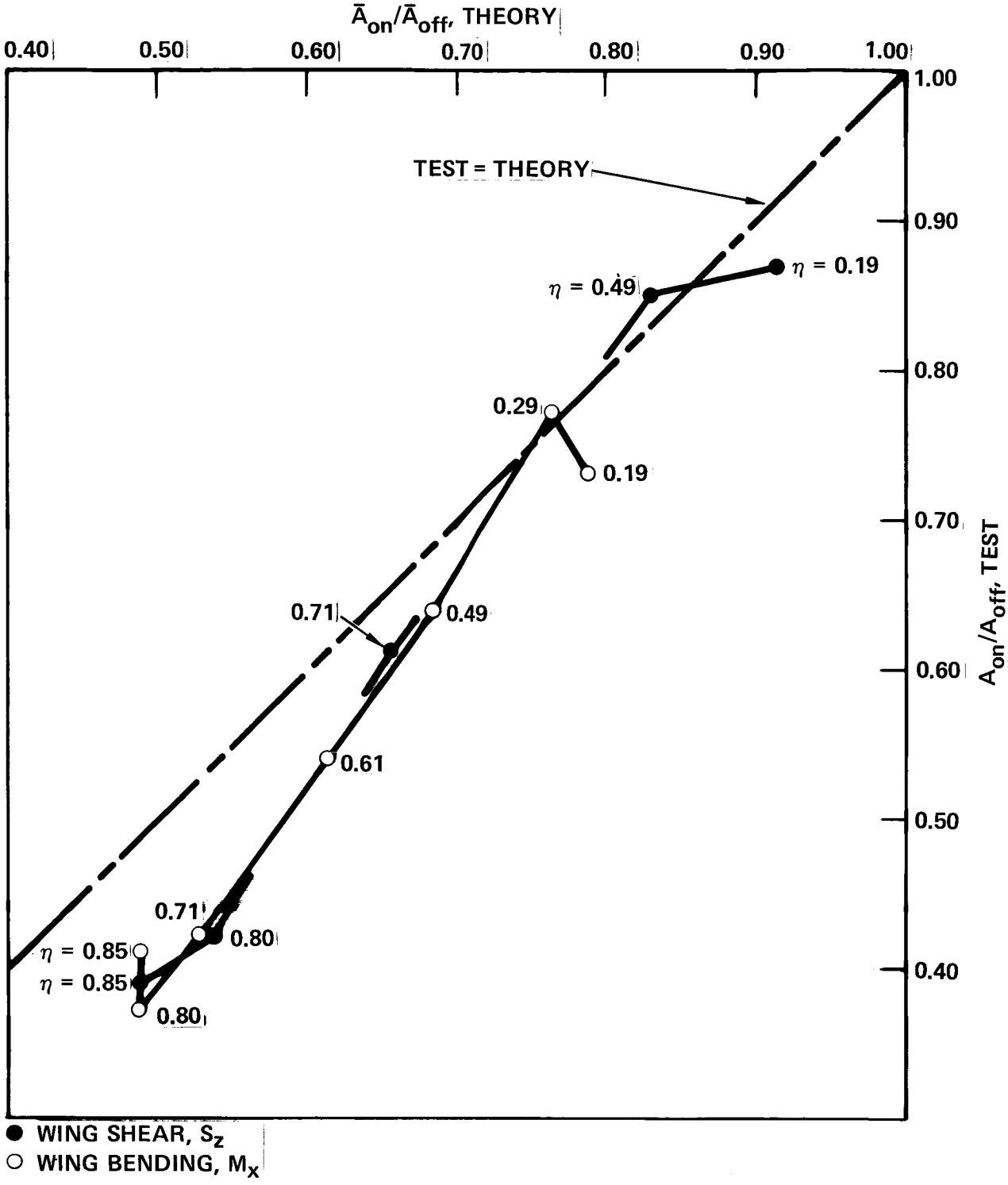

Figure 5-85. Load Reduction Due to Active Controls - Cross Spectrum Method, 1-D Theory - Bursts 5 and 6

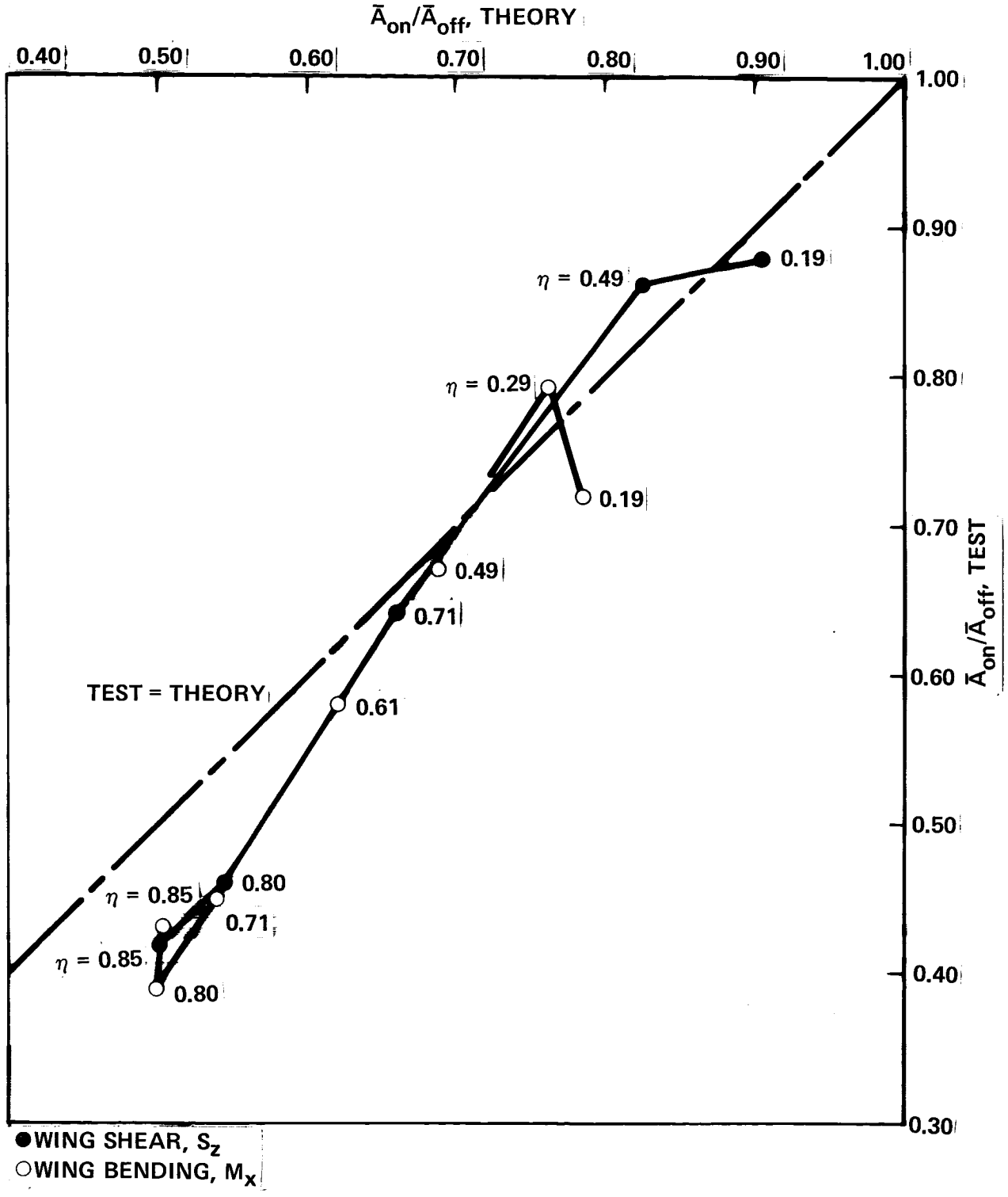

Figure 5-86. Load Reduction Due to Active Controls - Cross Spectrum Method, 1-D Theory - Bursts 5 and 6 with L = 305m (1000 ft)

The fact that shears and bending moments tend to lie on the same curve probably also is a real effect, inasmuch as the bending moment at a given location is very roughly equal to the shear at a more outboard location times a moment arm. It is observed that the range of theoretical reduction ratios for which the test data generally fall below the line - i.e., from 0.50 to 0.70 - includes the bending moments from $\eta = 0.49$ outboard; this is the region of the wing where gust loads tend to be critical for the extended span L-1011.

The one inconsistency appearing between Bursts 3 and 4 and Bursts 5 and 6 is in the higher values for S_z and M_x at $\eta = .85$ in Figure 5-84 than in Figures 5-85 and 5-86. The reason for this difference has not been determined. The shear point in Figure 5-84, however, which is much the farther of the two above the "test = theory" line, appears not to be representative of the data in general. The immediate source of the discrepancy is a relatively high cross-spectrum psd for Burst 4 from 0.1 to 0.4 H_z; this does not show up in bending moment at $\eta = 0.80$ or $\eta = 0.71$, contrary to what one would expect, nor does it show up at all in Burst 6. Inasmuch as this measurement is within the span of the outboard aileron, it may be that the load paths from the aileron into the wing box are such that this gage does not accurately reflect loads originating in the aileron. With airloads due to aileron displacement largely offsetting those due to turbulence in this frequency range, a small error here could lead to a magnified relative error in net shear.

Results of the low-speed, flaps-extended tests are shown in Figure 5-87. The agreement between test and theory is not as consistent as for the cruise speed tests, but the ACS is still seen to do about as well as predicted - and better for the outer wing bending moments. It will be recalled that this flight condition is pertinent only for fatigue. Consequently, shears tend to be much less important than bending moments.

Cross Spectrum Method and 3-D Cross Transfer Functions. The next two figures, Figures 5-88 and 5-89, show the effect of using the 3-D theoretical cross transfer functions instead of the 1-D theory in computing the theoretical $\overline{A}_{on}/\overline{A}_{off}$ ratios. These figures agree fairly closely with the corresponding 1-D plots, Figures 5-84 and 5-86 respectively. They do, however, show a small upward shift of the plotted data relative to the "test = theory" line. Actually the shift is to the left, rather than upwards. The test values of $\overline{A}_{on}/\overline{A}_{off}$ are, of course, unchanged, except for a very small difference related to the theoretical adjustment of the ACS-off $\overline{A}$'s to the ACS-on flight condition.

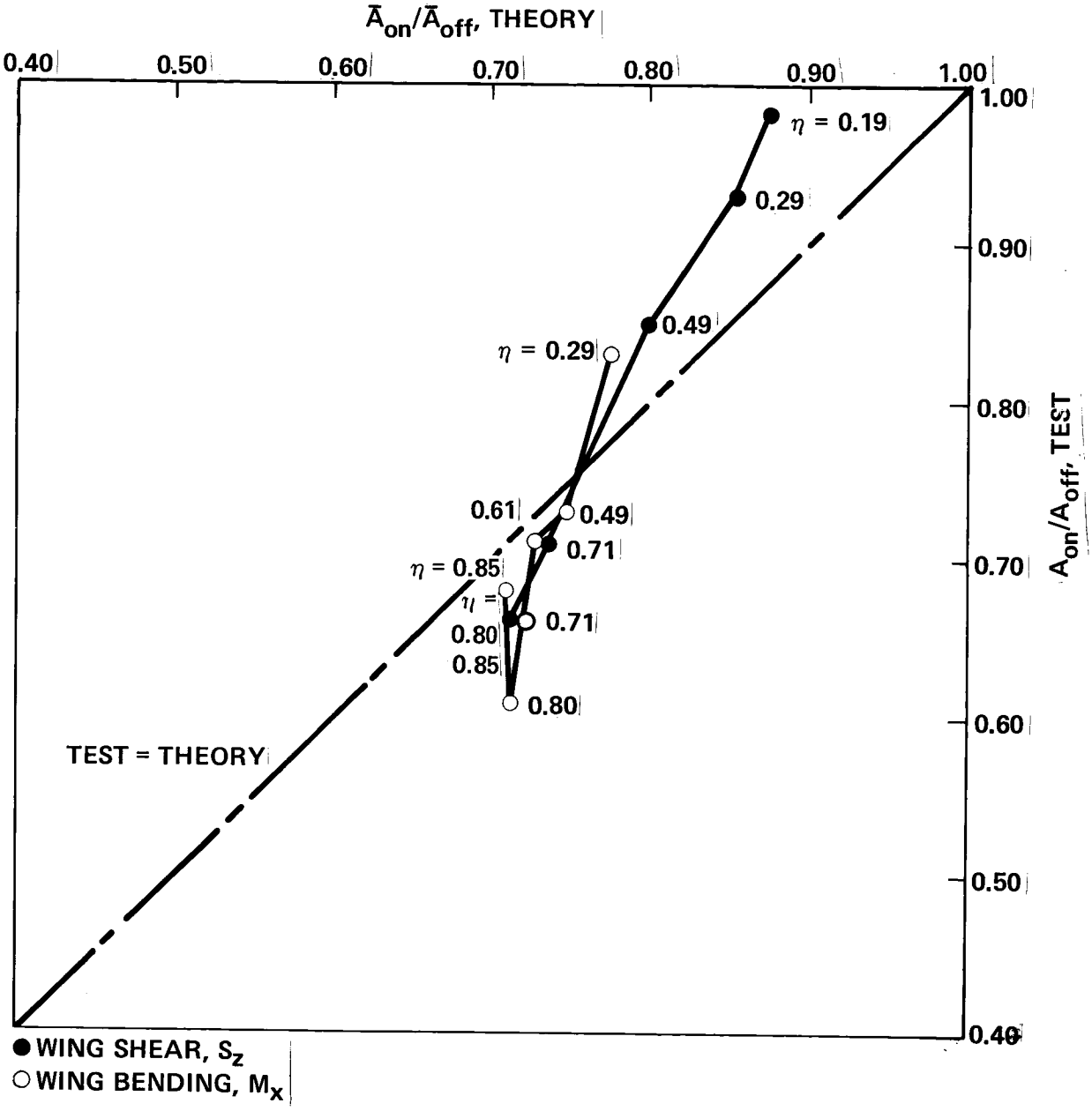

Figure 5-87. Load Reduction Due To Active Controls - Cross Spectrum Method, 1-D Theory - Bursts 9 and 10

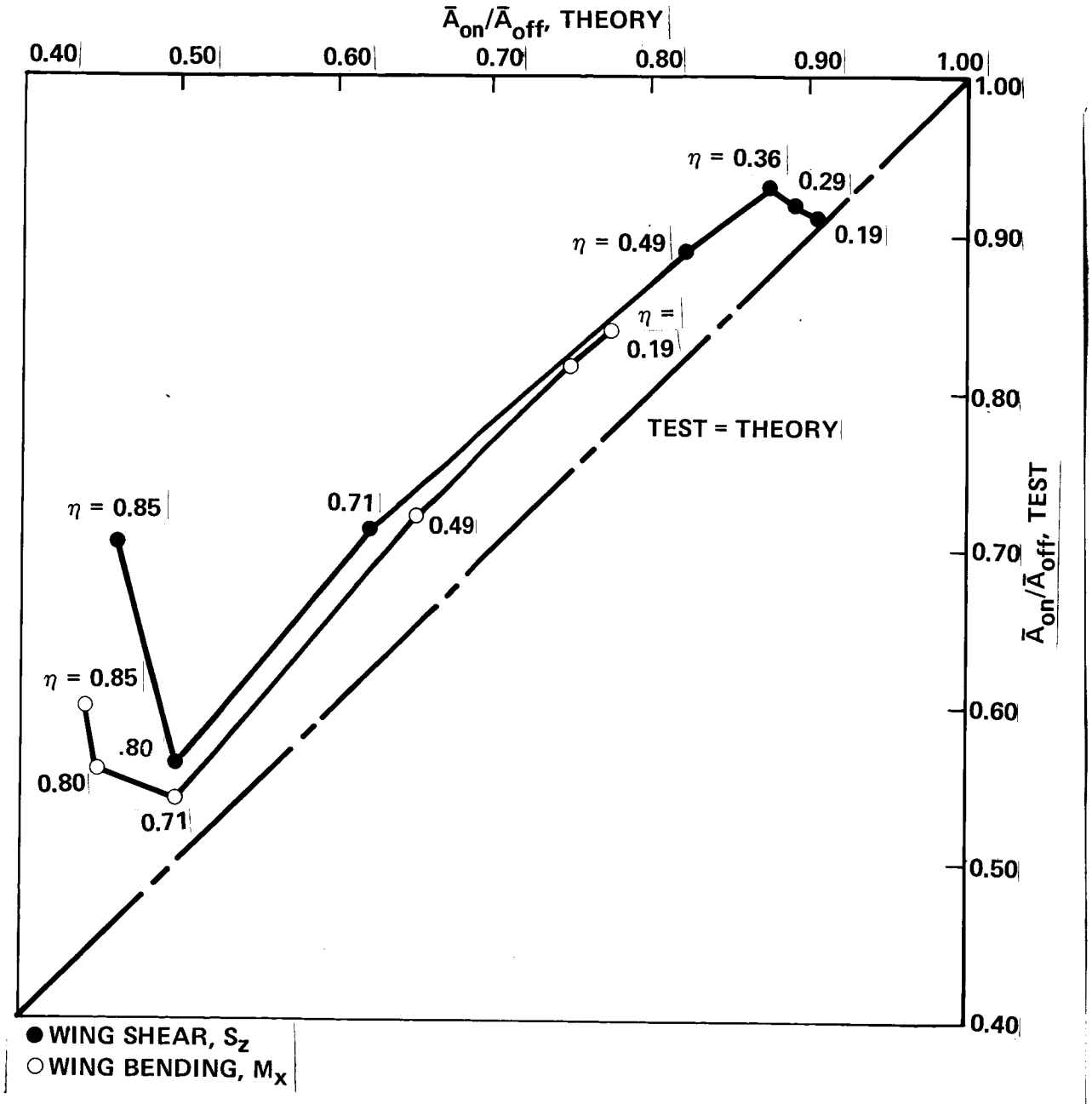

Figure 5-88. Load Reduction Due to Active Controls - Cross Spectrum Method and 3-D Cross Transfer Function Theory - Bursts 3 and 4

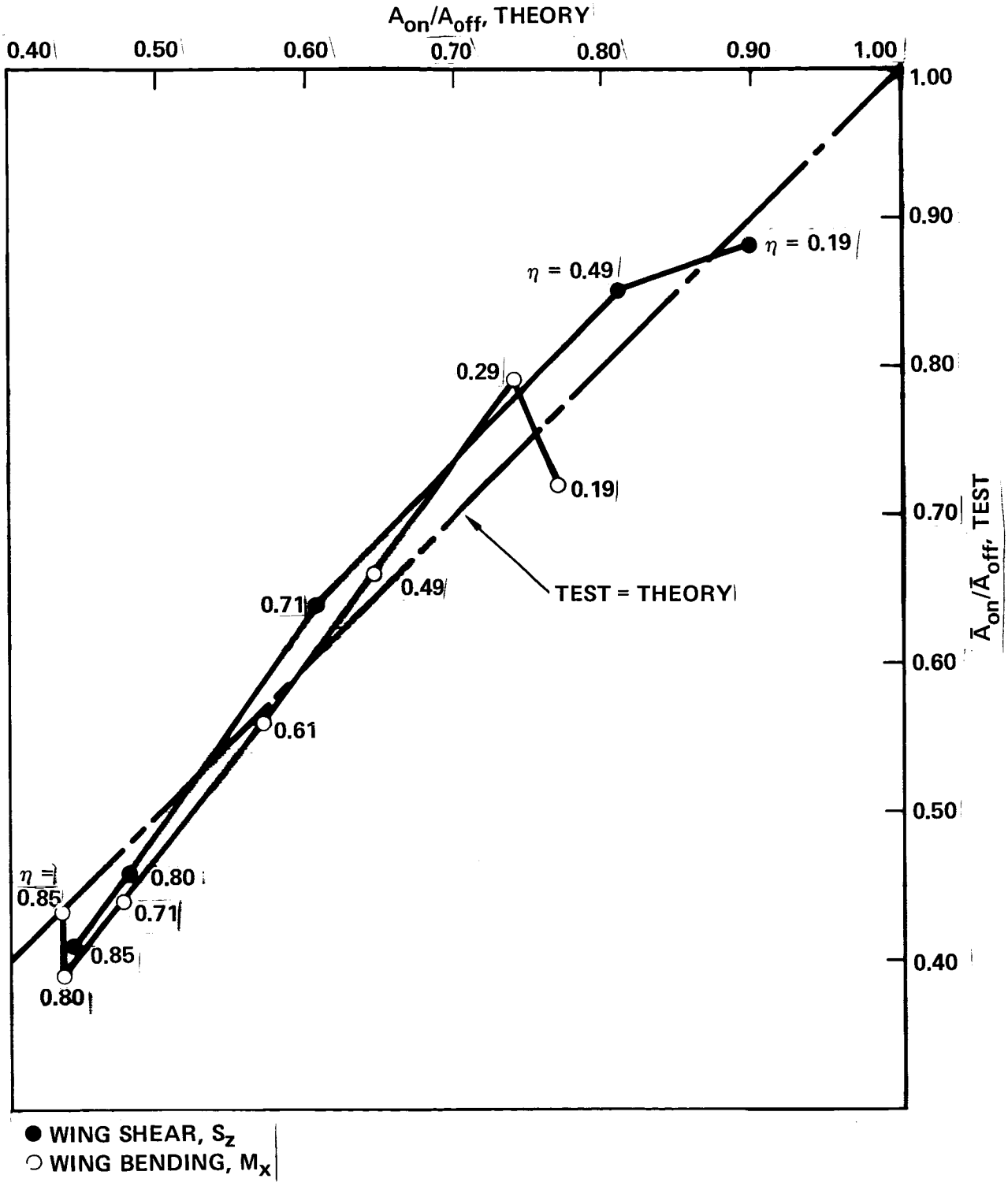

Figure 5-89. Load Reduction Due to Active Controls - Cross Spectrum Method and 3-D Cross Transfer Function Theory - Bursts 5 and 6 with L = 305m (1000 ft)

While the 3-D approach represented by Figures 5-88 and 5-89 appears to be more valid than the 1-D approach represented by Figures 5-83 through 5-86, the various small differences between test and theory that show on the plots may be within the accuracy to which dynamic gust loads can be established without an ACS, at the present state of the art. They may also be within the accuracy with which the effects of the ACS on gust loads can be determined by tests - in particular, tests limited to essentially a single flight condition.

Spectrum Method and 1-D Theory. Similar curves based on spectrum method test data and 1-D theory are shown in Figures 5-90 and 5-91. These must be used with the greatest caution, as they simply do not reflect at all accurately the actual ACS effectiveness. Indeed, the difficulty to be expected in drawing valid conclusions from these data is suggested at once by the vast difference between these two figures.

One of the major differences between the spectrum-method and cross-spectrum-method data is that the spectrum-method data include the effect of pilot control inputs, in both pitch and roll. In much of the test data, these are substantial. So far in this report, pilot inputs have been mentioned primarily in terms of their effect on the relation between spectrum-method and cross transfer functions, especially as reflected in the coherency function. In particular, it has been noted that any difference between spectrum-method and cross transfer functions below about 0.5 to 1.0 Hz is in all likelihood due primarily to pilot inputs.* Any difference between the two types of transfer function, however, will show up also in the psd's obtained therefrom. It will also show up, in turn, in the resulting $\overline{A}$'s. In terms of psd's, the effect of pilot input is clearly evident, for example, in Figure 5-71 (page 5-114); the area between the spectrum and cross-spectrum curves at frequencies up to about 0.5 to 1.0 Hz can be considered to be due almost entirely to pilot input. With $\overline{A}$ given by the square root of the area under the psd curve, the large contribution of pilot input to the spectrum-method $\overline{A}$ is evident.

Two significant effects of pilot input are discussed more fully in a later section, "Effect of Pilot Control Inputs" starting on page 5-166.

---

*Specific evidence that such differences are indeed due to pilot inputs is listed in the footnote on page 5-167, in connection with a more extensive discussion of the effects of pilot inputs.

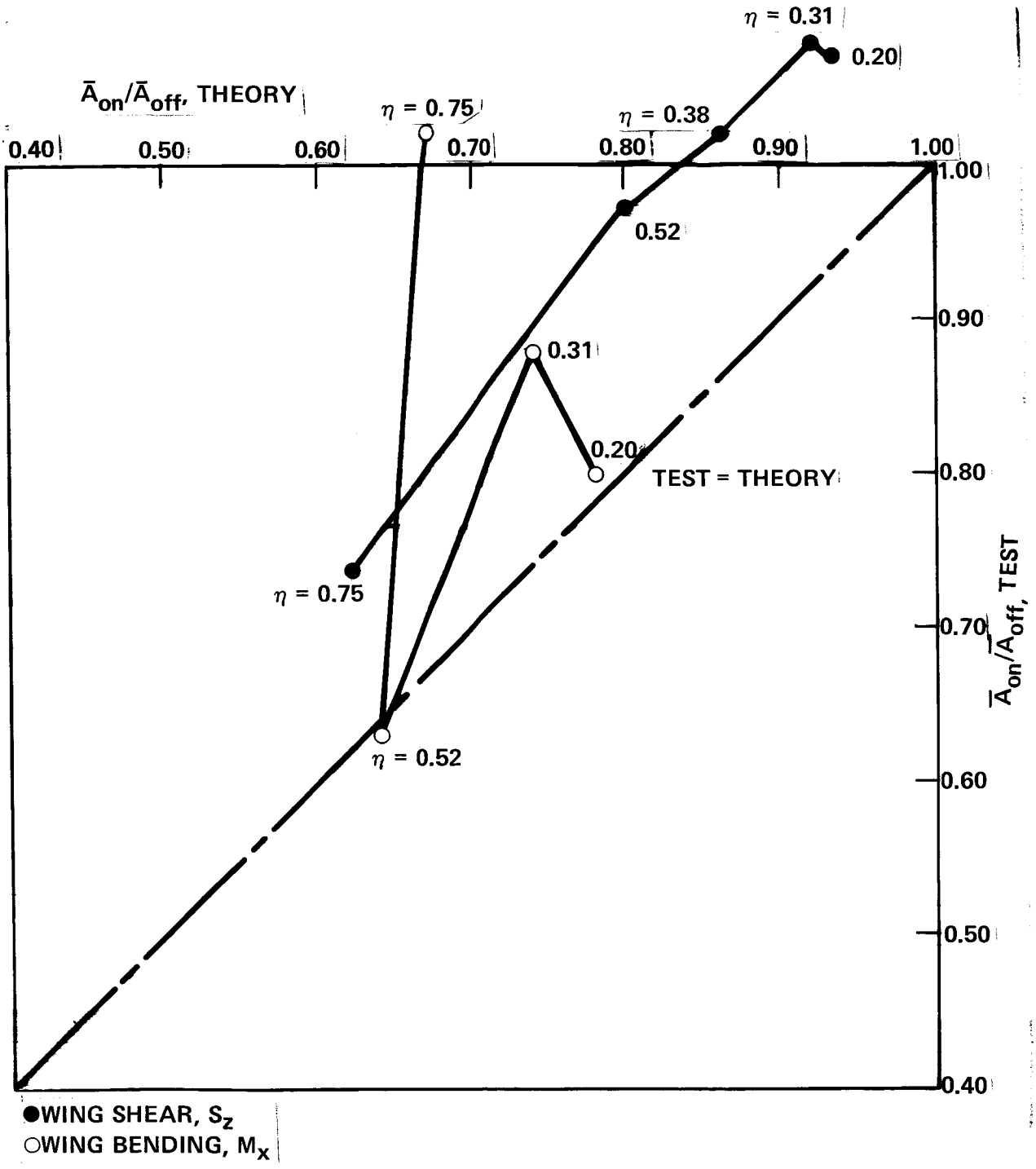

Figure 5-90. Load Reduction Due to Active Controls - Burst 1 and 2 - Spectrum Method and 1-D Theory

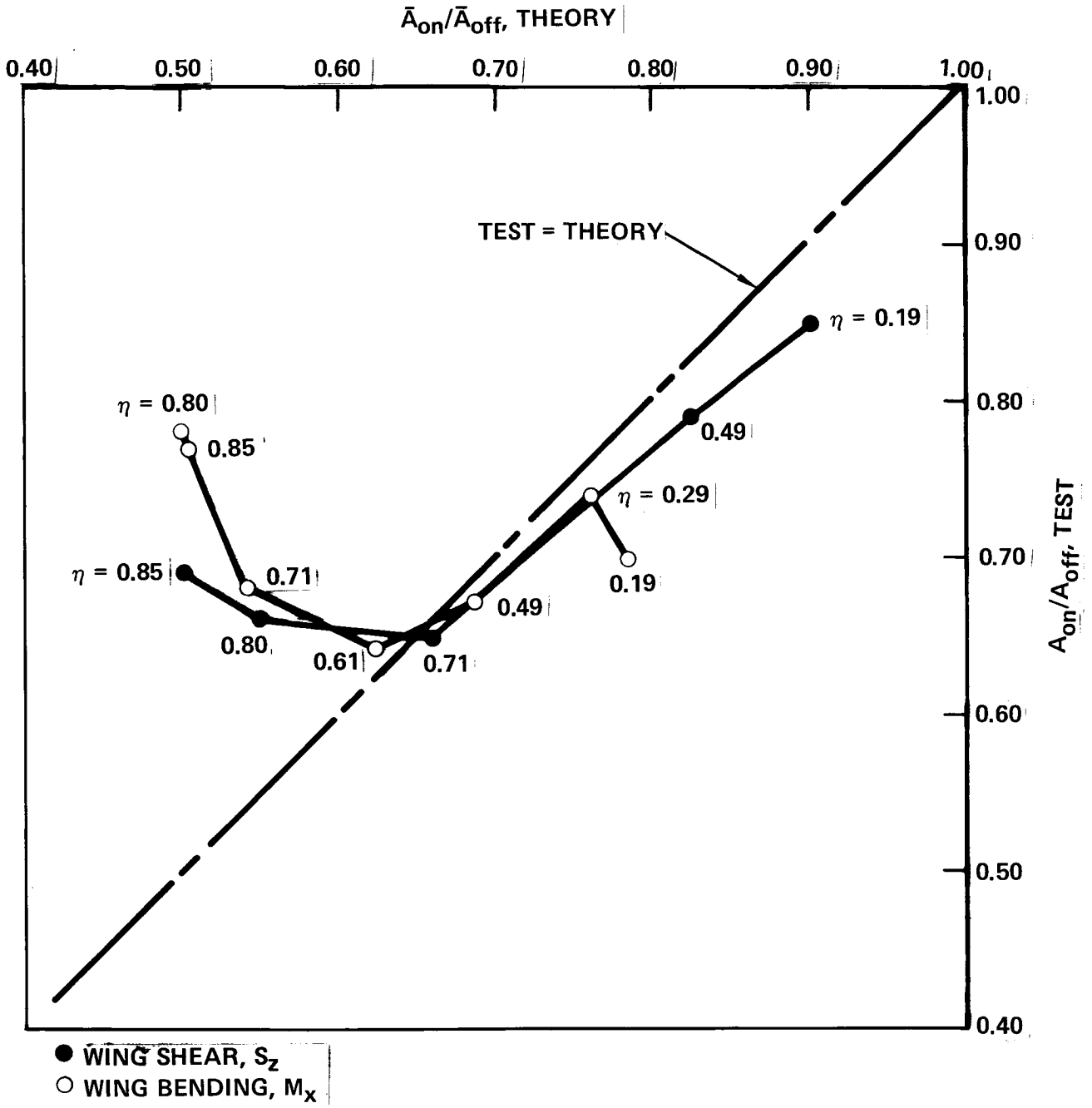

Figure 5-91. Load Reduction Due to Active Controls - Bursts 5 and 6 with L = 305m (1000 Ft) - Spectrum Method, 1-D Theory

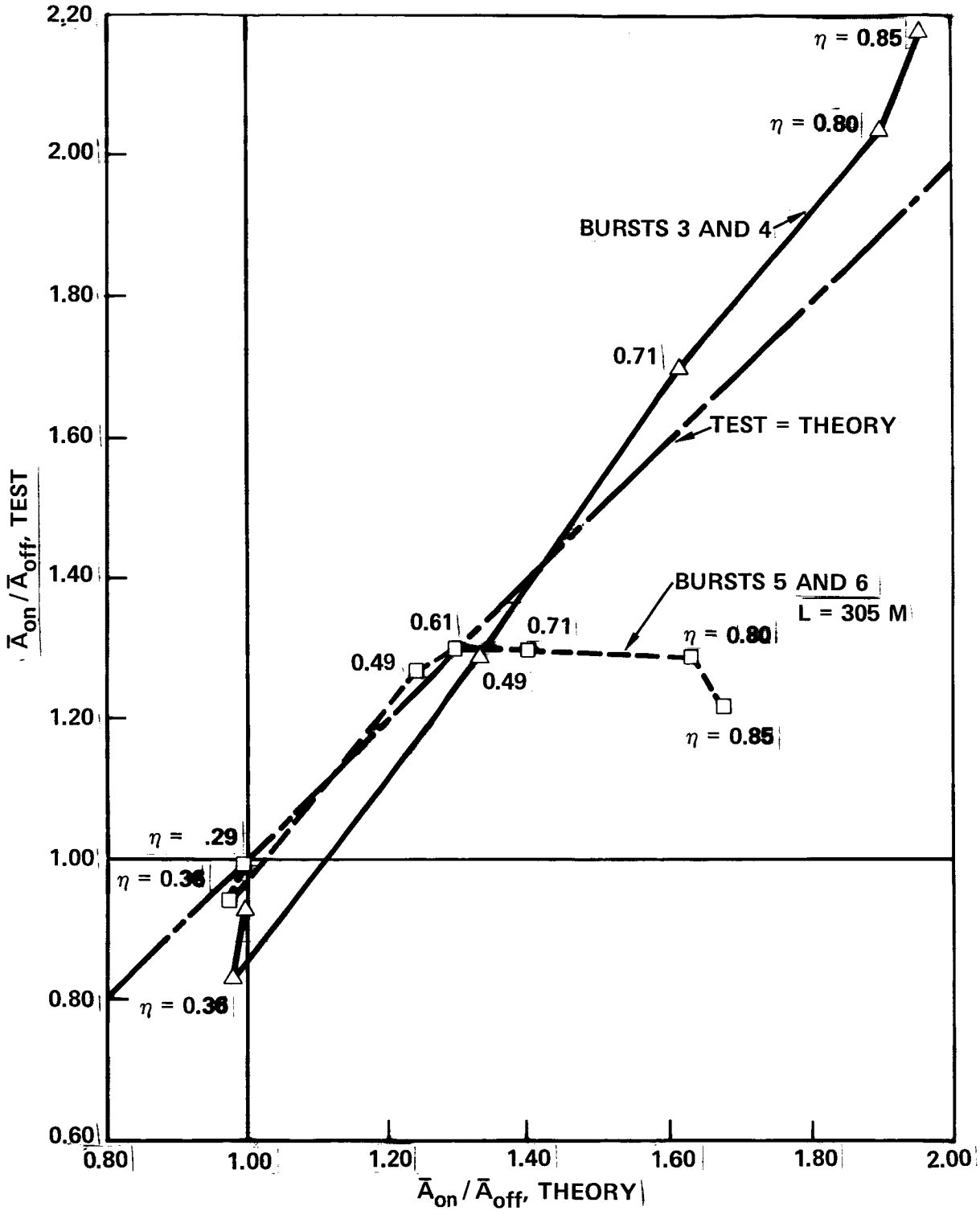

Figure 5-92. Wing Torsion Due to Active Controls Cross Spectrum Method and 1-D Theory

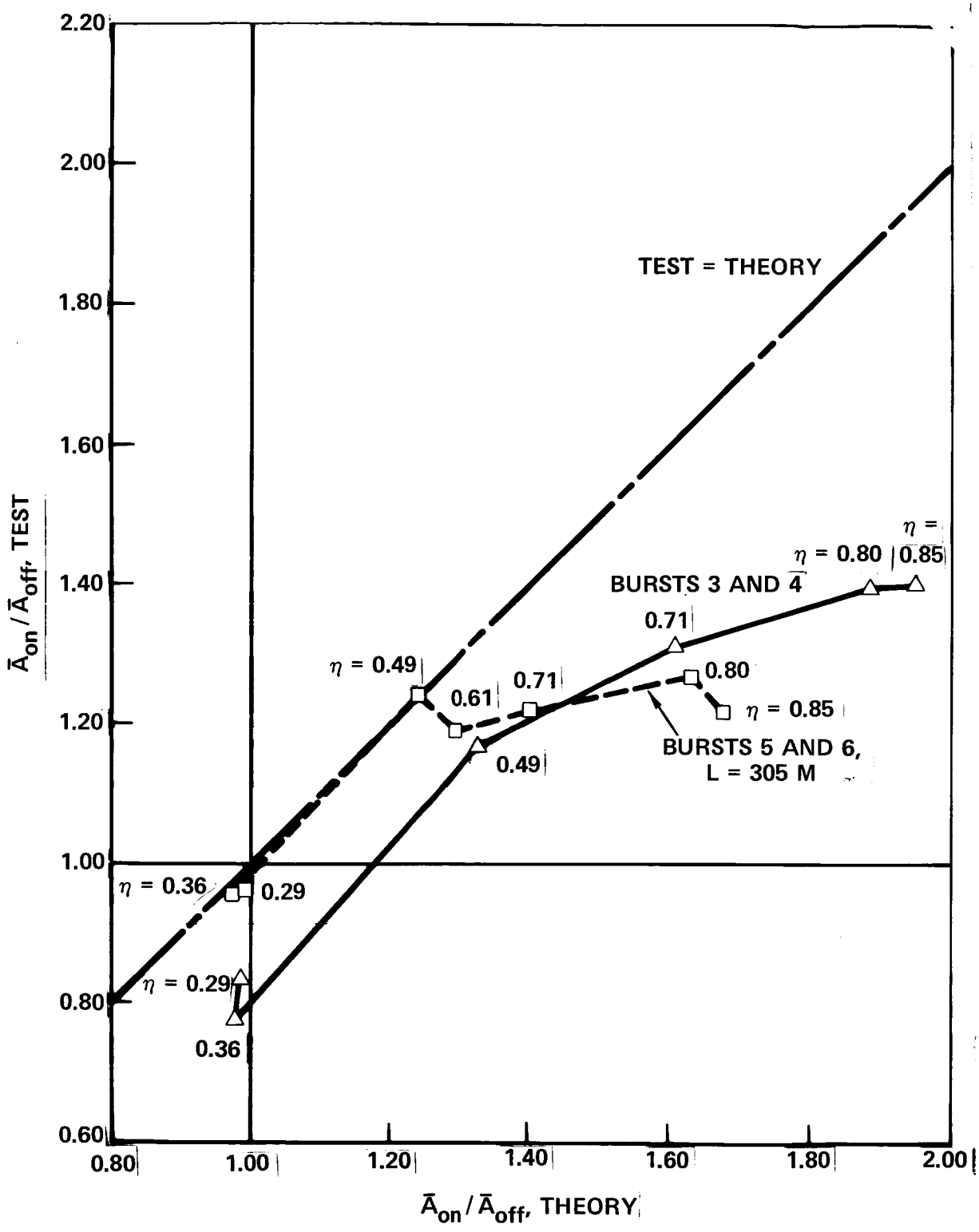

Figure 5-93. Wing Torsion Due to Active Controls Spectrum Method and 1-D Theory

First, pilot inputs are found to vary substantially and apparently randomly from burst to burst, so that any comparison of ACS-on with ACS-off data can be virtually meaningless. Returning to $\overline{A}_{on}/\overline{A}_{off}$ test to theory comparisons, Figure 5-90, for Bursts 1 and 2, reflects a situation in which the pilot inputs are substantially greater ACS-on (Burst 2a) than ACS-off (Bursts 1a and 1b). For shears at several locations, the greater pilot inputs more than make up for the reductions due to the ACS!

Second, in Figure 5-91, the distinctive shape of the curve — much different from that of Figure 5-90 — is characteristic of the effect of roll control inputs, even when the same for ACS-on and ACS-off bursts.

Wing Torsions. The effect of the ACS on wing torsions is shown in Figures 5-92 and 5-93. Torsions are expected to increase as a result of using outboard ailerons for wing load reduction; and these higher torsions are, of course, accounted for in the design loads. Ordinarily the structural weight increases due to the higher torsions are a very small fraction of the reductions due to the lower bending loads. Figure 5-92 is based on cross-spectrum test data and 1-D theory and Figure 5-93 on spectrum method test data and 1-D theory. Both figures show data for Bursts 3 and 4 and Bursts 5 and 6 (with L = 305 m). The test data generally fall close to or below the 45 degree "test = theory" line.

Response PSD's

Various response psd's are shown in Figures 5-94 through 5-101 and 5-103, 5-104. The figures are selected primarily from Bursts 3 and 4 and Bursts 5 and 6, the extended-span cruise-speed cases. Two figures from the baseline tests, however, are also included.

In all of these figures, the psd's shown are those given by the Von Karman gust psd in conjunction with the appropriate measured or theoretical transfer. function. A scale of turbulence of 762 m (2500 ft) was used for Bursts 1, 2, 3, and 4, and 305 m (1000 ft) for Bursts 5 and 6. The dash line shows the theoretical psd obtained using the 3-D cross transfer function.* The 1-D theoretical curves, not shown in the figures, would relate to the curves shown approximately as illustrated by Figure 5-71. Thus at the short-period psd peak at about 0.3 Hz,

*For Bursts 1 and 2, although the original data processing utilized only 1-D theory, 3-D computer runs were made later. The theoretical curves on these figures were hand plotted from these runs.

the 1-D theoretical curves would be very slightly higher than the curves shown. At the elastic mode peak at about 1.5 Hz, they would be 2 to 2.5 times as high. It might be remarked that the dotted line in Figure 5-71 indicates only that part of the 3-D psd that is coherent with the vertical gust velocity on the airplane centerline. The full 3-D psd would lie approximately midway between the two curves shown. The solid lines in Figures 5-94 through 5-104 show the flight data psd's - the heavy line the cross-spectrum values and the lighter line the spectrum-method values. The major emphasis in the present discussion is on the validity of the modeling as indicated by comparisons of the curves based on theoretical and measured cross transfer functions. Some observations are also made, however, with respect to the relation between spectrum-method and cross-spectrum-method measured psd's.

It is noted that in all of the figures the scales are the same in the upper and lower parts of the figure, to facilitate comparison. Also, the scales are the same for Bursts 3 and 4 as for Bursts 1 and 2; for Bursts 5 and 6 the scales are compressed by a factor of 2 or 2.5, approximately the factor 1.842 associated with the reduced scale of turbulence as noted under "Integrated Data - $\overline{A}$ Values" in Section 5.7.6.

Body Accelerations. Figures 5-94 through 5-96 compare psd's for body acceleration. The elastic-mode contributions are seen to be relatively small. For Burst 1 (baseline tests, ACS off), the agreement between theory and test (cross-spectrum method) is seen to be very good. The theoretical effect of the active controls (Burst 2) is seen to be small, as expected. The MLC/EMS reduces wing loads with only a very secondary effect on CG acceleration; and, as noted in Section 4.5, the constraints imposed on the synthesis of the GA function made it difficult to achieve a significant load reduction by this means. With ACS-on (Burst 2) the test curve is seen to be much less smooth, as a result of the shorter data sample (4 vs 9 blocks), and probably also the greater contamination by other inputs, suggested by the greater difference between cross-spectrum and spectrum method curves. But a faired curve would again agree closely with theory. The considerably greater difference between the two test curves (spectrum and cross-spectrum) ACS-on than ACS-off suggests a comparable increase in the magnitude of pilot inputs in pitch. This is believed to be unrelated to the presence of the active controls, inasmuch as no change in handling qualities has been evident to the pilots.

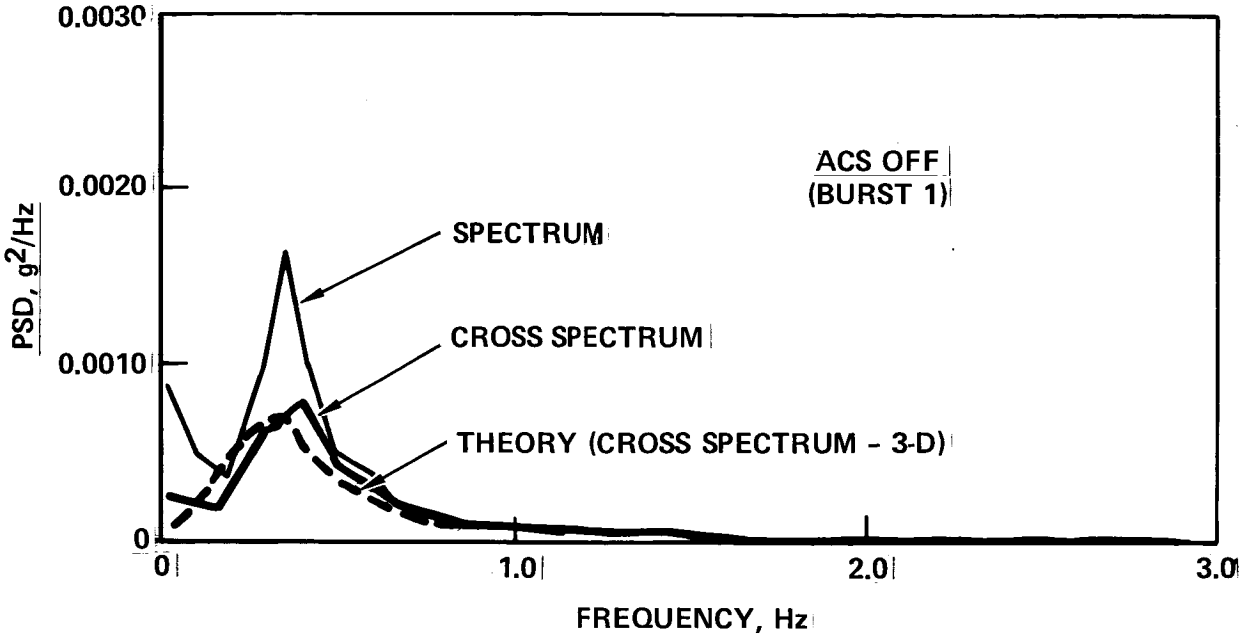

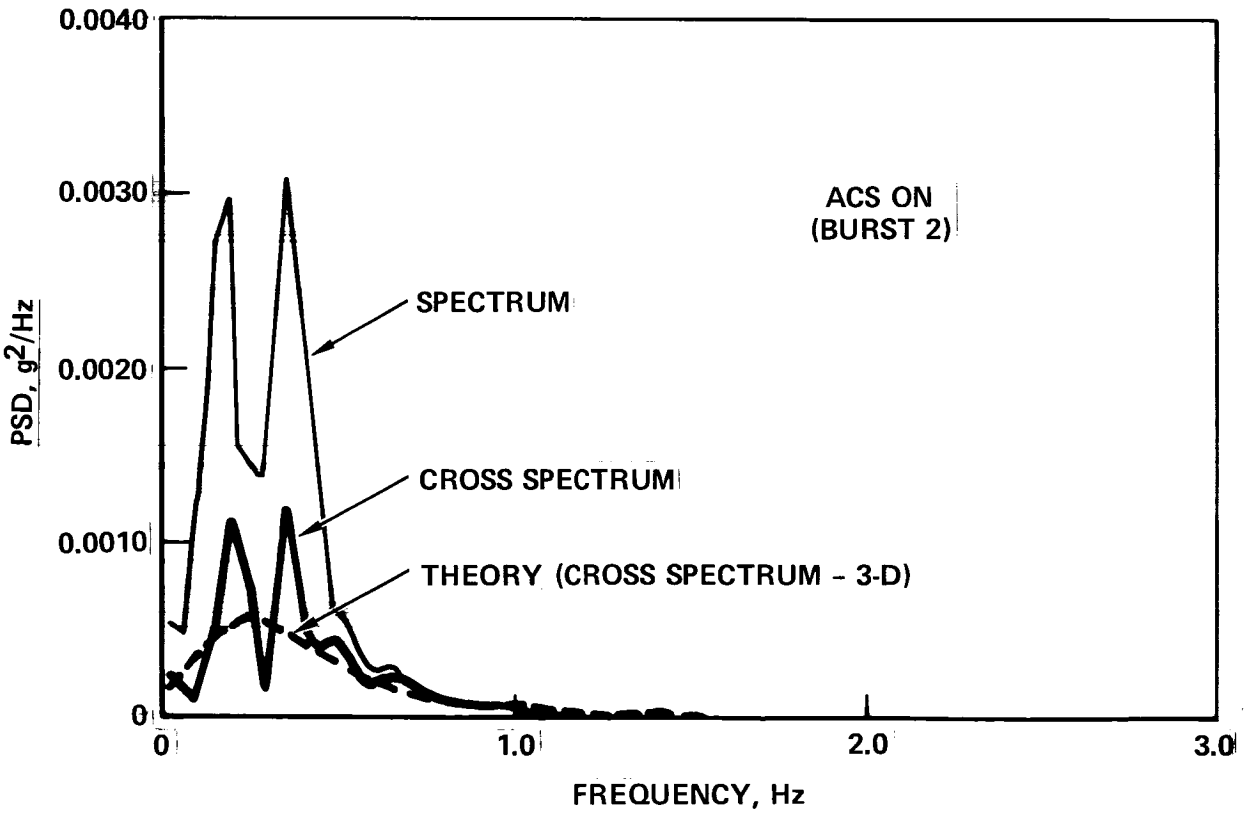

Figure 5-94. PSD of Fuselage C.G. Acceleration - Bursts 1 and 2

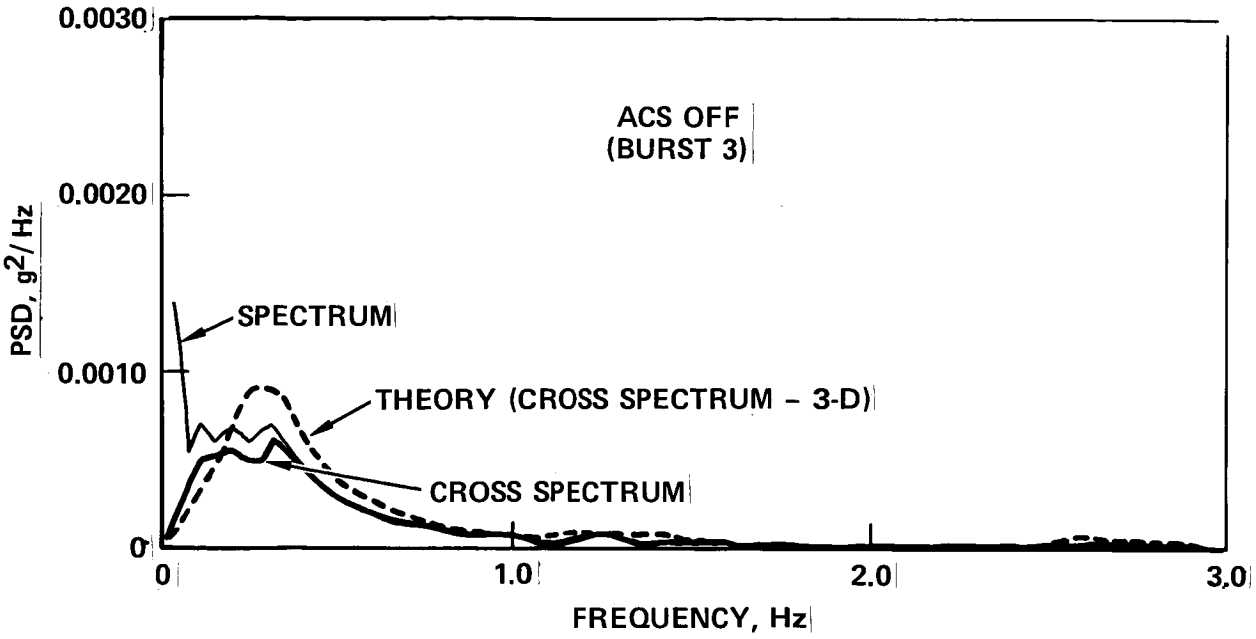

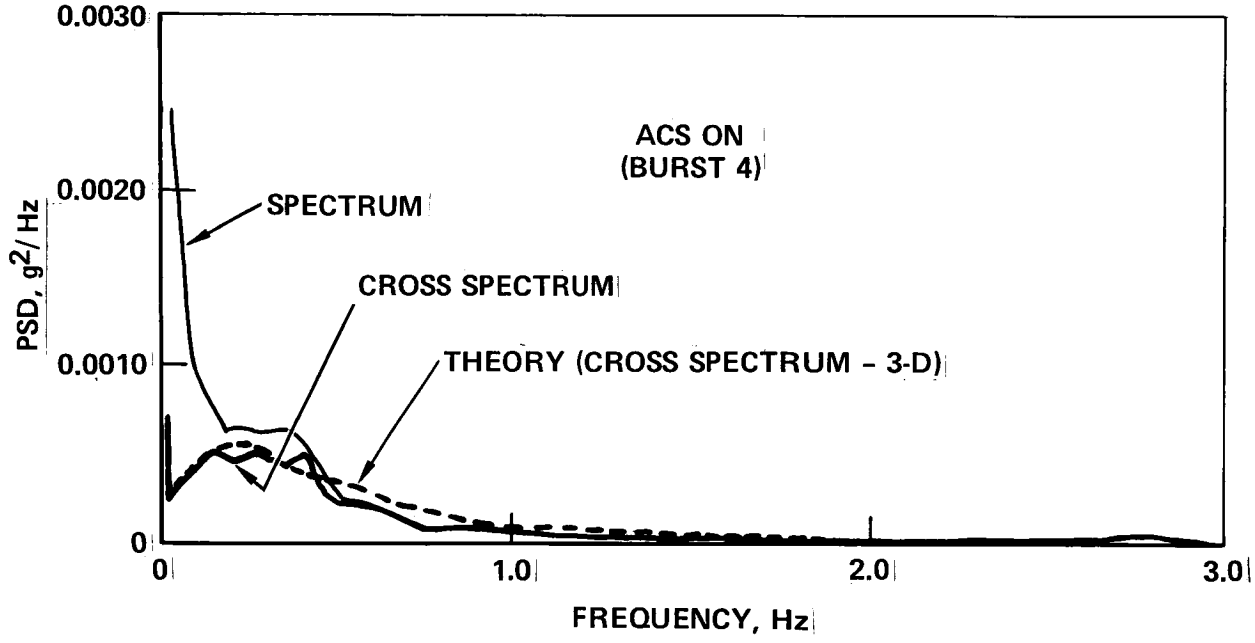

Figure 5-95. PSD of Aftbody Acceleration - Bursts 3 and 4

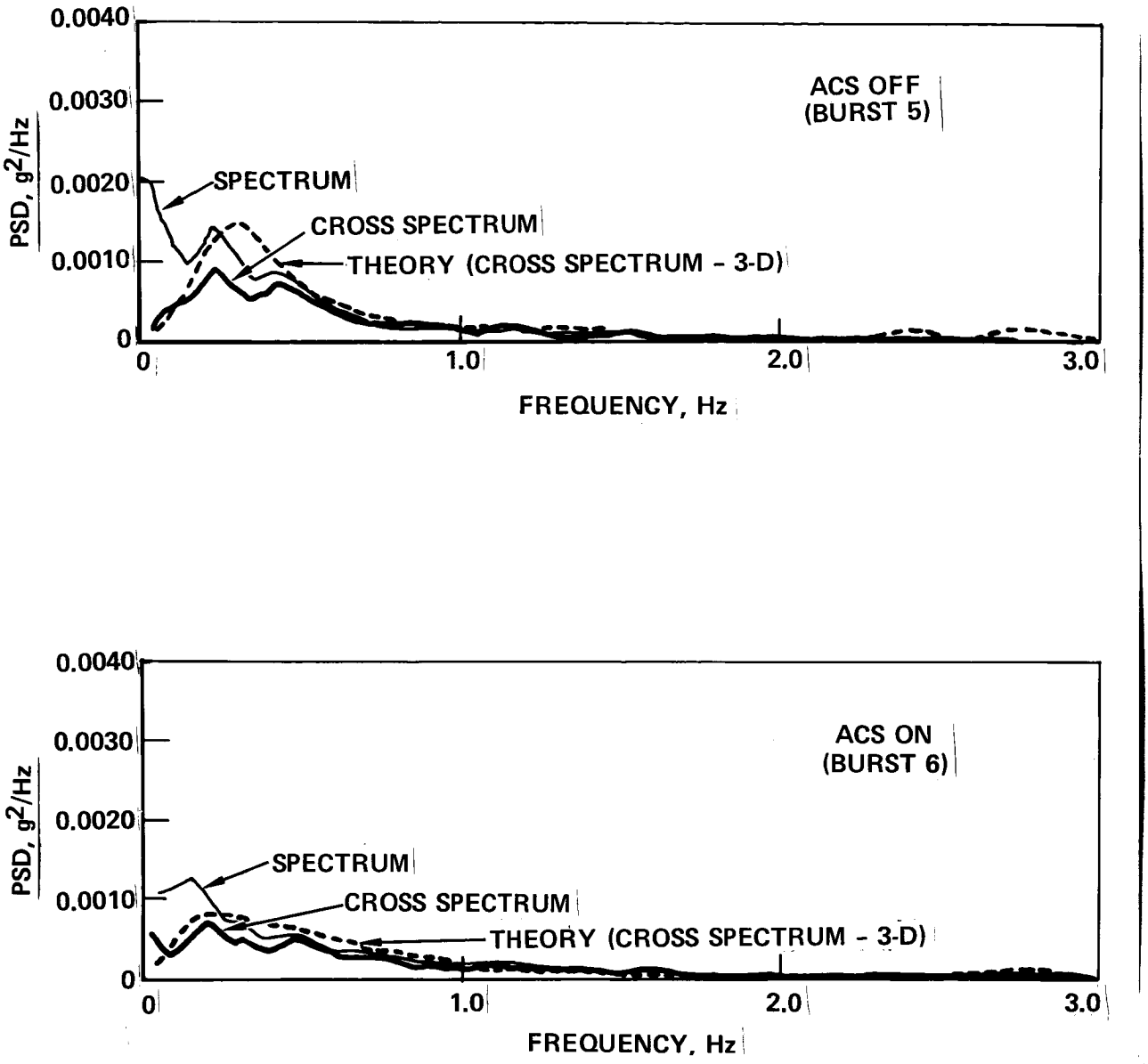

Figure 5-96. PSD of Aftbody Acceleration - Bursts 5 and 6 with L = 305m (1000 ft)

In the extended-span tests (Figures 5-95 and 5-96), the ACS results in a somewhat greater reduction in the theoretical short period psd peak. This is due to the increase in pitch damping resulting from the much higher GLA gain on the $\dot{\theta}$ feedback. (The reduction in psd is largely confined to the immediate vicinity of the resonance peak, however, so the effect on area under the curve is much less). In these tests, the measured curves fall somewhat below the theoretical. Also, in all four cases, the difference between spectrum and cross-spectrum test curves is smaller, indicating less pilot maneuver input.

Root Bending Moment. Figures 5-97 and 5-98 compare psd's for wing bending moment near the wing root ($\eta = 0.29$). With ACS off (Bursts 3 and 5), response peaks corresponding to the longitudinal short period mode (0.3 Hz) and first wing bending mode (1.5 Hz) are clearly evident. The test curves are below the theoretical at both short-period and elastic-mode peaks. Comparing the theoretical curve for Burst 4 with 3, or Burst 6 with 5, it is seen that the active controls are predicted to reduce both the short period and elastic-mode peaks. Reductions approximately as predicted by theory are indicated by the test data.

Bending Moment at $\eta = 0.71$. Psd's of bending moment at $\eta = 0.71$ ($\eta = 0.75$ for the baseline tests) are shown in Figures 5-99, 5-100, and 5-101. Here the theory indicates a major reduction in load due to the active controls in the short-period region - even greater for the extended span than the baseline tests, probably because of the larger aileron. The theory continues to indicate a good reduction in the elastic-mode region. It is interesting to observe that for the baseline airplane, with ACS off, the elastic-mode and short-period peaks are of comparable magnitude (Burst 1), whereas with extended span (Bursts 3, 5), the elastic mode peak is much lower than the short-period peak. The short-period peak is, of course, higher because of the tip extension. The elastic mode peak actually stays about the same, probably because of the very small additional mass and an increase in aerodynamic damping in the mode.

For bending moment at this location, the reductions due to the ACS in the elastic mode region are seen to be roughly as predicted by theory, for the extended span airplane (Figures 5-100 and 5-101), and perhaps even greater than predicted for the baseline airplane (Figure 5-99).

In the region of the short-period response, the effectiveness of the active controls is somewhat clouded, in Bursts 1 and 2 and Bursts 5 and 6, by distortions

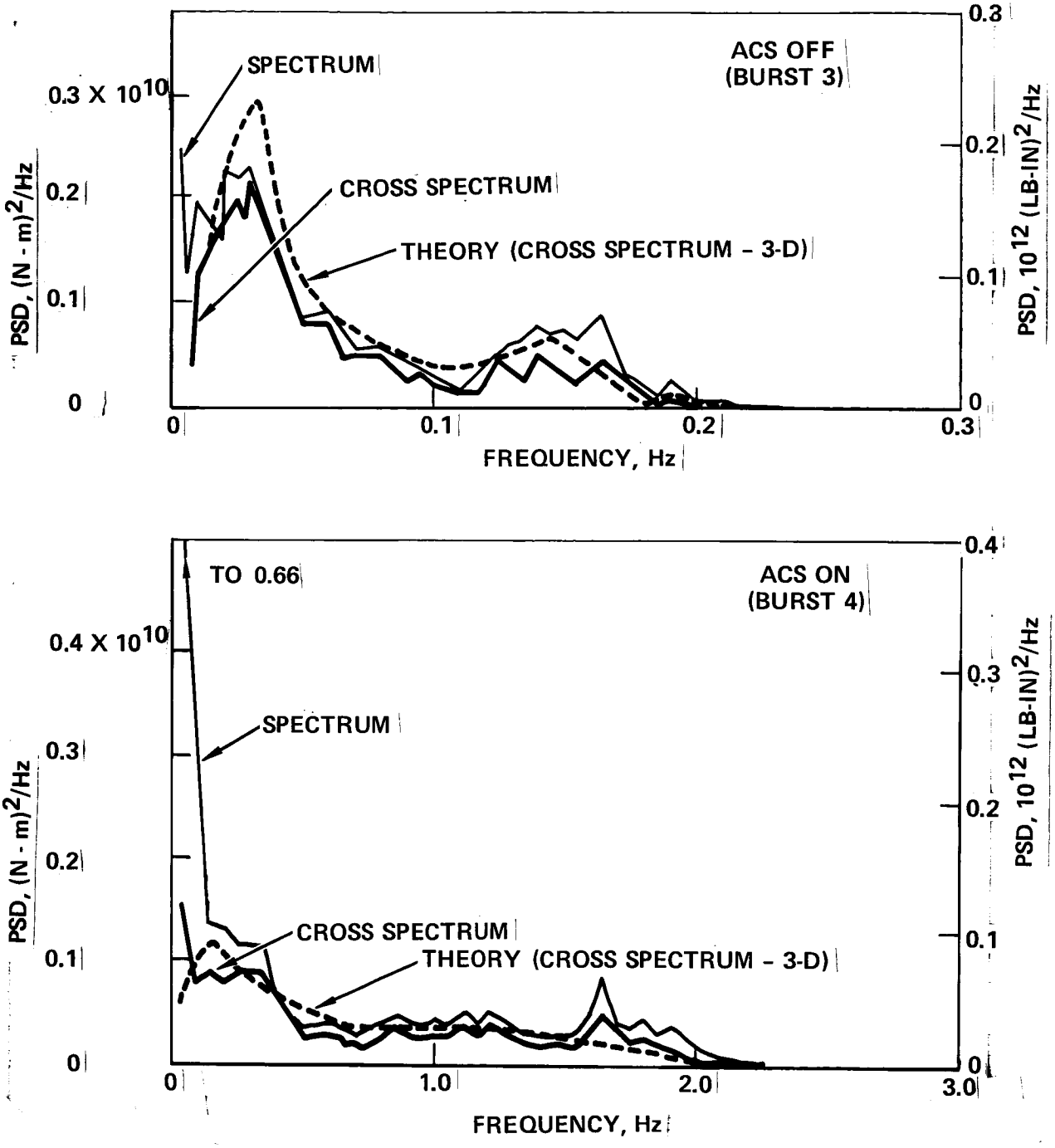

Figure 5-97. PSD of Wing Bending at η = 0.29 - Bursts 3 and 4

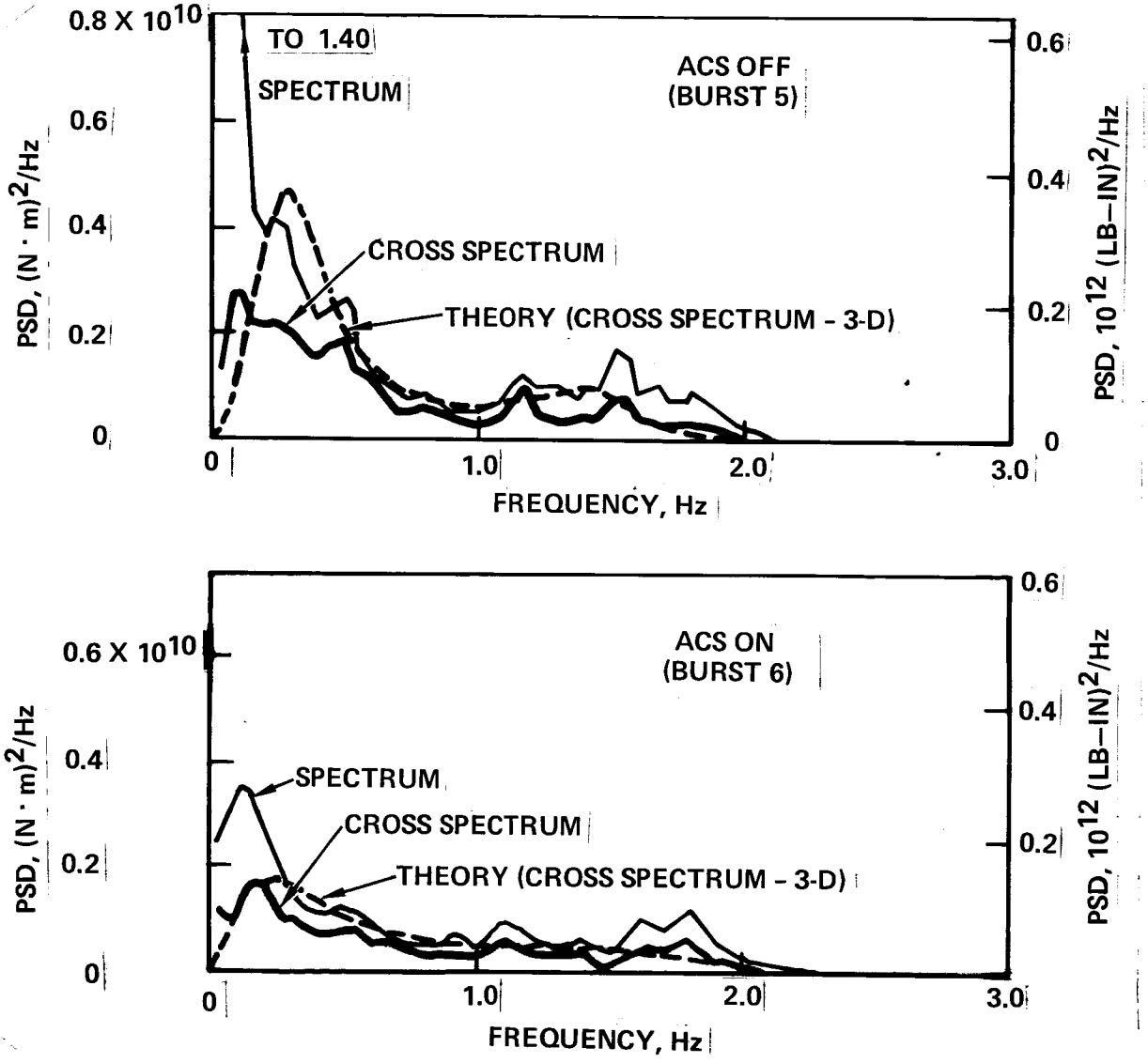

Figure 5-98. PSD of Wing Bending at η = 0.29 - Bursts 5 and 6 with L = 305m (1000 ft)

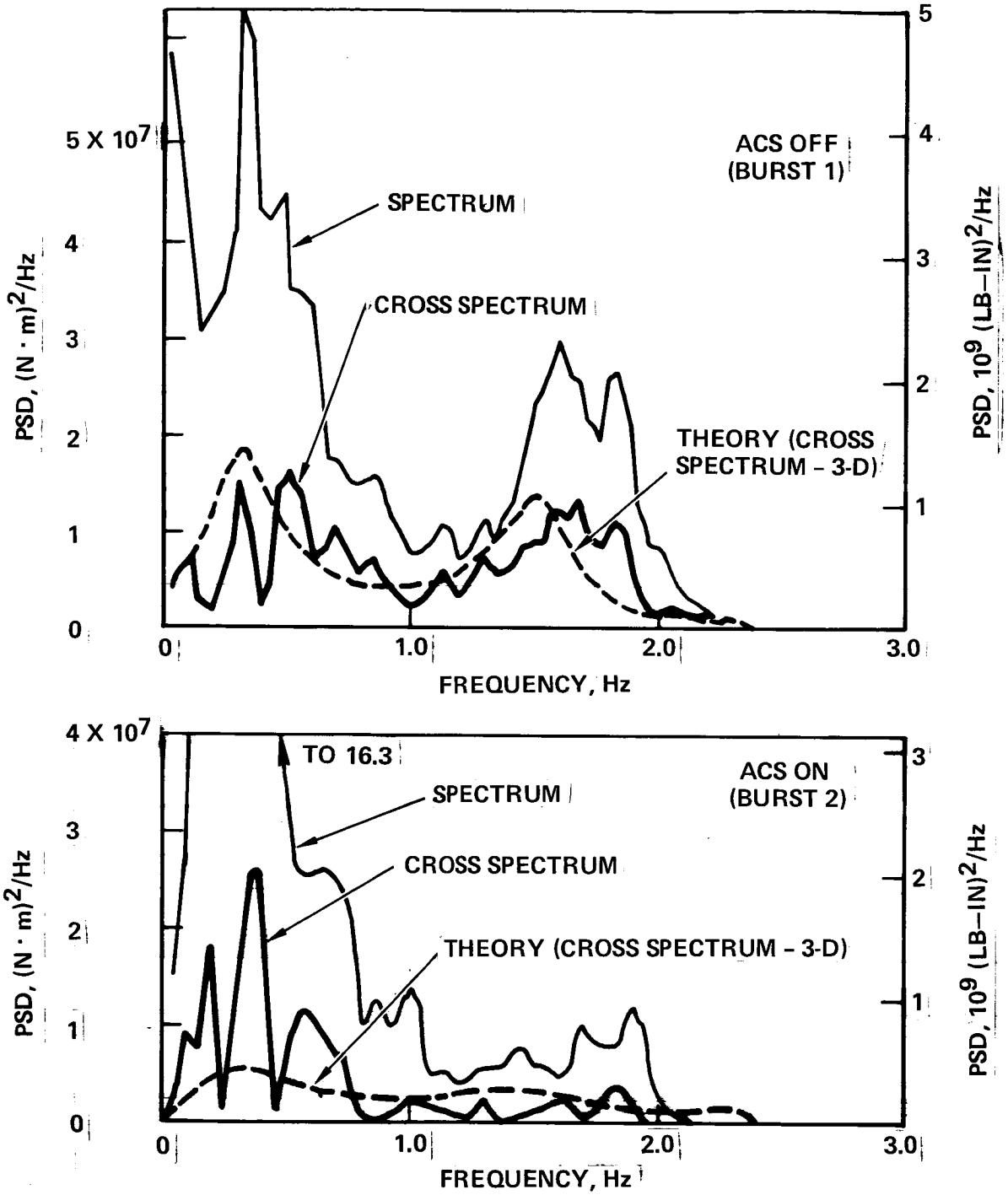

Figure 5-99. PSD of Wing Bending at η = 0.75 - Bursts 1 and 2

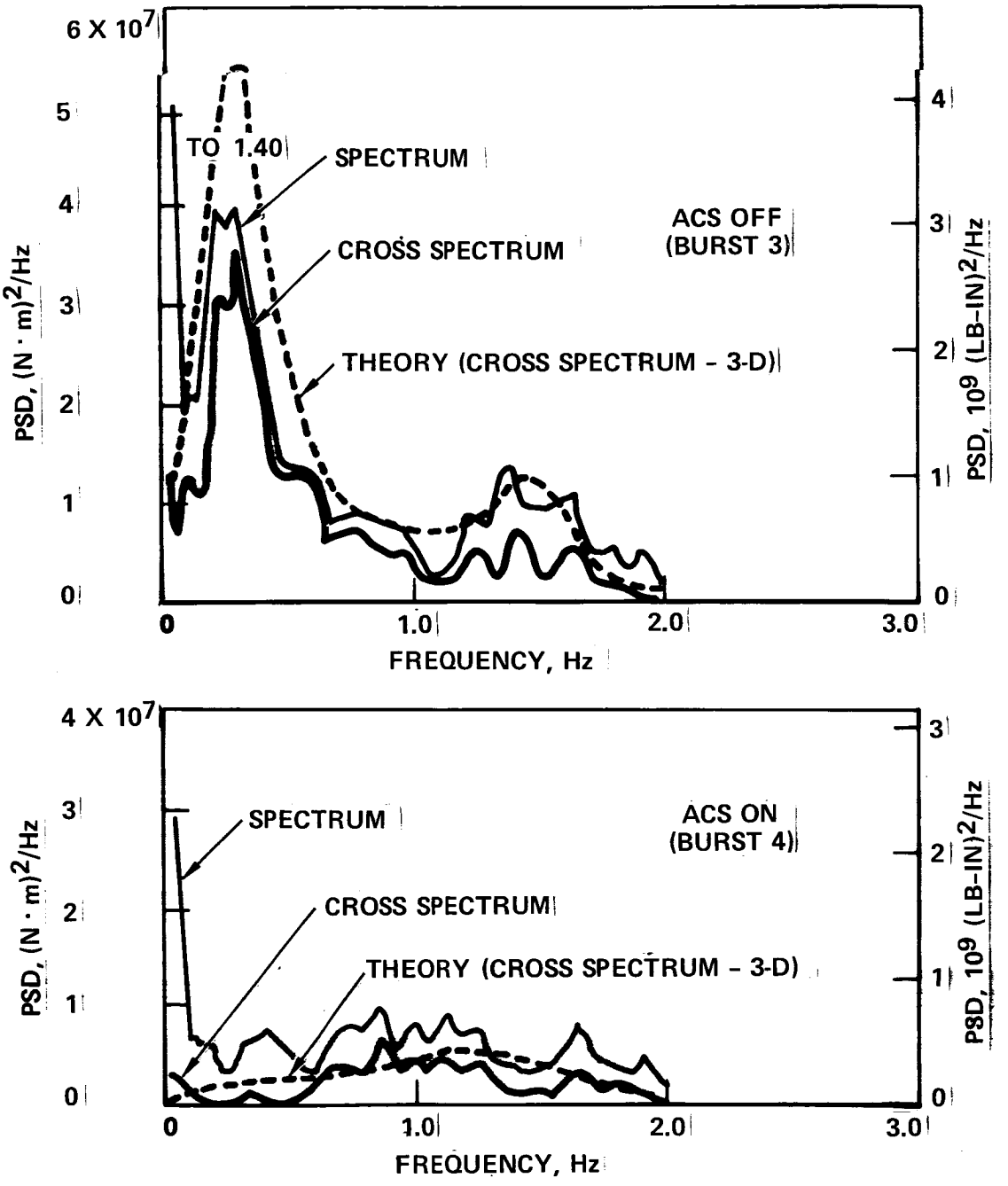

Figure 5-100. PSD of Wing Bending at η = 0.71 - Bursts 3 and 4

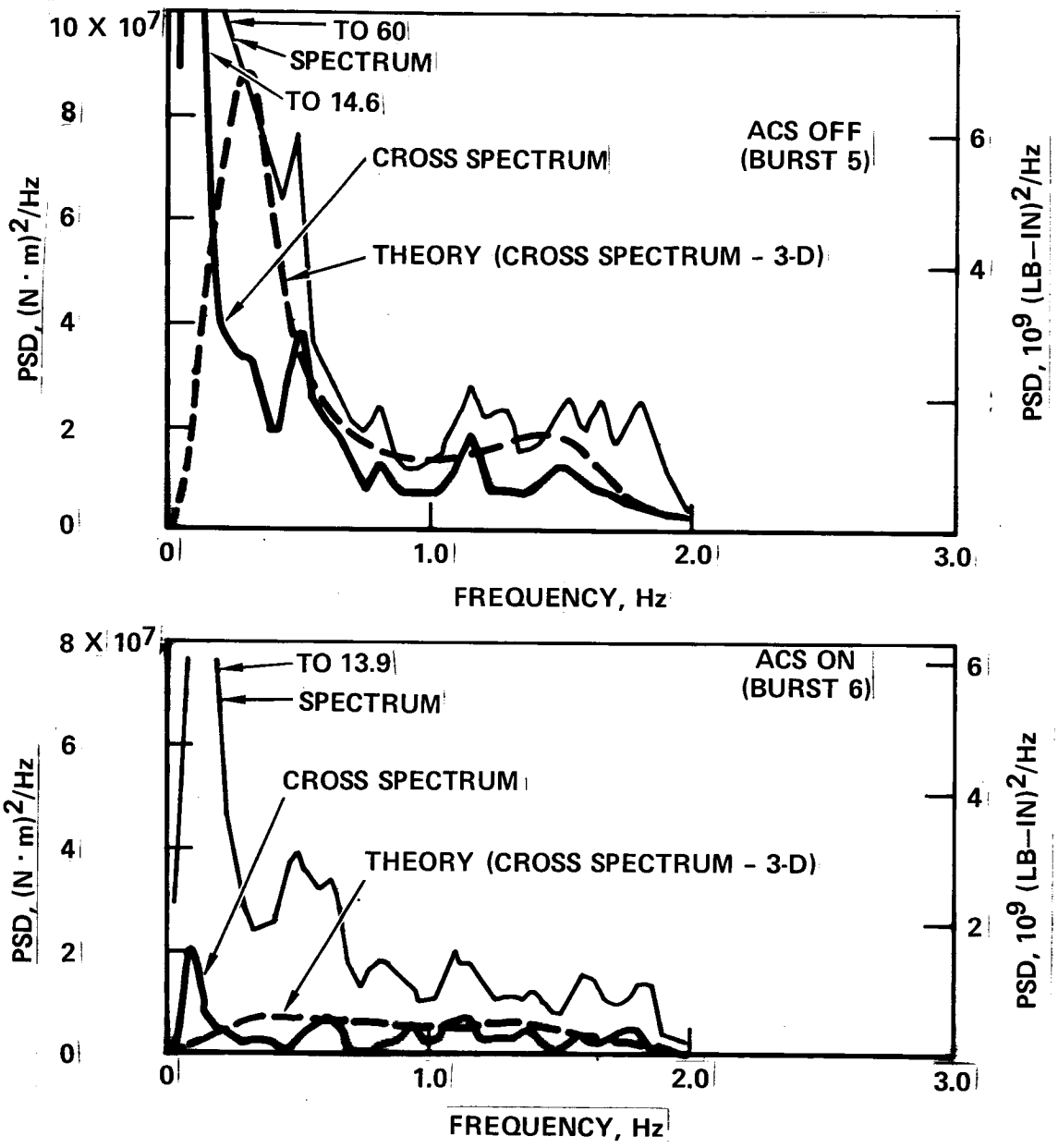

Figure 5-101. PSD of Wing Bending at η = 0.71 - Bursts 5 and 6 with L = 305m (1000 ft)

apparently due to pilot input. The pilot input effect, as measured by the difference between spectrum and cross-spectrum test curves, is much greater here than at more inboard locations, due to the influence of pilot roll control, which involves the outboard ailerons. For Bursts 3 and 4 (Figure 5-100), the pilot input effect is quite modest, and the theoretical reduction appears to have been achieved.

In Bursts 1 and 2 (Figure 5-99), the ACS is indicated to be much less effective, throughout the region of the short period response, than indicated by theory. The disagreement between cross-spectrum and theoretical curves below 1.0 Hz with ACS on is the primary source of the disagreement between test and theory noted for this quantity in Figure 5-83, which compared measured with theoretical load reductions due to the ACS.

This disagreement between the cross-spectrum and theoretical curves is believed to be due to the nature of the psd determinations from the test data. Experience has indicated that there is a limit to how low the computed cross spectrum psd can be relative to the spectrum method psd, even if it were to be zero in the absence of other inputs (maneuvers) or for a very long sample. The ratio of the cross spectrum psd to the spectrum psd is equal to the coherency function. But as mentioned in Section 5.7.6, experimental coherencies between quantities that should have zero coherency generally tend to oscillate between zero and some positive value when plotted against frequency. The magnitude of these oscillations has been determined as a function of record length for the present program by working with plots of the coherency between roll rate and vertical gust velocity, which theoretically is zero. Cumulative peak count curves were obtained for peaks occurring between 2.0 and 7.5 Hz; and cross curves vs length of burst were then plotted.* These are shown in Figure 5-102. For Burst 2, with a duration of 4 blocks, at the 3-peaks-per-Hz level, the expected height of peaks is 0.16. Accordingly, in Figure 5-99, the "minimum" cross-spectrum psd would contain peaks up to $(0.16)(16.3 \times 10^7) = 2.6 \times 10^7$ - roughly as shown. So the cross-spectrum psd curve shown could have been obtained even if the true cross spectrum psd were zero.

Consequently, it appears entirely likely that the active control system in the baseline tests was as effective in reducing loads due to vertical gust inputs at this location as well as others, as theory predicts. Thus the point in

*More generally, the appropriate parameter is probably the number of statistical degrees of freedom, equal to four times the number of FFT blocks.

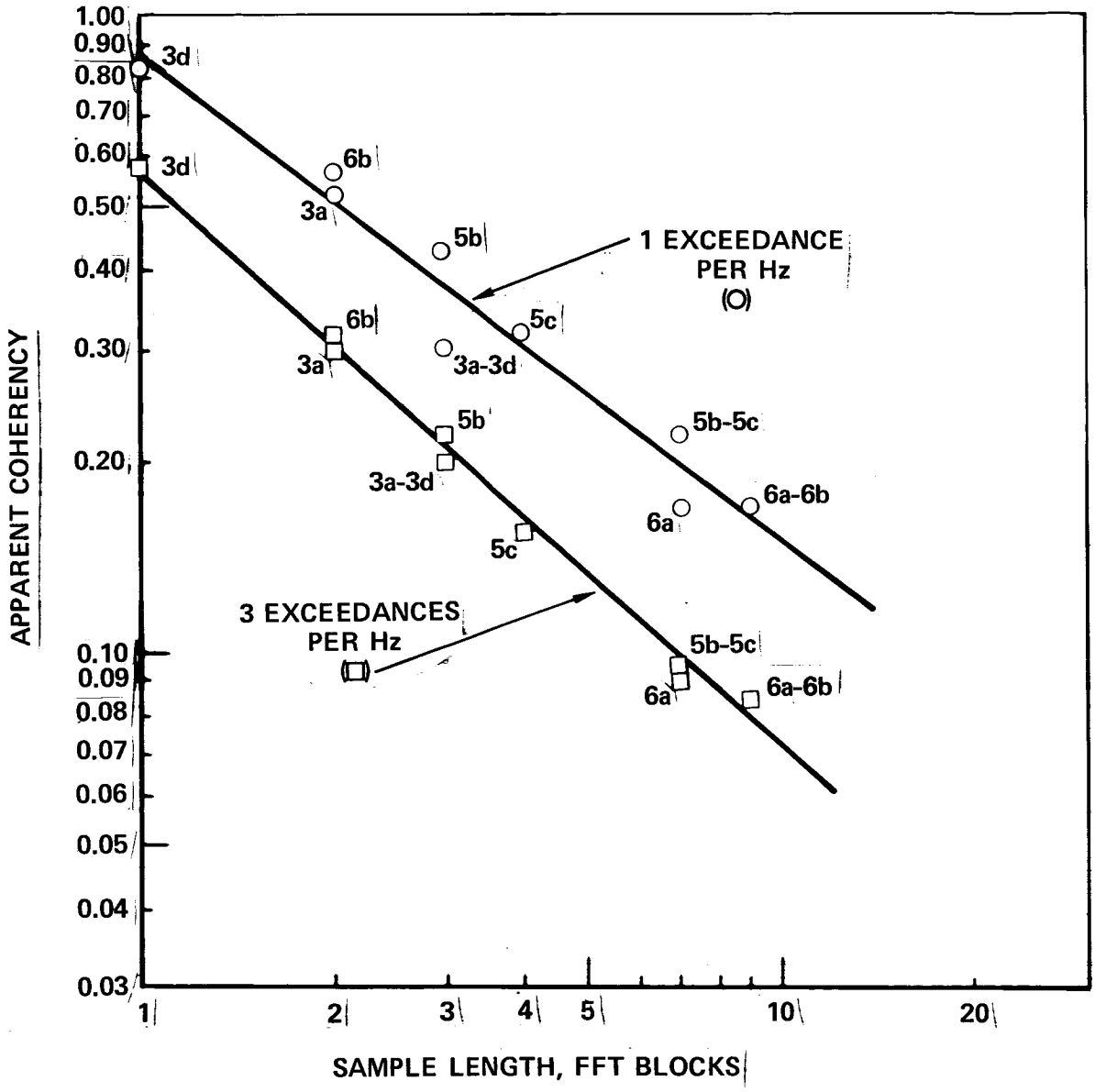

Figure 5-102. Observed Characteristics of Coherency Function as Measured When True Coherency is Zero

Figure 5-83 for M_x at $\eta = 0.75$ can be considered to be effectively on the "test = theory" line, like the other points in the figure.

In Bursts 5 and 6 (Figure 5-101), the effect of pilot input is somewhat less extreme, but the individual peaks in the cross-spectrum psd's for both Burst 5 and Burst 6 at about 0.10 Hz may well reflect in part the corresponding peaks in the spectrum method psd's.

Figure 5-100 makes clear why the ACS load reduction points in Figures 5-88 and 5-89 (3-D theoretical cross transfer functions) are slightly to the left of those in Figures 5-84 and 5-86 (1-D theory). This shift is related to the relative effectiveness of the ACS at the short-period and elastic-mode frequencies. The data in Figure 5-100 - both theoretical and test - show that the ACS does a much better job at the short-period peak than at the elastic-mode peak. The theoretical reduction in psd at the short-period peak is in the ratio 0.3/5.5 = 0.055; at the elastic mode peak, it is roughly 0.6/1.3 = 0.46. The test psd's show comparable reductions. The overall reduction in $\overline{A}$ due to the ACS, by either test or theory, will depend upon the relative weighting of the elastic mode and short-period psd peaks. As noted earlier, psd's based on theoretical 3-D cross-transfer functions are much lower, at the elastic mode peak, than given by 1-D theory, but about the same at the short period peak. Therefore, using the 3-D theory, the short-period peak will be more heavily weighted relative to the elastic mode peak, and the $\overline{A}_{on}/\overline{A}_{off}$ value will be less.

Torsion at $\eta = 0.71$. Wing torsion at $\eta = 0.71$ is also of interest; plots of the psd of this quantity are shown in Figures 5-103 and 5-104. ACS-off, theory shows a small short-period peak and a considerably larger elastic-mode peak. The small static torsion (short period peak) is probably due to an aerodynamic center location close to the load axis (see Figure 5-13, Section 5.4). The loads at the elastic mode peak are due primarily to inertia forces, however, and with the mass center farther off, act through a larger moment arm. The theoretical effect of the active controls is to introduce large torsions due to the aileron motion at both short-period and elastic-mode frequencies. The result in the short-period region is a large increase in torsion; in the elastic-mode region, however, the torsion from the ailerons has less effect than the reduction in elastic mode dynamic response. The test data confirm the predicted reduction at the elastic mode resonance. The prediction of a substantial increase at the short period frequency is also borne

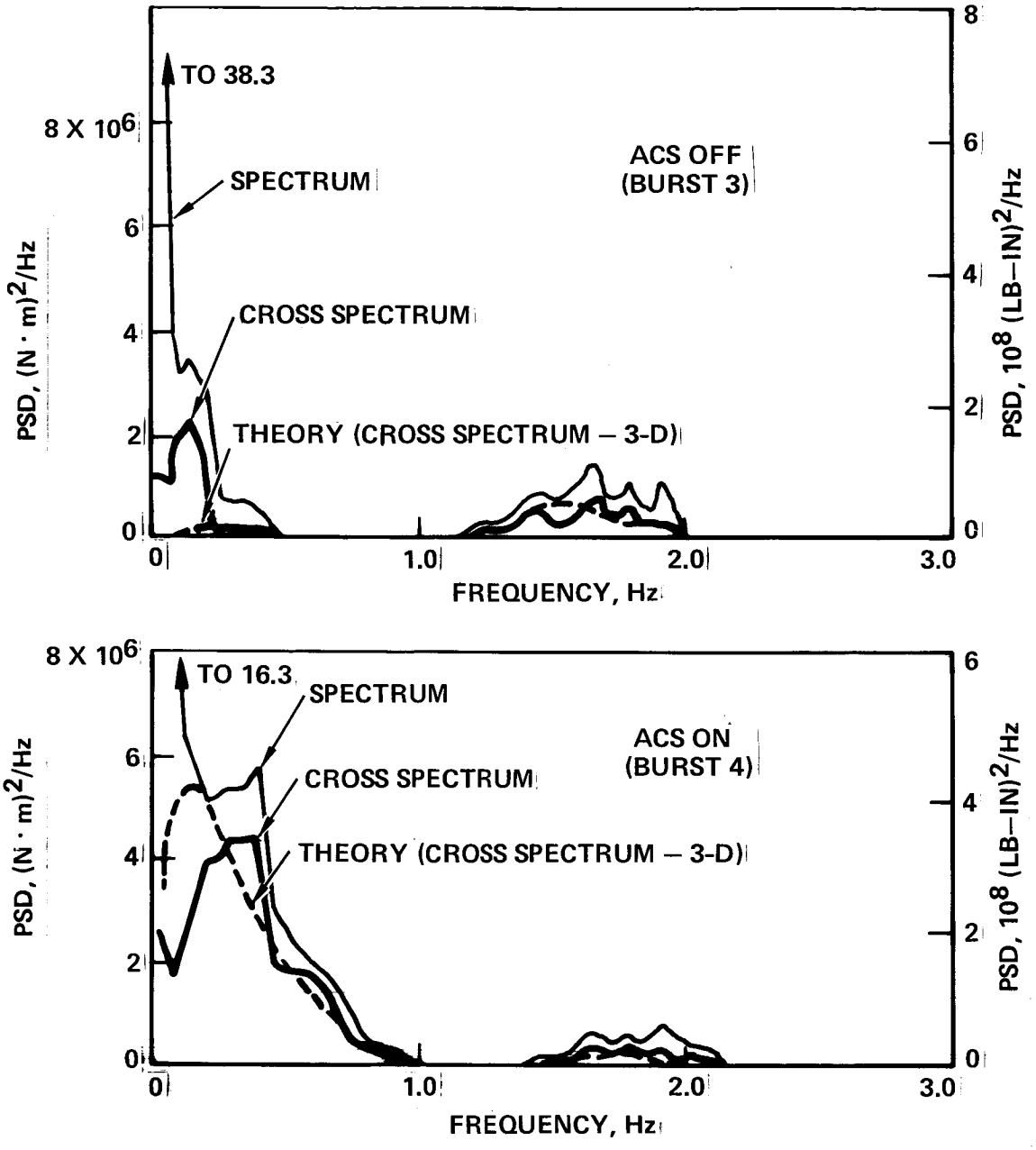

Figure 5-103. PSD of Wing Torsion at η = 0.71 - Bursts 3 and 4

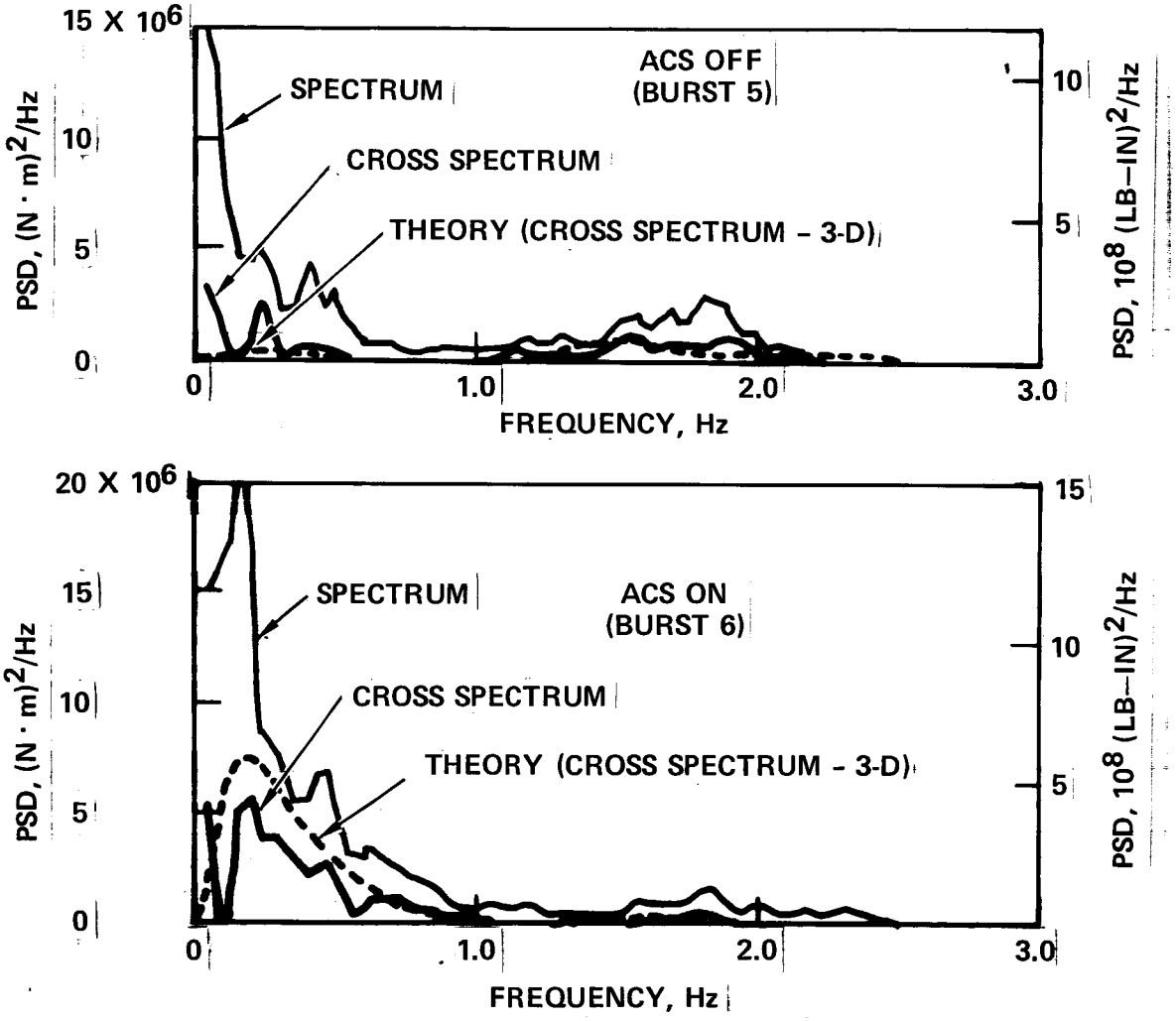

Figure 5-104. PSD of Wing Torsion at η = 0.71 - Bursts 5 and 6 with L = 305m (1000 ft)

out, although the quantitative relations are obscured by the lack of smoothness in the ACS-on plots.

One interesting observation from the psd plots generally is the much better agreement between test and theory, in the region of the first wing bending peak (1.5 Hz) achieved using the 3-D theory. In this region the test psd's (cross spectrum) generally agree excellently with the 3-D cross transfer function psd's; where there is a difference, the test psd's are below the theoretical. In contrast the 1-D psd's are higher than the 3-d psd's by a factor of 2 or more.

Effect of Pilot Control Inputs

Control inputs by the pilot in turbulence can affect both the interpretation of the test data and the load reduction ratios that the active control system achieves. The pilot inputs under consideration here may be loosely spoken of as maneuver inputs, but actually are simply the inputs that the pilot applies to restrict the airplane motions induced by the turbulence. Explicit maneuvers such as turns, pullups, and pushovers are believed to have been completely excluded from the flight data and are not included in the present discussion.

Pilot corrective inputs in turbulence can be in either pitch or roll. In the context of active controls effectiveness in reducing gust loads, these differ in two important respects.

First, wing loads due to pitch inputs generally, as well as loads due to pitch maneuvers in particular, are reduced by the MLC/EMS in much the same way and to much the same extent as are wing loads due to turbulence. (The GLA probably has very little effect on loads due to pitch control inputs, and its effect on gust loads, too, is not great; its effect can be largely ignored in the present discussion.) Wing loads due to roll control, on the other hand, can be substantial and are completely unaffected by the ACS. Roll control is inherently antisymmetric whereas the L-1011 ACS is symmetric both in its sensors and in its commands to the control surfaces.

Second, airplane roll motions, and consequently roll control inputs, are incoherent with the vertical gust velocity as measured on the airplane centerline. Pitch control inputs, on the other hand, can be at least partially coherent. Under autopilot control, coherencies of about 0.60 between stabilizer angle and vertical gust velocity have been obtained (in an extension of the present program under

Lockheed funding.) Under pilot control, however, these coherencies in the present tests are essentially zero. The difference is apparently due to the tendency of the pilot to apply intermittent corrections, in contrast to the continuously modulated inputs by the autopilot.

As noted earlier and illustrated by Figure 5-71 (page 5-114) pilot inputs in the gust response testing affect primarily the spectrum-method transfer functions and resulting psd's. The difference between spectrum and cross-spectrum psd's in the frequency range below about 1.0 Hz, is a measure of the effect of the pilot input.*

---

*Attributing differences between spectrum-method and cross-spectrum-method transfer functions at the lower frequencies primarily to pilot inputs is based on the following direct and indirect evidence:

1. In the 1971 L-1011 gust response flight tests, low coherency of wing torsion at $\eta = 0.75$ and $\eta = 0.38$ (just inboard of outboard and inboard ailerons, respectively) with vertical gust velocity, together with very high coherency of these quantities with aileron angle, throughout the frequency range 0-1.0 Hz (noted on page 5-130 herein). In Bursts 2, 6, and 10 of the present program, low coherency of wing bending moment at $\eta = 0.71$ (or 0.75) with vertical gust velocity is, similarly, associated with high coherency with antisymmetric aileron angle.

2. In the 1971 tests, good correlation between magnitude of load and acceleration psd spikes at very low frequency (below 0.15 Hz, as seen in Figure 5-67 herein) and psd's of stabilizer angle.

3. In the 1971 tests and in the current tests with ACS off, consistency between the psd shape for aileron or stabilizer angle (high psd at low frequency) and the drop-off at low frequency of coherencies of the various responses relative to vertical gust velocity.

4. Theoretical knowledge that if pilot control is significant it will indeed cause the results noted (low coherency of response with gust velocity and large difference between spectrum and cross spectrum transfer functions and psd's), together with lack of evidence of any other significant cause in the pertinent frequency range.

5. Qualitative prediction, by means of 3-D gust analysis with autopilot roll control, of the coherencies and A relationships observed in flight under pilot control, together with qualitative agreement of flight-measured aileron angle psd's with those given by the analysis (discussed on pages 5-168 through 5-171 herein).

6. Consistency in Table 5-12 herein between measures of pilot input based on response psd's (Columns 1 through 4) and direct measures of pilot input (Columns 5 and 6), discussed on pages 5-171 through 5-174 herein.

Effect of Roll Control. The loads due to roll control, as noted above, are not affected by the ACS. It is obvious that, when roll control loads are present, the full percentage reduction in loads achievable by the ACS under vertical gust excitation alone will not be achieved. The actual reduction in ACS effectiveness to be expected is expressed quantitatively in Figure 5-105. The nomenclature used in the figure, summarized graphically at the bottom of the figure, is as follows:

a = load due to vertical gust, ACS off

p = load due to pilot, or, in general, to a second input uncorrelated with the first and unaffected by the ACS

b = load due to a and p together, $b = \sqrt{a^2 + p^2}$

c = load due to vertical gust, ACS on, less than a

d = load due to c and p together, $d = \sqrt{c^2 + p^2}$

The coordinates of Figure 5-105 are essentially the same as those of the load reduction plots, Figures 5-83 through 5-91. The ratio c/a is identical to "$\bar{A}_{on}/\bar{A}_{off}$, theory." The ratio d/b is what one would expect to obtain in test for $\bar{A}_{on}/\bar{A}_{off}$, as a result of roll control, if the ACS were to achieve its theoretical load reduction in the absence of roll control.

In an earlier section (Overall Results), the distinctive trend of the test data in Figure 5-91 (page 5-147) was identified as due to the presence of roll control. This identification can readily be supported qualitatively in terms of Figure 5-105. In the inner part of the wing, the roll-control loads are much smaller than the gust-induced loads - say p/a = 0.2. Accordingly, the test points stay close to the "test = theory" line. Approaching the outboard aileron, however, the loads due to roll control may be comparable to those due to turbulence. At $\eta = 0.85$, therefore, with c/a = 0.50 and p/a assumed equal to 1.0, the curve would swing sharply upward, to a value approaching 0.80. This is exactly what is shown by the test data in Figure 5-91.

The roll-control explanation for the trend of the test data in Figure 5-91 can also be supported quantitatively. In Figure 5-106, the test data of Figure 5-91 have been repeated, and a second theoretical curve has been added. This curve was obtained by including the L-1011 autopilot in a GLP-6 3-D gust analysis run for Burst 6 with L = 305m. Only the roll and yaw autopilot channels were included; the turbulence mode gains were used. The ACS was on. Thus an indication was

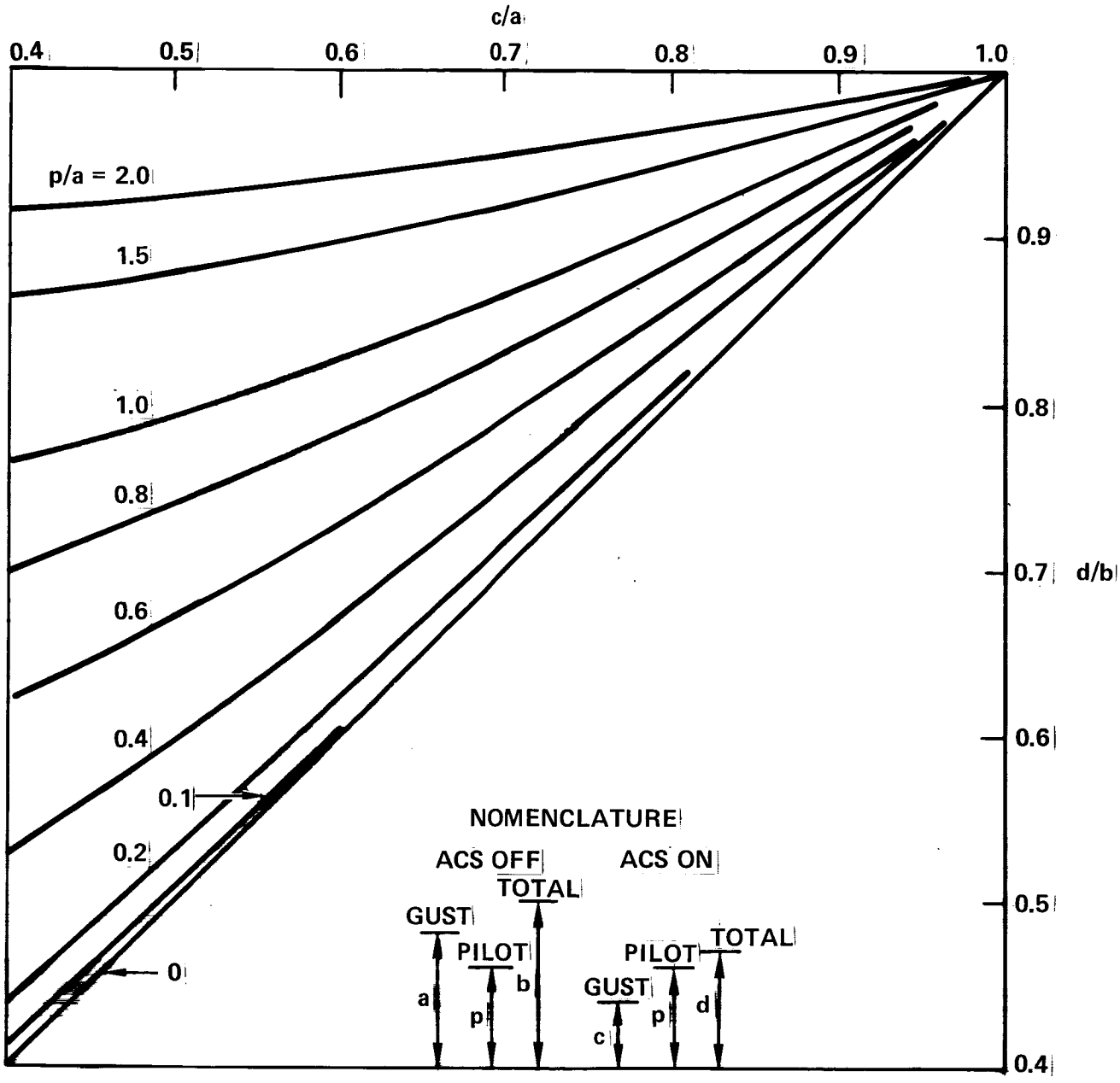

Figure 5-105. Effect of Second Input on Load Reductions Achievable by an Active Control System

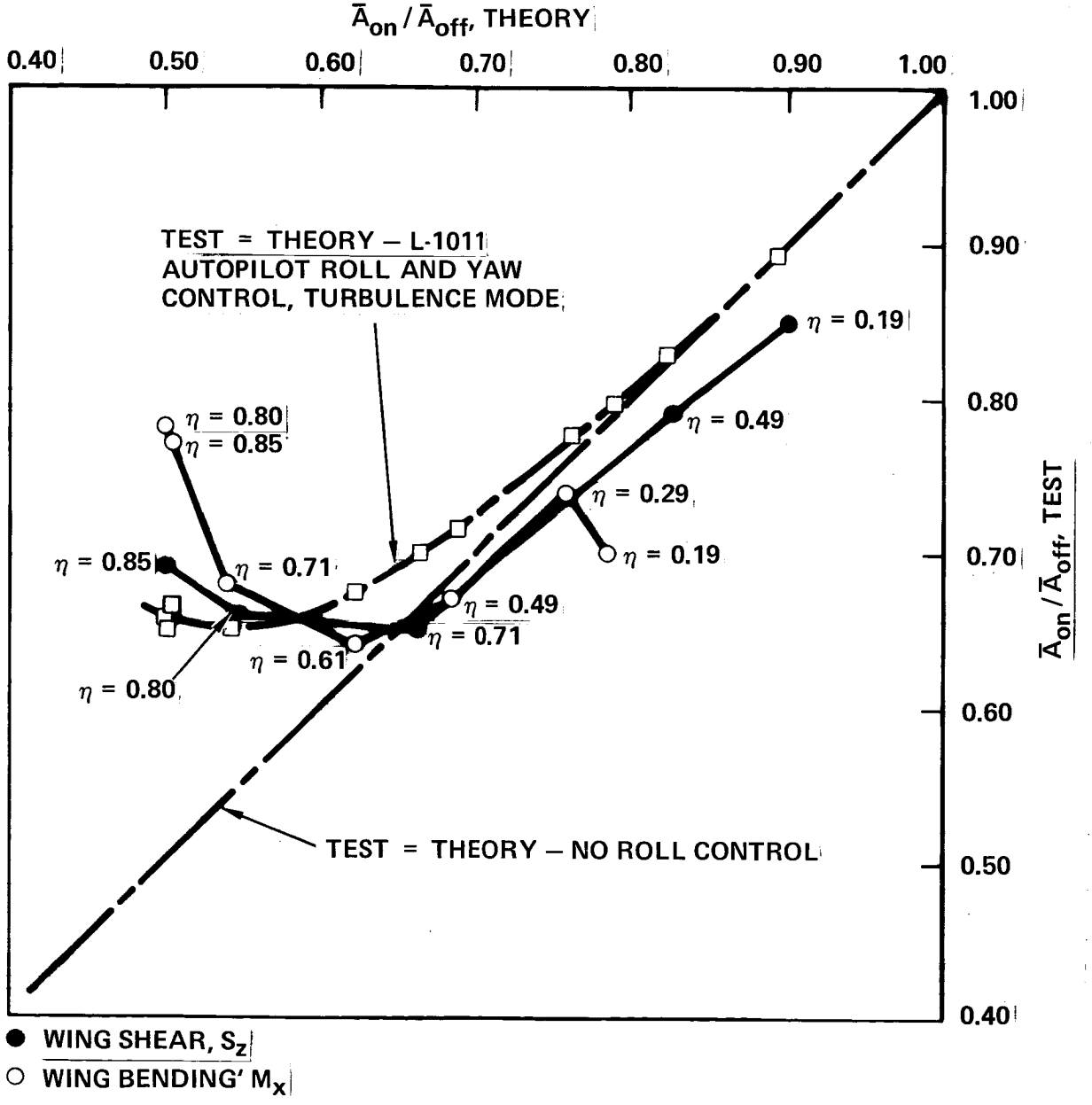

Figure 5-106. Load Reduction Due to Active Controls - Bursts 5 and 6 with L = 305 m (1000 ft) - Spectrum Method and 1-D Theory Adjusted for Effect of Roll Control

obtained of what roll control might do to the loads, regardless of whether the control is exercised by autopilot or pilot. (The corresponding theoretical effect of roll control on coherencies was shown in Figure 5-81, page 5-128; Figures 5-81 and 5-106 are qualitatively consistent.) It has been found that the amount of roll-control aileron activity varies immensely from pilot to pilot, and substantially for a single pilot from burst to burst. Nevertheless, the aileron motions produced by the autopilot appear to be representative, very generally, of those produced by a human pilot.*

The GLP-6 $\bar{A}$'s with and without autopilot provide values of d/c (see Nomenclature, Figure 5-105) for shears and bending moments at the various wing locations. Corresponding values of c/a were taken from Figure 5-91 or 5-105. From these two quantities, d/b can be computed.** The resulting points, plotted as "□" symbols in Figure 5-106, define with very little scatter the second theoretical curve, labelled "test = theory - L-1011 autopilot roll and yaw control, turbulence mode."

It is seen that this second theoretical curve reproduces very well the basic trend of the test data, even though the actual roll control used in the theory was a somewhat arbitrary approximation to the actual roll control exercised by the pilot.

It would appear that the reduction in ACS effectiveness due to the presence of roll control should be accounted for in establishing design loads for an airplane with active controls.

Effects of Burst-to-Burst Variations in Pilot Inputs. In the section "Overall Results," the apparently poor showing of the ACS on a spectrum-method basis, in Figure 5-90, was attributed to random differences in pilot technique from one turbulence penetration to another. In an earlier section, "Response PSD's," an indication of the differences in control inputs, for the same pair of bursts, was seen in the psd plots for cg acceleration, Figure 5-94; the greater difference between spectrum and cross-spectrum psd plots, ACS-on, was a clear indication that the control input was greater for the ACS-on burst.

*This conclusion follows from comparisons of rms aileron angles obtained in flight in turbulence and on the Lockheed Rye Canyon Visual Flight Simulator, under pilot control, with those given by the 3-D gust analysis for autopilot control.

** $\frac{d}{b} = \frac{\frac{d}{a}}{\sqrt{1 + \left(\frac{p}{a}\right)^2}}$, where $\frac{d}{a} = \frac{d/c}{c/a}$ and $\frac{p}{a} = \sqrt{\left(\frac{d}{a}\right)^2 - \left(\frac{c}{a}\right)^2}$

A more comprehensive and quantitative view of the effect of control inputs on the gust response results is provided by Table 5-12.

The first four columns of the table provide values of the parameter,

$$\frac{\bar{A}_{\text{additional}}}{\bar{A}\ \text{coherent ACS off}}$$

evaluated for each burst for each of four response variables. This parameter was selected as one measure of control input. The numerator is the square root of the area between the spectrum and cross-spectrum psd's (test), as shown, for example, in Figures 5-94 to 5-104. It approximates the $\bar{A}$ that would be given by the pilot inputs alone. (It is only an approximation, inasmuch as the difference between the two curves beyond about 1.0 Hz is due primarily to sources other than pilot input, and even below 1.0 Hz is due partially to such other sources.) The denominator is the square root of the area under the cross spectrum psd for the ACS-off case; this provides a common reference for ACS-on and ACS-off cases. This parameter is valid as a measure of roll control inputs. It is also valid as a measure of pitch control inputs when applied to a response variable such as a body acceleration (cg or aft-body) which is not significantly affected by the ACS. As applied to wing shears and bending moments, however, it is not entirely satisfactory as a measure of pitch control inputs. What it measures is pitch control <u>outputs</u>, and these are affected by the ACS. Thus, to the extent to which this parameter reflects the effect of pitch control, equal values of the parameter would indicate not <u>equal</u> inputs, but a <u>greater</u> input ACS on than ACS off. The "+" symbols in columns 2,3, and 4 of Table 5-12, for the ACS-on cases, serve as a reminder that these numbers would be larger by some unknown but probably substantial amount if they were to apply to control inputs rather than outputs.

The first column is for a quantity that reflects vertical gust and pitch control inputs only. Proceeding to Columns 2, 3, and 4, roll control has a progressively increasing influence.

Columns 5 and 6 list values of parameters which measure control inputs more directly - Column 5 for pitch control and Column 6 for roll control.

Generally the numbers in the table are consistent. Column 1 agrees uniformly with Column 5, as an indicator of whether pitch control is greater ACS on or ACS off for each pair of bursts. For Bursts 1 and 2, Columns 5 and 6 indicate that while

TABLE 5-12. PILOT INPUT COMPARISONS

	1	2	3	4	5	6
BURST	$\bar{A}$ ADD'L $\bar{A}$ COHERENT ACS OFF				RMS RATIOS*	
	n_z AFTBODY	S_z η = .19, .20	M_x η = .29, .31	M_x η = .71, .75	COL. POS CG n_z	ANTISYM δA VERT. GUST
12E1	.48	.65	.68	1.16		
1	.75	.78	.83	1.46	1.60	.233
2	1.14	1.05 +	.88 +	1.62 +	1.98	.209
3	.57	.65	.63	.83	.90	.066
4	.73	.79 +	.71 +	.74 +	1.38	.054
5	.95	.95	1.17	1.44	1.51	.172
6	.75	.70 +	.71 +	.97 +	1.22	.183
L = 305 m (1000 ft) 5	.81	.81	1.01	1.31	1.51	.172
L = 305 m (1000 ft) 6	.67	.66 +	.70 +	1.03 +	1.22	.183
9	1.13	1.41	1.36	1.62	3.55	.294
10	1.22	1.56 +	1.19 +	1.49 +	4.82	.321

Underlining indicates the higher value of each pair (ACS on vs ACS off) - solid for pair ratios > 1.30, dash for ratios < 1.30

*RMS ratios are based on integrating test psd's over the range f = .039 Hz to 7.5 Hz (Bursts 9 and 10 to 3.75 Hz). Gust velocity rms values are adjusted to Von Karman gust psd with L = 762 m (2500 ft)

pitch control is considerably greater in Burst 2, roll control is slightly greater in Burst 1. One would expect, therefore, that in Columns 1 through 4 the difference between Bursts 1 and 2 would diminish proceeding from Column 1 to Columns 2, 3, and 4, as the contribution of roll control increases. Such a trend is seen to occur, although it becomes less pronounced as qualitative consideration is given to the + symbols. Bursts 3 and 4 follow virtually the same trend as Columns 1 and 2. For Bursts 5 and 6 (with L=305 m), the value for Burst 6 relative to Burst 5 is expected to increase moving from Column 1 to Column 4. This increase is not borne out by the numbers themselves, but may, quite plausibly, be borne out when, in accordance with the + symbols, the Burst 6 numbers are considered to increase moving from Column 1 to 4 as a result of the increasing effect of the ACS on the loads due to pitch control.

The picture provided by Table 5-12 makes it quite evident that control inputs are greater for Burst 2 than Burst 1. For Bursts 3 and 4, although the general level of control inputs (relative to gust inputs) is much less than for Bursts 1 and 2, the ACS-on case again has the greater control input. For Bursts 5 and 6, the differences between ACS on and ACS off are not as great again accounting for the + symbols -- but now, in contrast to Bursts 1, 2 and 3, 4, the greater use of controls is ACS-off rather than ACS-on. Thus concrete support is lent to the conclusion that differences in control inputs between the ACS-on and ACS-off tests are entirely random, unrelated to the presence or absence of the active controls.

Accordingly, it is concluded that the spectrum-method load-reduction plots of Figures 5-90 and 5-91 do not indicate any deficiency in the capability of the ACS to achieve the load reductions indicated by theory beyond the acknowledged inability of the ACS to reduce the loads due to roll control (Figures 5-105 and 5-106), which must be accounted for in design.

$\bar{A}$ Test-to-Theory Ratios

The over-all agreement of measured with theoretical responses, separately for ACS-on and ACS-off flight, is indicated by the $\bar{A}$ test-to-theory ratios presented in Tables 5-13 and 5-14.

In both tables, the ratios were formed using test $\bar{A}$'s based on the cross-spectrum-method transfer functions. In Table 5-13 the theoretical $\bar{A}$'s, for consistency, were based on the theoretical (3-D) cross transfer functions. In Table 5-14, the theoretical $\bar{A}$'s were based on 1-D theory, in order that Bursts 1 and

TABLE 5-13. $\bar{A}$ TEST-TO-THEORY RATIOS BASED ON MEASURED AND THEORETICAL (3-D) CROSS TRANSFER FUNCTIONS

QUANTITY	Baseline	Ext'd span	$\bar{A}$ TEST-TO-THEORY RATIOS FOR THE BURST INDICATED							
			3	4	5	6	5 L = 305 m	6 L = 305 m	9	10
W S_z η =	.20	.19	0.90	0.91	0.98	0.95	0.96	0.94	0.86	0.92
	.31	.29	0.87	0.90	-	-	-	-	0.88	0.92
	.38	.36	0.77	0.82	-	-	-	-	-	-
	.52	.49	0.86	0.93	0.90	0.94	0.88	0.92	1.01	1.04
	.75	.71	0.80	0.91	0.93	0.95	0.88	0.93	0.99	0.98
		.80	0.82	0.91	1.04	0.94	0.95	0.90	1.06	1.02
		.85	0.98	1.48	0.99	0.90	0.89	0.84	0.98	0.99
W M_x η =	.20	.19	0.86	0.93	0.88	0.84	0.89	0.83	1.02	1.14
	.31	.29	0.86	0.95	0.89	0.93	0.86	0.91	0.95	0.98
	.52	.49	0.78	0.86	0.87	0.86	0.83	0.85	0.88	0.86
		.61	-	-	0.94	0.92	0.88	0.89	0.95	0.94
	.75	.71	0.73	0.79	1.02	0.91	0.92	0.86	1.00	0.97
		.80	0.72	0.89	1.04	0.89	0.91	0.82	0.94	0.89
		.85	0.66	0.90	1.01	0.98	0.90	0.90	1.07	1.13
W M_y η =	.31	.29	0.87	0.81	0.88	0.86	0.83	0.80	1.66	1.26
	.38	.36	0.91	0.77	0.85	0.75	0.79	0.74	1.28	0.90
	.52	.49	1.41	1.20	0.90	0.82	0.89	0.80	1.50	1.39
		.61	-	-	1.19	0.90	1.13	0.89	2.03	1.70
	.75	.71	1.25	0.95	1.35	0.81	1.23	0.80	2.08	1.64
		.80	1.30	0.99	1.87	0.86	1.58	0.84	1.87	1.62
		.95	0.96	0.79	1.66	0.71	1.37	0.70	1.15	1.30
HT S_z η =	.29	.29	1.01	0.81	1.24	0.91	1.17	0.88	1.24	1.11
M_x	.29	.29	0.85	0.68	1.03	0.78	0.98	0.75	1.54	1.21
M_x	.60	.60	0.67	0.54	0.76	0.59	0.72	0.57	1.78	1.29
M_y	.29	.29	1.10	0.91	1.08	0.93	1.04	0.88	1.29	1.10
n_z nose			0.61	0.67	-	-	-	-	0.81	0.85
pilot seat			0.66	0.71	0.59	0.69	0.58	0.66	0.85	0.86
ACS body			-	-	0.78	0.81	0.77	0.79	0.97	1.01
CG			0.88	-	0.76	0.82	0.76	0.81	0.89	0.98
aftbody			0.83	0.88	0.79	0.80	0.77	0.78	0.96	1.00
W engine n_z			0.79	0.83	0.68	0.72	0.64	0.68	0.89	0.89
n_y			0.47	0.38	0.44	0.44	0.42	0.43	0.46	0.43
W tip sym n_z			0.80	0.96	1.18	1.14	1.13	1.13	1.27	1.25
Stab tip n_z (L)			0.27	0.37	0.50	0.43	0.31	0.27	0.88	0.63
$\dot{\theta}$			0.94	1.10	0.94	0.75	0.91	0.71	0.89	0.94
Sym δ_a			-	0.93	-	0.86	-	0.86	-	1.03
δ_H			-	0.37	-	0.42	-	0.40	-	0.73

TABLE 5-14. $\bar{A}$ TEST-TO-THEORY RATIOS BASED ON MEASURED CROSS TRANSFER FUNCTIONS AND 1-D THEORY

QUANTITY	Baseline	Ext'd span	$\bar{A}$ TEST-TO-THEORY RATIOS FOR THE BURST INDICATED									
			1	2	3	4	5	6	5 L = 305m	6 L = 305m	9	10
W S_z η =	.20	.19	0.97	0.91	0.80	0.80	0.86	0.83	0.83	0.81	0.69	0.77
	.31	.29	-	-	0.76	0.78	-	-	-	-	-	-
	.38	.36	0.93	0.92	0.66	0.69	-	-	-	-	-	-
	.52	.49	0.94	0.95	0.74	0.79	0.77	0.79	0.74	0.77	0.78	0.83
	.75	.71	0.81	0.78	0.65	0.66	0.7	0.69	0.69	0.67	0.68	0.66
		.80	-	-	0.69	0.66	0.86	0.68	0.77	0.65	0.76	0.69
		.85	-	-	0.85	1.09	0.83	0.66	0.74	0.62	0.73	0.68
W M_x η =	.20	.19	0.82	0.84	0.75	0.78	0.75	0.70	0.75	0.68	0.78	0.92
	.31	.29	0.86	0.86	0.73	0.78	0.75	0.76	0.71	0.74	0.72	0.77
	.52	.49	0.76	0.76	0.65	0.66	0.70	0.66	0.66	0.64	0.63	0.62
		.61	-	-	-	-	0.76	0.67	0.70	0.65	0.67	0.65
	.75	.71	0.77	0.92	0.62	0.58	0.84	0.66	0.75	0.63	0.73	0.67
		.80	-	-	0.63	0.65	0.88	0.66	0.77	0.60	0.70	0.62
		.85	-	-	0.59	0.67	0.87	0.72	0.77	0.66	0.82	0.79
W M_y η =	.20	.19	1.08	1.12	-	-	-	-	-	-	-	-
	.31	.29	-	-	0.71	0.66	0.69	0.65	0.64	0.64	0.95	0.67
	.33	.26	0.83	0.99	0.73	0.61	0.66	0.59	0.61	0.59	0.69	0.45
	.52	.49	0.99	0.85	1.12	1.09	0.71	0.74	0.69	0.71	1.21	1.20
		.61	-	-	-	-	0.82	0.80	0.77	0.78	1.38	1.37
	.75	.71	1.04	0.91	0.81	0.86	0.84	0.73	0.76	0.71	1.01	1.16
		.80	-	-	0.85	0.92	1.15	0.80	0.98	0.77	0.73	0.99
		.85	-	-	0.66	0.74	1.08	0.66	0.89	0.65	0.50	0.69
Fus S_z	FS	930	1.06	1.11	-	-	-	-	-	-	-	-
	FS	1428	0.77	0.77	-	-	-	-	-	-	-	-
HT S_z η =	.29	.29	0.90	0.92	0.85	0.62	1.02	0.75	0.96	0.72	1.00	0.86
M_x	.29	.29	0.97	0.95	0.63	0.42	0.75	0.55	0.70	0.52	1.13	0.84
M_x	.60	.60	-	-	0.44	0.28	0.48	0.35	0.45	0.33	1.17	0.79
M_y	.29	.29	1.13	1.18	0.85	0.60	0.82	0.65	0.78	0.61	1.11	0.76
n_z Nose			0.62	0.65	0.51	0.54	-	-	-	-	0.59	0.57
Pilot Seat			0.75	0.78	0.55	0.58	0.48	0.56	0.46	0.53	0.63	0.60
ACS Body			-	-	-	-	0.73	0.76	0.71	0.74	0.90	0.94
CG			0.98	1.02	0.82	-	0.69	0.74	0.68	0.72	0.80	0.87
Aftbody			1.10	1.10	0.74	0.77	0.69	0.70	0.68	0.68	0.84	0.87
W Engine n_z			1.14	1.29	0.68	0.69	0.56	0.60	0.53	0.57	0.66	0.61
n_y			0.54	0.56	0.38	0.29	0.35	0.34	0.33	0.33	0.26	0.23
W tip sym n_z			0.80	0.70	0.55	0.62	0.77	0.72	0.73	0.72	0.53	0.54
Stabl tip n_z (L)			-	-	0.15	0.18	0.28	0.22	0.15	0.13	0.46	0.29
$\dot{\theta}$			1.35	1.87	0.88	0.99	0.87	0.68	0.84	0.64	0.82	0.85
Sym δ_a			-	1.02	-	0.89	-	0.80	-	0.79	-	0.78
δ_H			-	-	-	0.33	-	0.38	-	0.35	-	0.65

2 might be included; $\overline{A}$'s using the 3-D theoretical cross transfer functions were not available for those bursts. Table 5-13 is considered clearly the more valid of the two.

In Table 5-13, the ratios for wing shears and bendings for the cruise conditions are seen to range from .66 to 1.04, except only for a single value, shear at $\eta = 0.85$ for Burst 4, for which the value is 1.48. (As discussed earlier, under "Overall Results", this point is not representative and may not be valid.) Except for this one point, the ACS-on values range generally from .80 to 1.00; and the spread within any one burst tends to be less ACS-on than ACS-off. Thus these data lend support to a view that the theory applies at least as well to flight ACS-on as ACS-off.

Torsions at cruise ACS-on range from .70 to .99, except for a single value of 1.20. ACS-off, the ratios go considerably higher. Again, the theory appears to apply more reliably ACS-on then ACS-off. One reason for the better torsion agreement ACS-on than ACS-off is the larger values of the torsions relative to the shears. For the three outboard locations, η = .71, .80, and .85, the arm given by dividing the theoretical torsion $\overline{A}$ by the theoretical shear $\overline{A}$ is about 22 inches ACS-off but from 50 to 80 inches ACS-on.

This agreement is considered reasonably satisfactory, in view of the major contribution of the dynamic response in the elastic modes, the statistical nature of the test data, the uncertain degree of contamination of the results by the effects of other inputs, and the greater difficulty of properly distributing airloads over the airplane in comparison with predicting overall motions.

Table 5-14, based on 1-D theory, permits comparing all of the bursts comprising this program. Values for Bursts 1 and 2 are seen to be generally somewhat higher than for the extended-span bursts. This difference, however, is believed not to be related to the airplane configuration, inasmuch as the 1971 data for the baseline configuration, for a similar flight condition, gave ratios somewhat lower than the extended-span values. The differences, instead, may be related to the great difficulty of achieving the desired accuracy in subtracting out airplane motions in determining gust velocities.

5.7.9 Concluding Remarks

A great deal of gust response flight data has been assembled and compared with theory. From these data and comparisons it has been found that:

a. The analytical tools that have been developed over the years to establish vertical-gust design loads also apply reasonably well to the prediction of loads due to vertical gust inputs for airplanes with active controls.

b. With loads due to vertical gust inputs reduced by as much as 50 percent or more by the active controls, loads due to other inputs, previously accounted for implicitly in the design gust velocities, now become a larger fraction of the total and may require explicit consideration.

c. Pilot control inputs in both pitch and roll can have a substantial effect on the total loads occurring in turbulence. In examining these total loads, not normally accounted for explicitly in analytical design gust loads determination, it became evident that:

   o The amount of pilot control can vary randomly from one gust penetration to another, so that direct quantitative determination from the flight data of the effect of the active controls on the total loads is not feasible.

   o Loads due to pitch control can be presumed to be reduced by the active control system to about the same extent as loads due to vertical gust inputs or explicit pitch maneuvers. On the other hand, loads due to roll control are not reduced by the active controls. Consequently, the percentage reduction in total loads achievable by the active control system must be less than that computed on the basis of the vertical gust input alone.

   For airplanes without active controls, the effect of pilot inputs in turbulence can be considered to be accounted for implicitly in the design gust velocities. With active controls, however, the loads due to roll control become a bigger percentage of the vertical-gust loads; it appears that this increase in percentage should be designed for.

d. Three-dimensional gust analysis is a powerful tool, which:

   o Provides a theoretically valid direct comparison between flight-measured and theoretical transfer functions and associated

power-spectral densities, especially important at elastic-mode frequencies.

- Enhances the usefulness of the coherency function as a measure of the quality of the test data.
- Provides a theoretical basis for evaluating and understanding the effect of roll control on wing loads in turbulence.

(The traditional one-dimensional analysis, however, must be considered the primary means of defining design gust loads, for the time being, inasmuch as it was the analysis used to set design levels in relation to successful experience with earlier airplanes.)

SECTION 6

APPLICATION OF ACTIVE CONTROLS

6.1 HANDLING QUALITIES EFFECTS

There appears to be no measureable effect on L-1011 handling qualities due to Active Control System (ACS) operation. The project pilots who conducted maneuver loads and gust loads flight tests state that they were unable to differentiate between ACS-on and ACS-off system status on the basis of handling qualities. The pilots feel that the handling qualities of L-1011 S/N 1001 with Maneuver Load Control (MLC), Elastic Mode Suppression (EMS), and Gust Alleviation (GA) operating are essentially those of the basic airplane. These subjective evaluations are confirmed by the engineering data.

Figure 6-1 shows the column force gradients with positive incremental load factor at three flight conditions for the baseline tests. Flight test data points obtained during maneuver loads tests are shown solid for ACS-off (basic airplane) and open for ACS fully operative. Several points are shown as square symbols with MLC/EMS operating, but GA off. The circular symbols indicate points read during wind-up turns while the diamonds are from roller coaster, push and hold or pull and hold maneuvers. For the two high speed conditions (M = 0.80 and 0.88) the airplane gross mass was approximately 173,300 kg (380,000 lb). The low speed, flaps down condition had a mass of 145,100 kg (320,000 lb). The center of gravity is at approximately 23% MAC for all test points shown. Predicted column forces for the basic airplane are drawn as solid lines. 18 Newtons (4 pounds) breakout force is included in the prediction.

At each of the high speed flight conditions the column force data are closely grouped and can readily be faired with a single line regardless of ACS status. At M = 0.80 the ACS system off prediction provides a good fairing for all the test points. At M = 0.88 the system off prediction is slightly low. In both cases the column forces for maneuvering are the same with the ACS system operating as they are for the baseline airplane.

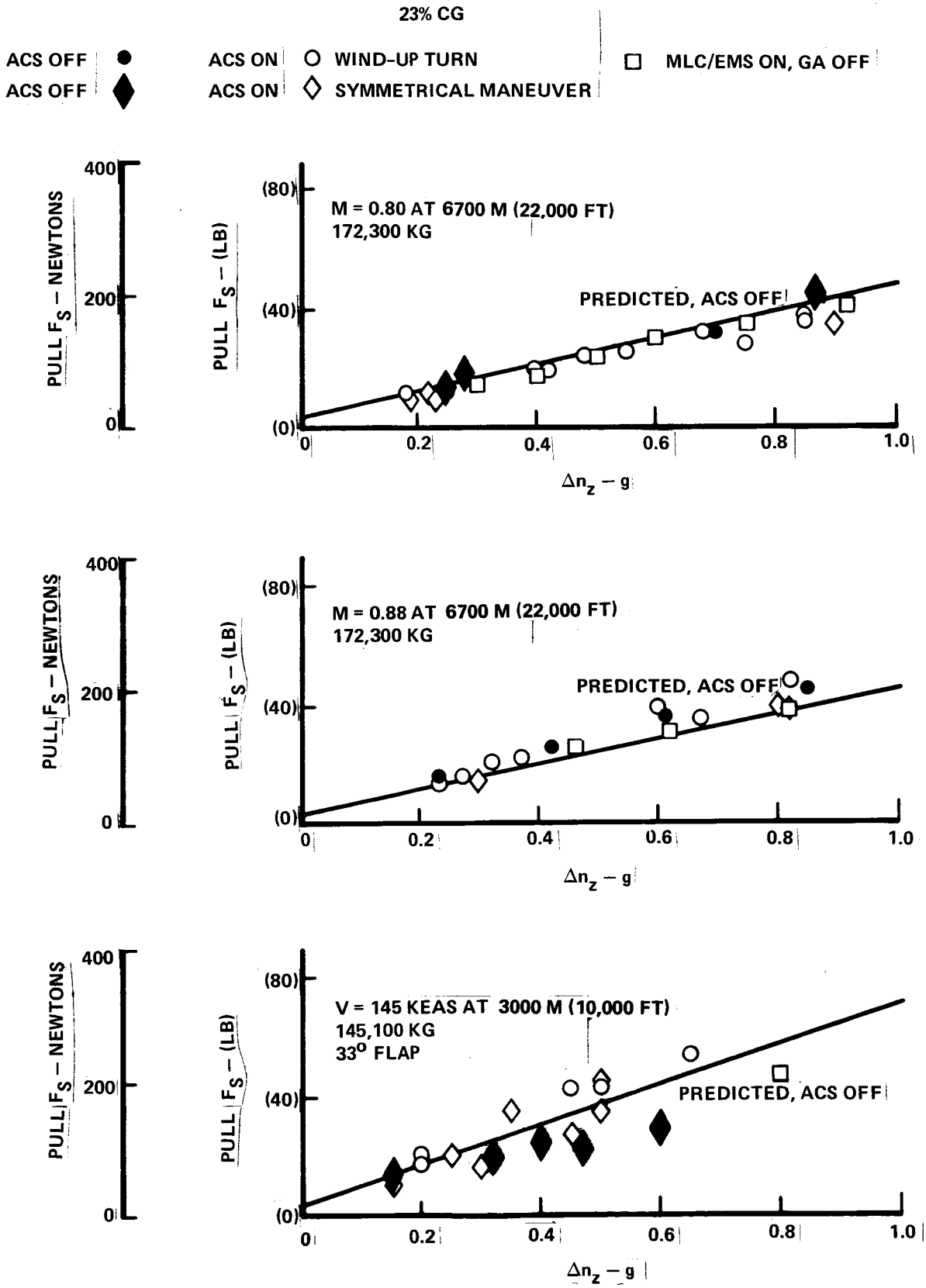

Figure 6-1. L-1011 S/N 1001 Column Force Maneuvering Gradient - Baseline Tests

At the low speed flight condition, with flaps in the landing position, the prediction provides a good fairing for the total population of test data points. In this case, however, there appears to be some differentiation between ACS-on and ACS-off forces at incremental load factors above 0.4 with the data for the latter being generally below their predicted value. It is apparent why the pilots were unable to distinguish system status when it is observed that scatter within the ACS-on data is as much as 90 Newtons (20 pounds) at some load factors. The demands of the flying task of holding sustained "g" levels where the lift coefficient is 2.0 or more obscure any small differences in flying qualities that might result from the ACS system status. At incremental load factors below 0.4 where normal maneuvers are conducted these data provide no indication of a difference in handling qualities from ACS operation.

Pilot subjective evaluations and engineering data resulting from both the baseline and extended span flight tests indicate that the load alleviation active controls system operation causes no degradation from the baseline L-1011 handling qualities.

6.2 ACS HARDWARE OPERATION

During all ground and flight tests the Active Control System was monitored to insure that all functions were operating. In addition to the system status lights and failure annunciators, two 8-channel oscillograph recorders were used to monitor key parameters within the system including sensors, computational outputs, and series servo activity.

Although breadboard techniques were used in building the computers there were no electronic failures that caused delay or cancellation of any test. The only system failure occurring in flight was a runaway failure of one of the wingtip accelerometers after an extended de-energized cold soak at high altitude during the baseline tests. The possibility of this failure mode had been recognized earlier, based on the manufacturer's environmental specification for the accelerometer. The runaway on re-energizing the ACS was detected by the aileron monitor. Switching to single channel operation isolated the accelerometer, permitting testing to continue.

During ground and flight tests, motion of the pilot's control column was visually perceptible when large amplitude oscillatory signals were applied to the

pitch series servo. This motion had been observed earlier in the Vehicle System Simulator and was of some concern. However, none of the pilots noted any objectionable feedback or change in control characteristics while maneuvering the aircraft with the Active Control System engaged, either in or out of turbulence. All agreed that it was virtually impossible to tell when the Active Control System was engaged.

6.3 BENEFITS ANALYSIS

The aircraft efficiency benefits attributable to active controls are brought about indirectly by making an airframe improvement not otherwise possible. The improvements sought increase aircraft lift to drag ratio (L/D) with a minimal empty mass increase or, if possible, a reduction in empty mass compared to a conventional design. The two active control concepts addressed in this study have immediate energy efficiency benefits for the aircraft on which the research was conducted, the Lockheed L-1011. The techniques and applications evolved here also can be extended to permit similar benefits for other contemporary and future generation commercial transports.

6.3.1 Load Alleviation

Structural load alleviation, as demonstrated in Task 3 of this study, permitted the extension of the L-1011 wing span by a total of 9 feet. The resulting aspect ratio increase of 10 percent should theoretically reduce the induced drag or drag-due-to-lift by a like amount. Since the induced drag is roughly one third of the total drag during cruise, an overall L/D improvement of 3 percent or more was expected. Flight tests conducted concurrently with this program have demonstrated increased specific air range (SAR) sufficient to provide an increase in range of 3 percent with a given payload. A comparable span increase accomplished without active control load alleviation would require significant structural beef-up resulting in a total operating empty mass (OEW) increase of 1.25%. Although the same drag improvement would result, the additional structural mass penalty would reduce the mission fuel saving to less than half the increment achieved with active controls.

The wing span modification and load alleviation concept developed in Tasks 1 and 3 of this study have been incorporated into the design of a long range derivative of the L-1011. This derivative, the L-1011-500, has been purchased by several airlines and is scheduled to enter commercial service in the spring of 1980.

6.3.2 Relaxed Static Stability

A second near term derivative of the L-1011 which would employ active controls has been proposed. The horizontal tail area of this derivative will be considerably smaller thereby requiring augmented stability (AS) in pitch. The smaller tail would contribute 3 percent improvement in cruise L/D due primarily to reduced parasite drag. The small tail airfoil section is to be cambered to provide the best tail L/D at nominal cruise trim tail load unlike the current tail which has a symmetrical section. The tail cruise L/D improvement supplements the parasite drag reduction to provide the total 3 percent benefit. Figure 6-2 shows the trimmed cruise L/D ratio of the L-1011 with small tail as a function of c.g. relative to the L/D of the big tail airplane trimmed at 25 percent c.g. both based on wind tunnel data. At the same cruise c.g. (25 percent MAC) the 3 percent improvement due to the small tail is indicated. This would be the total benefit if the existing L-1011 c.g. envelope is retained.

Further improvement of 1 to 1.5 percent would be available from balance changes which move the c.g. envelope and hence the nominal trim c.g. back 5 percent from the present location. The resulting c.g. envelope would have its aft limit at the aerodynamic stability neutral point. This is attainable with current augmentation technology as demonstrated by the Task 2 simulator study, Volume 2 of this report.

6.3.3 Relaxed Stability For Advanced Technology Wings

Significant improvement in cruise aerodynamic efficiency is available from wings employing advanced airfoil sections. The design of these airfoils, in order to minimize the region of supercritical local velocity and avoid adverse pressure ratio sufficiently strong to induce separation, is characterized by considerable mean line camber well aft of mid chord. This design

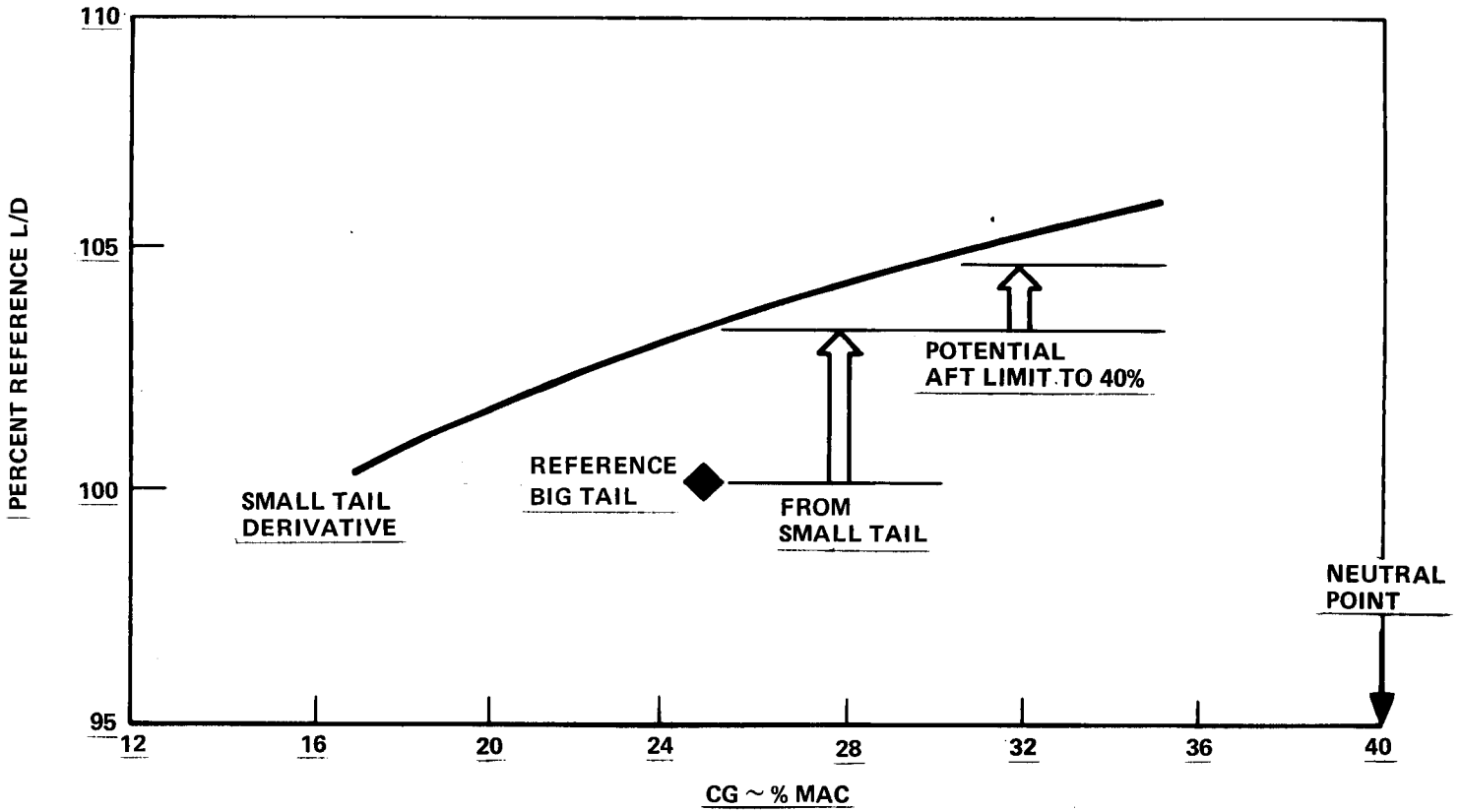

Figure 6-2. Relaxed Stability Benefit for Near Term Derivative Cruise L/D

characteristic results in the center of pressure at the design condition being farther aft than on a comparable conventional airfoil. Thus, benefits of advanced airfoils are reduced by trim drag unless the center of gravity is moved aft. To take full advantage of the benefits available from new generation wings, airplane c.g. limits must be located about 20 percent farther aft on the MAC than they are on current transports. This results in airframes which may be 10 to 15 percent statically unstable at the aft c.g. limit. Compared in Figure 6-3 are the trimmed cruise maximum L/D ratios obtained from wind tunnel tests for a current and an advanced technology subsonic transport wing. Both wings are optimized for the same design point and planform.

The reference L/D is defined at 25 percent MAC for the current technology wing. The advanced wing trimmed at 25 percent MAC has the same maximum L/D as the current wing, but if the trim c.g. is moved back to 45 percent MAC the advanced wing shows an advantage of 8 percent over the reference L/D and 3 percent over the state-of-the-art wing at the same aft trim c.g. To accomplish this the aft c.g. limit would be at approximately 50 percent MAC resulting in a 10 percent negative static margin.

To provide compensating pitch AS for such a configuration the system performance and reliability must exceed those of the current active control system evaluated in the Task 2 study. Development of advanced highly reliable active control systems and components should proceed concurrently with wing development for far term applications.

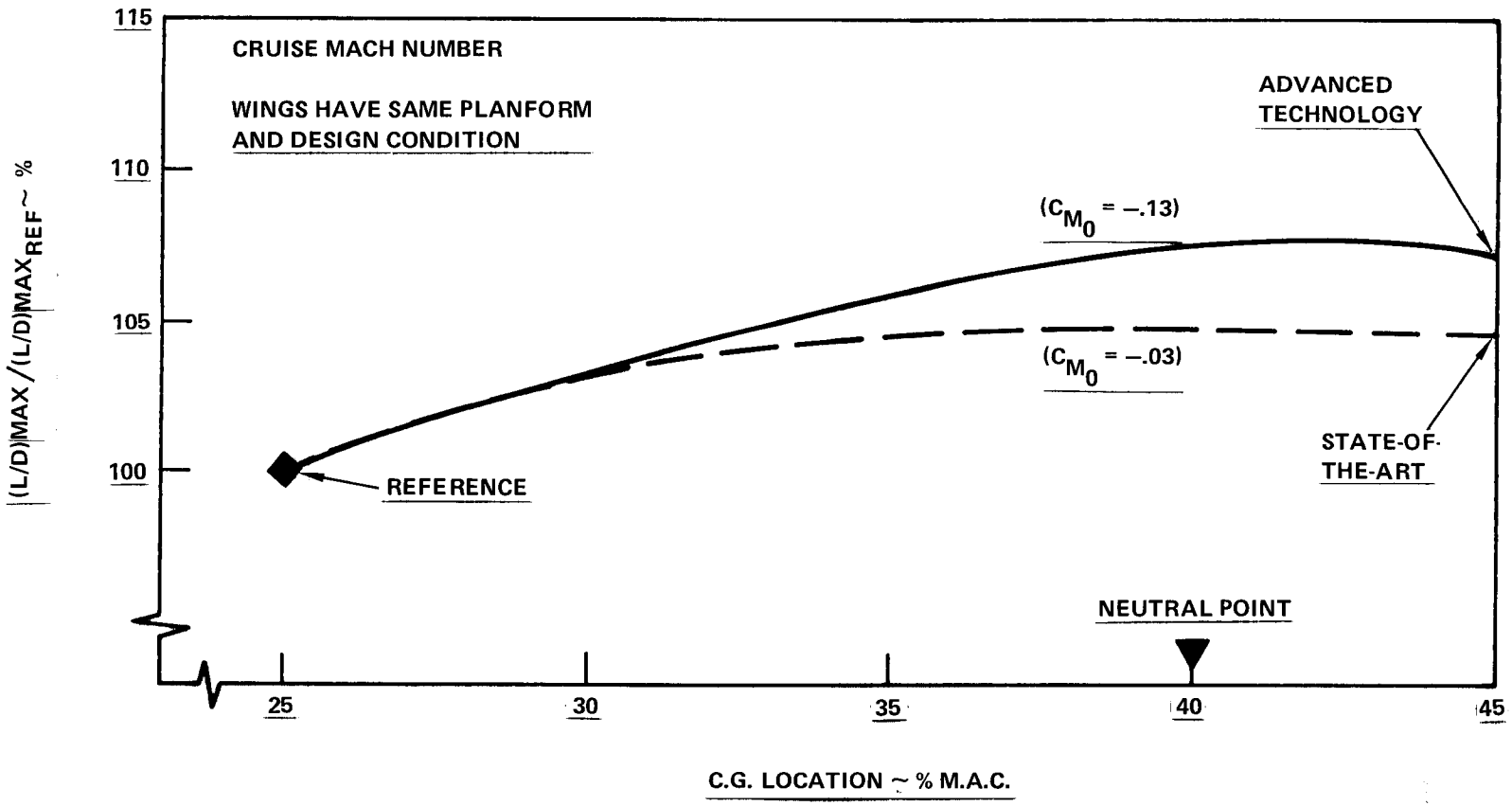

Figure 6-3. Relaxed Stability Benefit for Advanced Technology Wing

SECTION 7

CONCLUSIONS

Results of laboratory and flight tests and analysis of an active load alleviation system for the baseline and extended-span L-1011 aircraft have shown that:

1. The active control system provides the degree of wing load alleviation predicted by analysis, both for maneuvers and for gust encounters.

2. Where airplane elastic responses are involved, it is advisable to use the full production flutter and gust loads programs in deriving and verifying the load alleviation control laws.

3. Interactive graphics and their associated optimization techniques were effective tools in the above process.

4. The existing L-1011 data base and production mathematical techniques were adequate to describe the airplane static and dynamic responses and to prescribe the control laws.

5. The laboratory-developed breadboard active control system, containing fail-passive dual channels with monitoring and complete ground test/failure detection circuits, performed reliably, after initial burn-in, for its full 250 hours of laboratory testing and 70 hours of flight use. No tests were delayed by this system. A breadboard digital computer incorporated late in the program also performed reliably.

6. The ensemble of analytical techniques and active controls computers and hardware has provided a background for production use of active load alleviation with extended span for increased energy efficiency.

SECTION 8

REFERENCES

1. Flapper, J. A., and Throndsen, E.O.: L-1011 Flight Control System. AGARDograph AGARD-AG-224, April 1977.

2. Hoblit, F. M.: Effect of Yaw Damper on Lateral Gust loads in Design of the L-1011 Transport. Presented at 37th Meeting of the AGARD Structures and Materials Panel, The Hague, Netherlands, 7-12 October 1973.

3. Povinelli, F. P., Klineberg, J. M., and Kramer, J. J.: Improving Aircraft Energy Efficiency. AIAA Astronautics and Aeronautics, pgs. 18-31, February 1976.

4. Leonard, R. W., and Wagner, R. D.: Airframe Technology for Energy Efficient Transport Aircraft. SAE 1976 Transactions, Section 4, pgs. 2916-2931, September 23, 1977.

5. Johnston, J. F., and Urie, D. M.: Development and Flight Evaluation of Active Controls in the L-1011. NASA Conference Publication 2036, Part II, 1978.

6. Stauffer, W. A., Foss, R. L., and Lewolt, J. G.: Fuel Conservative Subsonic Transport. AGARDograph AGARD-AG-234, November 1978.

7. Ramsey, H. D., and Lewolt, J. G.: Design Maneuver Loads for an Airplane with an Active Control System. AIAA Paper No. 79-0738, April, 1979.

8. Harms, L. H.: L-1011 Tristar Vehicle Systems Simulator Test Program. SAE Paper AIR 1280, October 1972.

9. Stauffer, W. A., Lewolt, J. G., and Hoblit, F. M.: Application of Advanced Methods to Design Loads Determination for the L-1011 Transport. Journal of Aircraft, Vol. 10, No. 8, August 1973.

10. O'Connell, R. F., Hassig, H. J., and Radovcich, N. A.: Study of Flutter Related Computational Procedures for Minimum Weight Sizing of Advanced Aircraft. NASA CR-2607, March 1976.

11. Davis, W. J., Chiodi, O. A., and Rambin, R.: Practical Application of Optimal Control Theory. AIAA Paper No. 75-1030, August, 1975.

12. Luenberger, D. G.: An Introduction to Observers. IEEE Transactions on Automatic Control, Vol. AC-16, No. 6, December 1971.

13. O'Connell, R. F., and Messina, A. F.: Design, Development And Testing Of An Active Flutter Margin Augmentation System For A Commercial Transport Airplane. AIAA Paper No. 79-0790, April, 1979.

14. Graham, R. J.: Determination and Analysis of Numerical Smoothing Weights. NASA TR R-179, December 1963.

15. Houbolt, John C.; Steiner, Roy; and Pratt, Kermit G.: Dynamic Response of Airplanes to Atmospheric Turbulence Including Flight Data on Input and Response. NASA TR R-199, June 1964.

16. Keisler, Samuel R.; and Rhyne, Richard H.: An Assessment of Prewhitening in Estimating Power Spectra of Atmospheric Turbulence at Long Wavelengths. NASA TN D-8288, November 1976.

17. Eichenbaum, F. D.: Evaluation of 3-D Turbulence Techniques for Designing Aircraft. AFFDL-TR-74-151, March 1975.

1. REPORT NO.	2. GOVERNMENT ACCESSION NO.	3. RECIPIENT'S CATALOG NO.
NASA CR-159097		

4. TITLE AND SUBTITLE	5. REPORT DATE
ACCELERATED DEVELOPMENT AND FLIGHT EVALUATION OF ACTIVE CONTROLS CONCEPTS FOR SUBSONIC TRANSPORT AIRCRAFT VOLUME 1 - LOAD ALLEVIATION/EXTENDED SPAN DEVELOPMENT AND FLIGHT TEST	September 1979
	6. PERFORMING ORG CODE
7. AUTHOR(S)	8. PERFORMING ORG REPORT NO.
J. F. Johnston, et al	LR 29003-1
9. PERFORMING ORGANIZATION NAME AND ADDRESS	10. WORK UNIT NO.
LOCKHEED-CALIFORNIA COMPANY P.O. BOX 551 BURBANK, CALIFORNIA 91520	
	11. CONTRACT OR GRANT NO.
	NAS1-14690
12. SPONSORING AGENCY NAME AND ADDRESS	13. TYPE OF REPORT AND PERIOD COVERED
National Aeronautics & Space Administration Langley Research Center Hampton, Virginia 23665	Contractor Report
	14. SPONSORING AGENCY CODE

15. SUPPLEMENTARY NOTES

Final Report - Volume 1 (see CR 159098 - Volume 2)

16. ABSTRACT A cooperative NASA/Lockheed program investigated the use of active controls in a modern wide-body transport, the L-1011, for increased energy efficiency. This volume covers active wing load alleviation to extend the wing span by 5.8%, giving a 3% reduction in cruise drag. The active wing load alleviation used symmetric motions of the outboard ailerons for Maneuver Load Control (MLC) and Elastic Mode Suppression (EMS), and stabilizer motions for Gust Load Alleviation (GLA). The control laws were derived, after initial exploration of optimal control theory, with the aid of large-scale maneuver loads, flutter and gust loads programs. Results of laboratory tests showed good agreement with analysis. Slow maneuvers verified the MLC, and open- and closed-loop flight frequency response tests verified the aircraft dynamic response to symmetric aileron and stabilizer drives as well as the active system performance. Flight tests in turbulence verified the effectiveness of the active controls in reducing gust-induced wing loads. It was concluded that active wing load alleviation/extended span is proven in the L-1011 and is ready for application to airline service; it is a very practical way to obtain the increased efficiency of a higher aspect ratio wing with minimum structural impact.

17. KEY WORDS (SUGGESTED BY AUTHOR(S))	18. DISTRIBUTION STATEMENT
Active Controls Load Alleviation Gust Load Reduction Maneuver Load Control Elastic Mode Suppression	FEDD Document

19. SECURITY CLASSIF. (OF THIS REPORT)	20. SECURITY CLASSIF. (OF THIS PAGE)	21. NO. OF PAGES	22. PRICE*
Unclassified	Unclassified		